Dynamic Magnetism and Magnetisation Topology in Artificial Spin Ice

Yue Li

Submitted in fulfilment of the requirements for the

Degree of Doctor of Philosophy

School of Physics and Astromony

College of Science and Engineering

University of Glasgow

August 2018

Dedicated to my family.

"Imagination is more important than knowledge. Knowledge is limited. Imagination encircles the world."

Albert Einstein

Abstract

Artificial spin ice (ASI) is a class of magnetic patterned arrays consisting of interacting ferromagnetic nanomagnets. The nano-scale size and the elongated shape of each nanomagnet ensure the formation of a single domain, which behaves as a 'macrospin' and results in only two possible magnetisation directions along the long axis of the nanomagnet. ASI system has the potential ability not only as a magnonic crystal because of the microwave properties being associated with its intrinsically intricate magnetisation topologies and inter-element interaction, but as a tool to model the microstructure of atomic scale allowing its fundamental physics to be studied.

This thesis addresses the field-induced properties of the static and dynamic magnetisation in square and pinwheel ASI. Firstly, the magnetic properties of the square ASI specimens were characterised using alternating gradient force magnetometry, Brillouin light scattering and ferromagnetic resonance. Micromagnetic simulations were employed to assist in understanding the experimental results. Secondly, the field-induced evolution of the magnetisation configuration in a finite-size pinwheel ASI array was imaged using Lorentz transmission electron microscopy.

The square structure of the square ASI lattices allows a comparison of the response of the spin-wave modes in the two groups of magnetic elements which are orthogonally aligned to one another. The frequency of the spin-wave mode is dependent on the direction of the applied field, either along the easy or hard axes of the nanomagnet. It has been found that more spin-wave modes are found when the magnetic field lies along the hard axis of the nanomagnet compared to when the field is aligned with the easy axis of the island. This attributes to the formation of more edge modes of standing spin waves in the former case. The experimental behaviour of the static and dynamic magnetisation

can be well described via the micromagnetic simulations where only an individual island is considered with an assumption that the inter-island interaction is negligible. Additionally, the field direction with respect to the square ASI lattices is also responsible for the changes in spin-wave frequencies. The results imply that the square ASI could act as a reconfigurable microwave resonator due to its spin-wave frequency being dependent on the changes in magnetisation configuration that were controlled by the applied field.

The dependence of the nanomagnet thickness on the static and the dynamic properties of the square ASI was studied. The nanomagnet thickness is found to be responsible for the coercivity and the number of observed spin-wave modes of the square ASI array. The thicker ASI array has a larger coercive field and produces more spin-wave modes. Micromagnetic simulations suggest that the inter-island coupling contributes weakly to the coercivity and the spin-wave frequency of the thicker array whereas it is negligible for a thinner array. Furthermore, fitting to ferromagnetic resonance data allows for access to information on ferromagnetic parameters, such as gyromagnetic ratio and saturation magnetisation.

Finally, static and dynamic magnetisation topologies in a pinwheel ASI is explored as a function of magnetic field. The pinwheel ASI is a square ASI modified by rotating each nanomagnet 45° around its central axis in the same direction. The energy spread between the pinwheel vertices significantly decreased as the geometrical structure transforms from the square vertices to the pinwheel vertices. The ferromagnetic magnetisation process shows the domain growth mediated via the propagation of domain walls. Intriguingly, some of the observed mesoscopic domain-wall topologies resemble the Néel and the cross-tie walls seen in natural ferromagnetic films, while others mimic the configurations of the charged walls found in the ferroelectric materials. In addition, a rotational-field demagnetisation was carried out in order to anneal the pinwheel ASI to the ground state. The results show that the net moment of the entire array decreases and the short-range ground state is attained through the presence of the vortices (Type III) and antivortices (Type IV) vertices, rather than the global Landau-like flux closure structure predicted by Monte Carlo simulations.

Declaration

The work of this thesis is primarily conducted within the Materials and Condensed Matter Physics Group of School of Physics and Astronomy at the University of Glasgow during a period spanning from 2014 to 2018. The work herein is my own, except for where specific reference is cited to the work of others. The contributions from other collaborators on a part of experiments and simulations are listed as follow:

- Prof. Christopher Marrows and Dr. Sophie Morley, who are from the Condensed Matter Physics Group, School of Physics and Astronomy, University of Leeds, UK, provided the square ASI and a part of pinwheel ASI samples in Chapter 4, Chapter 5 and Chapter 6.

- Dr. Francesca Casoli, from the Institute of Materials for Electronics and Magnetism, Italian National Research Council, Italy, carried out the hysteresis loops measurements for the 10 nm and 30 nm thick square ASI specimens using alternating gradient force magnetometry in Chapter 4 and Chapter 5.

- Dr. Gianluca Gubbiotti from Istituto officina dei Materiali, Italian National Research Council, Italy, conducted the measurements of the 10 nm and 30 nm thick square ASI samples using Brillouin light scattering in Chapter 4 and Chapter 5.

- Dr. Francisco J T Gonçalves and myself performed the ferromagnetic resonance measurements and the analysis of data.

- Dr. Ciaran Ferguson fabricated the remaining pinwheel ASI samples in Chapter 6 in the James Watt Nanofabrication Centre at the University of Glasgow.

- Dr. Gary Paterson, Dr. Sam McFadzean and myself carried out the data acquisition related to the Lorentz TEM measurements in Chapter 6. Dr. Gary Paterson and myself conducted data analysis of Lorentz TEM measurements in Chapter 6.

- Prof. Fabio S Nascimento from the Department of Physics of Federal University of Vi(c)osa, Brazil, computed pinwheel vertex energy in Table 6.1 using Monte Carlo method. Mr. Gavin Macauley evaluated the pinwheel vertex energy in Table 6.1 using MuMax micromagnetic simulation.

- Dr. Ciaran Ferguson, Dr. Gary Paterson and myself performed the experiment of AC-field demagnetization protocol in Chapter 6.

Some of work presented in this thesis are parts of following publications:

1. **Brillouin light scattering study of magnetic-element normal modes in a square artificial spin ice geometry**, Y. Li, G Gubbiotti, F Casoli, F J T Gonçalves, S A Morley, M C Rosamond, E H Linfield, C H Marrows, S McVitie and R L Stamps, Journal of Physics D: Applied Physics, 50, 2017, 015003.

2. **Thickness dependence of spin wave excitations in an artificial square spin ice-like geometry**, Y. Li, G Gubbiotti, F Casoli, S A Morley, F J T Gonçalves, M C Rosamond, E H Linfield, C H Marrows, S McVitie and R L Stamps, Journal of Applied Physics, 121, 2017, 103903.

3. **Ferromagnetism and domain wall topologies in artificial 'pinwheel' spin ice**, Yue Li, Gary Paterson, Fabio S Nascimento, Ciaran Ferguson, Gavin Macauley, Sophie A Moreley, Donald A MacLaren, Christopher H Marrows, Stephen McVitie and Robert L Stamps (in preparation).

None of work reported in this thesis have been submitted for any other degree or qualification.

Acknowledgements

First, I would like to acknowledge my supervisor Prof. Robert Stamps, who offered me a great opportunity to work in the Glasgow. You have proposed numerous amazing ideas and insightful opinions to me throughout my PhD. I thoroughly enjoyed working with you. I would also like to thank my supervisor Dr. Stephen McVitie for your academic supervision and general encouragement. You always encouraged me to be optimistic and confident, which is invaluable in my life.

A special and big thanks must be given to my external collaborators, who provided great and generous help to me in the artificial spin ice project. Dr Sophie Morley, thank you for providing the expertise in sample fabrication for this thesis and making my time on the beamline time and at the MMM conference so much fun. Prof. Christopher Marrow, thanks for your considered guidance. Dr. Jose Maria Porro, it is a a pleasure for me to learn the x-ray technique with you in Diamond Light Source. I would particularly like to thank Dr. Gianluca Gubbiotti and Dr. Francesca Casoli, who provided the BLS and AGFM measurements in this thesis.

I am grateful to Dr. Francisco Gonçalves and Dr. Gary Paterson who patiently tutored me in the lab and showed me how to utilise Python to analyse data. Spin-ice guys, Gavin Macauley and Dr Rair Macedo, must be mentioned for their constructive discussions and great collaborations. I especially thank you for the patient proofreading of my thesis. Dr Sam McFadzean, Colin How and Billy Smith, thank you for the outstanding technical help and the tolerance to a lot of mistakes made by an "equipment killer" (my). My gratitude also needs to be given to Dr. Damien McGrouther and Dr Donald MacLaren for introducing me to TEM, and for the assistances in the lab as well. I need to say cheers to my office mates and all MCMP group members who helped cultivate a relaxing

but focused team environment to work in and allowed me to quickly adapt to a different culture.

Finally, a huge thanks to my family and friends. Thank my family for their love and support. Thanks to my best friend, Yingya Li, who has been companioning, supporting and encouraging me for the last 14 years ago. I also want to say thanks to my friends in Glasgow, Jiayu Zhan, Yixuan Zhu, Danyang Wang and Yaqi Ding, who organised a variety of entertainment which gave me a lot of fun memories.

Contents

List of Figures

List of Tables

Abbreviations

AGFM	Alternating Gradient Force Magnetometer
ASI	Artificial Spin Ice
BF	Bright Field
BFP	Back Focal Plane
BLS	Brillouin Light Scattering
CCD	Charged Coupled Device
CL	Condensed Lens
CTEM	Conventional Transmission Electron Microscopy
DF	Dark Field
DP	Diffraction Pattern
DPC	Differential Phase Contrast
EELS	Electron Energy Loss Spectroscopy
FEG	Field Emission Gun
FIB	Focused Ion Beam
FMR	Ferromagnetic Resonance
FPI	Fabry-Petot interferometer

LLG Landau-Lifshitz-Gilbert

LTEM Lorentz Transmission Electron Microscopy

OL Objective Lens

PBC Periodic Boundary Condition

TEM Transmission Electron Microscopy

STEM Scanning Transmission Electron Microscopy

VNA Vector Network Analyser

1

Thesis overview

1.1 Introduction

With the turn of the millenium came an upsurge in interest in novel artificial spin structures which emerge from geometric frustration [1]. This type of frustration is usually referred as occurring when the constraint of the lattice topology prevents the system from minimising all its interaction energies [2]. Consider simple square and triangular antiferromagnetic spin systems, such as those shown in Figs. 1.1 (a) and (b), respectively. These have spins sited at each corner and the systems will have minimal energy when all spins are aligned antiparallel to all its adjacent neighbours. In the case of the square lattice, any spin can be antiferromagnetically aligned with all its nearest neighbours and, as a result, the energy of the system is completely minimised. On a triangular lattice, however, once two of three spins align antiparallel to one another, the third spin is no longer able to anti-align with both its neighbours simultaneously. Such system is said to be frustrated.

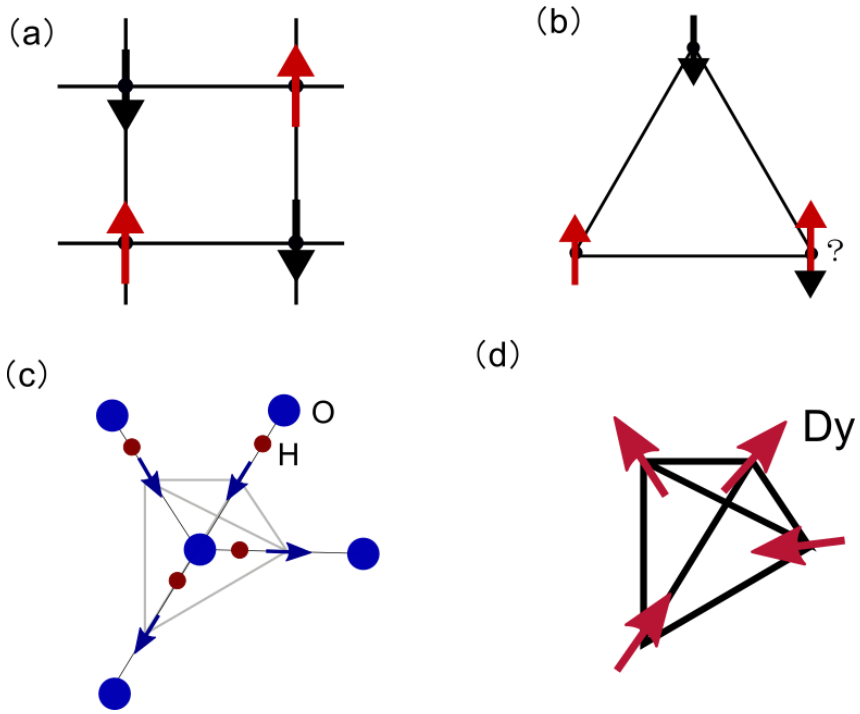

Figure 1.1: Schematic representations of antiferromagnetic systems where (a) total minimisation of energy is achieved and (b) geometric frustration is obtained [2]. Illustration of the ice rule for the (c) frozen water and the (d) spin ice [3]. The lowest-energy state of a water-ice tetrahedron has a configuration where the directions of electrostatic interactions (the dark blue arrows) at two ends at the tetrahedron point toward to the central oxygen whereas the other two point away from it. Equivalently, (d) the ground state of an individual spin-ice tetrahedron also has the 'two-in-two-out' spin configuration.

The first evidence of frustration was uncovered in frozen water in the year of 1935 [4]. In this case, the frustration arises from the inequivalent bonding distances between oxygen and hydrogen atoms in a frozen-water tetrahedron. A tetrahedral molecular structure of the ground-state water ice is shown in Fig. 1.1 (c) where two hydrogen ions are close to the central oxygen whereas the other two are sited far away. Consequently, the electrostatic interaction of the lowest energy at this tetrahedron lattice has a 'two-in-two-out' configuration, named as 'ice rule'. A given water ice tetrahedron provides six-fold-degenerate ground state, all obeying the so-called 'ice rule'. This led to the discovery of several intriguing phenomena, such as residual entropy at the lowest-energy state. L. Pauling [4] evaluated the residual entropy S of the N number water molecules as $S = k_B N/2\ln(3/2)$, where k_B is the Boltzmann constant.

Decades after the discovery of frustration in water ice, a similar behaviour was found in rare earth materials, such as pyrochlore $Dy_2Ti_2O_7$ [5, 6] and $Ho_2Ti_2O_7$ [7, 8], known as 'spin ice'. Pyrochlore materials possess the net ferromagnetic interaction between

nearest spins at each end tetrahedron. The spins point toward or away from the centre of this tetrahedron due to the strong crystalline anisotropy forcing them along the <111> axis [7, 9]. Figure 1.1 (d) shows a schematic magnetisation configuration of a single tetrahedron in the $Dy_2Ti_2O_7$ spin ice material at its lowest energy where two spins point toward the centre while the other two direct away from it. This configuration is considered to be analogous to the ground-state configuration of water ice so that it satisfies the 'ice rule'. The interesting physical phenomenon found in both water ice and spin ice materials, such as remnant entropy at the lowest state [4, 5], inspired the seminal work at the University of Pennsylvania. A synthetic 'spin-ice' system was proposed.

1.2 Artificial spin ice

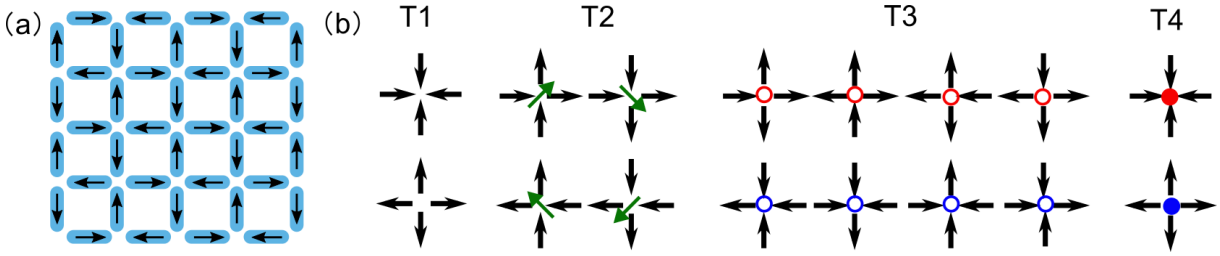

Figure 1.2: (a) Diagram showing the ground-state magnetisation configuration of a square ASI array. (b) Sixteen possible magnetisation topologies for a square vertex. Vertex energy increases from the T1 to the T4 structures, the green arrow representing the maximum net moment of the T2 vertex; the blue (red) disk indicating the presence of net negative (positive) charges. The circle illustrates the two net charges of the T3 vertex and the filled disk represents the four-charge T4 vertex.

In 2006, R. F. Wang *et al.* pioneered artificially engineering a two-dimensional ferromagnetic array that could be coupled to mimic the magnetic behaviour of spin ice media [1], and therefore called it as 'artificial spin ice (ASI)'. This ASI array was composed of interacting ferromagnetic mono-domain nanomagnets arranged into the so-called square lattice (see Fig. 1.2 (a)). Each nanomagnet has nano-scale size and elongated shape (the in-plane dimension and the thickness of the island are 80 nm × 220 nm and 25 nm) to ensure its magnetic moment to point to one of the two possible directions along the long axis. The unique orientation of the magnetic moments in the nanomagnet forms a single domain, thus, acting as a 'macrospin'. The properties of square ASI systems are usually described in terms of the ASI vertices. The vertex is defined as four nanomagnets meeting head on, as illustrated in Fig. 1.2 (b). All square vertices can be

classified into four types according to their energy and referred as 'T1', 'T2', 'T3' and 'T4'. Vertex energy increases from the T1 to the T4 vertices. T1 is the ground state and has the 'two-in-two-out' ice-rule configurations, with no net magnetic moment and no charge. The emergence of frustration, in this case, is due to its intrinsic magnetisation topology. In particular, the head-to-tail (or tail-to-head) magnetisation alignment between the first nearest neighbours is energetically favourable, while the head-to-head (or tail-to-tail) magnetisation alignment between the second nearest islands cost energy. This lowest-state cannot satisfy all system interactions at the same time. T2 vertices also obey the ice rule and thus have no magnetic charge, but they possess net moments. T3 vertices, 'three-in-one-out' magnetisation configuration, possess the net magnetic charges which lead to an interesting novel phenomenon known as the topological defect of emergent 'monopole'. T4 vertices are the highest energy states with four net magnetic charges and they are not often observed in experiment.

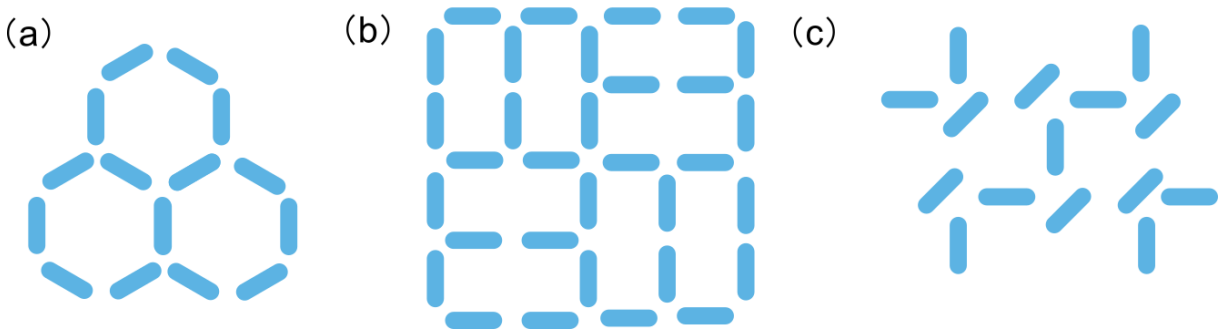

Figure 1.3: Different ASI geometries: (a) Kagome, (b) Shakti and (c) modified square.

One of promising aspects of ASI research is the capability of easily manipulating the systems magnetic degrees of freedom. For example, magnetic moment, shape anisotropy, inter-element interaction and array geometry can be controlled via the volume, shape, lattice constant and position of the nanomagnet. This flexible manipulation has been achieved due to recent advances in electron-beam lithography, a nanofabrication technique. Current studies of ASI are not only focused on fundamentally physical aspects [1,10–13], but also on potential applications [14]. In the former case, a variety of topological structures have been realised, such as Kagome [15–19] (Fig. 1.3 (a)), Shakti [20, 21] (Fig. 1.3 (b)) and modified square lattice [14] (Fig. 1.3 (d)). These systems are responsible for the emergence of a number of exotic properties, including a variety of multifold-degeneracy ground states [1,13,17,22], monopole mobility [18,23,24] and magnetic charge

ordering [15, 23, 25].

In addition to the geometry of ASI arrays, the composition of nanoelements has also gained interest. For example, the magnetic soft transition metals commonly used to fabricate ASI, such as iron, nickel and cobalt, exhibit high-frequency spin-wave resonances in the GHz range. This spin-wave excitation is sensitive to underlying magnetisation configurations. Therefore, the possibility of generating new functionality, namely, the potential for ASI to behave as a reconfigurable microwave resonator, was explored by combining the geometric and dynamic properties of ASI [26–28].

1.2.1 Athermally and thermally dynamic response of ASI

Studies of dynamic response of magnetisation in ASI usually falls into two categories: thermal and athermal dynamics. The former is driven by temperature and the latter is introduced by external magnetic fields at a fixed temperature. So far these studies mainly focused on understanding how to access the ground state of ASI and utilising it as a tunable resonator. The study of dynamics of both the micro-magnetisation (of individual nanomagnet) and collective magnetisation (of coupled macrospins in an array) is a crucial step to understand such thermal and athermal processes.

In such an artificially frustrated system, a great deal of work has attempted to access the lowest-energy state via annealing protocols [1,11,12,29]. In this respect, the two most used methods are athermal AC-field demagnetisation [1, 30–32] and thermal relaxation demagnetisation [12,17,33–35]. The rotational-field protocol only enables the square ASI system to approach the short-range low-energy state, with the presence of high-energy vertices (T3 and T4), while thermal annealing allows for the achievement of the long-range order [35]. A. Farhan *at el.* [12] address the potential energy landscapes of thermal-annealing processes in three finite-size Kagome ASIs (involving one, two and three Kagome rings). This study explicitly shows the magnetisation evolution of the macrospins of the islands from an excited state to a lowest energy state in real time and shows that the nature of the magnetisation configurational changes depends on the complexity (number of the Kagome rings) of the Kagome ASI system.

A variety of magnetisation topologies in an ASI system have been proposed to have potential as reconfigurable microwave devices [23, 27, 28, 36, 37, 37–40]. It has been predicted that the significant variation in magnetisation dynamic frequency is dependent on

the changes of magnetisation topologies, which is, in particular, associated with the number of the topological defects consisting of 'monopole' and Dirac string topologies [23]. This result and other similar works [27, 36, 37] suggest the possibility of employing ASI in reconfigurable resonator as they display the dependence of magnetic dynamics on the underlying magnetisation configuration. It should also be mentioned that X. Zhou *et al* [28] systematically explored how the static and dynamic magnetisation responses rely on the intrinsically geometrical arrangements of nanomagnets (see the insets of Fig. 1.4). They also reversed the structures of ASI, the nonmagnetic ASI-geometry hole embedded in a continuous magnetic thin film, and referred to it as anti-ASI geometry (in a similar manner to the well-studied antidot [41]). In Fig. 1.4, one can observe geometry- and anisotropy-dependent variance in the resonance modes measured using ferromagnetic resonance.

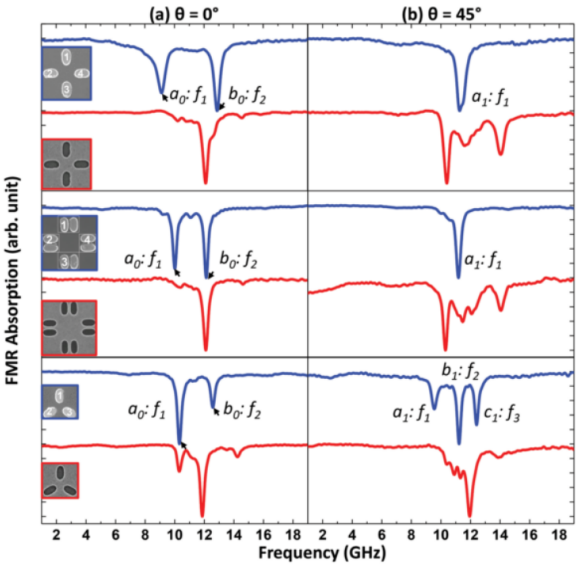

Figure 1.4: Ferromagnetic resonance spectra for artificial spin ice and anti-spin ice at 0° and 45° applied fields with amplitude of 1400 Oe with respect to ASI lattices. It shows how geometries of ASI systems influence the dynamic response [28]. Copyright (2016) by the John Wiley and Sons.

1.2.2 Mesoscopic domain and domain wall in ASI

A magnetic domain is usually referred to as the region where all magnetic moments point in the same direction. A domain wall is a boundary separating two domains possessing the different magnetisation orientations. Even though these are most commonly known as a property of continuous media, the analogous formation of domains has been shown to be of

fundamental importance when studying the magnetisation dynamics of the ASI system. Because it is well-established that the magnetic moment of an individual nanomagnet acted as an Ising spin, the mesocopic domain and domain wall were proposed in an attempt to describe the evolution of ground state and excited state in such systems. Additionally, the understanding of 'domain' and 'domain wall' allows, to a large extent, to address the magnetisation dynamic response of ASI to the magnetic field or temperature [42, 43].

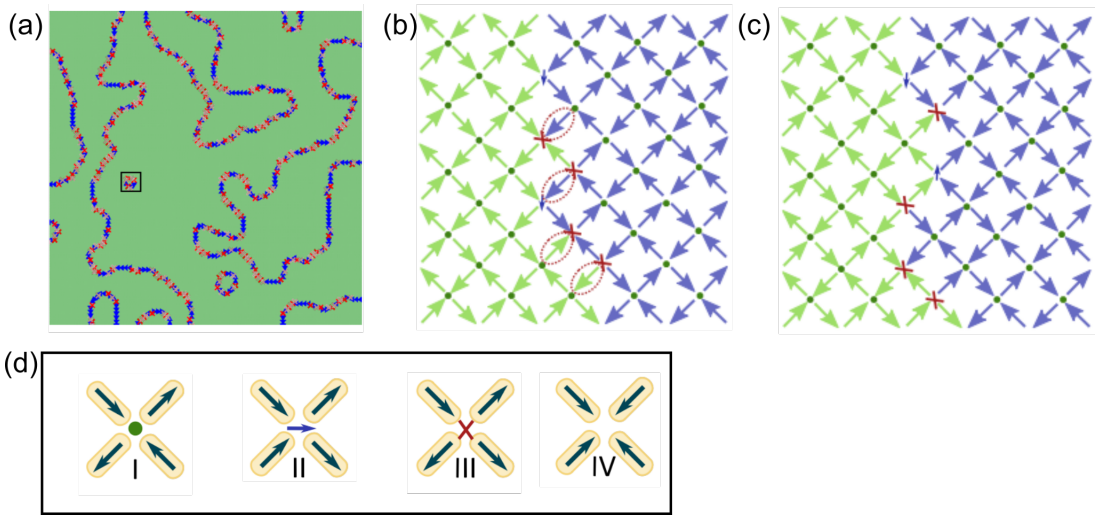

Figure 1.5: (a) An example of a simulated magnetisation map using Monte Carlo simulations which shows the domain (green region) consisting of type I vertices separated by the domain walls that are constructed by type II and type III vertices. Random domain wall motion from (b) to (c) which is mediated by the creation and annihilation of the type III vertices. (d) Examples of the four categories of vertices magnetisation configurations and the symbols in the centre represents the vertex magnetisation maps given in the (a), (b) and (c) [44].

The formation of such domains and domain walls is described in terms of the net moments of vertices [22, 33, 44–46]. For example, one-dimensional boundaries, constructed by excited square vertices, were observed separating domains [33] consisting of T1 vertices. Monte Carlo simulations performed by Z Budrikis *et al.* [33] provide insights on the formation and evolution of these mesoscope domains and domain walls. The simulated magnetisation maps (Fig. 1.5 (a)) obtained at finite temperature also showed great agreement with experimental results as shown by Morgan *et al* [33]. Results show that domains are formed by the ground state vertices (type I) and domain walls are formed by the higher energy vertices (type II and type III). The dynamics of domain walls led to the domain growth (or shrinkage). In addition, it was found that domain wall nucleation always starts at the dislocation, which refers to array edge or a so-called defect point where three islands meet on the square-ASI background aiming to create different frustration in

a system [46].

1.3 A novel geometry

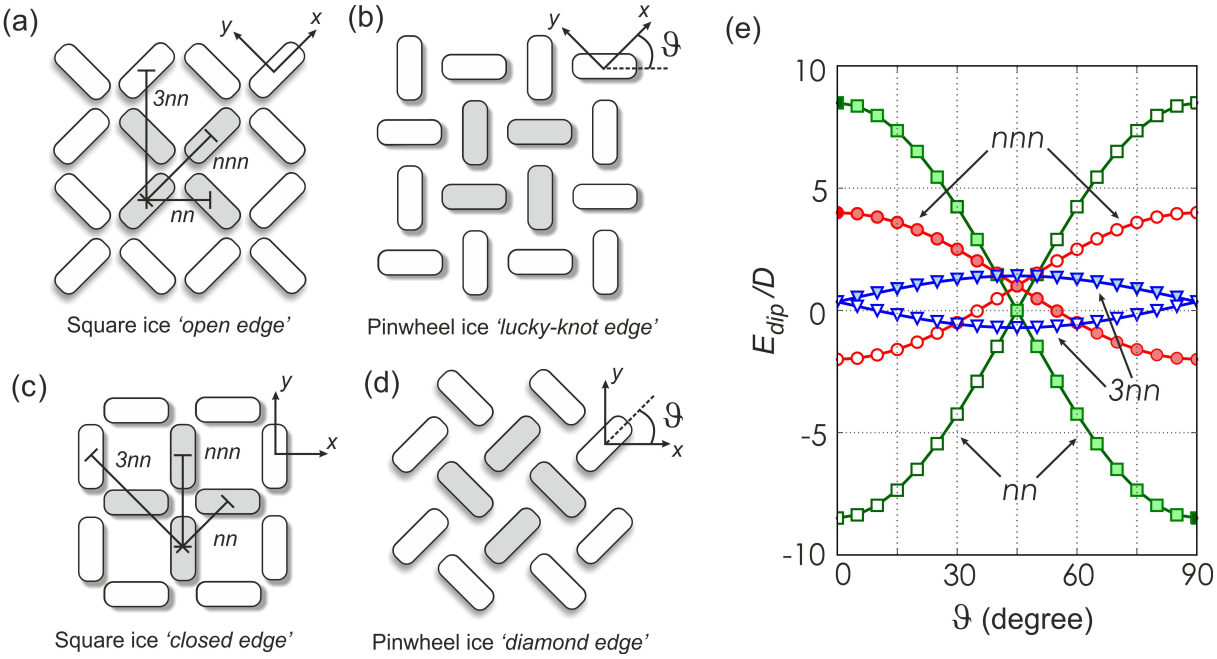

Figure 1.6: Artificial spin ice geometries and their neighbouring interaction: Square ice lattice arrangements with (a) 'open edges' and (c) 'closed edges'. Respective arrangements, when the rotation angle $\alpha = 45$ ° named 'pinwheel' ice, with (b) 'lucky-knot' edges and (d) 'diamond edges'. (e) Dipolar energy for nearest-neighbours (nn), next-nearest-neighbours (nnn) and third-nearest-neighbours (3nn) as a function of rotation angle α. The lattice constant a is taken as the distance between nnn spins. Open symbols are for favourable arranged spin pairs and closed symbols are for unfavourable arranged spin pairs [47].Copyright (2018) by the American Physical Society, DOI: http://dx.doi.org/10.1103/PhysRevB.98.014437.

Recently, a new type of ASI has emerged, *pinwheel* spin ice. This ASI can be obtained through rotating each island of the square ASI around its central axis by 45° and has 'pinwheel'-shape vertex. Figures 1.6 (a-d) show the rotation processes from square ASI arrays with the open and closed edges to pinwheel ASI arrays. Interestingly, this simple rotation leads to significant changes in dipolar interaction between neighbouring spin pairs [47]. In Chapter 6, the energies and details of the pinwheel vertices will be displayed.

S. Gliga [10] found the emergence of collectively chiral rotation in a finite-size pinwheel ASI array, which was designed to be structurally chiral, as illustrated by the white (or black) array in Fig. 1.7. Chiral dynamics refers to the presence of a preferred sense of rotation in the course of thermal relaxation, which exhibits that the average net moment always rotates in a clockwise sense rather than anticlockwise sense (see Fig. 1.7). Micro-

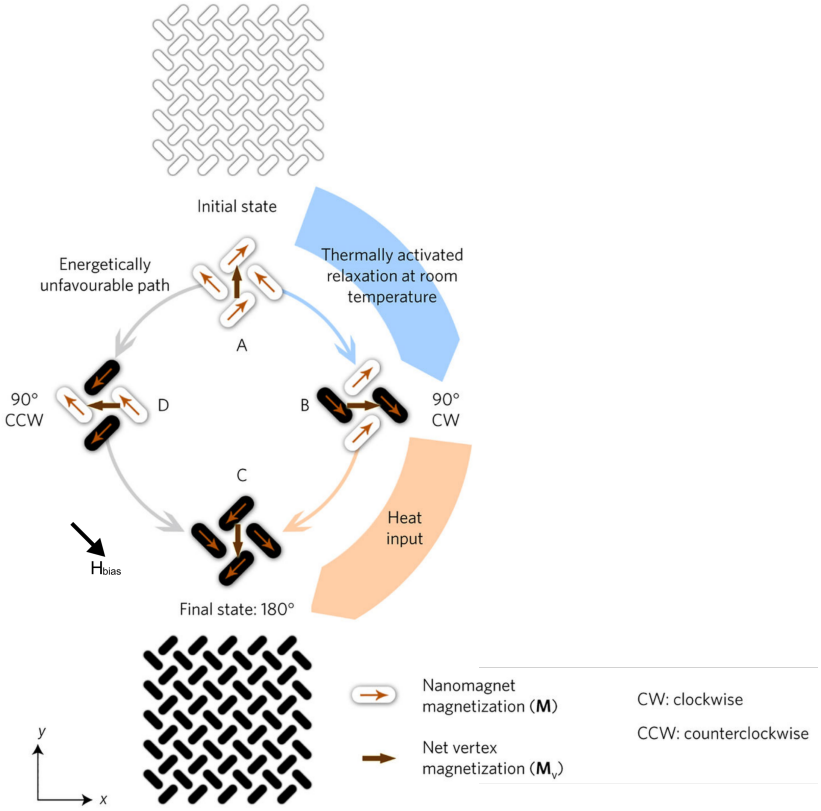

Figure 1.7: Schematic illustration of the evolution of the net magnetisation at an individual 'pinwheel' vertex in an array [10]. The collective rotation in terms of the vertex moment undergoes in a unique clockwise sense from state A to B, and will continue after being subject to a thermal treatment (heating sample by several Kelvins). In the whole experimental process, there is a bias magnetic field with amplitude between 50 μT and 80 μT. Copyright (2017) by the Springer Nature.

magnetic simulation explains that asymmetric stray fields at the edges of this array are responsible for such unidirectional behaviour.

1.4 Thesis outline

This thesis aims to explore the athermal magnetisation dynamics in square and pinwheel ASI systems. This investigation has been conducted using a combination of experiments and simulations. The static and dynamic magnetisation behaviours of square ASI were characterised using alternating gradient force magnetometry, Brillouin light scattering and ferromagnetic resonance techniques. Micromagnetic simulations based on Mumax were also employed to reproduce and understand the experimental results. Finally, the magnetisation process of pinwheel ASI was imaged using Lorentz transmission electron microscopy.

In Chapter 2, the relevant physical principles of nanomagnetism are introduced. This involves aspects of energy terms, domain walls and phenomena of magnetisation dynamics.

In Chapter 3, descriptions of the sample fabrication process and the theories of the experimental instruments used in this thesis are provided, including alternating gradient force magnetometry, Brillouin light scattering, ferromagnetic resonance and transmission electron microscopy. Basic concepts and performance of micromagnetic simulation throughout this thesis are also addressed.

In Chapter 4, experimental and numerical static magnetisation properties and spin-wave behaviour are displayed. Results show that they are strongly dependent upon the field angle with respect to square ASI lattices. The dynamic response of magnetisation to the shape anisotropy of individual nanomagnets is also discussed.

In Chapter 5, the dependence of static and dynamic magnetisation of square ASI on nanomagnet thickness is examined. The nanomagnet thickness is responsible for a substantial variation in the frequency and the number of spin-wave modes. A comparison between experimental results and micromagnetic simulations is presented. The final part of this chapter concentrates on the possibility of dynamic coupling due to the strength of the magnetostatic interaction (determined by the separation between nanomagnets).

In Chapter 6, athermal dynamics in a finite-size pinwheel ASI array is explored. This pinwheel lattice has been predicted to be a highly-degenerate system with very similar energies for all vertex types. The formation of the mesoscopic walls were observed during magnetisation reversal, including domain walls that analogise ferromagnetic Néel walls and some unusual charged walls. In addition, the proprieties of such mesoscopic walls are qualitatively and quantitatively discussed. These domain walls show dependences on the angle of magnetic field with respect to the array.

Lastly, in Chapter 7, a summary of this thesis and relevant future work is presented.

Bibliography

[1] R F Wang, C Nisoli, R S Freitas, J Li, W McConville, B J Cooley, M S Lund, N Samarth, C Leighton, V H Crespi, et al. Artificial 'spin ice' in a geometrically frustrated lattice of nanoscale ferromagnetic islands. *Nature*, 439(7074):303, 2006.

[2] R Moessner and A P Ramirez. Geometrical frustration. *Phys. Today*, 59(2):24, 2006.

[3] C Castelnovo, R Moessner, and S L Sondhi. Spin ice, fractionalization, and topological order. *Annu. Rev. Condens. Matter Phys.*, 3(1):35, 2012.

[4] L Pauling. The structure and entropy of ice and of other crystals with some randomness of atomic arrangement. *Journal of the American Chemical Society*, 57(12):26804, 1935.

[5] A P Ramirez, A Hayashi, R al Cava, R Siddharthan, and B S Shastry. Zero-point entropy in 'spin ice'. *Nature*, 399(6734):333, 1999.

[6] B C den Hertog and M J P Gingras. Dipolar interactions and origin of spin ice in ising pyrochlore magnets. *Physical Review Letters*, 84(15):3430, 2000.

[7] M J Harris, S T Bramwell, D F McMorrow, T Zeiske, and K W Godfrey. Geometrical frustration in the ferromagnetic pyrochlore $Ho_2Ti_2O_7$. *Physical Review Letters*, 79(13):2554, 1997.

[8] R G Melko, Byron C den Hertog, and M J P Gingras. Long-range order at low temperatures in dipolar spin ice. *Physical Review Letters*, 87(6):067203, 2001.

[9] C Castelnovo, R Moessner, and S L Sondhi. Magnetic monopoles in spin ice. *Nature*, 451(7174):42, 2008.

[10] S Gliga, G Hrkac, C Donnelly, J Büchi, A Kleibert, J-Z Cui, A Farhan, E Kirk, R V Chopdekar, Y Masaki, et al. Emergent dynamic chirality in a thermally driven artificial spin ratchet. *Nature Materials*, 16(11):1106, 2017.

[11] J C Gartside, D M Arroo, D M Burn, V L Bemmer, A Moskalenko, L F Cohen, and W R Branford. Realization of ground state in artificial kagome spin ice via topological defect-driven magnetic writing. *Nature Nanotechnology*, 13(1):53, 2018.

[12] A Farhan, P M Derlet, A Kleibert, A Balan, R V Chopdekar, M Wyss, L Anghinolfi, F Nolting, and L J Heyderman. Exploring hyper-cubic energy landscapes in thermally active finite artificial spin-ice systems. *Nature Physics*, 9(6):375, 2013.

[13] D Shi, Z Budrikis, A Stein, S A Morley, P D Olmsted, G Burnell, and C H Marrows. Frustration and thermalisation in an artificial magnetic quasicrystal. *Nature Physics*, 14:309, 2018.

[14] Y-L Wang, Z-L Xiao, A Snezhko, J Xu, L E Ocola, R Divan, J E Pearson, G W Crabtree, and W-K Kwok. Rewritable artificial magnetic charge ice. *Science*, 352(6288):962, 2016.

[15] B Canals, I-A Chioar, V-D Nguyen, M Hehn, D Lacour, F Montaigne, A Locatelli, T O Menteş, B S Burgos, and N Rougemaille. Fragmentation of magnetism in artificial kagome dipolar spin ice. *Nature Communications*, 7:11446, 2016.

[16] Y Qi, T Brintlinger, and J Cumings. Direct observation of the ice rule in an artificial kagome spin ice. *Physical Review B*, 77(9):094418, 2008.

[17] A Farhan, A Kleibert, P M Derlet, L Anghinolfi, A Balan, R V Chopdekar, M Wyss, S Gliga, F Nolting, and L J Heyderman. Thermally induced magnetic relaxation in building blocks of artificial kagome spin ice. *Physical Review B*, 89(21):214405, 2014.

[18] E Mengotti, L J Heyderman, A F Rodríguez, F Nolting, Remo V Hügli, and H-B Braun. Real-space observation of emergent magnetic monopoles and associated dirac strings in artificial kagome spin ice. *Nature Physics*, 7(1):68, 2011.

[19] G Möller and R Moessner. Magnetic multipole analysis of kagome and artificial spin-ice dipolar arrays. *Physical Review B*, 80(14):140409, 2009.

[20] I Gilbert, G-W Chern, S Zhang, L O'Brien, B Fore, C Nisoli, and P Schiffer. Emergent ice rule and magnetic charge screening from vertex frustration in artificial spin ice. *Nature Physics*, 10(9):670–675, 2014.

[21] G-W Chern, M J Morrison, and C Nisoli. Degeneracy and criticality from emergent frustration in artificial spin ice. *Physical Review Letters*, 111(17):177201, 2013.

[22] Y Perrin, B Canals, and N Rougemaille. Extensive degeneracy, coulomb phase and magnetic monopoles in artificial square ice. *Nature*, 540(7633):410, 2016.

[23] S Gliga, A Kákay, R Hertel, and O G Heinonen. Spectral analysis of topological defects in an artificial spin-ice lattice. *Physical Review Letters*, 110(11):117205, 2013.

[24] R C Silva, R J C Lopes, L A S Mól, W A Moura-Melo, G M Wysin, and A R Pereira. Nambu monopoles interacting with lattice defects in a two-dimensional artificial square spin ice. *Physical Review B*, 87:014414, 2013.

[25] S D Pollard, V Volkov, and Y Zhu. Propagation of magnetic charge monopoles and dirac flux strings in an artificial spin-ice lattice. *Physical Review B*, 85(18):180402, 2012.

[26] J Li, X Ke, S Zhang, D Garand, C Nisoli, P Lammert, V H Crespi, and P Schiffer. Comparing artificial frustrated magnets by tuning the symmetry of nanoscale permalloy arrays. *Physical Review B*, 81(9):092406, 2010.

[27] V S Bhat, J Sklenar, B Farmer, J Woods, J T Hastings, S J Lee, J B Ketterson, and L E De Long. Controlled magnetic reversal in permalloy films patterned into artificial quasicrystals. *Physical Review Letters*, 111(7):077201, 2013.

[28] X Zhou, G-L Chua, N Singh, and A O Adeyeye. Large area artificial spin ice and anti-spin ice $Ni_{80}Fe_{20}$ structures: Static and dynamic behavior. *Advanced Functional Materials*, 26(9):1437, 2016.

[29] Z Budrikis, J P Morgan, J Akerman, A Stein, P Politi, S Langridge, C H Marrows, and R L Stamps. Disorder strength and field-driven ground state domain formation in artificial spin ice: Experiment, simulation, and theory. *Physical Review Letters*, 109(3):037203, 2012.

[30] J H Rodrigues, L A S Mól, W A Moura-Melo, and A R Pereira. Efficient demagnetization protocol for the artificial triangular spin ice. *Applied Physics Letters*, 103(2013):092403, 2013.

[31] X Ke, J Li, C Nisoli, Paul E Lammert, W McConville, R F Wang, V H Crespi, and P Schiffer. Energy minimization and ac demagnetization in a nanomagnet array. *Physical Review Letters*, 101(3):037205, 2008.

[32] R F Wang, J Li, W McConville, C Nisoli, X Ke, J W Freeland, V Rose, M Grimsditch, P Lammert, V H Crespi, and P Schiffer. Demagnetization protocols for frustrated interacting nanomagnet arrays. *Journal of Applied Physics*, 101:09J104, 2007.

[33] J P Morgan, A Stein, S Langridge, and C H Marrows. Thermal ground-state ordering and elementary excitations in artificial magnetic square ice. *Nature Physics*, 7(1):75, 2011.

[34] V Kapaklis, U B Arnalds, A Harman-Clarke, E T Papaioannou, M Karimipour, P Korelis, A Taroni, P C W Holdsworth, S T Bramwell, and B Hjörvarsson. Melting artificial spin ice. *New Journal of Physics*, 14(3):035009, 2012.

[35] J M Porro, A Bedoya-Pinto, A Berger, and P Vavassori. Exploring thermally induced states in square artificial spin-ice arrays. *New Journal of Physics*, 15(5):055012, 2013.

[36] V S Bhat, J Sklenar, B Farmer, J Woods, J B Ketterson, J T Hastings, and L E De Long. Ferromagnetic resonance study of eightfold artificial ferromagnetic quasicrystals. *Journal of Applied Physics*, 115(17):17C502, 2014.

[37] J Sklenar, V S Bhat, L E DeLong, and J B Ketterson. Broadband ferromagnetic resonance studies on an artificial square spin-ice island array. *Journal of Applied Physics*, 113(17):17B530, 2013.

[38] M B Jungfleisch, W Zhang, E Iacocca, J Sklenar, J Ding, W Jiang, S Zhang, J E Pearson, V Novosad, J B Ketterson, et al. Dynamic response of an artificial square spin ice. *Physical Review B*, 93(10):100401, 2016.

[39] I R B Ribeiro, J F Felix, L C Figueiredo, P C Morais, S O Ferreira, W A Moura-Melo, A R Pereira, A Quindeau, and C I L de Araujo. Investigation of ferromagnetic resonance and magnetoresistance in anti-spin ice structures. *Journal of Physics: Condensed Matter*, 28(45):456002, 2016.

[40] Y Yahagi, C R Berk, B D Harteneck, S D Cabrini, and H Schmidt. Dynamic separation of nanomagnet sublattices by orientation of elliptical elements. *Applied Physics Letters*, 104(16):162406, 2014.

[41] A Castellanos, R Wördenweber, G Ockenfuss, A V D Hart, and K Keck. Preparation of regular arrays of antidots in $YBa_2Cu_3O_7$ thin films and observation of vortex lattice matching effects. *Applied physics letters*, 71(7):962–96, 1997.

[42] K Zeissler, M Chadha, E Lovell, L F Cohen, and W R Branford. Low temperature and high field regimes of connected kagome artificial spin ice: the role of domain wall topology. *Scientific Reports*, 6:30218, 2016.

[43] K Zeissler, S K Walton, S Ladak, D E Read, T Tyliszczak, L F Cohen, and W R Branford. The non-random walk of chiral magnetic charge carriers in artificial spin ice. *Scientific reports*, 3:1252, 2013.

[44] Z Budrikis, K L Livesey, J P Morgan, J Akerman, A Stein, S Langridge, C H Marrows, and R L Stamps. Domain dynamics and fluctuations in artificial square ice at finite temperatures. *New Journal of Physics*, 14(3):035014, 2012.

[45] D Levis and L F Cugliandolo. Out-of-equilibrium dynamics in the bidimensional spin-ice model. *EPL (Europhysics Letters)*, 97(3):30002, 2012.

[46] J Drisko, T Marsh, and J Cumings. Topological frustration of artificial spin ice. *Nature Communications*, 8:14009, 2017.

[47] R Macẽdo, F S Nascimento, G M Macauley, and R L Stamps. Apparent ferromagnetism in pinwheel-tiled spin ice. *Physics Review B*, 98:014437, 2018.

2

Physical properties of nanomagnets

2.1 Introduction

Nanomagnetism, focused on magnetic properties of nanostructured magnetic objects, has attracted wide interest in material science in the past decades. This comes as a consequence of the development of nanofabrication techniques and multidisciplinary applications of nanomagnetic systems. At present, fundamental research in nanomagnets has been focused on thin films [1–4], multilayers [5–8], nanoparticles [9–13] and patterned arrays [14–16]. These systems exhibit exotic properties arising from the competition between energy terms due to their low dimensionality and nanoscale size. So far, potential applications of nanomagnetic structures include ultrahigh-density information storage [17–23], biomedicine [9, 24–26], nanosensors [27–30] and catalysts [31–34] [28].

The main purpose of this thesis is to explore the dynamic response of artificial spin ice systems to magnetic fields. These are patterned arrays of magnetic nanoelements, which is studied using several characterisation techniques and micromagnetic simulation. The

details of characterisation and simulation methods will be presented in Chapter 3. This chapter concentrates on the physics of ferromagnetic behaviour in a magnetic medium, free energy terms and basic concepts of domains and domain walls. It also presents the principle of magnetisation dynamics of ferromagnets which are incorporated in Section 2.6.

2.2 Magnetism of nanostructures

Magnetic behaviour in materials is usually described in terms of magnetic moments, m. The magnetic moment is associated with two electronic angular momenta: orbital angular momentum (L) and intrinsic spin angular momentum (S). The orbital angular momentum of an electron charge results from the electron motion around a proton and intrinsic spin angular momentum arises from the electron spinning on its axis. In this approach, the contribution from the intrinsic angular momentum of a proton is usually neglected as it is so small compared to that of the electron. Therefore, the net moment of an atom is the sum of the orbital angular momentum and the spin angular momentum. The average of the magnetic moment of electrons in a material is usually described by the magnetisation density (M), the total magnetic moment per unit volume $M = \sum m/V$ (A/m), where V is the volume of the material. Considering that a magnetic field H interacts with electrons, the field-induced magnetisation is dependent on the electron orbital configurations [35]. Thus, this relationship between the induced magnetisation M and the applied field is given by

$$M = \chi H \tag{2.1}$$

where χ is the dimensionless magnetic susceptibility and H is the magnetic field strength (A/m).

In most materials, electrons are paired in the orbitals and thus their opposite spin angular momenta cancel. In this context, an external magnetic field induces the opposite magnetisation due to the electromotive force from the orbital rotation of the electrons according to Lenz's law. This type of magnetic behaviour is referred to as 'diamagnetism' and exhibits $\chi < 0$. Although all substances have the diamagnetic response, most are sufficiently weak to be neglected. By contrast, those in which there are uncompensated

moments in the electron shells possess net magnetic moments even without the applied field. In the presence of an applied field, their net magnetic moments are forced into the same orientation as the magnetic field. Such magnetic materials have 'paramagnetism' and, therefore, $\chi > 0$. The induced magnetisation decreases to zero with the removal of the magnetic field. This stems from the weak interaction between neighbouring electron spins giving rise to their random directionality across the material. However, if the interaction between adjacent atoms is strong, all spins are parallel aligned even in the absence of magnetic field, which results in the net moment being retained. This phenomenon can be found in transition metal elements, for instance, iron (Fe), nickel (Ni) and cobalt (Co) etc, and is defined as ferromagnetism. The ferromagnetic susceptibility χ exhibits a saturation at a certain strength of the magnetic field. The magnetic object, in which the net electrons spins are antiparallel coupled, is known as an antiferromagnet. An additional magnetic ordering is ferrimagnetism. The spins in ferrimagnetic materials are antiferromagnetically coupled, but the net moment is generated as the strength of magnetic moment of one sublattice is stronger than the other. These magnetic orders of the ferromagnetic, antiferromagnetic and ferrimagnetic systems are schematically illustrated in Fig. 2.1.

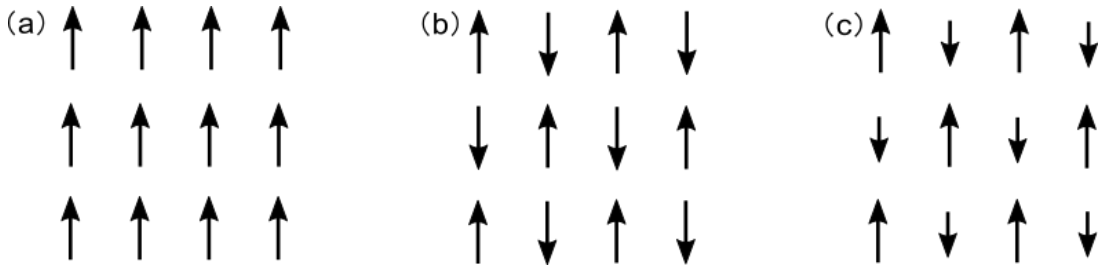

Figure 2.1: Schematic diagrams illustrating the magnetic orderings of (a) ferromagnetic, (b) antiferromagnetic and (c) ferrimagnetic systems, where the black arrows represent magnetic moments.

One of the characteristics of ferromagnetism is the existence of spontaneous magnetisation even at $H = 0$ [36, 37]. However, the spontaneous magnetisation vanishes at the Curie temperature, above which the magnetic order becomes paramagnetic [38, 39].

2.3 Magnetic free energy terms

A total free energy in a ferromagnetic system generally results from contributions of exchange energy, magnetostatic energy, Zeeman energy, anisotropy energy and magne-

tostrictive energy [35]. Note that, in this context, the term 'free' means that thermal fluctuations are not taken into account. An equilibrium state of magnetisation is, therefore, achieved by minimising the total free energy. These energy terms are discussed in the following sections.

2.3.1 Exchange energy

One of the simplest approaches used to describe the coupling of electrons in a microscopic spin system is that of Heisenberg. This *exchange* interaction is given by a Hamiltonian of the form [40]

$$\hat{\mathcal{H}} = -J_{ij} \sum_{ij} \vec{S}_i \cdot \vec{S}_j, \tag{2.2}$$

where S is the spin of an electron at a site i or j, which only arises from the intrinsic electron angular momentum as the orbital angular momentum is cancelled, and J_{ij} denotes the exchange constant. The sign of J defines the nature of the spin alignment so that if J is positive a ferromagnetic ordering is seen, while negative J gives rise to an antiferromagnetic ordering.

In a continuum approximation, with the assumption of ignoring the discreteness of spins at crystal lattices, Eq. 2.2 can be modified using Taylor expansion [41] and then becomes

$$E_{ex} = A \int_V (\nabla m)^2 d^3r, \tag{2.3}$$

where A is the exchange stiffness constant (J/m) and is given by $A = 2JS^2z/a$, in which z is the number of sites in the unit crystal cell and a is the distance separating neighbouring moments. Eq. 2.3 is particularly useful when computing the exchange energy in micromagnetic simulations (see Section 3.8).

2.3.2 Magnetostatic energy

Magnetostatic energy results from dipole interactions induced by surface magnetic charges of a sample, as schematically displayed in Fig.2.2 (a). In this case, uniform magnetisation M generates surface charges which act as dipole fields. This surface charge and the net volume charge create a demagnetisation field together, H_d, pointing to the opposite

direction of M. The internal field experienced by the sample is $H_{int} = H - H_d$, where H is an external field. This demagnetisation (or magnetostatic) energy E_d is given by

$$E_d = -\frac{\mu_0}{2} \int_V M \cdot H_d dV, \tag{2.4}$$

where μ_0 is the permeability constant of free space (H/m), V is the volume of magnetic sample and

$$H_d = -NM \tag{2.5}$$

is the demagnetisation field, here N being a demagnetisation tensor which is dependent on the shape of sample. It is possible to compute the demagnetisation factors of a cuboid using the method introduced by A. Aharoni [42] (see more details in Section 5.3.3).

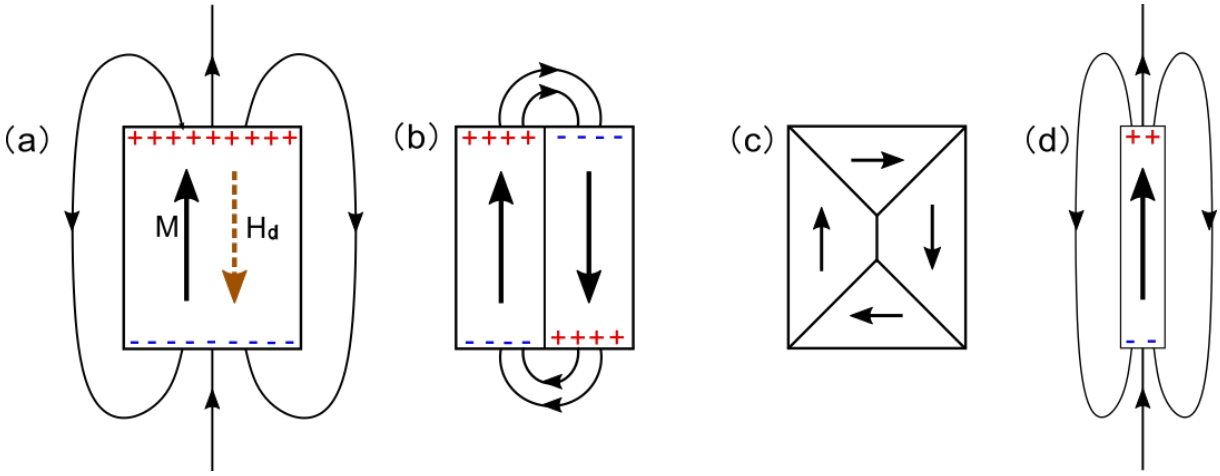

Figure 2.2: (a) Uniform magnetisation in a rectangular ferromagnetic object, in which the curved lines outside the object represent the stray fields and the red (blue) pluses (minus) represent the positive (negative) surface magnetic charges. Domain formation into (b) two domains and (c) a closure structure in order to minimised the magnetostatic energy for elements of same dimensions. (d) By decreasing the width of the object (a) creates a single-domain magnetic bar.

The magnetostatic energy is mainly responsible for the formation of domains, in which the direction of magnetisation is the same, such as the monodomain case shown in Fig. 2.2 (a). However, the demagnetisation energy is maximal here so that the total energy of the system is not minimised. Therefore, in some cases, this single domain would be divided into two domains whose magnetisation orientations are aligned antiparallel to one another in order to reduce the demagnetisation energy, as shown in Fig. 2.2 (b). The minimal demagnetisation energy can be obtained in certain cases, for instance, where a

closure flux structure of magnetisation (also known as 'Landau domain') is formed, as illustrated in Fig. 2.2 (c).

2.3.3 Zeeman energy

The Zeeman energy term describes the interaction between an external field and a sample's magnetisation. Applying an external field allows the magnetisation of a ferromagnetic system to align with the field direction. In the presence of the external field, H, the potential energy is given by

$$E_z = -\mu_0 \int_V M \cdot H dV. \tag{2.6}$$

2.3.4 Anisotropy energies

In a system of spins such as that described by Eq. 2.2, the magnetisation is considered to be isotropic, that is, this expression does not illustrate any information about the energetically favourable direction of magnetisation of the system. However, in real magnetic objects, the magnetisation tends to be aligned along a particular direction. Two common cases are crystalline anisotropy and shape anisotropy.

Crystalline anisotropy is a directional effect which induces the magnetisation to align with a certain crystallographic axis and usually occurs in a single crystal. This anisotropy is a result of spin-orbit coupling [43]. The crystal axis on which the magnetisation tends to lie is called the 'easy axis', while the crystallographic axis which is energetically less favourable for magnetisation to align to is termed as the 'hard axis'. In this study, permalloy was used, which is a polycrystalline alloy. Thus, the contribution of crystalline anisotropy on the magnetisation is very weak.

Shape anisotropy is a result of the minimisation of demagnetisation energy due to the shape of sample. An ellipsoid, where the demagnetising field is assumed to be spatially uniform, is a prime example of shape anisotropy [44]. In the presence of an applied field H, the demagnetising field along the polar axis is $H_d^a = -N_a M$, and along the short axis is $H_d^b = -N_b M$, as shown in Figs. 2.3 (a) and (b), respectively. The relative distance between two surface magnetic poles determines the value of demagnetising factors, for this ellipsoid, $N_a < N_b$ [45]. Therefore, the easy direction of this magnetic ellipsoid is

along the long axis where the demagnetisation energy is lower, while its hard direction is along the short axis where the demagnetisation energy is higher.

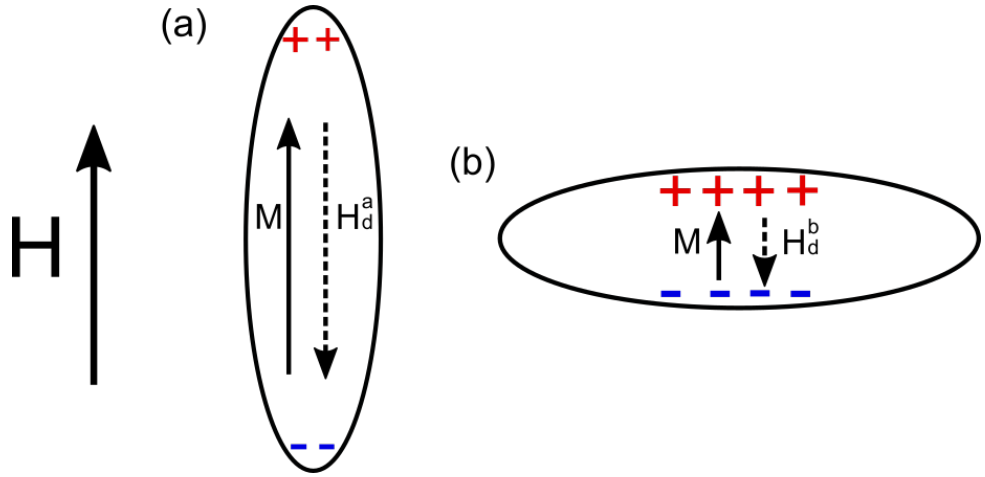

Figure 2.3: Diagrams showing (a) easy axis and (b) hard axis of a ellipsoidal disk in the presence of an external field H which is dependent on the demagnetising field H_d.

The anisotropy energy constrained by sample geometry is, therefore, described in terms of the difference between energetically favourable and unfavourable states, and it is given by [46]

$$E_s = -\frac{\mu_0}{2}\int_V (N_b - N_a) M_s^2 dV, \tag{2.7}$$

where M_s is the saturation magnetisation. In this way, the shape anisotropy plays an essential role in the formation of single-domain nanomagnet. If the size and the shape of a nanomagnet are designed to be small enough (i.e. at the nanometer scale) and elongated, the exchange energy will be dominant instead of the demagnetisation energy so that the magnetic moments are forced along the same direction. This direction is usually along the easy axis of the sample due to the shape anisotropy. Therefore, a single domain can be structured in this nanomagnet, as sketched in Fig. 2.2 (d). Such single-domain nanomagnets have been used as fundamental units in ASI systems which have already been mentioned in Section 1.2.

2.4 Domain walls

As discussed previously, the multiple domains, in which the directions of the magnetisation are different in a given magnet, are created so as to minimise the total energy of a system.

A boundary separating two adjacent domains is defined as a domain wall. The formation of domain wall in a ferromagnet system, however, is energetically costly. This can be due to its magnetic moments not being parallel to each other (increasing the exchange energy) and misaligned with the easy axis (increasing the anisotropy energy) [35].

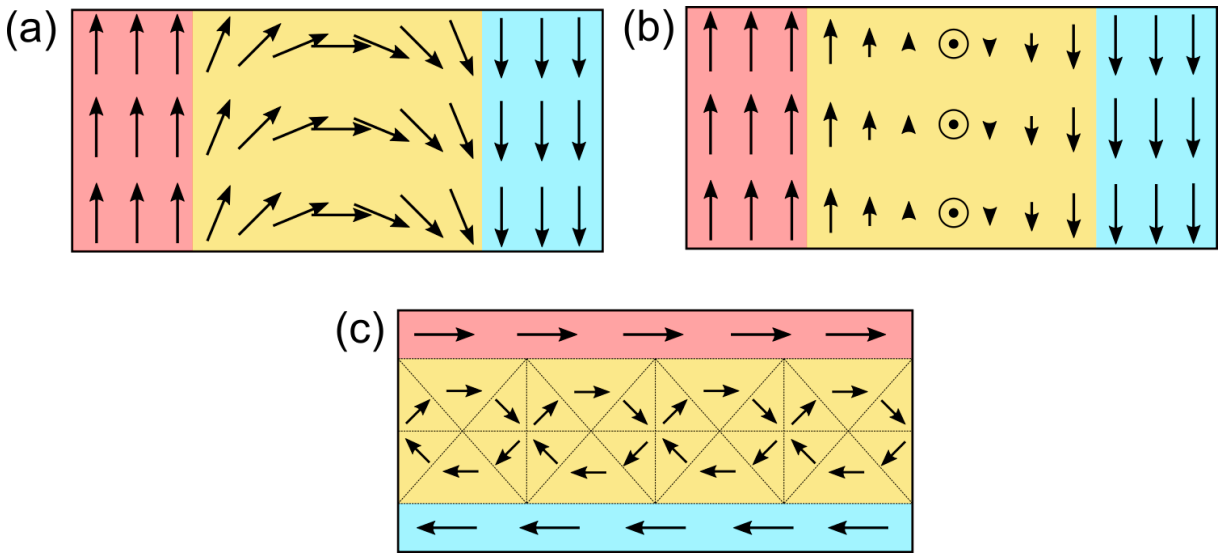

Figure 2.4: Schematic representations of (a) Néel wall, (b) Bloch wall and (c) cross-tie wall in a thin film. The red (blue) and yellow shadow regions indicate the position of domain and domain wall, respectively.

Figure 2.5: Schematic diagrams of magnetic charge distribution of (a) Néel and (b) Bloch walls, where the plus and minus signs represent positive and negative charges. The polarisation in Néel wall forms volume charges, while in the Bloch wall leads to surface charges.

Domain walls are usually classified as 180° and non-180° walls according to the angle of magnetisation orientation between the neighbouring domains. These two types of walls can be further classified due to the difference in the topology of the magnetic structure. For example, in thin films there are three main cases: Néel walls, Bloch walls and cross-tie walls. The thickness of the film is responsible for the formation of these three walls. The first type, Néel walls, are those which are energetically favourable in thinner samples (the theoretical thickness $< 70nm$ in a ferromagnetic film [47]). A Néel wall is defined as a transition region where the magnetisation rotates by 180° in plane [48, 49], as shown in Fig. 2.4 (a). The second type, Bloch walls, mainly occur in thicker samples (the calculated thickness $>$ 100 nm [47]). For those the magnetisation rotates out of plane within the film. Figure 2.4 (b) schematically shows the magnetisation configurations within a

Bloch wall region [50, 51]. Finally, cross-tie walls are 90° wall structure separating perpendicular neighbouring domains and forming vortices and antivortices of magnetisation topologies (see Fig. 2.4 (c)) [52–54]. This type of domain wall is always seen in films with intermediate thickness (from approximately 30 nm to 90 nm in NiFe films [55]). The magnetisation configuration of this wall is usually a consequence of multiaxial anisotropy or an applied field perpendicular to the easy axis of an uniaxial material.

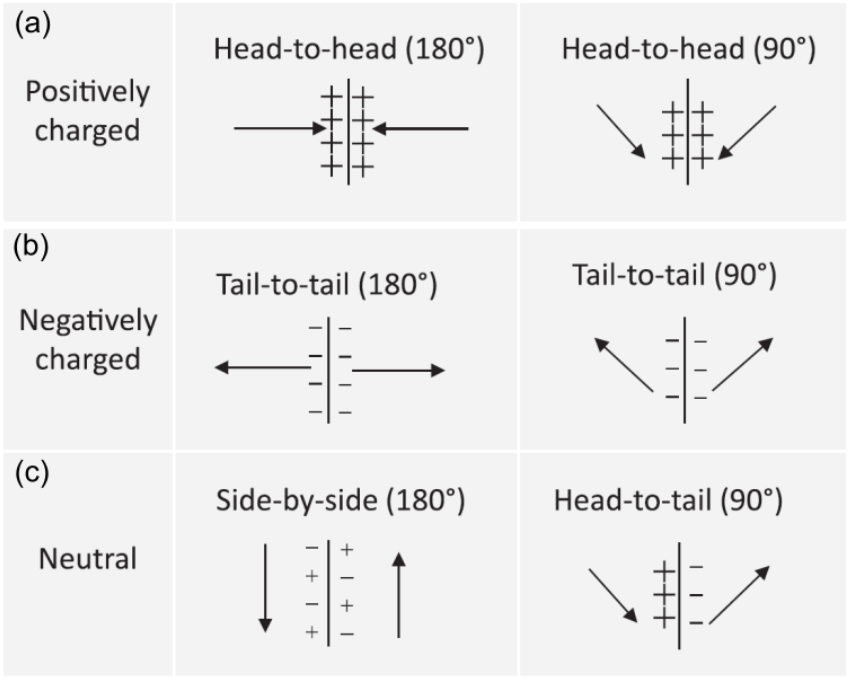

Figure 2.6: Illustrations of charged and neutral 180° and 90° domain-wall configurations in ferroelectric materials [56]. The orientations of adjacent spontaneous polarisation determine the charge behaviour in domain walls. (a) Head-to-head configuration carries positive bound charge and (b) tail-to-tail configuration possesses negative bound charges. (c) Neutral walls satisfy the condition of electrostatic compatibility. Copyright (2015) on the IOP Publishing.

These walls give rise to the interesting consequences on charge ordering. Fig. 2.5 (a) shows that Néel wall induces volume charges, while the Bloch wall in Fig. 2.5 (b) produces surface charges. In both cases, the walls are considered to be neutral walls due to the divergence of the polarisation is zero, that is, the spontaneous polarisation is continuous across the walls [57]. Nevertheless, analogous charged domain walls have been reported in multiferroic materials, such as $BaTiO_3$ [58], $PbTiO_3$ [59], SbSl [60] and $PbZr_{0.2}Ti_{0.8}O_3$ [61]. Figures 2.6 (a) and (b) schematically describe charged 180° and 90° wall configurations, respectively. Here, the polarisation orientation defines the sign of electronic bond charges. A wall separating the 180° and 90° head-to-head electric polarisations carry positive bound charges, while the tail-to-tail arrangements lead to negative

bound charges. In comparison with neutral walls, uncompensated charge walls are those where the local divergence of electrostatic potentials is nontrivial [56]. However, the width of the domain walls (could be up to tens of nanometers) in ferromagnetic film is much greater than those in Ferromagnetic materials which have a few lattice constants [62]. This derives from the origins of the formation of spontaneous polarization are different in ferromagnetic and ferroelectric objects. It has been introduced in Section 2.2 that the dipole moment of ferromagnetism arises from the orbital and spin angular momenta, while the dipole moments of ferroelectricity is generated due to noncentrosymmetric structure [62]. In addition, equivalent charged walls have also been observed in nanowires due to their strong shape anisotropy [63–65]

The intrinsic magnetisation topology of the domain wall has been suggested as the route to some novel physical phenomena. These walls and their properties have already been recently exploited in the context of potential application in information storage [66, 67].

2.5 Hysteresis loops of single-domain nanomagnets

In previous sections, how the size and shape of magnetic structures affect the magnetisation configurations has been discussed. However, the influences of an external applied field on the magnetisation of a magnetic nanostructure have not been stated. The response of the magnetisation of a magnetic solid to an applied field can be described by a hysteresis loop. An example of the hysteretic behaviour of a single-domain ferromagnetic nanomagnet is given in Fig. 2.7. From Eq. 2.1 it is inferred that the relationship between strength of the magnetisation and external field is linear for a magnetic solid, but not always for a ferromagnet. Ferromagnets have saturation strengths of magnetisation, M_s. This means that the increase of the magnetisation peaks at M_s and remains the same even for a greater external applied field. As has been introduced already, ferromagnets possess remnant magnetisation with the removal of the magnetic field known as M_r. The magnetisation will be reversed, however, when an external field is applied in the opposite direction. The field at which this occurs is referred to as coercive field, H_c.

Strong shape anisotropy of a single-domain nanomagnet is responsible for the field-induced behaviours of hysteresis loops. This study was initially conducted by E. C. Stoner

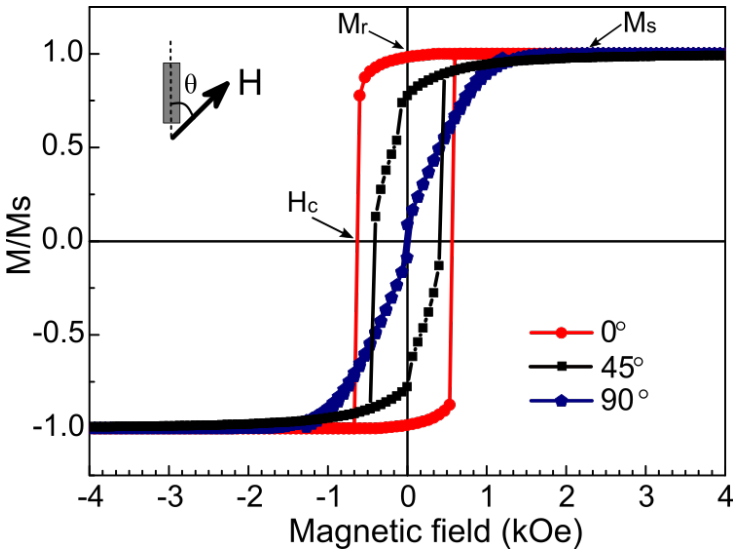

Figure 2.7: Simulated hysteresis loops of a cuboid single-domain permalloy nanomagnet at magnetic fields of $\theta = 0°$, $\theta = 45°$ and $\theta = 90°$ with respect to the easy axis (indicated by the dash line) using Mumax. The inset displays the direction of the magnetic field H with respect to the nanomagnet. The dimension of the magnetic island is $240 \times 80 \times 10$ nm^3.

and E. P. Wohlfarth [44]. Their Stoner-Wohlfarth model predicts that the system energy E of a single-domain particle in the presence of an applied field is described by

$$E = KV \sin(\theta - \phi)^2 - \mu_0 M_s V H \cos\theta \tag{2.8}$$

where K is the shape anisotropy parameter of the nanomagnet, given by $K = \frac{1}{2}\mu_0 N M_s^2$, θ is the magnetic field angle with respect to the long axis of the elongated nanomagnet (the dashed vertical line in the inset of Fig. 2.7) and ϕ is the angle between the direction of magnetisation and the long axis of the nanomagnet. Eq. 2.8 addresses why the easy axis of the single-domain particle is at $\phi = 0, 180°$ where E reaches a minimum and the hard axis is where the magnetisation is at $\phi = 90°$. Figure 2.7 illustrates the hysteresis loops at $\theta = 0°, 45°, 90°$ with respect to the easy axis of a single-domain nanomagnet. Comparing them, it can be seen that the remnant magnetisation and the coercivity decrease as the angle θ increases.

2.6 Magnetisation dynamics

2.6.1 Ferromagnetic resonance

Dynamic magnetisation, involving precessional motion and damping, can be described by the Landau-Lifshitz-Gilbert (LLG) equation [68],

$$\frac{d\vec{M}}{dt} = -\frac{\gamma}{1+\alpha^2}(\vec{M} \times \vec{H}_{eff}) + \frac{\alpha}{M_s}(\vec{M} \times \frac{d\vec{M}}{dt}), \tag{2.9}$$

where M is the magnetisation, M_s is the saturation magnetisation, γ is a gyromagnetic ratio, α is the dimensionless damping coefficient and H_{eff} is an effective field. The first term of Eq. 2.9 describes the precessional motion of a magnetisation vector M around the H_{eff} axis (the equilibrium state of the system). This motion is driven by a torque, $-M \times H_{eff}$, as schematically illustrated in Fig. 2.8. The second term is related to a Gilbert dissipative relaxation which forces the magnetisation toward the direction of H_{eff}, in other words, approaching the equilibrium state. There is another expression of the relaxation given by $-\frac{\lambda}{M_s^2}(M \times M \times H_{eff})$ [69], where $\lambda = 1/\tau$ is the damping constant and τ is the inverse relaxation time τ. This describes phenomenological dissipative motion, as displayed in Fig. 2.8. Figure 2.8 shows that the magnetisation vector follows a spiral trajectory due to the combined effect of these two contributions. If an external driving force is employed, the magnetisation M will experience precessional torque around and is eventually restored to the effective field axis. The amplitude and phase of magnetisation precession results from a combination of the amplitude of driving energy and resonant conditions of the magnetic system.

A common interest in the area of magnetisation dynamics is the resonant precessional frequency which depends on static and dynamic magnetic fields. For instance, consider spins processing uniformly, as shown in Figs. 2.9 (a) and (b). Such a uniform magnetisation precession, known as the Kittel mode, has resonant frequency ω depending on the magnetic field which is given by Kittel formula [70]

$$\omega = \gamma\sqrt{[H_{ext} + (N_z - N_H)4\pi M_s] \times [H_{ext} + (N_{H,\perp} - N_H)4\pi M_s]}, \tag{2.10}$$

where H_{ext} represents the applied field; γ is the gyromagnetic ratio, N_z is the demagnetising factor along the z direction and N_H ($N_{H,\perp}$) is the demagnetising constant along

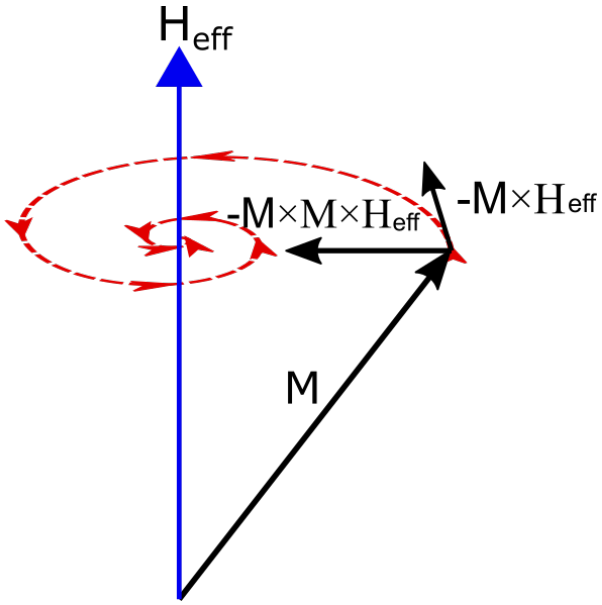

Figure 2.8: Schematic diagram showing the torque terms, described by LLG equation, acting on the magnetisation. The magnetisation precesses around the effective field axis and the magnetisation motion dissipates aiming to align to the equilibrium H_{eff} axis.

(perpendicular to) the orientation of applied field H. This equation can be fitted with the results measured using ferromagnetic resonance measurements to quantitatively approximate the value of γ and M_s. In this thesis, I will describe how to employ the Kittel equation to fit with experimental data in Section 5.3. In addition to the uniform precession where all spins precess at the same frequency and phase, the magnetic excitations are likely to precess out of phase but with the same frequency, which will be discussed in the next section.

2.6.2 Spin waves

In real magnetic systems, magnetisation precessions are also spatially inhomogeneous so that the changes in magnetisation are functions of time and position. These collectively excited spins with energy above the ground state can be described by a wave propagation process. This is illustrated in Figs. 2.9 (c) and (d), side and top views, respectively. Such spatially periodic and time-dependent magnetisation fluctuations at finite temperature are commonly defined as 'spin waves' (or magnons). Figure. 2.9 (d) shows the deviations between consecutive spins forming a wave with a characteristic wavelength λ. The wavevector k can be obtained by $k = 2\pi/\lambda$ and its direction is parallel to the wavelength λ.

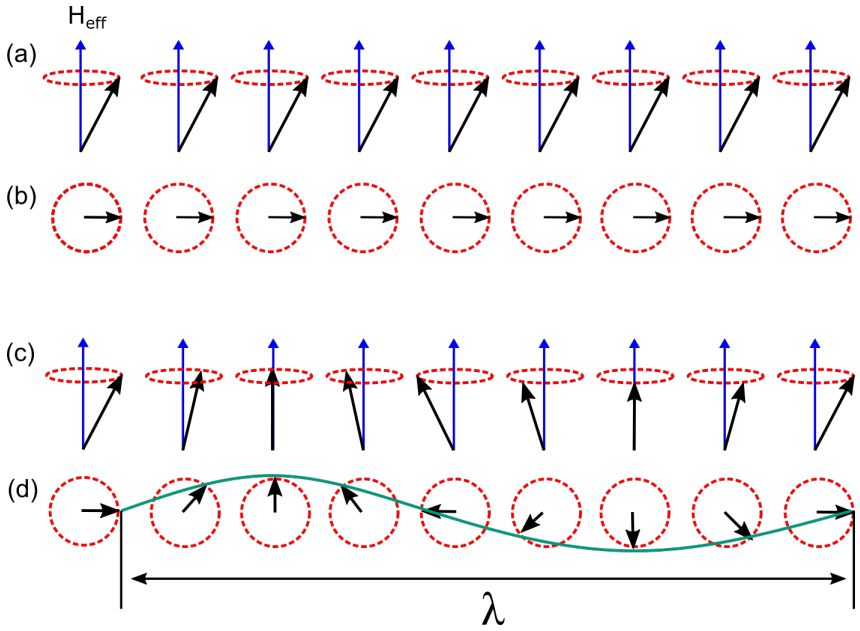

Figure 2.9: Comparison between spin precession of uniform modes and spin waves. (a) Lateral and (b) top-view spins precessing in phase with wavevector $k = 0$. (c) Side and (d) top views of consecutive spins that precess out of phase to form a spin wave with characteristic finite wavelength λ and wavevector $k = 2\pi/\lambda$.

The orientation of the spin wave wavevector with respect to the static magnetisation determines the propagation feature and spatial profile of the excited spin wave [71]. Two common forms of spin wave modes are considered: Damon-Eschbach and backward volume [72]. Damon-Eshbach mode is a configuration where the direction of the wavevector of a spin wave is perpendicular to the static magnetisation, $\vec{k} \perp M$, as shown in Fig. 2.10 (a). Backward volume modes have the wavevector of spin waves that is aligned parallel to the static magnetisation, $\vec{k} \parallel M$(see Fig. 2.10 (b)).

The physical boundary of the sample strongly affects properties of spin waves, especially, when the dimension of the sample decreases significantly. In small-dimension magnetic elements, the propagation effects are usually too weak or even negligible [73]. Also, due to the low dimension, only certain spin-wave modes could be confined and observed [74].

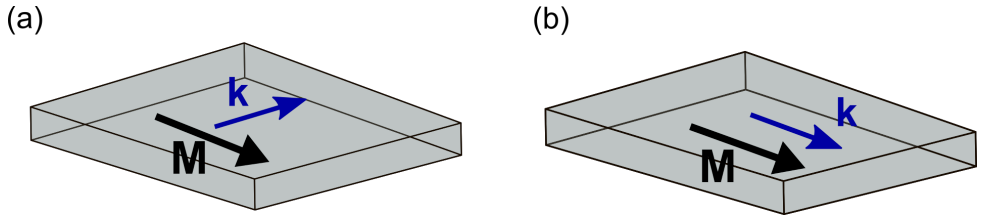

Figure 2.10: (a) Schematic diagrams showing the configuration of the directions of the spin-wave wavevector with respect to the static magnetisation of a magnetic object (the grey box) in the (a) Damon-Eschbach and (b) backward volume configurations.

Bibliography

[1] M Yamanouchi, D Chiba, F Matsukura, and H Ohno. Current-induced domain-wall switching in a ferromagnetic semiconductor structure. *Nature*, 428(6982):539, 2004.

[2] R Hertel, S Gliga, M Fähnle, and C M Schneider. Ultrafast nanomagnetic toggle switching of vortex cores. *Physical Review Letters*, 98(11):117201, 2007.

[3] D Chakraborti, J Narayan, and J T Prater. Room temperature ferromagnetism in $Zn_{1-x}Cu_xO$ thin films. *Applied Physics Letters*, 90(6):062504, 2007.

[4] C Y Liang, S M Keller, A E Sepulveda, W Y Sun, J Z Cui, C S Lynch, and G P Carman. Electrical control of a single magnetoelastic domain structure on a clamped piezoelectric thin film-analysis. *Journal of Applied Physics*, 116(12):123909, 2014.

[5] S I Kiselev, J C Sankey, I N Krivorotov, N C Emley, R J Schoelkopf, R A Buhrman, and D C Ralph. Microwave oscillations of a nanomagnet driven by a spin-polarized current. *Nature*, 425(6956):380, 2003.

[6] O Ozatay, P G Gowtham, K W Tan, J C Read, K A Mkhoyan, M G Thomas, G D Fuchs, P M Braganca, E M Ryan, K V Thadani, et al. Sidewall oxide effects on spin-torque-and magnetic-field-induced reversal characteristics of thin-film nanomagnets. *Nature Materials*, 7(7), 2008.

[7] C Moreau-Luchaire, C Moutafis, N Reyren, J Sampaio, C A F Vaz, N Van Horne, K Bouzehouane, K Garcia, C Deranlot, P Warnicke, et al. Additive interfacial chiral interaction in multilayers for stabilization of small individual skyrmions at room temperature. *Nature Nanotechnology*, 11(5):444, 2016.

[8] M T Johnson, P J H Bloemen, F J A Den Broeder, and J J De Vries. Magnetic anisotropy in metallic multilayers. *Reports on Progress in Physics*, 59(11):1409, 1996.

[9] Q A Pankhurst, N T K Thanh, S K Jones, and J Dobson. Progress in applications of magnetic nanoparticles in biomedicine. *Journal of Physics D: Applied Physics*, 42(22):224001, 2009.

[10] A-H Lu, E L Salabas, and F Schüth. Magnetic nanoparticles: synthesis, protection, functionalization, and application. *Angewandte Chemie International Edition*, 46(8):1222, 2007.

[11] M Lewin, N Carlesso, C-H Tung, X-W Tang, D Cory, Dd T Scadden, and R Weissleder. Tat peptide-derivatized magnetic nanoparticles allow in vivo tracking and recovery of progenitor cells. *Nature Biotechnology*, 18(4):410, 2000.

[12] J-H Lee, Y-M Huh, Y-W Jun, J-W Seo, J-T Jang, H-T Song, S Kim, E-J Cho, H-G Yoon, J-S Suh, et al. Artificially engineered magnetic nanoparticles for ultra-sensitive molecular imaging. *Nature Medicine*, 13(1):95, 2007.

[13] P Tartaj, M del Puerto Morales, S Veintemillas-Verdaguer, T González-Carreño, and C J Serna. The preparation of magnetic nanoparticles for applications in biomedicine. *Journal of Physics D: Applied Physics*, 36(13):R182, 2003.

[14] T Thomson, G Hu, and B D Terris. Intrinsic distribution of magnetic anisotropy in thin films probed by patterned nanostructures. *Physical Review Letters*, 96(25):257204, 2006.

[15] D Bhowmik, L You, and S Salahuddin. Spin hall effect clocking of nanomagnetic logic without a magnetic field. *Nature Nanotechnology*, 9(1):59, 2014.

[16] J F Bobo, L Gabillet, and M Bibes. Recent advances in nanomagnetism and spin electronics. *Journal of Physics: Condensed Matter*, 16(5):S471, 2004.

[17] S D Bader. Colloquium: Opportunities in nanomagnetism. *Reviews of Modern Physics*, 78(1):1, 2006.

[18] C Chappert, A Fert, and F N Van Dau. The emergence of spin electronics in data storage. *Nature Materials*, 6(11):813, 2007.

[19] M Mannini, F Pineider, P Sainctavit, C Danieli, E Otero, C Sciancalepore, A M Talarico, M-A Arrio, A Cornia, D Gatteschi, et al. Magnetic memory of a single-molecule quantum magnet wired to a gold surface. *Nature Materials*, 8(3):194, 2009.

[20] S Y Chou, M S Wei, P R Krauss, and P B Fischer. Single-domain magnetic pillar array of 35 nm diameter and 65 gbits/in. 2 density for ultrahigh density quantum magnetic storage. *Journal of Applied Physics*, 76(10):6673, 1994.

[21] Z Z Bandić, D Litvinov, and M Rooks. Nanostructured materials in information storage. *MRS Bulletin*, 33(9):831, 2008.

[22] H-W Zhang, Y Liu, and S-H Sun. Synthesis and assembly of magnetic nanoparticles for information and energy storage applications. *Frontiers of Physics in China*, 5(4):347, 2010.

[23] B Lambson, D Carlton, and J Bokor. Exploring the thermodynamic limits of computation in integrated systems: magnetic memory, nanomagnetic logic, and the landauer limit. *Physical Review Letters*, 107(1):010604, 2011.

[24] M Angelakeris, Z-A Li, M Hilgendorff, K Simeonidis, D Sakellari, M Filippousi, H Tian, G Van Tendeloo, M Spasova, M Acet, et al. Enhanced biomedical heat-triggered carriers via nanomagnetism tuning in ferrite-based nanoparticles. *Journal of Magnetism and Magnetic Materials*, 381:179–187, 2015.

[25] Â Andrade, R Ferreira, J Fabris, and R Domingues. Coating nanomagnetic particles for biomedical applications. In *Biomedical Engineering-Frontiers and Challenges*. InTech, 2011.

[26] C C Berry and A S G Curtis. Functionalisation of magnetic nanoparticles for applications in biomedicine. *Journal of Physics D: Applied Physics*, 36(13):R198, 2003.

[27] C Granata, A Vettoliere, R Russo, M Fretto, N De Leo, and V Lacquaniti. Three-dimensional spin nanosensor based on reliable tunnel josephson nano-junctions for nanomagnetism investigations. *Applied Physics Letters*, 103(10):102602, 2013.

[28] S Da Dalt, P C Panta, and J C Toniolo. *Nanomagnetic Materials*, pages 23–39. Springer Berlin Heidelberg, Berlin, Heidelberg, 2011.

[29] E Esposito, C Granata, M Russo, R Russo, and A Vettoliere. High sensitive magnetic nanosensors based on superconducting quantum interference device. *IEEE Transactions on Magnetics*, 49(1):140, 2013.

[30] R Russo, C Granata, E Esposito, A Vettoliere, B Ruggiero, D Peddis, D Fiorani, and M Russo. Nanosensors based on superconducting quantum interference device for nanomagnetism investigations. In *Sensors*, pages 223–226. Springer, 2014.

[31] A R Kiasat and J Davarpanah. Fe_3O_4@ silica sulfuric acid nanoparticles: An efficient reusable nanomagnetic catalyst as potent solid acid for one-pot solvent-free synthesis of indazolo[2, 1-b]phthalazine-triones and pyrazolo[1, 2-b]phthalazine-diones. *Journal of Molecular Catalysis A: Chemical*, 373:46, 2013.

[32] A Schätz, T R Long, R N Grass, W J Stark, P R Hanson, and O Reiser. Immobilization on a nanomagnetic co/c surface using rom polymerization: generation of a hybrid material as support for a recyclable palladium catalyst. *Advanced Functional Materials*, 20(24):4323, 2010.

[33] A R Kiasat and S Nazari. Magnetic nanoparticles grafted with β-cyclodextrin–polyurethane polymer as a novel nanomagnetic polymer brush catalyst for nucleophilic substitution reactions of benzyl halides in water. *Journal of Molecular Catalysis A: Chemical*, 365:80, 2012.

[34] E Kolvari, N Koukabi, and O Armandpour. A simple and efficient synthesis of 3, 4-dihydropyrimidin-2-(1h)-ones via biginelli reaction catalyzed by nanomagnetic-supported sulfonic acid. *Tetrahedron*, 70(6):1383–1386, 2014.

[35] A H Morrish. *The physical principles of magnetism*, volume 74. Wiley, New York, 1965.

[36] J M D Coey, A P Douvalis, C B Fitzgerald, and M Venkatesan. Ferromagnetism in Fe-doped SnO_2 thin films. *Applied Physics Letters*, 84(8):1332–1334, 2004.

[37] S Blundell. *Magnetism in condensed matter*. Oxford University Press, Oxford, 2003.

[38] C C Tsuei, G Longworth, and S C H Lin. Temperature dependence of the magnetization of an amorphous ferromagnet. *Physical Review*, 170(2):603, 1968.

[39] A Bell, G Aromí, S J Teat, W Wernsdorfer, and R E P Winpenny. Synthesis and characterisation of a {Ni 8} single molecule magnet and another octanuclear nickel cage. *Chemical Communications*, (22):2808–2810, 2005.

[40] W Heisenberg. Zur theorie des ferromagnetismus. *Zeitschrift für Physik*, 49(9-10):619–636, 1928.

[41] S Blundell. *Magnetism in condensed matter*. Oxford University Press, Oxford, 2003.

[42] A Aharoni. Demagnetizing factors for rectangular ferromagnetic prisms. *Journal of Applied Physics*, 83(6):3432, 1998.

[43] W J Carr Jr. Theory of ferromagnetic anisotropy. *Physical Review*, 108(5):1158, 1957.

[44] E C Stoner and E P Wohlfarth. A mechanism of magnetic hysteresis in heterogeneous alloys. *Philosophical Transactions of the Royal Society of London A: Mathematical, Physical and Engineering Sciences*, 240(826):599–642, 1948.

[45] J A Osborn. Demagnetizing factors of the general ellipsoid. *Physical Review*, 67(11-12):351, 1945.

[46] K J. O'Shea. *Putting a leash on the domain wall: a TEM investigation into the controlled behaviour of domain walls in ferromagnetic nanostructures.* PhD thesis, University of Glasgow, 2010.

[47] W F Brown Jr and A E LaBonte. Structure and energy of one-dimensional domain walls in ferromagnetic thin films. *Journal of Applied Physics*, 36(4):1380–1386, 1965.

[48] A Tonomura. Electron-holographic interferometry. In *Electron Holography*, pages 78–132. Springer-Verlag, Berlin, Heidelberg, 1999.

[49] M R Scheinfein, J Unguris, R J Celotta, and D T Pierce. Influence of the surface on magnetic domain-wall microstructure. *Physical Review Letters*, 63(6):668, 1989.

[50] T Trunk, M Redjdal, A Kákay, M F Ruane, and F B Humphrey. Domain wall structure in permalloy films with decreasing thickness at the bloch to néel transition. *Journal of Applied Physics*, 89(11):7606–7608, 2001.

[51] U Hartmann and H H Mende. Observation of subdivided 180° bloch wall configurations on iron whiskers. *Journal of Applied Physics*, 59(12):4123–4128, 1986.

[52] E E Huber Jr, D O Smith, and J B Goodenough. Domain-wall structure in permalloy films. *Journal of Applied Physics*, 29(3):294–295, 1958.

[53] M Löhndorf, A Wadas, H A M Van Den Berg, and R Wiesendanger. Structure of cross-tie wall in thin co films resolved by magnetic force microscopy. *Applied Physics Letters*, 68(25):3635–3637, 1996.

[54] R Hertel and C M Schneider. Exchange explosions: Magnetization dynamics during vortex-antivortex annihilation. *Physical Review Letters*, 97(17):177202, 2006.

[55] S Middelhoek. Domain walls in thin Ni – Fe films. *Journal of Applied Physics*, 34(4):1054–1059, 1963.

[56] D Meier. Functional domain walls in multiferroics. *Journal of Physics: Condensed Matter*, 27(46):463003, 2015.

[57] P S Bednyakov, T Sluka, A K Tagantsev, D Damjanovic, and N Setter. Formation of charged ferroelectric domain walls with controlled periodicity. *Scientific Reports*, 5:15819, 2015.

[58] T Sluka, A K Tagantsev, P Bednyakov, and N Setter. Free-electron gas at charged domain walls in insulating $BaTiO_3$. *Nature Communications*, 4:1808, 2013.

[59] E G Fesenko, V G Gavrilyatchenko, M A Martinenko, A F Semenchov, and I P Lapin. Domain structure peculiarities of lead-titanate crystals. *Ferroelectrics*, 6(1):61–65, 1973.

[60] A A Grekov, A A Adonin, and N P Protsenko. Encountering domains in sbsl. *Ferroelectrics*, 13(1):483–485, 1976.

[61] C-L Jia, S-B Mi, K Urban, I Vrejoiu, M Alexe, and D Hesse. Atomic-scale study of electric dipoles near charged and uncharged domain walls in ferroelectric films. *Nature Materials*, 7(1):57–61, 2008.

[62] N A Spaldin. Analogies and differences between ferroelectrics and ferromagnets. In *Physics of Ferroelectrics*, pages 175–218. Springer, 2007.

[63] D Petit, H T Zeng, J Sampaio, E Lewis, L O'Brien, A-V Jausovec, D Read, R P Cowburn, K J O'Shea, S McVitie, et al. Magnetic imaging of the pinning mechanism of asymmetric transverse domain walls in ferromagnetic nanowires. *Applied Physics Letters*, 97(23):233102, 2010.

[64] K J O'Shea, S McVitie, J N Chapman, and J M R Weaver. Direct observation of changes to domain wall structures in magnetic nanowires of varying width. *Applied Physics Letters*, 93(20):202505, 2008.

[65] L K Bogart, D Atkinson, K O'Shea, D McGrouther, and S McVitie. Dependence of domain wall pinning potential landscapes on domain wall chirality and pinning site geometry in planar nanowires. *Physical Review B*, 79(5):054414, 2009.

[66] X Marti, I Fina, C Frontera, J Liu, P Wadley, Qing He, R J Paull, J D Clarkson, J Kudrnovskỳ, I Turek, et al. Room-temperature antiferromagnetic memory resistor. *Nature Materials*, 13:367–374, 2014.

[67] S S P Parkin, M Hayashi, and L Thomas. Magnetic domain-wall racetrack memory. *Science*, 320(5873):190–194, 2008.

[68] T L Gilbert. A lagrangian formulation of the gyromagnetic equation of the magnetization field. *Physical Review*, 100:1243, 1955.

[69] L Landau and E M Lifshitz. On the theory of the dispersion of magnetic permeability in ferromagnetic bodies. *Physikalische zeitschrift der Sowjetunion*, 8(153):101–114, 1935.

[70] C Kittel. On the theory of ferromagnetic resonance absorption. *Physical Review*, 73(2):155, 1948.

[71] I Neudecker. *Magnetization dynamics of confined ferromagnetic systems*. PhD thesis, University of Regensburg, 2006.

[72] G Gubbiotti, Malagò P, S Fin, S Tacchi, L Giovannini, D Bisero, M Madami, G Carlotti, J Ding, A O Adeyeye, and R Zivieri. Magnetic normal modes of bicomponent permalloy/cobalt structures in the parallel and antiparallel ground state. *Physical Review B*, 90(2):024419, 2014.

[73] R L White and I H Solt Jr. Multiple ferromagnetic resonance in ferrite spheres. *Physical Review*, 104(1):56, 1956.

[74] K Perzlmaier, M Buess, C H Back, V E Demidov, B Hillebrands, and S O Demokritov. Spin-wave eigenmodes of permalloy squares with a closure domain structure. *Physical Review Letters*, 94(5):057202, 2005.

3

Sample characterisation and simulation methods

3.1 Introduction

In this chapter, the experimental and numerical techniques are discussed, which were used as part of this thesis to study of the magnetisation dynamics of ASI. ASI specimen preparation using electron beam lithography will be outlined in Section 3.2. In Section 3.4, the principles of an alternating gradient force magnetometer (AGFM), employed to measure hysteresis loops of ASI systems, are discussed. The main purpose of this thesis is to understand the field and thickness dependence of magnetisation dynamics in square ASI using Brillouin light scattering (BLS) and ferromagnetic resonance (FMR) techniques. As such, these experimental set-ups will be detailed in Sections 3.5 and 3.6, respectively. Transmission electron microscopy (TEM) is another useful means to directly visualise the magnetisation behaviour of pinwheel-type ASI. The basic structure

of TEM and its use in characterising the physical structures of sample are described in Section 3.7.1. Then, the Lorentz TEM techniques, Fresnel imaging and differential phase contrast (DPC) imaging, will be focused on in Section 3.7.2. These methods allow us to visualise the evolution of magnetisation reversal of pinwheel ASI. In Section 3.8, a brief introduction to micromagnetic simulation based on Mumax package will be given, and the computation of the energy of system and magnetisation static and dynamic behaviour induced by external magnetic fields will be explained.

3.2 Sample fabrication

The ASI specimens studied throughout this thesis were fabricated using electron beam (E-beam) lithography. The pinwheel sample with the 'asymmetric' edge in Chapter 6 was patterned by Dr. Ciaran Ferguson at the University of Glasgow. Other ASI arrays, such as square (Chapters 4 and 5) and pinwheel (the 'symmetric' boundary of Chapter 6) ASI, were made by our collaborator Dr. Sophie Morley at the University of Leeds. The details of the ASI specimen fabrication via E-beam lithography and metallisation will be outlined here, which are summarised from the Ref. [1, 2].

First, the substrates, such as thermally oxidised silicon for the FMR and BLS experiments and silicon nitride (Si_3N_4) for the TEM measurements, is cleaned. A thin film of the electron sensitive resist (ZEP520A), is applied to the clean substrate by spin coating. The resist is subsequently exposed to a high-voltage electron beam. This is used to 'write' a desired ASI pattern. The positive tone resist becomes more soluble in the exposed area due to scission of the polymer chains by electrons. The next step is the development in which the exposed resist is dissolved away into the solution [3]. A thin layer of permalloy ($Ni_{80}Fe_{20}$) is then deposited using electron beam evaporation. After metallisation, the remaining resist and excess metal are lifted off using a solvent. In the end, the remaining result is an array of permalloy islands - the ASI system. However, the lift off in the E-beam lithography will fail if the gap between nearest neighbouring islands is too small. For instance, this separation is equal to or less than 20 nm in pinwheel ASI with the 170 nm $\times$ 470 nm nanomagnet.

3.3 Characteristics of permalloy

Permalloy, also referred to as $Ni_{80}Fe_{20}$, is commonly used in magnetic recording heads due to its low coercivity, high relative permeability and small magnetocrystolline anisotropy [4, 5]. The low coercivity means that the magnetic state can be easlily varied in the presence of a small field and the high permeability can obtain high magnetisation at the small applied field. It is well known that microstructures of the magnetic materials are responsible for their magnetic properties. Most of permalloy samples have polycrystalline structure, resulting in the weak magnetocrystalline anisotropy. The weak magnetocrystalline anisotropy is ideally suited for the study of ASI because the magnetic shape anisotropy can be dominant to form single domain in each nanomagnet. S. Lamrani shows that the grains size and lattice constant of the polycrystalline permalloy that is deposited on SiNWs using electrochemical process are 14 nm and 3.53897 Å $\pm$ 0.0002 Å [6]. These magnetic and microstructual charateristics of permalloy attract interest to be ultilised as ASI, which is investigated for potential information storages.

3.4 Alternating gradient force magnetometer

There are a number of laboratory magnetometers which are capable of measuring the magnetisation of material, including superconducting quantum interference devices (SQUID); Faraday force magnetometries; magneto-optic Kerr effect optical magnetometries and alternating gradient force magnetometies (AGFM). AGFM is one of the most sensitive instruments to detect magnetic moment, with resolution up to 10^{-5} A·m^2 [7–9]. Thus, this technique is very suitable as a probe of the magnetic moments of ASI arrays. For example, each nanomagnet of the square ASI in Chapter 4 and 5 has the net moment on the order of 10^{-2} A·m^2.

An AGFM is ultimately based on a force measurement. Figure 3.1 displays the schematic diagram of a vertical AGFM. A sample is mounted on the end of a quartz fiber that is connected to a piezoelectric bimorph. The sample is magnetised by a DC field from the magnets. Simultaneously, it experiences a vertical alternating gradient force which is exerted due to alternating field gradients. The alternating field gradient is created by two gradient circular coils. The alternating currents (AC) flow in the opposite directions in this pair of coil so that the AC magnetic fields generated on their mirror

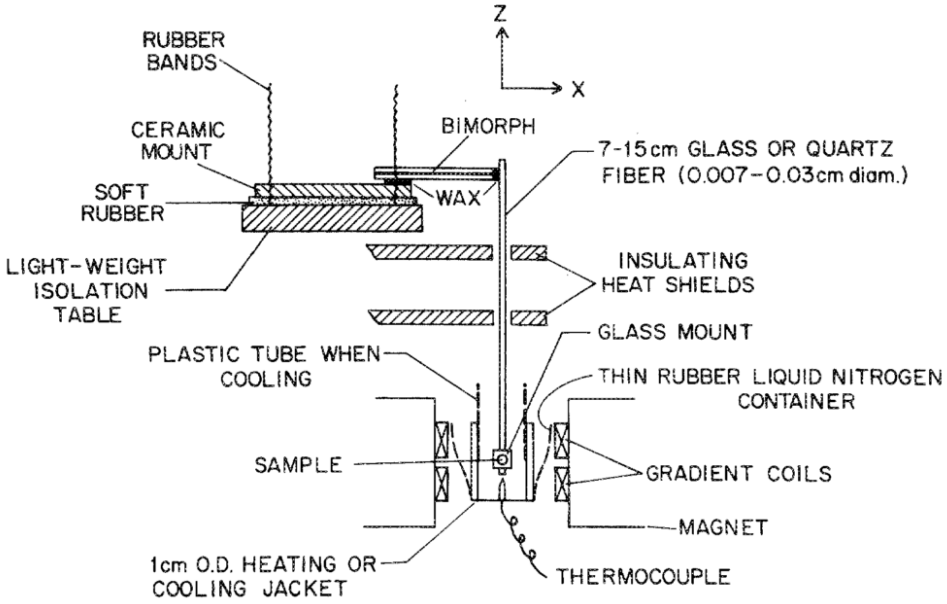

Figure 3.1: Schematic diagram of a vertical AGFM setup designed by P.J. Flanders [10]. Copyright (1990) by the AIP Publishing.

plane, where the sample is placed in Fig. 3.1, can be cancelled, but the field gradient still exists. The AC gradient force can be given by

$$\vec{F} = \nabla(\vec{m} \cdot \vec{h}), \tag{3.1}$$

where m is the magnetic moment, and $\vec{h}$ is the AC magnetic field vector, the magnitude of which is $h_0 \sin(wt)$. Alternatively, the direction of field gradient can be controlled by varying the positions of pairs of coils, such that the coils within a pair have opposite currents [8, 11]. The gradient force along z direction F_z is written as,

$$F_z = m_z \frac{dh_z}{dz}. \tag{3.2}$$

This alternating gradient force leads to a displacement of the quartz fibre. This deflection is measured by the output voltage of a piezoelectric bimorph. In order to amplify the deflected signal, the measurement is performed at around the mechanical resonance of this cantilever, typically, operation frequency being 100-1000Hz [8].

All AGFM measurements in Chapters 4 and 5 were carried out by Dr. Francesca Casoli at the IMEM-CNR, Italy. There, a magnetometer is able to apply a magnetic field up to 2T. For our purposes, the DC applied field was swept from -0.4 T to +0.4 T.

3.5 Brillouin Light Scattering

Brillouin light scattering (BLS) is an effective technique to probe spin waves in a magnetic solid. In particular, it allows for measurements of spin-wave frequencies [12–15] and dispersion relations [16–18]. A general BLS set-up is able to resolve the spin-wave frequencies from 1 GHz to 150 GHz. The behaviour of spin waves in square ASI array in this thesis was investigated via these two aspects, which have been performed by Gianluca Gubbiotti at CNISM, Italy, and will be discussed in Chapters 4 and 5. In addition, BLS is able to resolve spin-wave modes, including those which are not spatially uniform and are often impossible to be detected by FMR.

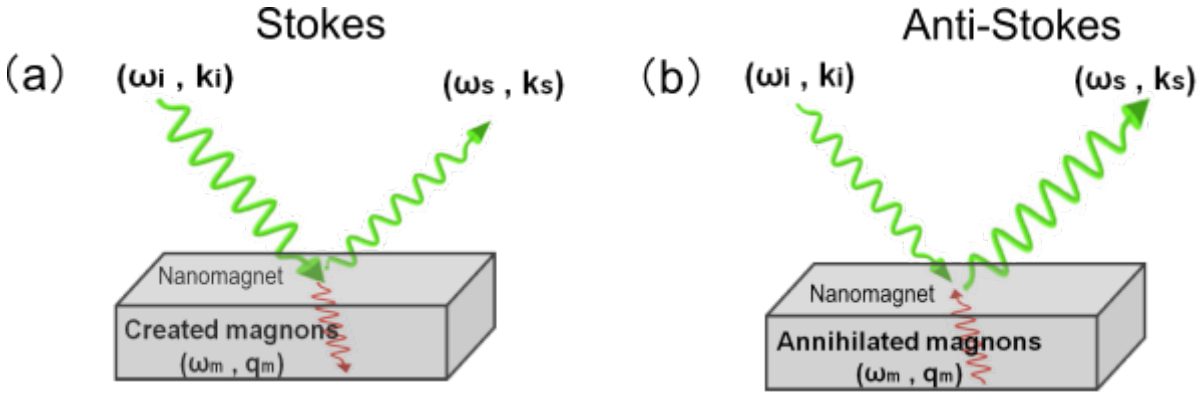

Figure 3.2: Two categories of Brillouin inelastic-scattering interactions in a nanomagnet: (a) Stokes process in which a magnon is created and (b) anti-Stokes case in which a magnon is annihilated. The green-waveform arrow indicates the travelling direction of the incident (or scattered) light and the red arrow represents the transferred magnon during inelastic process.

The mechanism by which spin waves (also referred as 'magnons') are detected in BLS relies on the magneto-optical interaction. As introduced in Section 2.6.2, a magnon is regarded as a wave-like oscillation of magnetisation with certain periodicity. The dielectric inhomogeneity arising from the discrepancy of wave velocity between magnons and photons can be regarded as a quasi-static lattice so that the incident light can be scattered. Typically, the velocity of magnon waves range from 10^3 ms^{-1} to 10^4 ms^{-1} which is much less than that of light 3×10^8 ms^{-1}.

In general, there are two light scattering processes: elastic and inelastic scatterings. An example of elastic scattering is Rayleigh scattering [19]. In elastic scattering, the energy and the momentum of the incident and the scattered photons are identical. By contrast, Raman [20] and Brillouin scattering are examples of inelastic processes. In these cases, the energy and momentum conversion occurs between photon and magnon.

Brillouin scattering is the basis of BLS. This involves Stokes and anti-Stokes scattering processes. Figure 3.2 (a) shows energy loss of the scattered light, $\hbar\omega_i - \hbar\omega_m$, so as to create a magnon ($+\hbar\omega_m$) in the Stokes case, where ω_i, ω_s and ω_m are frequency of incident photon, scattering photon and magnon. On the contrary, anti-Stokes scattering involves the annihilation of a magnon, $-\hbar\omega_m$, so that the energy is transferred to the scattered photon. These two processes are depicted in Fig. 3.2. Energy and momentum conservation in the Stokes and the anti-Stokes processes can be given by

$$\pm\hbar\omega_m = \hbar\omega_i - \hbar\omega_s \tag{3.3}$$

$$\pm\hbar q_m = \hbar k_i - \hbar k_s, \tag{3.4}$$

where k_i, k_s and q_m are the wavevector of incident light, scattering light and magnon. Thus, the change in frequency of the scattered photon is a direct consequence of the interaction between photon and spin-wave oscillation in a nanomagnet. This interaction manifests itself through a variation in transverse light polarisation dependent on the magnitude and the orientation of magnetisation due to the Lorentz force. By contrast, the detected signal will be weak if the light wavevector is collinear to the direction of magnetisation. In most cases, the wave vector of light is always set perpendicular to the magnetisation, referred to as Damon-Eshbach configuration mentioned in Section 2.6.2.

In the back-scattering geometry, where a lens in Fig. 3.2 acts to focus incident beam and collect the back-scattered beam by magnetic sample, the wavevector of spin wave, which is related to the wavevector component of light in the plane of the specimen $q_{\parallel}$, is given by

$$q_{\parallel} = 2k_i sin(\theta_i), \tag{3.5}$$

where θ_i is the incident angle of incoming light with respect to the specimen. Eq. 3.5 shows that the wavevector of incoming light can be controlled by varying the incident angle with respect to the specimen surface. In this manner, the spin-wave dispersion can be detected. This dispersion relation allows us to detect the inter-island interaction. For example, in this study (see Section 4.4.1), the almost flat dispersion curves, in which there are no significant changes in spin-wave frequencies as a function of the wavevector of light,

suggest that standing spin-wave modes occurs and are confined to the nanoislands rather than collective excitations across many magnetic islands.

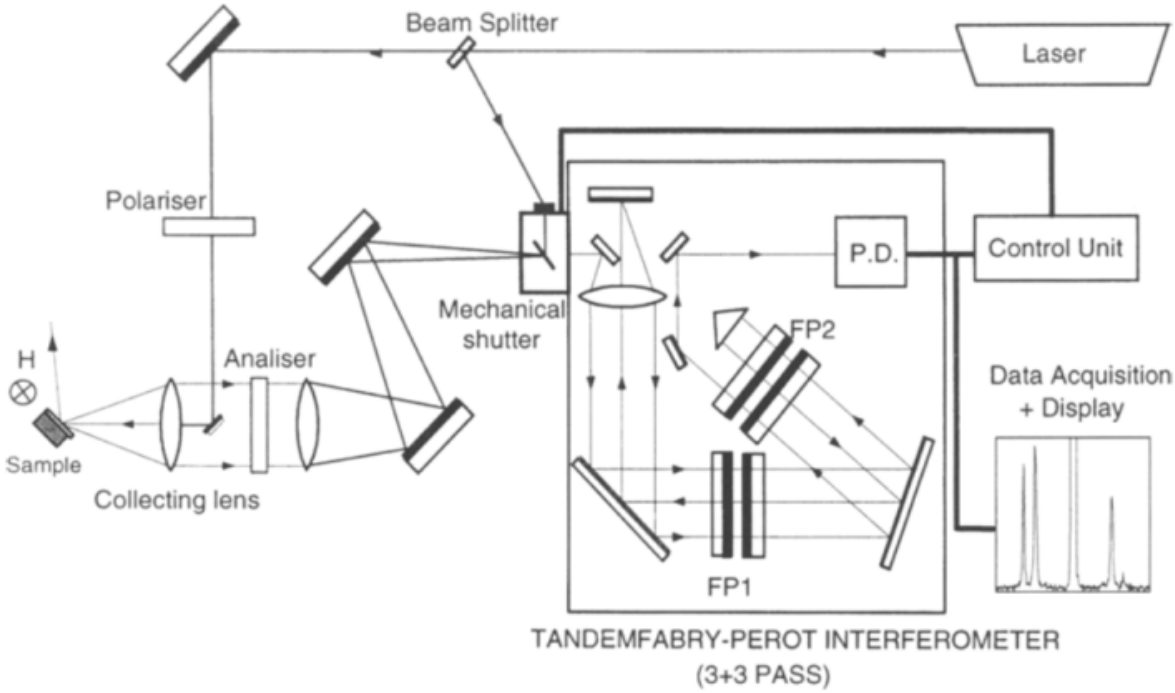

Figure 3.3: Schematic diagram of a BLS experimental setup [21], including back-scattering geometry operation and tandem multipass Fabry Perot interferometer (withãĂĂthe kind permissions of Società Italiana di Fisica and authors).

Figure 3.3 displays a conventional BLS apparatus, comprising a solid state laser and a tandem multipass Fabry-Perot interferometer (FPI). A 200 mW monochromatic light beam of wavelength 532 nm from the solid state laser is focused on the sample surface. In this case, the illuminating spot size of the laser beam was 30 μm. This means that several hundred islands are illuminated and so the information in the BLS spectra is an average over a large number of magnetic elements [21]. The applied magnetic field, H, is always set perpendicular to wavevector of the light. The backscattering photon is collected and channelled into the FPI to be analysed.

FPI is the core part of the BLS setup. It allows discrimination between the extremely weak inelastic light signal and much stronger elastic component. A tandem multipass FPI [22, 23] is used in order to reduce the stray light and increase the resolution in comparison with a single FPI unit. The tandem multipass FPI used in this work had 6 passes, as shown in the box of Fig. 3.3. The light in the FPI undergoes multiple reflections and then interferes constructively or destructively with a reference beam. This reference

beam arises from scattered light at the beam splitter directed towards interferometer though a mechanical shutter. This mechanical shutter is a double shutter, which acts as an entrance of the reference beam and the scattered light but also as a screening of the central elastic light. The reflected intensity achieves a maximum value when the reference and scattered beams interfere constructively.

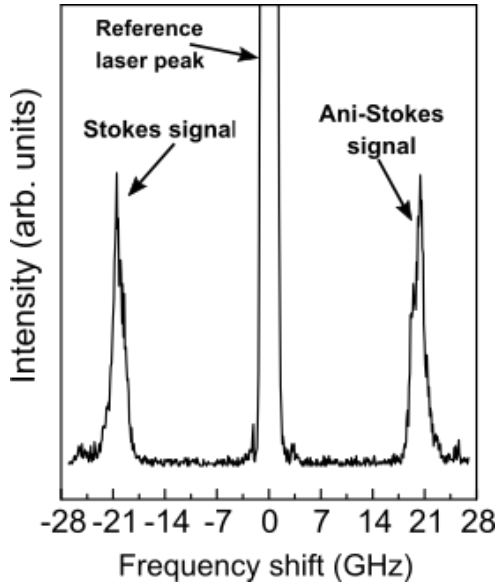

Figure 3.4: BLS spectrum of the square ASI sample at 45° magnetic field of 0.4 T with respect to the square lattices, exhibiting the central reference peak and the frequency shifts of the Stokes and the Anti-Stokes peaks. Each nanomagnet has the 240 nm × 80 nm in-plane dimension and the 10 nm thickness.

Figure 3.4 shows a typical result of the 10 nm thick square ASI specimen at magnetic field of 0.4 T. The central signal at the zero position is the peak of the reference beam. The Stokes peaks have the negative frequency shift with respect to the reference peak. On the contrary, the frequency of Anti-Stokes peaks shift towards the positive direction.

3.6 Ferromagnetic resonance

Ferromagnetic resonance (FMR) refers to uniform spin precessional motion, sometimes called the 'Kittel mode', in a magnetic solid. The basic principle of ferromagnetic resonance has been introduced in Section 2.6.1. Measurements of FMR in this dissertation were performed using a vector network analyser (VNA) and a broadband coplanar waveguide. FMR studies of square ASI and their dependence on angle and direction of magnetic field with respect to the square ASI lattices are discussed in Section 5.3.

A diagram of the VNA-FMR setup is shown in Fig. 3.5 (a). It is composed of a two-port VAN, two coaxial cables, a power source, two inductive copper coils, a coplanar waveguide and a PC. The VNA is connected to the two-port coplanar waveguide via coaxial cables. The waveguide is placed between two copper coils. The copper coils are electromagnets that produce direct current (DC) fields when current is supplied. This DC field, H, is used to magnetise the specimen. On the waveguide, the sample surface has to be touched with the signal line of waveguide, as illustrated in Fig. 3.5 (b). In this way, an oscillating field h_{rf} can penetrate the sample layer (see Fig. 3.5 (c)). All equipment are controlled by an in-house Labview programs.

A two-port VNA is capable of generating and measuring high-frequency microwave signals. In general, this signal is a complex quantity including magnitude and phase. The VNA apparatus of FMR experiment is a Rohde & Schwarz ZNA40, with a frequency range from 0.1 MHz to 40 GHz. An alternating microwave with a GHz frequency is applied from Port 1 of the VNA to the central conductor of the waveguide, which is enclosed by two-side ground planes. This centre signal line corresponds to the inner conductor of the coaxial cable and the ground planes are related to the outer conductor. The waveguide has a 50 Ω characteristic impedance (Z_0) which matches the coaxial cable. The alternating microwave passing through the signal line is measured via Port 2. This oscillating current leads to a high-frequency electromagnetic field h_{rf} in the plane of sample, as shown in Fig. 3.5 (c). Since the conductor has a rectangular shape, the radiofrequency magnetic field it generates is inhomogeneous, i.e. it forms an elliptic shape [24]. The measured specimen is biased using the static DC H produced by the Kepco power supply with the limits of $\pm$ 10 A ($\pm$ 100 V), and then subject to alternating fields, h_{rf} . The directions of static and oscillating fields are perpendicular so that the driving field h_{rf} interacts with the dynamic magnetisation of the sample as biased by the static field. A Gauss meter (not shown in the diagram) is used to probe the strength of magnetic field in the vicinity of specimen.

The concept of a scattering parameter was proposed as a standard quantity in microwave measurement. The scattering parameter is defined to be a coefficient of reflection or transmission signals. Most importantly, this quantity is associated with the variation in characteristic impedance of the signal which passes through a magnetic specimen. The equivalent circuit is a two-wire transmission line, as depicted in Fig. 3.6. The parameter,

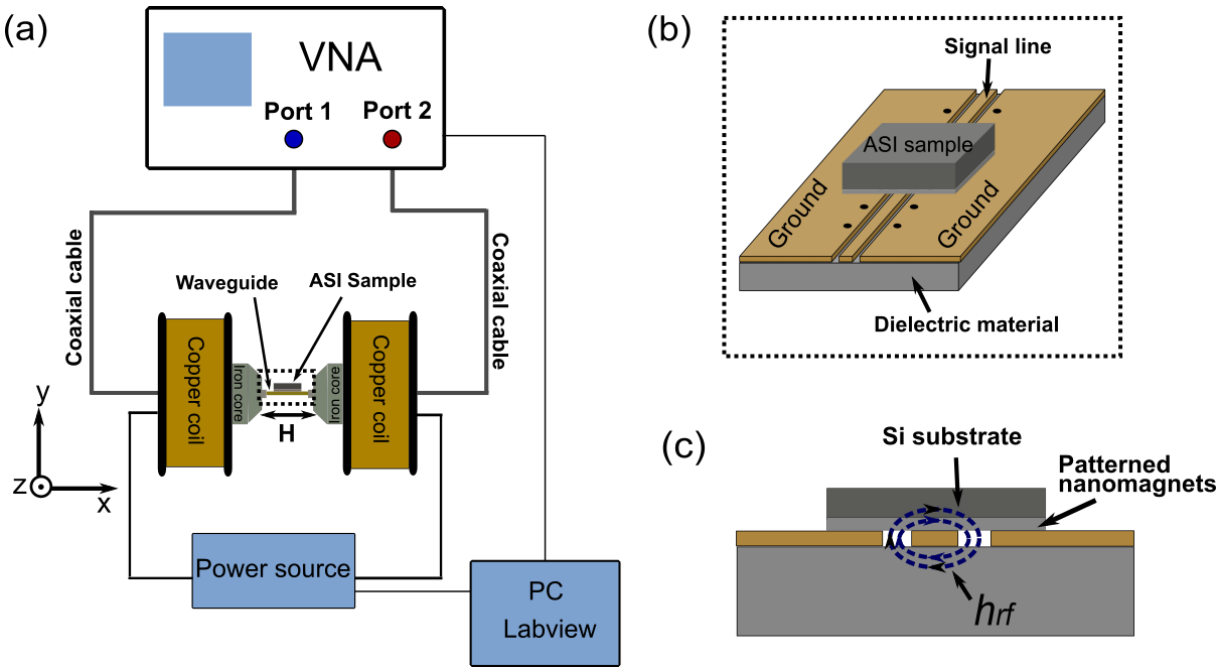

Figure 3.5: (a) A schematic diagram of the whole VNA-FMR apparatuses; (b) A zoom-in top view of configuration combined a coplanar waveguide and a specimen, which is labelled by a dashed box in (a). (c) The oscillating current from VNA flows though the signal part along x direction of (a) and create a high-frequency driven field (h_{rf}). The surface of specimen gently touch the waveguide so as to ensure the strength of h_{rf} acting on sample is sufficient.

a_i, refers to the incoming microwave power while b_i is the reflected or transmitted microwave power, where 'i' represents the port number of the VNA. The magnitude of input and output microwave power in terms of total voltage V_i, current I_i and characteristic impedance Z_{0i} are given by [25]

$$a_i = \frac{1}{2}\left(\frac{V_i}{\sqrt{Z_{0i}}} + I_i\sqrt{Z_{0i}}\right) \tag{3.6}$$

$$b_i = \frac{1}{2}\left(\frac{V_i}{\sqrt{Z_{0i}}} - I_i\sqrt{Z_{0i}}\right), \tag{3.7}$$

where a_i is the input signal (a_1, a_2) holds the power and b_i is the output power (b_1, b_2). The relationship between them can be described in terms of scattering parameter, which follows

$$b_i = Sa_i, \tag{3.8}$$

where S is the scattering matrix. Figure 3.6 shows that there are two types of measurable quantities for a two-port waveguide: reflected and transmitted microwave signal. If a

signal is emitted from the Port 1 (Port 2) and reflected via the Port 1 (Port 2), the reflecting coefficient is referred to as 'S_{11}' ('S_{22}'). Another type of scattering is the coefficient of transmission. In this case, the input microwave signal from Port 1 (Port 2) transmits and outputs through Port 2 (Port 1). This coefficient is labelled by 'S_{12}' ('S_{21}'). It can be summarised this using a matrix:

$$\begin{bmatrix} b_1 \\ b_2 \end{bmatrix} = \begin{bmatrix} S_{11}, S_{12} \\ S_{21}, S_{22} \end{bmatrix} \begin{bmatrix} a_1 \\ a_2 \end{bmatrix} \tag{3.9}$$

As has been previously stated, the VNA is utilised to measure magnitude and phase of a given complex S parameter. In order to calibrate the extra mode that may be generated from the port and the connector, a full-port calibration is essential to correct any variations in magnitude and phase arising from the VNA ports and connecting cables. The most common calibration method is called SOLT (short-open-load-thru). The short circuit, open circuit and load circuit are connected in turn to each port of the VNA so that the signal reflection is calibrated. The 'thru' (through) circuit calibrates the transmission signal via connecting Port 1 and Port 2 together [26]. In our experiment, the waveguide calibration kit for the VNA is one manufactured by R&S [25].

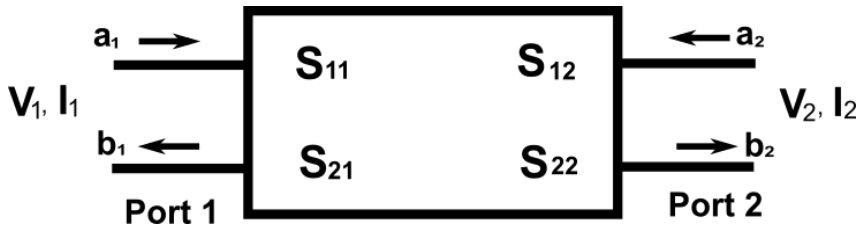

Figure 3.6: The diagram illustrating the definition of scattering parameters S for a two-port waveguide. a_1 and a_2 are incoming microwaves signal and b_1 and b_2 are measured signal. Consequently, four types of scattering parameters are available, S_{11}, $S12$, S_{21} and S_{22}. V and I represent the voltage and current at each port.

In addition, it is necessary to consider external factors and their effects on FMR measurements. These include environmental noise and mechanical vibration etc. FMR has been found to be slightly time dependent in our measurement: that is, the position and FWHM of the resonance peaks vary with time [25]. In this study, the transmission scattering parameter S_{21} is measured, so as to illustrate the magnetisation dynamics induced by an external field. In order to increase the signal-to-noise ratio of this S signal, a reference scattering parameter S_{21}^0 is also obtained at a fixed magnetic field. This fixed field has to be higher than the maximum of the external field applied. The quantity S_{21}^0

is acquired at every experimental data point and is applied to normalise the measured parameter S_{21}, S_{21}/S_{21}^{0}. This normalised signal is able to reduce the possible influence of time-dependent source, i.e. from VNA instability or from stress between waveguide and sample. Furthermore, a vibration isolation system, Stabilizer Technology, is used to minimise the vibration caused by environmental noises in the lab.

Two categories of measurements have been performed to examine the ferromagnetic resonance of square ASI systems in this dissertation, namely, their dependences on magnetic field strength and field angle. Firstly, the strength of a external DC field was created by supplying to the copper coils. The maximum magnetic field strength was ±200 mT which corresponds to a maximum of ±2 A from the power source. This current limit is determined by a combination of 40 Ω coil sets and the 100 V limit of the power supply. Secondly, the field angle with respect to the square lattice was adjustable using a rotational mount with angle indicator. The backside of the ASI specimen was glued to this angle adjustor and the specimen surface was gently touched to the signal line of waveguide. Given Fig. 3.7 (a) shows that the FMR absorption peak appears close to 16.5 GHz with 0° magnetic field with the amplitude of 150 mT upon the square ASI. Figure 3.7 (a) is a contour plot showing the evolution of the frequency of the FMR resonance peak as a function of applied magnetic field. More relevant discussion about them will be detailed in Section 5.3.

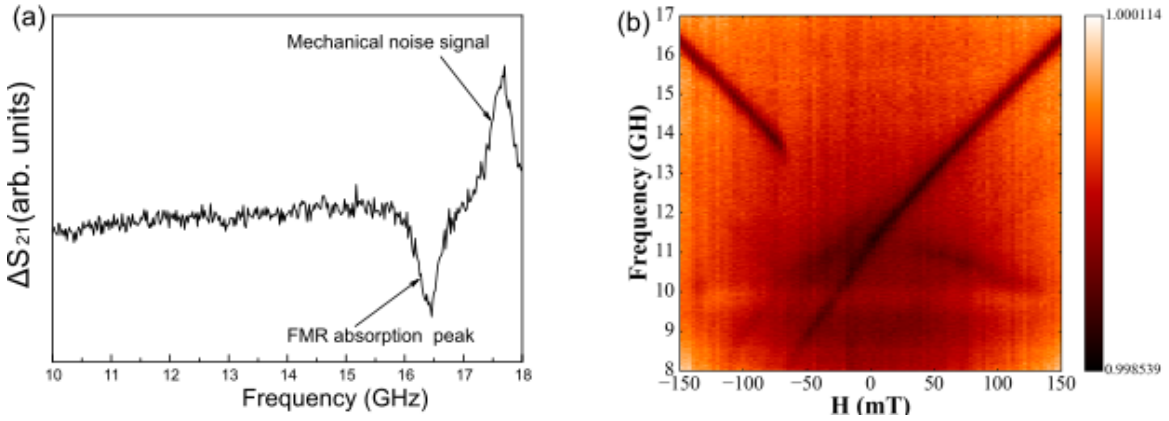

Figure 3.7: (a) FMR spectrum of the square ASI at 150 mT magnetic field of 0° with respect to the square ASI lattices. The island size is 240 × 80 × 30 nm^3. (b) Contour plot of the FMR results displaying the frequency of resonance as a function of the magnetic field sweeping from 150 mT to -150 mT.

3.7 Transmission electron microscopy

Transmission electron microscopy (TEM) is widely utilised to characterise not only the physical microstructures [27–31] and chemical properties [32–35] of materials, but also their magnetic behaviour [36–44]. In this section, the operation of TEM instruments is described and how structural imaging processes are achieved with a particular focus on magnetic imaging is highlighted.

Optical transmission microscopy was first used to magnify images of a small object using visible light. However, the spatial resolution of this microscope is indeed fundamentally limited by the finite wavelength of the light probe. This means there is a limit to the resolution of the image. For example, visible light with a wavelength of 500 nm can only image the micro-structural details of 200 nm [45]. To overcome this restriction, by means of decreasing wavelength, a better spatial resolution on principle could be achieved. In 1925, Louis De Brogilie postulated that matter particles could behave as waves. He put forward a theory of electron wavelength in terms of Plank constant h and electron momentum p. This well-known de Broglie wavelength is given by

$$\lambda = h/p. \tag{3.10}$$

In 1932, Knoll and Ruska built the first electron microscope based on this idea. The relationship between wavelength, λ, of an electron and the accelerating voltage V in an microscope is given by

$$\lambda = \frac{h}{\sqrt{2m_0eV}}, \tag{3.11}$$

where m_0 is the rest mass of an electron and eV is the kinetic energy of the electron. In most common TEM operations, the accelerating voltage is often greater than 100 kV. The electron is then moving at relativistic speeds and there is a correction to Eq. 3.11. In particular, it is found that

$$\lambda = \frac{h}{\sqrt{2m_0eV(1+\frac{eV}{2m_0c^2})}}, \tag{3.12}$$

where $c = 3 \times 10^8 m/s$ is the speed of light. The accelerating voltage applied in this work was 200 kV, the relativistic wavelength is found to be 2.51 pm using Eq. 3.12, for

comparison, which is smaller than 2.73 pm non-relativistic wavelength [46]. The electrons as a radiation source thus are sensitive to smaller length scales. JEOL ARM 200cF TEM with the aberration correction at the University of Glasgow is able to achieve sub-atomic spatial resolution, down to 0.078 nm .

3.7.1 Imaging in TEM

TEM has been proved to be a versatile tool in a variety of fields. However, the fundamentals operation of all commercial TEMs remains the same: magnify and image sample down to nanoscale or smaller. Commonly, there are two main TEM modes: conventional TEM (CTEM) and scanning TEM (STEM). In CTEM mode a fixed parallel electron beam illuminates a broad region of the specimen, whereas in STEM mode a convergent beam illuminates a small area and scans across the sample. Fresnel imaging is the primary characterisation method in this thesis for imaging magnetic structure (see Chapter 6). This is performed in CTEM. As a result, the discussion will be focused on image formation in CTEM, with a brief introduction to STEM in Section 3.7.2.3.

3.7.1.1 TEM instrumentation

Figure 3.8 shows the basic setup of a TEM in a standard CTEM mode. The fundamental structure of a TEM consists of five parts: the electron source system, the condenser system, the objective systems, the projector system and the detector. The standard imaging process is as follows: electrons are emitted from an electron gun and can be accelerated by anodes. The beams are produced to illuminate the specimen with parallel rays via the condensed lens. The transmitted and scattered electron beams from the specimen are imaged by the objective lens to form a real-space magnified image using the projector lens on a viewing screen or detector.

The electron gun is a source of electrons and commonly installed at the top of the TEM. Here two types of gun are discussed: thermionic emission gun and field-emission gun (FEG). A thermionic gun is able to produce electrons under the application of heat. At high temperatures, electrons gain sufficient energy to overcome the work function of the filament and are eventually emitted. Tungsten (W) or lanthanum hexaboride (LaB_6) crystals are usually used as a cathode in thermionic guns. A Welnet cylinder with a small negative bias (approximately a few kV) converges these emanating electrons to a

point, in essence acting as an electrostatic lens. This convergent point of electron beam is termed as the gun cross-over and occurs between Wehnelt and an anode. The anode is used to accelerate electrons imparting kinetic energy. The FEI Tecnai T20 TEM at the University of Glasgow is equipped with either tungsten or LaB_6 filament. Another category of emission source is FEG. There are two types of FEG, cold FEG and the Schottky FEG. The cold FEG works at ambient temperatures in ultra-high vacuum with a smaller source size, while Schottky FEG is operated at elevated temperate with better stability of the beam. A cold FEG is employed in the JEOL ARM 200cF TEM at the University of Glasgow. A FEG makes use of an extremely fine tungsten tip as the cathode. This tip has a radius on the order of 100 nm [47]. One significant difference of FEG in comparison with a thermionic gun is that two sets of anodes are used, as shown in Fig. 3.8. The first anode has a positive bias field and creates a strong electron field gradient at tip which forces electron out of the tip. The second anode acts to accelerate the electrons to a desired speed. The combination of an extraction and an accelerating anodes also behaves as an electrostatic lens to converge electrons to the gun crossover.

Each type of gun has both advantages and disadvantages. The LaB_6 filament as the thermionic gun has tremendous advantages in comparison with tungsten. Namely, it has a better brightness due to higher current density, a better coherency due to smaller source size and longer lifetime. Regarding the cold FEG applied in this study, it possesses much higher brightness, much better spatial coherency (small beam size) and longer lifespan (as much as 50 times) compared to thermionic gun. However, this comes at expense of the stability of the gun emission current .

The most crucial units in a TEM are electron lenses and apertures. The combination of a series of lenses and apertures acts to converge, diverge and screen the beam. The electron lenses used in TEMs are electromagnetic lenses which consist of two polepieces and copper coils around a soft-iron core. When current flows through the copper wires, a magnetic field is created in the bore. This magnetic field is inhomogeneous along the long axis of the lens that is perpendicular to the optic axis of TEM (see Fig. 3.8), whereas it is axially symmetrical. An enormous advantage of such a lens is that, unlike the fixed glass lens in a standard optical microscope, the strength of magnetic field can be controlled by varying current. Apertures are used to remove the stray rays far from optic axis. These stray rays reduce resolution by spherical aberration. A smaller aperture provides a better

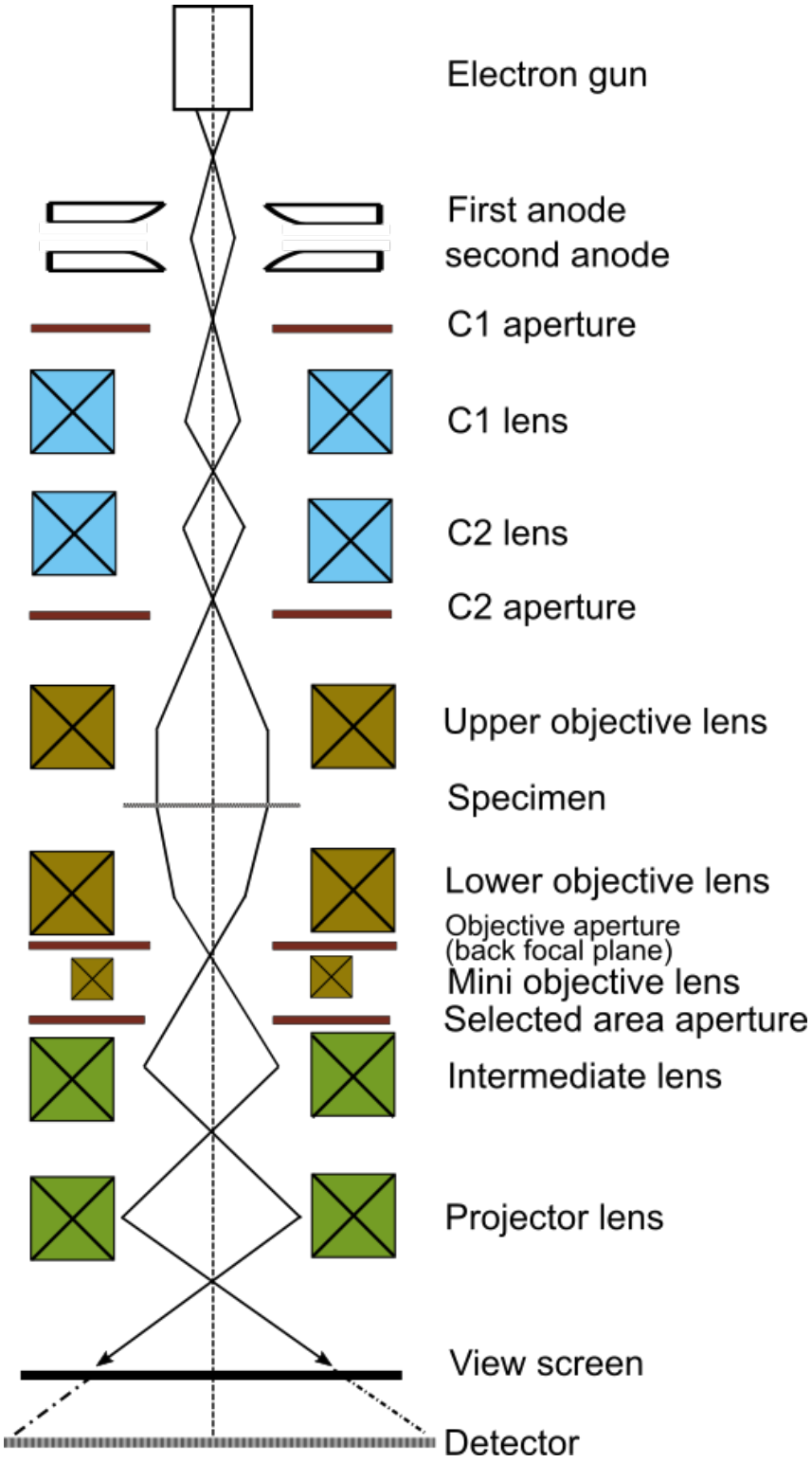

Figure 3.8: A simplified ray diagram of the imaging formation in a CTEM mode, where the central dash line is the optic axis. The TEM is composed of gun column, condensed lens, objective lens and projectors lens. The lens and electron beam path are not scaled.

resolution, but weakens the intensity.

Inherent imperfections in the manufacturing of lenses and apertures limit the resolution of TEMs. The three main factors are spherical aberration, chromatic aberration and astigmatism. Spherical aberration is an effect caused by the rays further from the optic axis being focused more strongly than those close to the optic axis. Thus, it refers to a breakdown in the paraxial approximation. This leads to a converging disk instead of a point in the Gaussian image plane, consequently, image resolution is degraded. The radius of this disk r_s is given by

$$r_s = C_s \beta^3, \tag{3.13}$$

where C_s is the spherical aberration coefficient of the lens. β is the maximum angle of electron collection by an aperture. The coefficients of the spherical aberration in the T20 and ARM TEMs are 1.2 mm and 0.5 mm, respectively. To avoid this problem, a corrector with quadrupoles, hexapoles [48, 49] or octapoles [50] was proposed to correct the spherically aberrated disk of the objective lens. The aberration corrector in our ARM TEM with a combination of these three types correctors allows for the achievement of a better resolution of r_s, down to 0.075 nm.

Another intrinsic aberration, chromatic aberration, is related to the wavelength of the electrons. This effect results from electrons with a variety of wavelengths so that the probe is non-monochromatic. The beam cannot be converged to a point. A source which generates monochromatic electrons plays a vital point in eliminating this aberration, such as the use of a cold FEG in JEOL ARM TEM.

Furthermore, the third aberration from a lens is astigmatism. This arises from an inhomogeneous magnetic field. An astigmator, therefore, is employed to minimise this affect by applying an opposite field to counteract the asymmetry. In order to obtain better resolution, the astigmatism of condensed lens (CL) and objective lens (OL) always needed to be compensated during the TEM alignment via the astigmators which are installed below the lens in our T20 and ARM TEMs.

Now three fundamental components of a TEM are described: illumination system, objective lens and imaging system. The illumination system is composed of the electron gun and the condenser lenses. In this system, electrons are generated and shaped to illuminate the specimen in a parallel fashion on the specimen, as shown in Fig. 3.8.

Condenser system is composed of C1 and C2 lenses. The C1 lens demagnifies the rays to a point and the C2 lens allows this crossover beam to travel parallel to the specimen. The strength of the C1 lens contributes to the spot size of beam in the plane of specimen, while the C2 lens controls the beam brightness.

The OL, the heart of the TEM, consists of an upper OL and a lower OL. The upper OL in practical use works as a third condenser lens, providing a more parallel beam, as it is impossible for the C2 lens to generate perfectly parallel rays. The lower OL behaves as an imaging lens. In our TEM, the specimen is inserted between the upper and the lower OLs rather than placed above OLs as in some other TEMs. The strength of the magnetic field from the OLs can be on higher than 2 T. In Lorentz TEM imaging, these OLs are switched off to create a low field environment for the magnetic sample. In this case, a mini OL takes the place of the function of the lower OL, which is to converge electron beam from the object plane.

Resolution is the key function of a microscope. The role of the image system is to magnify and image the nanostructural details of the specimen. The image system includes the intermediate lens, the projector lens and the view screen/detector. The intermediate and projector lens are mainly used to magnify the specimen structure and project the image on to the fluorescent screen or detector. The fluorescent screen at the bottom of the TEM is coated by a layer of ZnS. This layer emits visible light when an electron strikes it. The image can be recorded by various detectors, charged-coupled device (CCD, for bright and dark field images and diffraction pattern) in CTEM or spectrometer (for electron energy loss spectroscopy (EELS)) in STEM. A CCD was the main detector used in this thesis. It is sensitive to electrons that are converted to photons through the scintillation and then an image in terms of digital signal at each pixel can be generated, readout and amplified in this CCD chip.

For the purpose of analysing the internal nanostructure, a TEM specimen is required to be electron-transparent. For example, specimen thickness should not exceed 100 nm for a 200 kV electron beam. There are two approaches to fabricate the thin TEM specimens. The TEM substrate of ASI in Chapter 6 was a silicon nitride (Si_3N_4) membrane (see its schematics in Fig. 3.9), whose TEM window has only a 30 nm thickness but is still robust [2]. The nanomagnets were patterned on top of this membrane. Additionally, a focused ion beam (FIB) can be used to mill sections of a bulky material to be a foil.

This allows electrons to transmit the cross section of a specimen in order to observe its microstructure in TEM.

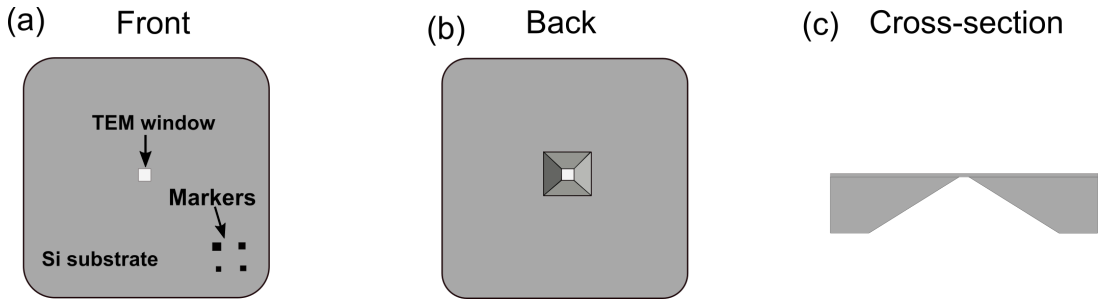

Figure 3.9: Schematics of the (a) front, (b) back and (c) cross-section sides of the TEM silicon nitride membrane. This membrane is composed of the central silicon nitride membrane (TEM window is around 30 nm thick) in the silicon supporting frame. The black squares on the right-bottom corner are the markers for E-beam lithography.

3.7.1.2 Characterising structure

Two common operations in CTEM provide information on the nanostructure of a specimen: diffraction mode and image mode. The diffraction pattern (DP) provides atomic or crystalline details of the sample. Image mode including bright field (BF) and dark field (DF) images gives direct visualisation of the morphology of a sample, i.e. grain size, grain boundary or defects.

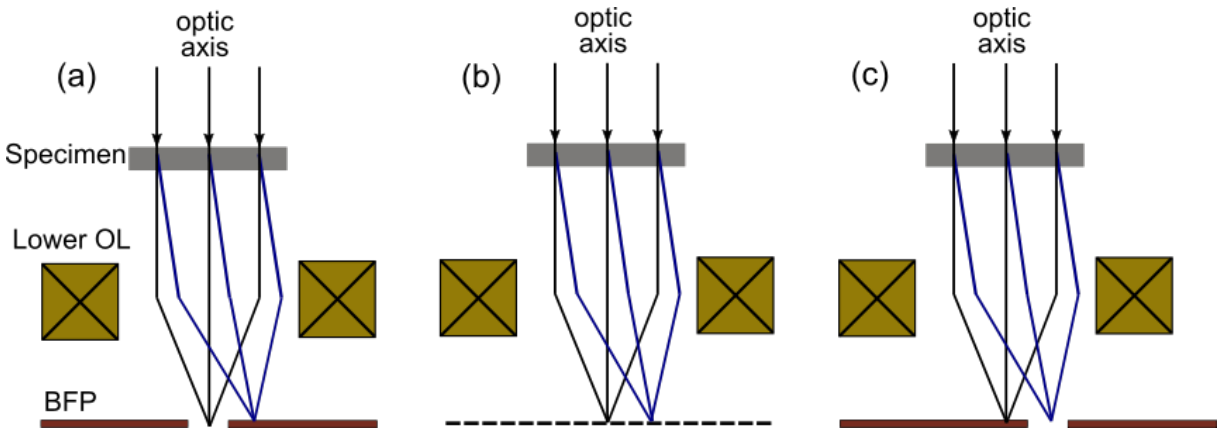

Figure 3.10: Simplified diagram of the imaging formation of (a) BF, (b) DP and (c) off-axis DF images. Their formations depend on the selection of direct beam or scattering beam by the objective aperture at the BFP.

Assume that three parallel plane waves are incident onto a crystal plane within the specimen at some angle, θ, and they are reflected by this plane. DP is formed when these scattered plane waves constructively interfere. This interference satisfies the Bragg's condition,

$$n\lambda = 2d\sin\theta, \tag{3.14}$$

where n is an integer; λ is the wavelength of the electrons; d is the distance between two crystal planes. Once the DP forms in the back focal plane (BFP), as schematically shown in Fig. 3.10, the intermediate projector lens can magnify and project reciprocal lattice points onto a view screen. An example of DP from silver nanoparticles is displayed in Fig. 3.11 (b). A selected-area aperture (see Fig. 3.8) is inserted into the image plane of the objective lens. It acts as a virtual aperture above the specimen to select a desired region of the specimen. In this way, the desired region only contributes to the DP.

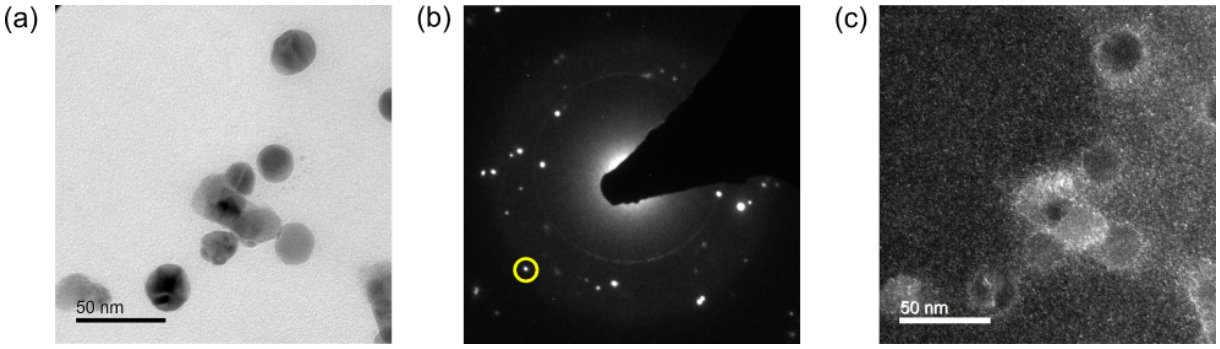

Figure 3.11: Examples of a (a) BF image and (b) corresponding DPs from silver nanoparticles deposited on a carbon grid, which was obtained on an FEI Tecnai T20. (c) A DF image is formed from the scattered spot marked by the yellow circle (Courtesy of Jack Brennan at University of Glasgow).

Figure 3.10 illustrates that the DPs created at the BFP contain a bright central spot (black rays) and some scattered spots (blue rays). These two categories of DPs can be independently selected so as to form two basic outputs in CTEM modes. The image formed by the central direct beam is known as BF image (see Fig. 3.10 (a)). An example of BF image of silver nanoparticles is shown in Fig. 3.11 (a). The image arising from scattered electrons is termed a DF image (see Fig. 3.10 (c)). A DF image of the silver nanoparticles, constructed from the diffraction spot marked by a yellow circle of Fig. 3.11 (b), is displayed in Fig. 3.11 (c). Selection of a specific spot is achieved via the OL aperture in the BFP. To summarise, a BF image is produced using just the direct beam, while an off-axis DF image is formed using certain diffraction spots. DF images are useful to understand the microstrucuture of materials with variations in thickness, mass and crystal orientation, since a greater scattering angle can be obtain over a thicker area or because of a higher atomic number. However, electrons further away from the optic

axis suffer from the spherical aberration and the astigmatism. To avoid this distortion, the scattered electron should emerge near to the optic axis. Thus, double-deflection coils above the specimen are applied to tilt the incident beam so that the scattered electrons now travel along the optic axis. This operation is called the centre DF imaging.

3.7.2 Magnetic imaging in TEM

In addition to characterising structure, TEMs can be exploited to extract information on magnetic behaviours of nano-scale materials [36, 41, 51, 52]. This TEM operation of magnetic imaging is known as Lorentz microscopy. Three of the most widely-utilised approaches in Lorentz microscopy are Fresnel imaging [39, 53, 54], DPC [55–57] and electron holography [58, 59].

3.7.2.1 Lorentz microscopy

Lorentz TEM measurements were carried out to image magnetic behaviour of ASI using the FEI Tecnai T20 and the JEOL ARM 200cF TEMs at the University of Glasgow. The strength of magnetic field created by OLs in an ordinary TEM is on the order of 2 T and the field direction is perpendicular to the plane of specimen (see Fig. 3.17 (b)). Such a strong field not only destroys the desired magnetisation state of specimen but also suppresses any magnetic contrasts arising from the deflection in trajectory of the electrons, as illustrated by deflected rays of Fig. 3.12 (a). The upper and lower OLs thus must be switched off to produce a low-field environment. Yet there still exists a remnant field of about 100-150 Oe in the neighbourhood of the specimen. By applying an opposite current (deguassing current) to the OL using a Magnetic Field Neutralizer device, this residual stray field can be compensated. Consequently, magnetic fields of less than 1 Oe near to the specimen can be achieved. Under this low-field condition, two additional mini OLs act in place of the main OLs, and are thus responsible for imaging [52]. The JEOL ARM 200cF instrument provides extremely high spatial resolution of about 1 nm with a C_s corrector in the STEM mode [60].

Lorentz microscopy makes use of the interaction between the motion of electrons and the magnetic induction they encounter. Assume electrons travelling along the z direction though a thin magnetic film in Fig. 3.12 (a). They experience the deflections produced by Lorentz force arising from the magnetic induction B. The expression of Lorentz force

F acting on a electron is described by

$$\vec{F} = -e(\vec{v} \times \vec{B}). \tag{3.15}$$

where e is the magnitude of electron charge and $\vec{v}$ represents the velocity vector of electron.

Generally, TEM image contrast is generated when the electron beams are scattered by specimens. Both amplitude and phase of the scattered electron can be varied and contribute to the image contrast. In particular, DP, BF and DF images are formed by variation of the electron wavefunction in amplitude, while the formation of Lorentz images is associated with the phase. There are two approaches to understanding the beam deflection due to the magnetic induction of samples. They rely on the classical and quantum perspectives.

In the classical regime, the deflection angle, β, on passing through a uniform film of thickness, t, can be described approximately by [36]

$$\beta = \frac{eB_s \lambda t}{h}, \tag{3.16}$$

where e is the electron charge, $B_s = \mu_0 M_s$ is the saturation induction, λ is the electron wavelength, and h is Planck's constant. For example, in our experiment, the deflection angle is on the order of 6.5 μrad for a 10 nm thick permalloy nanomagnet whilst the electron energy is 200 kV. This deflection angle is much smaller than that arising from Bragg diffraction typically, about 10^{-2} mrad [61].

The above classical description provides a qualitative explanation about phenomenon of the Lorentz force, but it cannot produce the accurate magnetic induction. Therefore, a quantum mechanical description is proposed as it is related to interference phenomenon. This gives a quantitative insight into magnetic induction. The electron wave has a phase shift when it passes through the specimen because of the Aharonov-Bohm effect [62]. This phase shift is produced between two electron beams. These two beams start from the same point and end to same point through different paths. The phase shift is then given by [62]

$$\phi_m = \frac{e}{\hbar} \oint_{-\infty}^{+\infty} A \cdot dl, \tag{3.17}$$

where A is the magnetic vector potential and l is the integral path. Indeed $\oint A\dot{dl}$ describes

the magnetic flux through the cross-section area of magnet, as presented in Fig. 3.12 (b). Thus, based on the Stokes theorem Eq. 3.17 also can be written as

$$\phi_m = \frac{e}{\hbar} \int B \cdot dS, \tag{3.18}$$

where S is the surface area (the xz plane) of the sample which the magnetic induction B is perpendicular to. For the sake of simplicity, the magnetic induction is spatially homogeneous, $B = B_s$, and the thickness t is constant (along z direction). As a result, the phase shift ϕ_m becomes

$$\phi_m = \frac{e}{\hbar} t \int B \cdot dx = \frac{eB_s tx}{\hbar}. \tag{3.19}$$

Compared with Eq. 3.16, the quantitative description of the Eq. 3.19 differential phase $\nabla\phi_m$ is similar to the expression of the classical deflection angle β. The relationship between the phase difference and the deflected angle is found to be

$$\phi_m = \frac{2\pi\beta x}{\lambda}. \tag{3.20}$$

If calculated the differential phase difference of Eq. 3.20 along the x axis, it follows

$$\nabla\phi_m = \frac{2\pi\beta}{\lambda}. \tag{3.21}$$

Eq. 3.21 reveals that the differential phase difference is proportional to the deflected angle β which is associated to the magnetic induction. Therefore, the quantum mechanical expression allows for the image simulation and calculation. Figure 3.12 (b) presents the profiles of electrostatic phase (ϕ_e), phase difference (ϕ_m), differential phase difference ($\nabla\phi_m$) (for differential phase contrast) and Laplacian phase difference ($\nabla^2\phi_m$). Intensity of the Fresnel image, which will be introduced later, makes use of the Laplacian phase difference ($\nabla^2\phi_m$) to characterise the magnetic information.

3.7.2.2 Fresnel Imaging

Fresnel imaging is a rapid way to observe the magnetic domain wall by means of changing the imaging lens with certain defocus length $\triangle f$. This imaging approach is conducted in CTEM mode. The schematic diagrams of this image formation are illustrated in Fig.

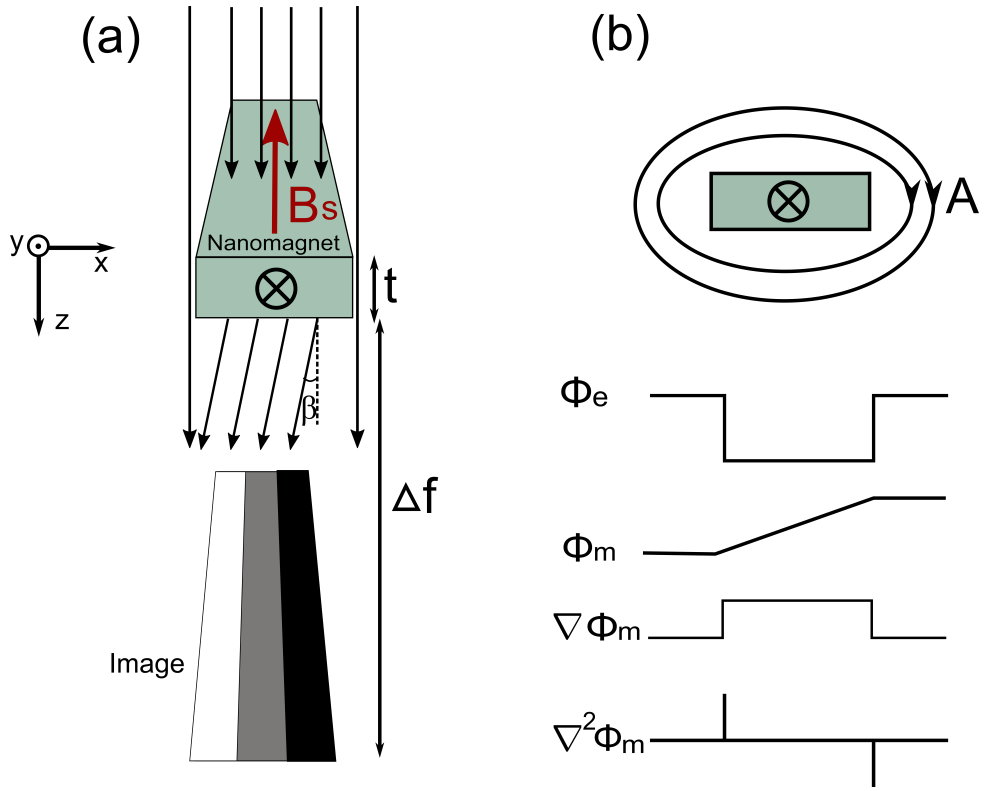

Figure 3.12: (a) Schematic diagram of the Fresnel contrast formation from a single-domain nanomagnet. The bright and dark magnetic contrast are created along the two sides of one island that allows us to identify direction of the magnetisation. (b) The top diagram shows the vector potential surround the nanomagnet. The bottom diagram is the theoretical profile of the electromagnetic phase (ϕ_e), magnetostatic phase shift (ϕ_m), differential magnetic phase shift ($\nabla\phi_m$) and Laplacian magnetic phase shift ($\nabla^2\phi_m$) across the the nanomagnet along x axis.

3.12 (a) and Fig. 3.13. The principle of Fresnel imaging takes advantage of the deflection of electrons due to the magnetic induction. This results in converging/diverging beams interference and forms the brighter/darker contrast on the grey region as the indication of the domain wall. This uniform grey area represents where the domain is. Increasing the $\triangle f$ generates an increment in the contrast. Assuming the $\triangle f$ is low, the imaging intensity (I) of the Fresnel images is linearly associated to the Laplacian of magnetic phase shift [63]:

$$I = 1 - \frac{\triangle f \lambda}{2\pi} \nabla^2 \phi_m. \tag{3.22}$$

In practice, the $\triangle f$, however, must be efficiently large to form the magnetic contrast, resulting in the intensity becoming non-linear with the Laplacian of magnetic phase difference [36]. Thus, the quantitative analysis of the magnetic induction based on the Fresnel images is not rigorous. An alternative approach of Lorentz TEM, DPC (see Section

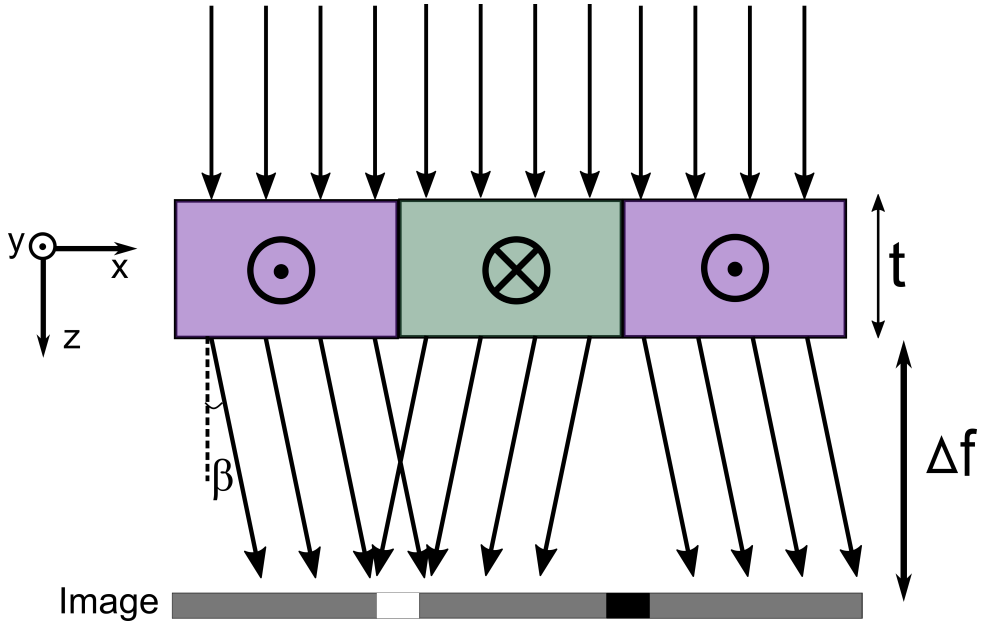

Figure 3.13: Schematic illustration of the Fresnel contrast imaging to reveal the position of two 180° domain walls. White or dark contrast in the image arises from the deflection of electron beam because of the Lorentz force and β is the deflection angle.

3.7.2.3), is capable of the quantitative interpretation.

Increasing defocus nevertheless comes at the expense of image resolution. A suitable defocus should be selected so as to image the magnetisation whilst retaining the structural information of the specimen. The resolution of the Fresnel image is able to achieve about a few nanometers [64]. This imaging mode in principle is implemented in a free-field environment. However, for cases, where a small field is required to act as an external field to magnetise the specimen, a small current therefore can be applied to the OLs. Combined with tilting the sample, this allows for the introduction of the in-plane magnetic field (detailed in Section 3.7.2.4). Most importantly, Fresnel phase contrast is taken at an under-focus or over-focus position (that is at a defocus distance $\triangle f$ above or below the image plane). Empirical analysis of our Lorentz TEM measurements suggests that the formation of image contrasts of the single domain of a nanomagnet at underfocus is more noticeable than at overfocus.

As has been introduced in Chapter 1.2, each magnetic island of ASI is assumed to be a single domain. Therefore, the intensity contrast generated by the moment of each island is formed at the two sides of imaging island and a uniform grey region in the middle corresponds to the domain, which is schematically described in Fig. 3.12 (a). An example of the Fresnel image of an ASI array is presented in Fig. 3.14 (a). The single-

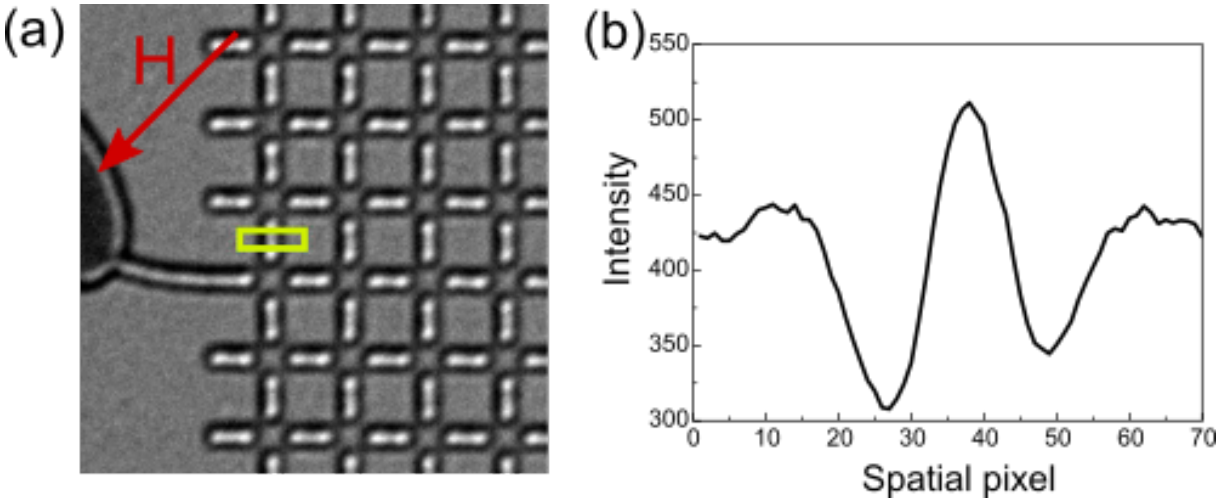

Figure 3.14: (a) Fresnel image of a square ASI array at 45° applied field H with the amplitude of 845 Oe with respect to the nanomagnets. The volume of each nanomagnet is $190 \times 60 \times 6$ nm^3 and the centre-to-centre distance between nearest islands is 335 nm. (b) Average profile (marked by a yellow box) integrating 20 scanning lines illustrates the intensity difference at the two sides of the nanomagnet as a result of single domain behaviour.

domain nature of each island gives rise to a dark and a less dark edges along the long axis. Figure 3.14 (b) shows the intensity difference between these two edges. In addition, the magnetisation direction can be identified using Eq. 3.15 and the position of the darker edge. Compared with other Lorentz imaging techniques (for instance the DPC), Fresnel imaging is beneficial at field- or temperature-driven magnetisation dynamics as it has faster acquisition time. This dissertation mainly concentrates on field-induced studies.

Apart from the magnetic phase ϕ_m, there is also another phase shift due to the electrostatic effects, ϕ_e. Thus intensity of the image, I, is associated to the contributions of magnetic and electron phases. How to extract simplified magnetic information by Fresnel imaging is detailed in section 3.7.2.4.

3.7.2.3 Differential phase contrast (DPC)

Differential phase contrast (DPC) imaging is able to quantitatively analyse the magnetic induction of thin samples and is performed in STEM mode. Unlike the parallel beam illuminating a specimen in CTEM, the electron beam in STEM is converged to a fine point on the surface of the specimen, as shown in Fig. 3.15. A set of scan coils are used to focus the beam, and then this converging beam acts as a probe which is rastered across the sample. The beam is deflected through an angle of β due to the magnetic induction, and is projected onto an 8-segment detector by the descan coils. Figure 3.15

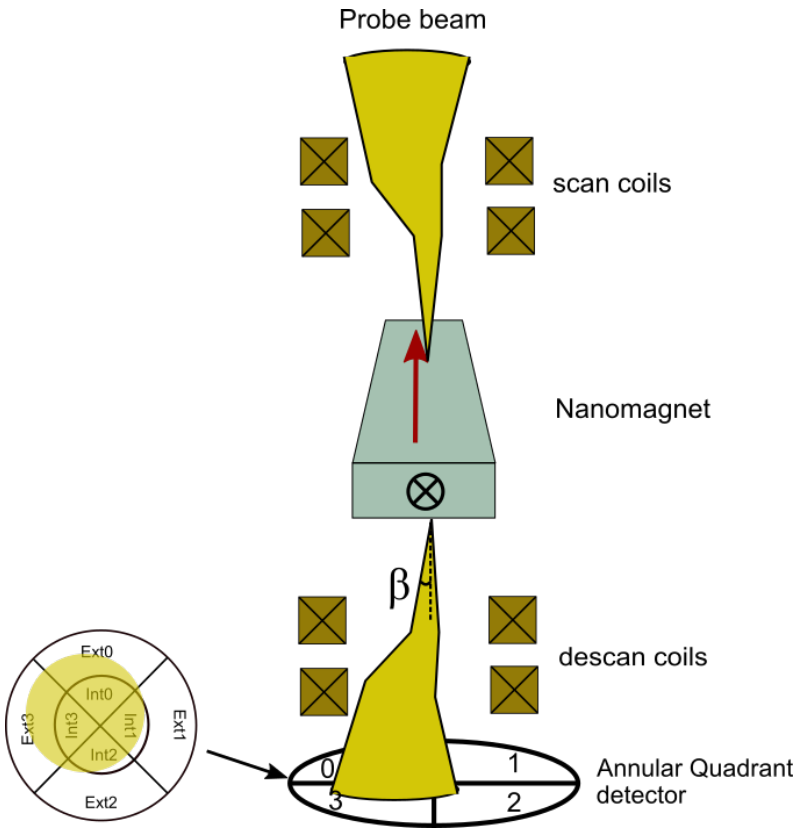

Figure 3.15: Ray diagram of the DPC in an STEM mode. The electron beam is converged through scan coils to focus on and raster scan the surface of a specimen. Scanning beam is deflected by an angle of β by the Lorentz force arising from in-plane magnetic induction of specimen. This deflection on a segment quadrant leads to a shift from the centre of detector. Difference of signals between two opposite quadrants, e.g. EXT1-EXT3 or EXT0-EXT2, reveals the magnetic induction associated to beam deflection. The inset is the top-view schematic of the segment detector consisting of the internal (INT) and the external (EXT) parts, showing how the probe beam is shifted on the detector.

shows that this projected disc shifts position due to the local magnetic induction that it experiences from the nanomagnet. The 8-segment detector consists of 4 internal and 4 external parts, as shown in the inset of Fig. 3.15. DPC image is achieved by subtracting the signals of diagonally opposite quadrants, i.e. EXT1-EXT3 or EXT0-EXT2, where 'EXT' represents the external segment. The advantage of calculating the signal difference in the external region is to improve the sensitivity of the shift detection [65]. On the other hand, by summing the intensities over the 4 quadrants which contain an internal and external parts, a bright field image can be acquired.

DPC has a better spatial resolution (approximately 1 nm) compared with Fresnel imaging. However, the resolution of DPC imaging is limited by the radius of the probe (as DPC is fundamentally a scanning mode) and the aberration correction. The dimension of specimen and strength of magnetic induction is relative to quality of the DPC image.

The larger sample and stronger magnetic induction enable to achieve the better contrast for the DPC image. Figure 3.16 shows DPC images of a small ASI array. Figures 3.16 (a) and (b) respectively present the two distinct integrated magnetic induction; one for each of the vertical and horizontal directions. The information on magnetic state is not obvious from these two images as there is also a contribution from electrostatic phase. An approach to extract the magnetic information provided by the Fresnel and DPC images is proposed in the next section.

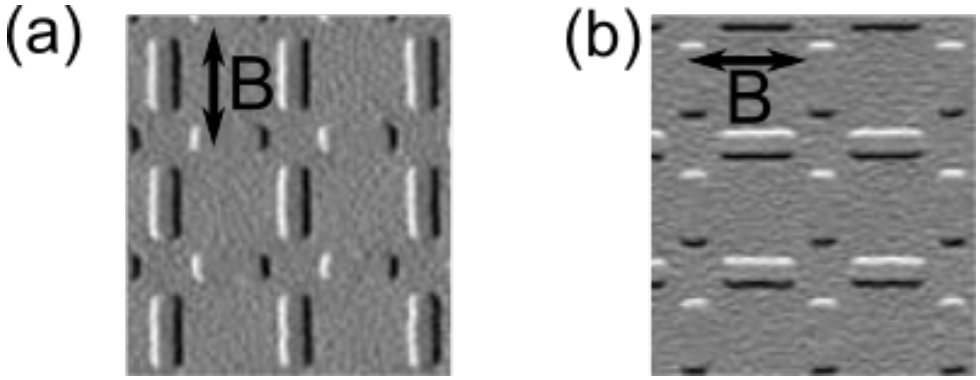

Figure 3.16: Examples of the DPC images show magnetic domains of a small part of ASI array where each nanomagnet possesses $190 \times 60 \times 6$ nm^3 dimension. The direction of integral magnetic induction B are indicated by a black double arrow. Differential phase distribution from two different subtractions of signal: (a) EXT1-EXT3 and (b) EXT0-EXT2.

3.7.2.4 *In-situ* TEM and extracting magnetic information

An in-plane magnetic field can be introduced by tilting the specimen rod around its central axis. Figure 3.17 depicts the process of such a *In-situ* operation. This is useful for visualising reversal processes and magnetisation dynamics. The in-plane field is a component of an external field generated from the OLs. The direction and the strength of in-plane magnetic field are controlled by the titled angle α. This in-plane component of the fixed field, $H_{\parallel}$, in terms of objective-lens field and tilted angle is computed via

$$H_{\parallel} = H \times sin(\alpha), \tag{3.23}$$

where H is the magnetic field from the OL and α is the angle of specimen with respect to the horizontal direction. The maximum angle α is imposed by the design of the TEM rod. In this work, the range of possible angle is $\pm 25°$. Even at full tilt, the sample still experience a significant out-of-plane magnetic field. This should act to magnetise the

sample out of plane. However, it has a weak influence on ASI nanomagnets as they have strong in-plane magnetisation restrained by the two-dimensional nanomagnet due to the shape anisotropy.

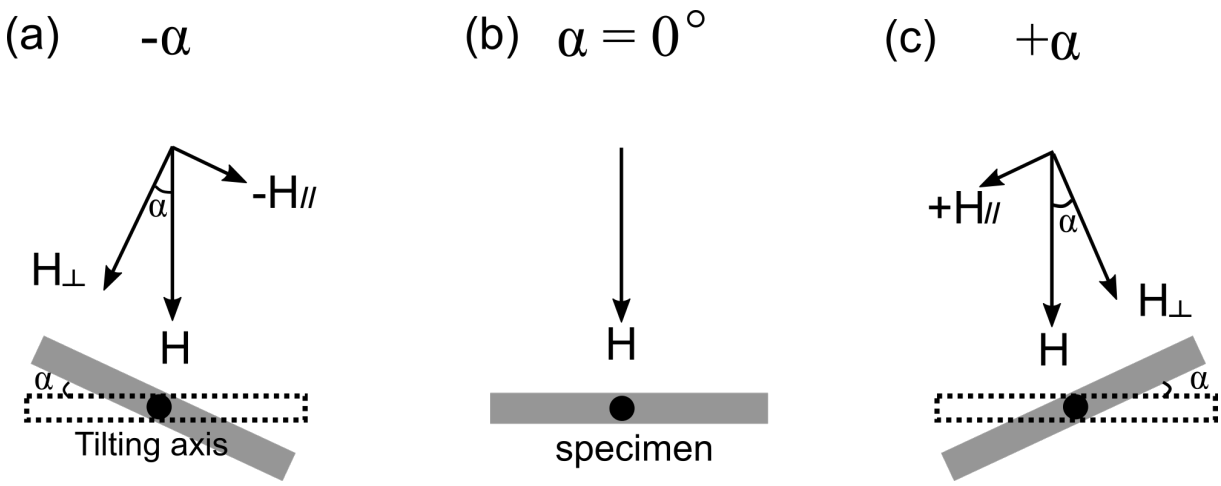

Figure 3.17: Tilting sample around the tilting axis to *In-situ* introduce the in- and out-plane magnetic field from the objective lens to the plane of specimen. Schematics describe three cases to apply a in-plane field: (a) negative field at negative tilting angle $-\alpha$, (b) zero field at $\alpha = 0°$ and (c) positive field at $+\alpha$.

In-situ TEM measurement in our work has two possibilities. The first is to capture magnetisation dynamics as a function of field whilst tilting the specimen holder. A combination of video recording and a MatLab-controlled tilting GUI that automatically tilts the TEM rod was developed at the University of Glasgow [2]. The advantage of this operation is that the acquisition of the magnetic state of the sample at each field step is stable in the tilting process. The relevant image processing and experimental results about field-driven magnetisation dynamics of pinwheel ASI are discussed in Section 6.3.

The other method is to tilt the rod by a certain angle α to magnetise sample and subsequently tilt it back to 0° to acquire image. The schematic diagram of this operation is displayed in Fig. 3.18. This procedure allows for the extraction of pure magnetic information. The intensity of the Fresnel image contains information not only on the Laplacian of the magnetic phase difference ($\nabla^2\phi_m$) and also on the electrostatic phase shift ($\nabla^2\phi_e$) that is associated with the specimen thickness and mass. Therefore, the total intensity I of a TEM image arises from two contributions, $I = I_e(\nabla^2\phi_e) + I_m(\nabla^2\phi_m)$. The electrostatic phase also varies with the tilted angle as the scattering process of the beam alters correspondingly. It is however identical at the same tilting position. Moreover, when the magnetic field decreases to zero the remanence of each nanomagnet only slightly

changes due to its ferromagnetic property. By acquiring an image always at $\alpha = 0°$, one can therefore ensure that the variation in image contrast only arises from the magnetisation change whilst the I_e remain unchanged. Assume m reverses, the total intensities of images A and B in Fig. 3.18 are given by

$$I_A = I_e - I_m \tag{3.24}$$

$$I_B = I_e + I_m, \tag{3.25}$$

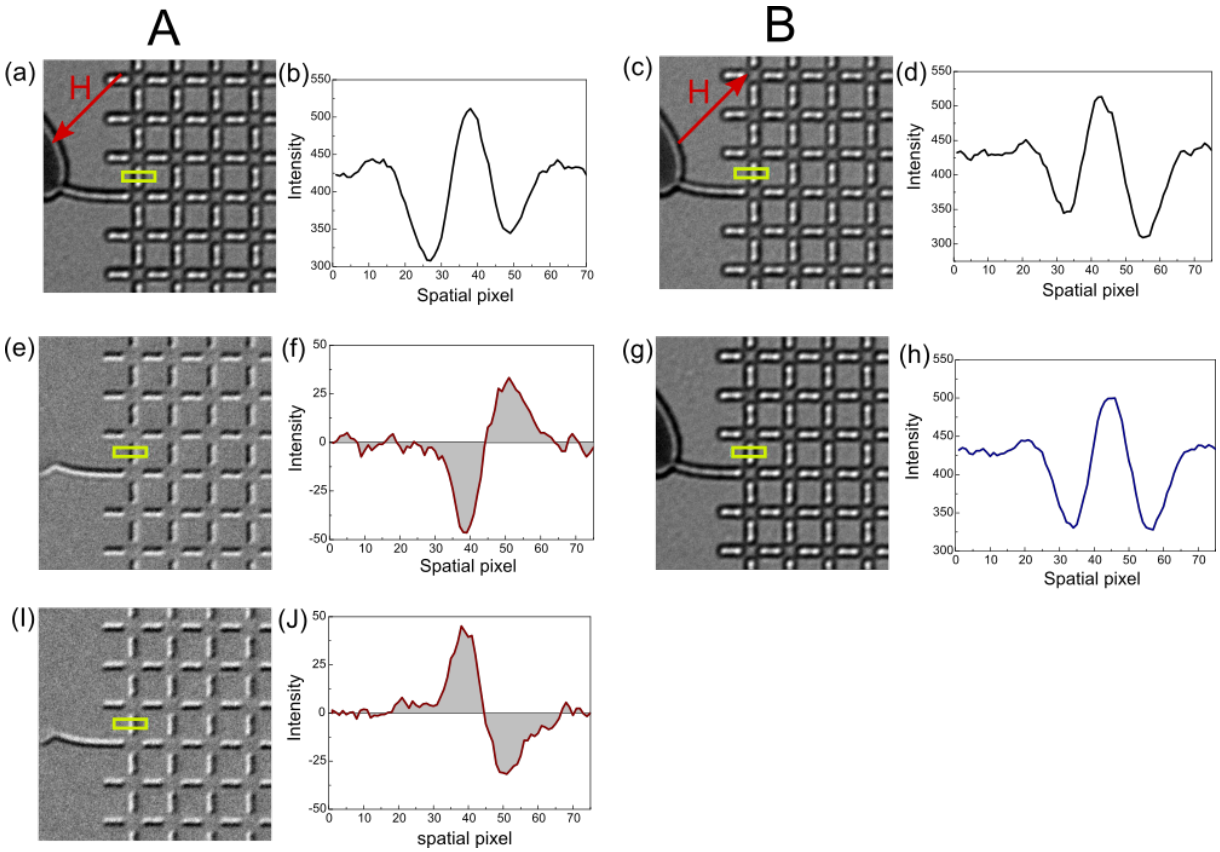

Figure 3.18: Illustration of separating magnetic and electrostatic contrasts using two Fresnel images of an ASI array that possess opposite magnetisation states and are fully saturated. Examples of two Fresnel images where nanomagnets are completely magnetised by the magnetic fields of (a) -845 Oe and (c) 845 Oe prior to acquisition at $\alpha = 0$, their corresponding intensity profiles integrating 20 lines are in (b) and (d). Processing results show images of two magnetic states created by magnetic field of (e, f)-845 Oe and (i, j) 845 Oe. The consequence of extracting (g) electrostatic-related contrast and (h) its averaging intensity profile. The dimension of each nanomagnet is $190 \times 60 \times 6$ nm^3 and the centre-to-centre separation between second nearest nanomagnets is 335 nm.

where the magnetic states of ASI specimen is opposite and respectively magnetised by saturation fields of -845 Oe (A) and +845 Oe (B), as illustrated in Figs. 3.18 (a) and (c).

Electrostatic intensity and magnetic intensity are obtained using $-I_m = (I_A - I_B)/2$ and $I_e = (I_A + I_B)/2$. The images associated with just the magnetic and electrostatic phases are shown in Figs. 3.18 (e), (g) and (I). The integral scanning profiles in Figs. 3.18 (f) and (h) reveal the behaviour of the magnetic and electrostatic phases along the short axis of one island (labelled by the yellow box). The same amplitudes of intensities at two sides of islands imply the contrast change in Figs. 3.18 (a) and (c) just results from the variation in magnetic state of nanomagnet. Figures 3.18 (f) and (J) is in the absence of uniform grey region between two darker and brighter edges, as schematically illustrated in Fig. 3.12, which should indicates the domain region. This is ascribed to a narrow width of the nanomagnet and undefocus image mode. As a result, Fresnel imaging is technique limited by specimen size.

Using the same imaging process, the magnetic contrast from DPC can be extracted as well. However, the magnetic intensity I_m of the DPC image is associated with the differential phase difference ($\nabla\phi_m$) rather than the Laplatian phase shift ($\nabla^2\phi_m$) of the Fresnel image. Figures. 3.19 (a) and (b) show the raw DPC images of square ASI lattices from net difference of Ext1-Ext3 orthogonal parts, which is respectively experienced two opposite-direction fields with strength of 845 Oe, are displayed in. The images only containing magnetic information are shown in Figs. 3.19 (d) and (e). Figures 3.19 (d) and (e) not only enable magnetisation distribution to be visualised in comparison with the raw images, but also the end states of island and the stray field surround island could be even imaged. It is obvious that DPC imaging with a high resolution provides greater magnetic details about individual nanomagnet. On the other hand, the long acquisition time imposes restriction on the use of DPC imaging for dynamical measurement. Compared with Fresnel images, DPC requires a greater accuracy of position alignment at $\alpha = 0^\circ$ where the image is taken after the specimen is magnetised by the magnetic field. The result of magnetisation extraction using two edge-misaligned DPC image are instanced in Figs. 3.19 (c) and (f).

3.8 Micromagnetic simulations

Micromagnetic simulation is a ubiquitous tool in nanomagnetism to predict static and dynamic magnetisation and provides interpretation to relevant experiments [66–70]. To date,

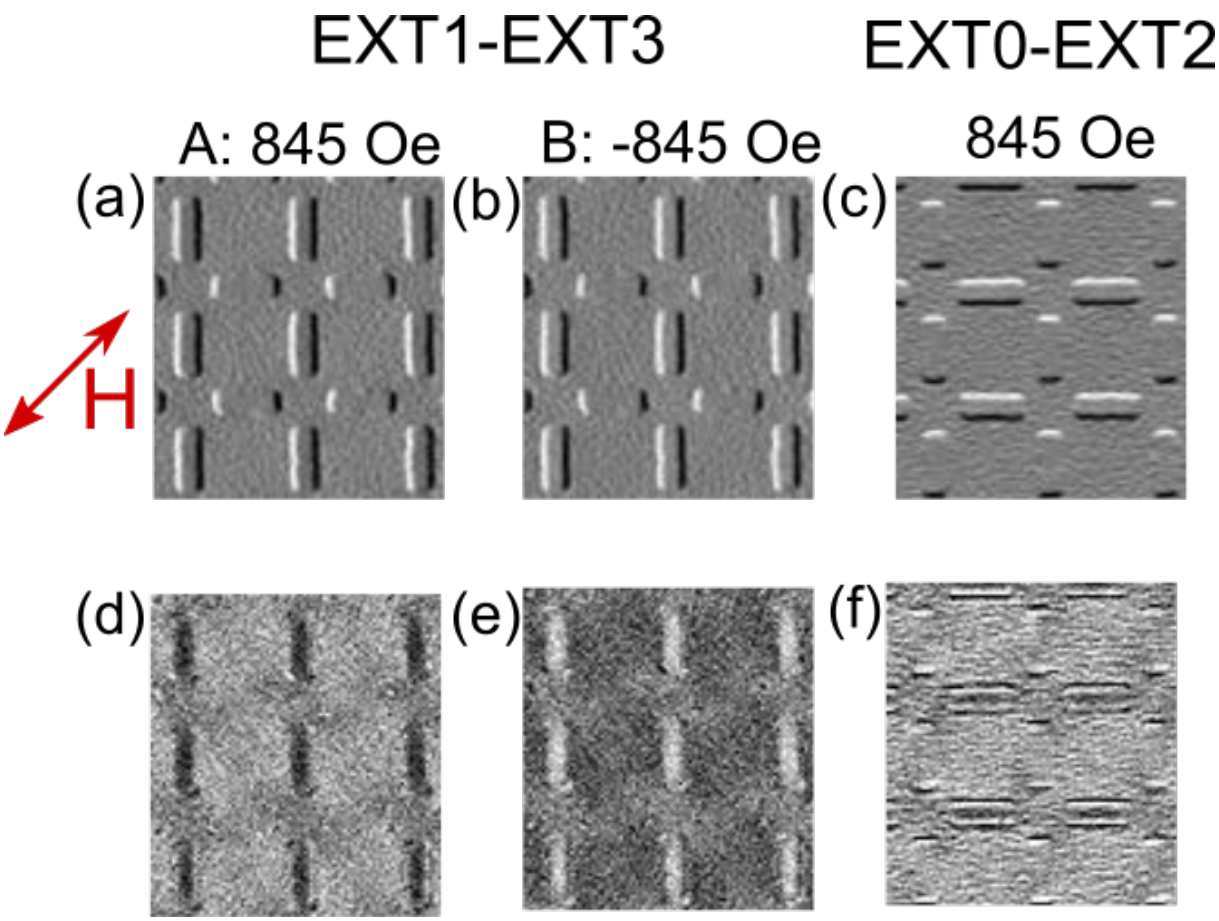

Figure 3.19: DPC images of part of a square ASI array with net difference between quadrants 1 and 3 magnetised by (a) 845 Oe and (b) -845 Oe magnetic fields prior to acquisition. Each magnetic island normally has a $190 \times 60 \times 6nm^3$ volume, and the lattice constant in an array is 350 nm. Subtracting the electrostatic contrast provides information on magnetic induction of each nanomagnet and stray field surround it at applied fields of (d) 845 Oe and (e) -845 Oe. The magnetic field is at the 45° with respect to a square lattice. However, the weak magnetic induction due to its small volume of ASI nanomagnet can lead to a (f) unobvious contrast for (c) the other subarray as a extremely good alignment is needed between two DPC images for image processing.

a variety of open-source and commercial packages have been created, such as OOMMF [71] and NMag [72] and GpMagnet [73] etc. The open-source program Mumax [74] was used to implement all numerical computations throughout this dissertation. Chapter 4 and Chapter 5 include the equilibrium configurations, hysteresis loops and magnetisation dynamics of a square ASI found through numerical simulations. In addition, the ground state energy of pinwheel ASI system is examined in Chapter 6.

Mumax is a GPU accelerated code. This is in contrast to the widely-applicable OOMMF that is a CPU-based micromagnetic solver instead. The GPU-based Mumax is capable of the speedup of computation compared to the OOMMF [73,75], which suits the huge numerical evaluation of magnetization dynamics in this study. Mumax computes

the time- and space-dynamics of magnetisation distribution using a finite-difference discretization approach. This involves dividing the simulation universe into a collection of cuboidal cells, whose dimensions are on the order of a few nanometers. An alternative method is to use finite-element discretization, where a grid is formed by a large number of discretization elements with different arbitrary-shaped volumetric mesh cells. The finite difference method is simple to compute the magnetization as the sizes of cells are constant. On the contrary, the primary disadvantage of this approach is that it does not accurately handle the curved structure. This can lead to "staircasing" - in effect in introducing spurious local anisotropy at the curved sections, as shown in the inset of Fig. 3.20. The problem can be solved by using smaller cell sizes or finite element discretization.

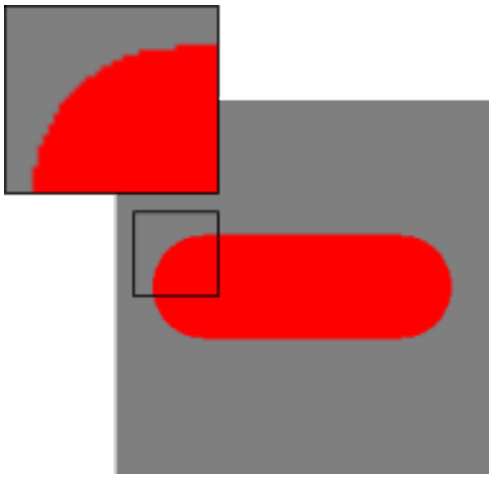

Figure 3.20: Example showing the "staircase" effect (the inset) of round edge of the simulation nanomagnet in a grid box.

In the simulation, the time-evolution magnetisation $m(x,y,z,t)$ is described by the LLG equation, given by Eq. 2.9. This equation describes the precessional motion of a magnetisation vector m around H_{eff} and a dissipative relaxation. This forces the magnetisation to spiral in toward the direction of H_{eff}, approaching equilibrium state. The effective field that the magnetisation, m, experiences the functional derivative of the energy density with respect to the magnetisation m [73]

$$H_{eff} = -\frac{1}{\gamma M_s}\frac{\delta \epsilon}{\delta m}. \tag{3.26}$$

where H_{eff} is a result of the contribution from the external field (B_{ext}), the magnetostatic field (B_{demag}), the exchange field (B_{exch}), the magneto-crystalline anisotropy field (B_{anis}), the Dzyaloshinskii-Moriya exchange field (B_{dm}) and thermal field (B_{therm}).

The equilibrium (or ground state) where the total energy E_{tot} approaches a minimum, $E_{tot}(m) = \int_V \epsilon(m) d^3r$ and V is the volume of a grid cell.

In a simulation, one of characteristic lengths, exchange length l_{ex}, is necessary to consider. l_{ex} follows

$$l_{ex} = \sqrt{\frac{2A_{ex}}{\mu_0 M_s^2}}, \tag{3.27}$$

where A_{ex} is the exchange constant and μ_0 is magnetic permeability in free space [76]. This exchange length is to determine the magnetostatic interaction is dominant in comparison with the anisotropy. The size of each cell usually is set to be smaller than the l_{ex}, especially in soft material. For instance, assign the typical material parameters of the Permalloy ($M_s = 800$ kA/m and $A_{ex} = 10^{-11}$ J/m) into the Eq. 3.27, the exchange length of the permalloy is $l_{ex} = 5nm$. A grid with the 2.4 nm $\times$ 2.4 nm in-plane cell size was used in the simulation of Chapters 4 and 5 which is less than the theoretical exchange length of 5 nm.

Mumax allows for an incorporation of periodic boundary condition (PBC). This enables the magnetisation to wrap around at the edges of grid box in the periodic condition. The PBC can remove the discontinuity of exchange energy at the boundary surface as exchange energy is related to the gradient of magnetisation (see Eq. 3.28), and the discontinuity of demagnetisation field as well. In addition, this approach is advantageous as it allows for the simulation of a small section of an array rather than the whole sample. This results in less time consuming and computationally demanding. An example will be given in Fig. 3.23.

3.8.1 Potential Energy terms and static magnetisation

Considering the case of ASI, the contribution of the total energy E_{tot} principally arises from the Zeeman energy ϵ_{ext}, the magnetostatic energy ϵ_{demag} and the exchange ϵ_{exch}. The total energy is quantitatively computed by $E_{tot} = \int_v (\epsilon_{ext} + \epsilon_{demag} + \epsilon_{exch}) d^3r$. Substituting the expression of each energy term, as already introduced in Section 2.3, the equation of total energy is written as

$$E_{tot} = \int_V [-m_i B_{ext} - \frac{1}{2} m_i B_{demag} + A_{ex} (\nabla m_i)^2] d^3r, \tag{3.28}$$

where m_i is the uniform magnetisation in the i^{th} cell such that the corresponing magnetostatic field in cell i is $B_{demag} = -M_s N_i$, N_i being the demagnetisation tensor. The material parameters, including the saturation magnetisation M_s, exchange constant A_{ex}, the damping coefficient α and the gyromagnetic ratio γ (α and γ are associated with the set of evaluation of dynamic response in Section 3.8.2), determines the behaviour of material of the simulation model. For example, in this thesis, the M_s and A_{ex} of the permalloy ASI nanomagnet are set as the standard values 8×10^5 Am^{-1} and 10^{-11} Jm^{-1}, respectively. Additionally, the initial magnetization state in a micromagnetic simulation is essential. In this thesis, the random initial magnetisation state was employed when evaluating the hysteresis loop and the magnetisation dynamic response, yet the specific initial state of the magnetic moment of each nanomagnet must to be set so as to compute the static energy. Final output of the energy is an average value. All micromagnetic simulations throughout this dissertation were performed at absolute zero temperature for the computational efficiency. An example to evaluate of system energy is provided in Fig. 3.21. The simulations are used to estimate the approximately magnetostatic coupling interaction of the system so that the exchange energy E_{ex} is set to be zero (without relaxing in the simulation). The E_{tot} of states E_+ and E_- are identical, approximately 1.44×10^{-17} J.

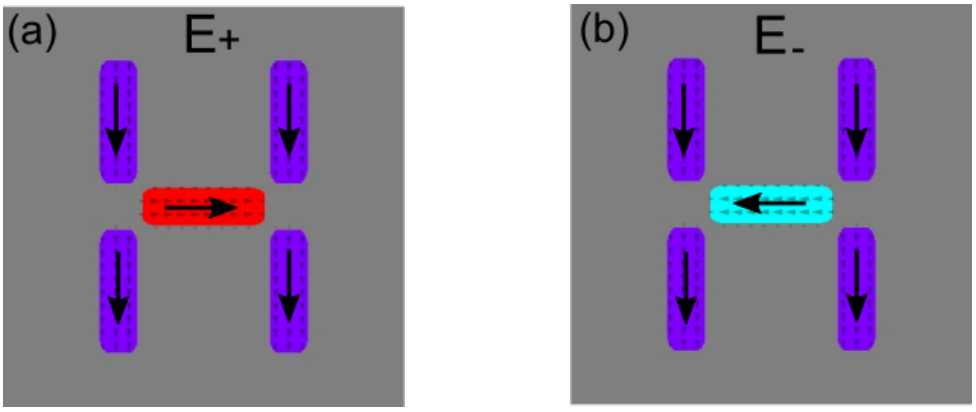

Figure 3.21: The static magnetisation configurations of a 5-element array showing two different orientations of magnetisation for the central element: state E_+ and its reversed state E_-. The colour represents the magnetisation direction labelled by black arrows. The grey region is free space. The dimension of each nanomagnet is $470 \times 170 \times 10$ nm^3 and the centre-to-centre separation between second nearest islands is 360 nm.

The equilibrium state satisfies $m \times H_{eff} = 0$ [73], which is the condition of zero torque. This should give the magnetisation state when a local energy is minimal. A normalised static magnetisation and a spatially discrete magnetisation can both be obtained in Mu-

max. The evolution of the mean magnetisation against the external field allows us to plot a hysteresis loop, as shown in Figs. 4.3 and 5.1. A spatial-dependent magnetisation is utilised to plot spatial profile in the sample by using FFT (see Fig. 4.7).

3.8.2 Micromagnetic dynamic response

Micromagnetic simulations also provide an approach to reproduce the dynamical behaviour of magnetic materials. In order to obtain the oscillating strength of magnetisation, an AC field pulse is performed. In Fig.3.22 (a), a schematic of simulation to obtain time-varying magnetisation is presented, where an individual nanomagnet is magnetised by an static external field H_{ext} and is driven simultaneously by an low-amplitude oscillating field H_z. The aim of this simulation is to reproduce the spin-wave modes measured using BLS, as presented in Chapters 4 and 5. Two categories of excitation pulses were applied: time-varying uniform and nonuniform pulse.

In the first case, the field pulse created by a sinc function (sampling function) follows

$$h_z(t) = h_0 \frac{\sin\left(\triangle\omega(t-t_0)\right)}{\left(\triangle\omega(t-t_0)\right)} = sinc(\triangle(t-t_0)), \tag{3.29}$$

where h_0 is the amplitude of the field pulse, $\triangle\omega$ is the bandwidth of the field pulse and t_0 is the offset time. Figure 3.22 (b) displays this time-varying sinc pulse. The strength and orientation of the field pulse vary as the running time changes, and this field is uniform over the entire space of the simulation box. The bulk mode with wavevector $k = 0$ is effectively excited using such a pulse. The corresponding response of z component is plotted in Fig. 3.22 (c), showing a driven oscillation motion decaying as a function of time. The resonance of uniform modes can be obtained by performing the FFT of the time-domain m_z, as illustrated in Fig. 3.22 (d).

Although the uniform pulse is able to provide some information about dynamic magnetisation, a field pulse that varies with time and space is required to excite other spin-wave modes (k $\neq$ 0). This allows for study of the dispersion relation (frequency vs. k) [77]. This pulse can be given by

$$h_z = h_z(t) \times \frac{\sin\left(\triangle k(r-r_0)\right)}{\left(\triangle k(r-r_0)\right)} = h_z(t) \times sinc(\triangle k(r-r_0)), \tag{3.30}$$

where $\triangle k$ is the bandwidth of possible spatial frequencies that can be excited, $r(x, y, z)$

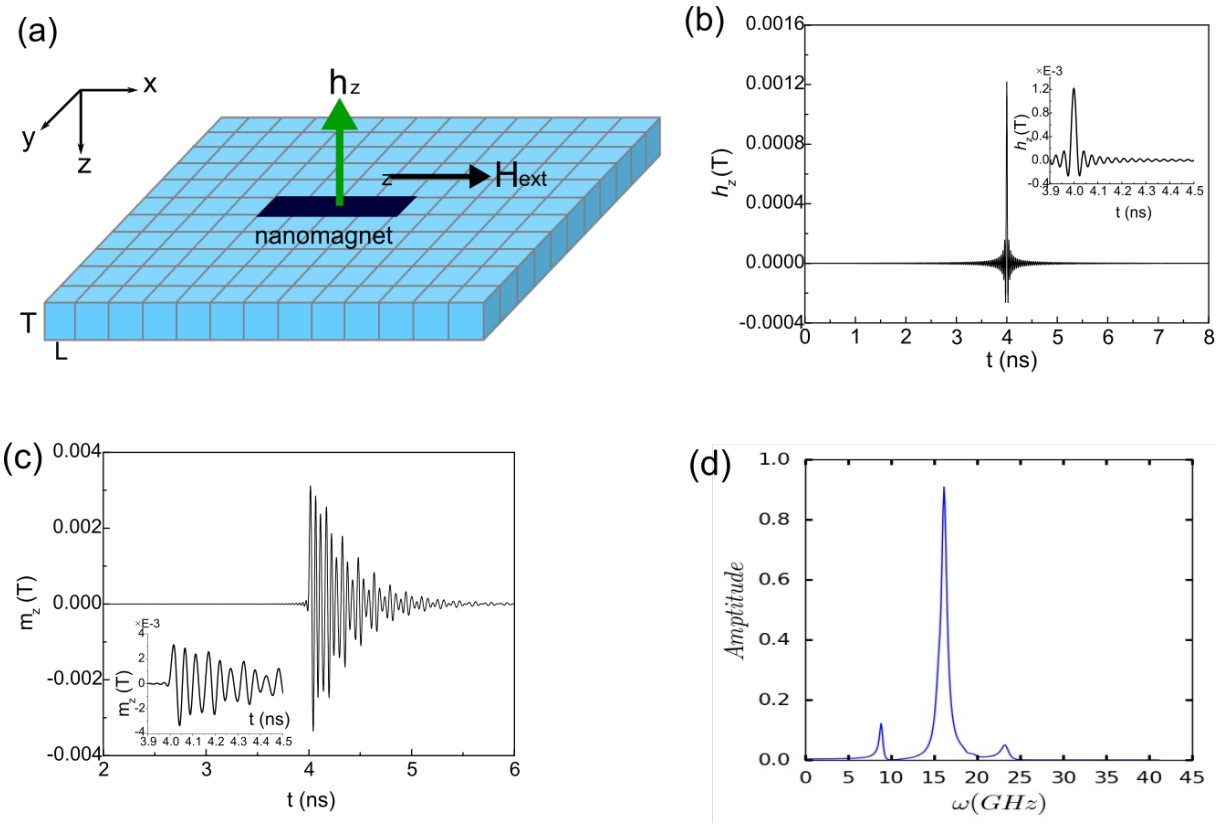

Figure 3.22: (a) Schematic configuration of a simulation model where a single nanomagnet ($240 \times 80 \times 10$ nm^3) is centred in the simulation box. This island is magnetised by an applied field H_{ext} of 0.2 T in the direction of y and a time-vary excitation field h_z that is perpendicular to H_{ext} along the z direction. The simulation is based on a 3D mesh grid in which T and L represents the length and thickness of each cell. (b) The amplitude of exciting field pulse h_z as a function of running time t. (c) The response of m_z to h_z versus time. The insets of (b) and (c) zoom in the details of the h_z and m_z during the time period from 3.9 s to 4.5 s. (d) The resonance peaks obtained by FFT of $m_z(t)$.

indicates the direction of wavevector and r_0 is the spatial offset with respect to the centre of a simulation box. Figure 3.23 (b) presents the spatial distribution of a nonuniform field, $h_z = h_z(t) \times sinc(\triangle k(y - y_0))$, in a simulation grid whose wavevector is along y direction. This excitation allows for excitation of Demon-Eshbach mode observed in BLS, where the wavevector of spin wave mode is normal to an applied field. The magnitude of the pulse is highest at the centre and it decays when the field is far away from the centre. This uniform field pulse is able to excite resonance modes when a single element is centred in the simulation grid (see Fig. 3.22). This is the case where the use of independent-island model is considered in Chapters 4 and 5. For the case of an array (see Fig. 3.23 (a)), this pulse is, nevertheless, infeasible to excite all their possible modes. Specifically, Fig. 3.23 (c) shows that only islands located near to the central position of the grid, where the strongest amplitude of the pulse occurs, can be significantly excited. The result of

the resonance spectrum (not shown here) is identical as Fig. 3.22 (d). This suggests that all simulated resonance modes arise from the horizontal island, while the modes from the vertical island are not excited due to the weak amplitude.

In order to avoid islands in an array to experience the inhomogenous amplitude of the nonuniform field pulse, n number multiple nonuniform pulses could be applied simultaneously just at the locations of all islands. The multiples can be given by $h_z = \sum_0^i sinc(\triangle k(y - y_0^i))n_0))$ where i represents the number of islands and y_0^i represents the spatial shift of the island i with respect to the centre of simulation grid. However, the superposition of the i number of field pulses with the k along y (or x) axis does not work in the Mumax. The results show that only one valid pulse is able to be applied in the simulation. In this context, an approach with multiple circularly nonuniform pulses is further developed. This field pulse follows $h_z = h_z(t)sinc(\triangle k(x - x_0))sinc(\triangle k(y - y_0))$ and, thus their wavevectors are along circular symmetry. Figure 3.23 (d) displays the spatial distributions of those pulses, a local driven field being produced on each nanomagnet (its location being (x_0, y_0)). By using this approach, all islands can experience the equivalent driven field and the field pulse can be flexibly shifted. The resonance peaks of all islands (see Fig. 3.23 (e)) can be obtained via the FFT calculation of $m_z(t)$. Compared to the 3.22 (d), Fig. 3.23 (f) shows that the more spin-wave modes from all islands (including horizontal and vertical islands) can be obtained. Therefore, this method is useful for the case of an ASI array. More discussion of the results is presented in Fig. 5.12.

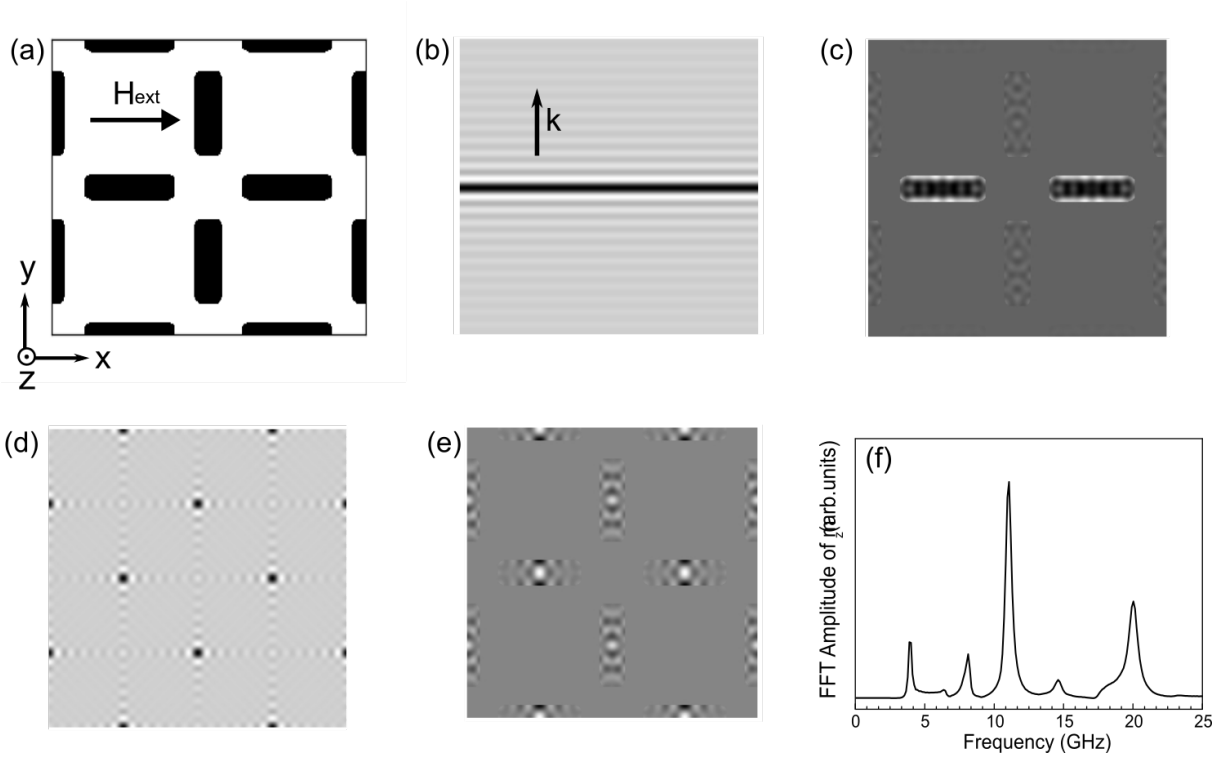

Figure 3.23: (a) A diagram displays the geometry of a part of ASI array, in which PBC is performed to create a two-times larger array. The dimension of each island is the same as that in Fig. 3.22. (b) Snapshot of the spatial distribution of a nonuniform pulse h_z with the wavevector along y axis and its corresponding (c) m_z response, only the spin wave mode localised at centre of simulation is strongly excited. The gray colour represents the nonmagnetic region in the simulations. (d) Snapshot of circularly spatial distribution with a number of local exciting pulses which enable to excite each island and the responses of m_z for each nanomagnet. (f) The resonance peaks obtained via excitation of the local field pulses and is a result of the superposition of peaks from horizontal and vertical islands, respectively (see Fig. 5.12).

Bibliography

[1] S A Morley. *The Dynamics of Artificial Spin Ice in Real and Reciprocal Space*. PhD thesis, University of Leeds, 2015.

[2] C Ferguson. *Imaging spin textures in advanced magnetic nanostructures using Lorentz microscopy*. PhD thesis, University of Glasgow, 2016.

[3] A A Tseng, K Chen, C D Chen, and K J Ma. Electron beam lithography in nanoscale fabrication: recent development. *IEEE Transactions on Electronics Packaging Manufacturing*, 26(2):141–149, 2003.

[4] D H Han, J G Zhu, J H Judy, and J M Sivertsen. Effect of stress on exchange coupling field, coercivity, and uniaxial anisotropy field of nife/nio bilayer thin films. *Applied Physics Letters*, 70(5):664, 1997.

[5] E I Cooper, Cn Bonhôte, J Heidmann, Y Hsu, P Kern, J W Lam, M Ramasubramanian, N Robertson, L T Romankiw, and H Xu. Recent developments in high-moment electroplated materials for recording heads. *IBM Journal of Research and Development*, 49(1):103, 2005.

[6] S Lamrani, A Guittoum, R Schäfer, M Hemmous, V Neu, S Pofahl, T Hadjers, and N Benbrahim. Morphology, structure and magnetic study of permalloy films electroplated on silicon nanowires. *Journal of Magnetism and Magnetic Materials*, 396:263, 2015.

[7] H Zijlstra. A vibrating reed magnetometer for microscopic particles. *Review of Scientific Instruments*, 41(8):1241–1243, 1970.

[8] P J Flanders. An alternating-gradient magnetometer (invited). *Journal of Applied Physics*, 63(8):3940–3945, 1988.

[9] EW Hill, P Nazran, and P Tailor. A versatile vibrating reed and magneto-optic magnetometer. *IEEE Transactions on Magnetics*, 32(5):4899–4901, 1996.

[10] P J Flanders. A vertical force alternating-gradient magnetometer (abstract). *Journal of Applied Physics*, 67(9):5475, 1990.

[11] J C Mallinson. Gradient Coils and Reciprocity. *IEEE Transactions on Magnetics*, 27(6):4398–4399, 1991.

[12] Gianluca Gubbiotti, Giovanni Carlotti, Fabrizio Nizzoli, Roberto Zivieri, Takuya Okuno, and Teruya Shinjo. Magnetic properties of submicron circular permalloy dots. *IEEE Transactions on Magnetics*, 38(5):2532–2534, 2002.

[13] F Montoncello, L Giovannini, F Nizzoli, P Vavassori, M Grimsditch, T Ono, G Gubbiotti, S Tacchi, and G Carlotti. Soft spin waves and magnetization reversal in elliptical Permalloy nanodots: Experiments and dynamical matrix results. *Physical Review B - Condensed Matter and Materials Physics*, 76(2):024426, 2007.

[14] G Gubbiotti, G Carlotti, T Okuno, M Grimsditch, L Giovannini, F Montoncello, and F Nizzoli. Spin dynamics in thin nanometric elliptical Permalloy dots: A Brillouin light scattering investigation as a function of dot eccentricity. *Physical Review B - Condensed Matter and Materials Physics*, 72(18):184419, 2005.

[15] G Gubbiotti, L Albini, G Carlotti, M De Crescenzi, E Di Fabrizio, A Gerardino, O Donzelli, F Nizzoli, H Koo, and R D Gomez. Finite size effects in patterned magnetic permalloy films. *Journal of Applied Physics*, 87(9):5633, 2000.

[16] S Tacchi, M Madami, G Gubbiotti, G Carlotti, H Tanigawa, T Ono, and M P Kostylev. Anisotropic dynamical coupling for propagating collective modes in a two-dimensional magnonic crystal consisting of interacting squared nanodots. *Physical Review B - Condensed Matter and Materials Physics*, 82(2):024401, 2010.

[17] M P Kostylev, G Gubbiotti, J G Hu, G Carlotti, T Ono, and R L Stamps. Dipole-exchange propagating spin-wave modes in metallic ferromagnetic stripes. *Physical Review B - Condensed Matter and Materials Physics*, 76(5):054422, 2007.

[18] A A Serga, A V Chumak, and B Hillebrands. YIG magnonics. *Journal of Physics D: Applied Physics*, 43(26):264002, 2010.

[19] A J Cox, A J DeWeerd, and J Linden. An experiment to measure mie and rayleigh total scattering cross sections. *American Journal of Physics*, 70(6):620–625, 2002.

[20] C V Raman. A Change of Wave-length in Light Scattering. *Nature*, 121:619–619, 1928.

[21] G Carlotti and G Gubbiotti. Brillouin scattering and magnetic excitations in layered structures. *La Rivista del Nuovo Cimento*, 22(12):1–60, 1999.

[22] J R Sandercock. *Light Scattering in Solids III*, chapter Trends in brillouin scattering: Studies of opaque materials, supported films, and central modes. Springer-verlag, Berlin, Heidelberg, 1982.

[23] F Nizzoli, J R Sandercock, G K Horton, and A A Maradudin. Dynamical properties of solids. *Amsterdam, North-Holland*, 6, 1990.

[24] Y Ding, T J Klemmer, and T M Crawford. A coplanar waveguide permeameter for studying high-frequency properties of soft magnetic materials. *Journal of Applied Physics*, 96(5):2969–2972, 2004.

[25] F T J Gonçalves. *Engineering of demagnetisation fields in exchange biased antidots studied using ferromagnetic resonance and Lorentz microscopy.* PhD thesis, University of Glasgow, 2015.

[26] Z Popović and E F Kuester. Principles of RF and microwave measurements, 2001.

[27] J C Meyer, A K Geim, M I Katsnelson, K S Novoselov, T J Booth, and S Roth. The structure of suspended graphene sheets. *Nature*, 446(7131):60–63, 2007.

[28] P Poizot, S Laruelle, S Grugeon, L Dupont, and J-M Tarascon. Nano-sized transition-metal oxides as negative-electrode materials for lithium-ion batteries. *Nature*, 407(6803):496–499, 2000.

[29] J S Kim, T LaGrange, B W Reed, M L Taheri, M R Armstrong, W E King, N D Browning, and GH Campbell. Imaging of transient structures using nanosecond in situ TEM. *Science*, 321(5895):1472–1475, 2008.

[30] H Vora and T J Moravec. Structural investigation of thin films of diamondlike carbon. *Journal of Applied Physics*, 52(10):6151–6157, 1981.

[31] V Radmilovic, H A Gasteiger, and P N Ross. Structure and chemical composition of a supported Pt-Ru electrocatalyst for methanol oxidation. *Journal of Catalysis*, 154(1):98–106, 1995.

[32] F Morales, F M F de Groot, O L J Gijzeman, A Mens, O Stephan, and B M Weckhuysen. Mn promotion effects in Co/TiO_2 Fischer–Tropsch catalysts as investigated by XPS and STEM-EELS. *Journal of Catalysis*, 230(2):301–308, 2005.

[33] K Kimoto, T Asaka, T Nagai, M Saito, Y Matsui, and K Ishizuka. Element-selective imaging of atomic columns in a crystal using STEM and EELS. *Nature*, 450(7168), 2007.

[34] M Bosman, V J Keast, J L Garcia-Munoz, A J D'alfonso, S D Findlay, and L J Allen. Two-dimensional mapping of chemical information at atomic resolution. *Physical Review Letters*, 99(8):086102, 2007.

[35] K Kimoto, T Sekiguchi, and T Aoyama. Chemical shift mapping of si L and K edges using spatially resolved EELS and energy–filtering TEM. *Microscopy*, 46(5):369–374, 1997.

[36] J N Chapman. The investigation of magnetic domain structures in thin foils by electron microscopy. *Journal of Physics D: Applied Physics*, 17(4):623, 1984.

[37] N Nagaosa and Y Tokura. Topological properties and dynamics of magnetic skyrmions. *Nature Nanotechnology*, 8(12):899–911, 2013.

[38] X-Z Yu, J P DeGrave, Y Hara, T Hara, S Jin, and Y Tokura. Observation of the magnetic skyrmion lattice in a MnSi nanowire by Lorentz TEM. *Nano letters*, 13(8):3755–3759, 2013.

[39] M Schneider, H Hoffmann, and J Zweck. Lorentz microscopy of circular ferromagnetic permalloy nanodisks. *Applied Physics Letters*, 77(18):2909–2911, 2000.

[40] W Coene, F Hakkens, R Coehoorn, D B De Mooij, C De Waard, J Fidler, and R Grössinger. Magnetocrystalline anisotropy of Fe_3B, Fe_2B and $Fe_{1.4}Co_{0.6}B$ as studied by Lorentz electron microscopy, singular point detection and magnetization measurements. *Journal of Magnetism and Magnetic Materials*, 96(1-3):189–196, 1991.

[41] S McVitie, G S White, J Scott, P Warin, and J N Chapman. Quantitative imaging of magnetic domain walls in thin films using Lorentz and magnetic force microscopies. *Journal of Applied Physics*, 90(10):5220–5227, 2001.

[42] S McVitie and J N Chapman. Reversal mechanisms in lithographically defined magnetic thin film elements imaged by scanning transmission electron microscopy. *Microscopy and Microanalysis*, 3(2):146–153, 1997.

[43] X-X Liu, J N Chapman, S McVitie, and C D W Wilkinson. Introduction and control of metastable states in elliptical and rectangular magnetic nanoelements. *Applied Physics Letters*, 84(22):4406–4408, 2004.

[44] I MacLaren, L-Q Wang, D McGrouther, A J Craven, S McVitie, R Schierholz, A Kovács, J Barthel, and R E Dunin-Borkowski. On the origin of differential phase contrast at a locally charged and globally charge-compensated domain boundary in a polar-ordered material. *Ultramicroscopy*, 154:57–63, 2015.

[45] M G L Gustafsson. Surpassing the lateral resolution limit by a factor of two using structured illumination microscopy. *Journal of microscopy*, 198(2):82–87, 2000.

[46] D B Williams and C B Carter. The transmission electron microscope. In *Transmission electron microscopy*, page 14. Springer, 1996.

[47] A V Crewe, D N Eggenberger, J Wall, and L M Welter. Electron gun using a field emission source. *Review of Scientific Instruments*, 39(4):576–583, 1968.

[48] M Haider, H Rose, S Uhlemann, E Schwan, B Kabius, and K Urban. A spherical-aberration-corrected 200kV transmission electron microscope. *Ultramicroscopy*, 75(1):53–60, 1998.

[49] M Haider, H Rose, S Uhlemann, B Kabius, and K Urban. Towards 0.1 nm resolution with the first spherically corrected transmission electron microscope. *Microscopy*, 47(5):395–405, 1998.

[50] O L Krivanek, N Dellby, and A R Lupini. Towards sub-Å electron beams. *Ultramicroscopy*, 78(1):1–11, 1999.

[51] J N Chapman, I R McFadyen, and S McVitie. Modified differential phase contrast Lorentz microscopy for improved imaging of magnetic structures. *IEEE Transactions on Magnetics*, 26(5):1506–1511, 1990.

[52] S McVitie and G S White. Imaging Amperian currents by Lorentz microscopy. *Journal of Physics D: Applied Physics*, 37(2):280, 2003.

[53] C Phatak, M Tanase, A K Petford-Long, and M De Graef. Determination of magnetic vortex polarity from a single Lorentz Fresnel image. *Ultramicroscopy*, 109(3):264–267, 2009.

[54] J Raabe, R Pulwey, R Sattler, T Schweinböck, J Zweck, and D Weiss. Magnetization pattern of ferromagnetic nanodisks. *Journal of Applied Physics*, 88(7):4437–4439, 2000.

[55] T Uhlig and J Zweck. Direct observation of switching processes in permalloy rings with Lorentz microscopy. *Physical Review Letters*, 93(4):047203, 2004.

[56] D M Donnet, J N Chapman, H W Van Kesteren, and W B Zeper. Investigation of domain structures in Co/Pt multilayers by modified differential phase contrast microscopy. *Journal of Magnetism and Magnetic Materials*, 115(2-3):342–352, 1992.

[57] N Shibata, S D Findlay, Y Kohno, H Sawada, Y Kondo, and Y Ikuhara. Differential phase-contrast microscopy at atomic resolution. *Nature Physics*, 8(8):611–615, 2012.

[58] T P Almeida, A R Muxworthy, A Kovács, W Williams, P D Brown, and R E Dunin-Borkowski. Direct visualization of the thermomagnetic behavior of pseudo–single-domain magnetite particles. *Science Advances*, 2(4):e1501801, 2016.

[59] T P Almeida, T Kasama, A R Muxworthy, W Williams, L Nagy, T W Hansen, P D Brown, and R E Dunin-Borkowski. Visualized effect of oxidation on magnetic recording fidelity in pseudo-single-domain magnetite particles. *Nature Communications*, 5:5154, 2014.

[60] S McVitie, D McGrouther, S McFadzean, D A MacLaren, K J O'Shea, and M J Benitez. Aberration corrected lorentz scanning transmission electron microscopy. *Ultramicroscopy*, 152:57–62, 2015.

[61] K J O'Shea. *Putting a leash on the domain wall: a TEM investigation into the controlled behaviour of domain walls in ferromagnetic nanostructures.* PhD thesis, University of Glasgow, 2010.

[62] Y Aharonov and D Bohm. Significance of electromagnetic potentials in the quantum theory. *Physical Review*, 115(3):485, 1959.

[63] S McVitie and M Cushley. Quantitative Fresnel Lorentz microscopy and the transport of intensity equation. *Ultramicroscopy*, 106(4-5):423–431, 2006.

[64] D T Ngo. *Lorentz TEM characterisation of magnetic and physical structure of nanostructure magnetic thin films*. PhD thesis, University of Glasgow, 2010.

[65] M Krajnak, D McGrouther, D Maneuski, V O'Shea, and S McVitie. Pixelated detectors and improved efficiency for magnetic imaging in STEM differential phase contrast. *Ultramicroscopy*, 165:42–50, 2016.

[66] R P Cowburn, D K Koltsov, A O Adeyeye, M E Welland, and D M Tricker. Single-domain circular nanomagnets. *Physical Review Letters*, 83(5):1042, 1999.

[67] C Abert, G Wautischer, F Bruckner, A Satz, and D Suess. Efficient energy minimization in finite-difference micromagnetics: Speeding up hysteresis computations. *Journal of Applied Physics*, 116(12):123908, 2014.

[68] M Asmat-Uceda, L Li, A Haldar, B Shaw, and K S Buchanan. Geometry and field dependence of the formation of magnetic antivortices in pound-key-like structures. *Journal of Applied Physics*, 117(17):173902, 2015.

[69] Y Telepinsky, V Mor, M Schultz, Y-M Hung, A D Kent, and L Klein. Towards a six-state magnetic memory element. *Applied Physics Letters*, 108(18):182401, 2016.

[70] F J T Goncalves, G W Paterson, R L Stamps, S O'Reilly, R Bowman, G Gubbiotti, and D S Schmool. Competing anisotropies in exchange-biased nanostructured thin films. *Physical Review B*, 94(5):054417, 2016.

[71] M J Donahue. OOMMF user's guide, version 1.0. Technical report, 1999.

[72] T Fischbacher, M Franchin, G Bordignon, and H Fangohr. A systematic approach to multiphysics extensions of finite-element-based micromagnetic simulations: Nmag. *IEEE Transactions on Magnetics*, 43(6):2896–2898, 2007.

[73] L Lopez-Diaz, D Aurelio, L Torres, E Martinez, M A Hernandez-Lopez, J Gomez, O Alejos, M Carpentieri, G Finocchio, and G Consolo. Micromagnetic simulations using graphics processing units. *Journal of Physics D: Applied Physics*, 45(32):323001, 2012.

[74] A Vansteenkiste, J Leliaert, M Dvornik, M Helsen, F Garcia-Sanchez, and B Van Waeyenberge. The design and verification of MuMax3. *AIP Advances*, 4(10):107133, 2014.

[75] A Vansteenkiste and B Van de Wiele. Mumax: a new high-performance micromagnetic simulation tool. *Journal of Magnetism and Magnetic Materials*, 323(21):2585–2591, 2011.

[76] J Ben Youssef, N Vukadinovic, D Billet, and M Labrune. Thickness-dependent magnetic excitations in Permalloy films with nonuniform magnetization. *Physical Review B*, 69(17):174402, 2004.

[77] D Kumar, O Dmytriiev, S Ponraj, and A Barman. Numerical calculation of spin wave dispersions in magnetic nanostructures. *Journal of Physics D: Applied Physics*, 45(1):015001, 2011.

4

Spin-wave excitations introduced by a magnetic field in a square artificial spin ice

4.1 Introduction

In this chapter, how information on magnetic configurations of square ASI can be obtained through light scattering from microwave excitations is discussed. Previous investigations of spin wave modes in rectangular islands elements have been performed for arrays in which the magnetisation of all islands are orientated in the same direction [1, 2]. Our general findings are that all features observed in BLS experiment can be described by the modes associated with individual elements in the square ASI. The elements lie along the two sides of a square array, as shown in the Fig. 4.1 (a), and the frequencies of modes depend upon whether the magnetisation of individual elements are aligned by the applied field along easy or hard directions of the elements. It is found that, depending on the direction of the applied field, the frequency evolution exhibits complex and peculiar

features. Mode softening and 'bell' shape in frequency vs magnetic field (H) have been observed in coincidence with the magnetisation reversal for H applied along the ASI edge. For H at 45° with respect the ASI edge, the frequency monotonically evolves as a function of the applied field. Micromagnetic simulation was employed to identify the excitations measured in the independent elements.

In this study, square ASI specimen was fabricated by Dr. Sophie Morley at the University of Leeds. Hysteresis loops were measured by Francesca Casoli using AGFM in the Institute of Materials for Electronics and Magnetism (IMEM) of Italy. The BLS measurement was performed by Gianluca Gubbiotti of CNISM Italy. I operated all micromagnetic simulations in this chapter, plotted the spin-wave dispersions and analysed all data.

4.2 Sample preparation

The square ASI specimen were prepared by collaborators at the University of Leeds. The square ASI lattices ($Ni_{80}Fe_{20}$) were patterned on an oxidised silicon substrate by electron beam lithography. A mask with the square lattice array shape was written and developed by the 100 kV electron beam on the positive resist. The NiFe was electron-beam evaporated and then the unpatterned NiFe film and mask were removed. The square ASI consists of the islands of intended 240 nm × 80 nm in size and 10 nm thickness, with a 450 nm lattice constant, as displayed in Fig. 4.1. Correspondingly, the corner-to-corner distance between the first nearest neighbouring islands is approximately 92 nm, as sketched in Fig. 4.1 (b). The measured in-plane dimension of one island in Fig. 4.1 is approximately 245.6 nm × 79.5 nm. The dimensions of most islands are consistent.

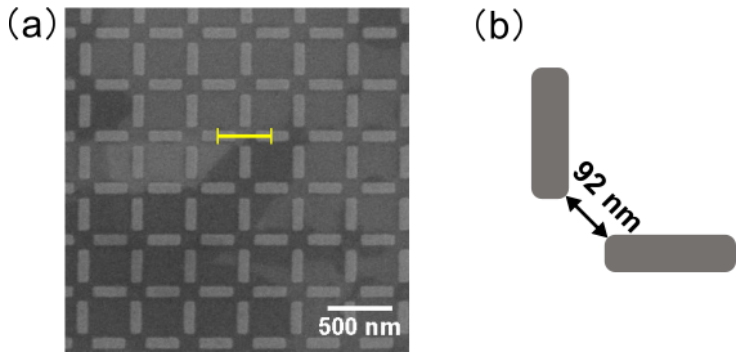

Figure 4.1: (a) A SEM of part of square ASI array formed by islands with the 240 nm × 80 nm lateral size and the 10 nm thickness. The lattice constant (sketched by the yellow line) is 450 nm. (b) Schematic indicating the 92 nm corner-to-corner distance between nearest nanomagnets.

4.3 Static magnetisation of the square ASI

4.3.1 AGFM hysteresis

Hysteresis loops of the square ASI were measured using AGFM. The magnetic field was applied along directions that make angles of 0° and 45° with the axes of the ASI square lattices, with values between +5 kOe to -5 kOe. The experimental hysteresis loops are shown by the black solid lines in Figs. 4.2 (a) and (b). In Fig. 4.2 (a), the magnetic field is aligned along a horizontal edge of the square array (0°), and in Fig. 4.2 (b) the field is aligned along a diagonal (45°) direction with respect to a square lattice.

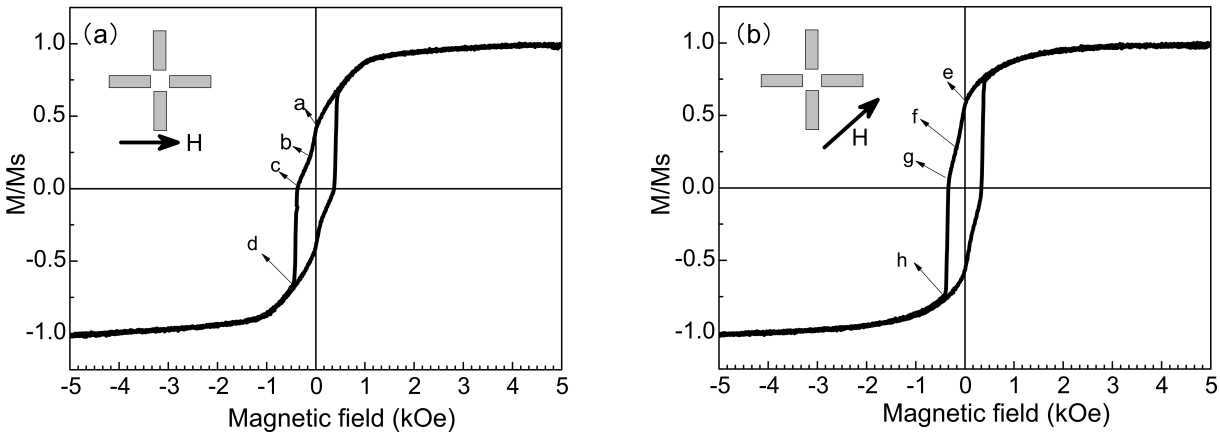

Figure 4.2: Hysteresis loops of the AGFM measurements at (a) 0° and (c) 45° applied field with respect to an ASI lattice. The insets indicate the field direction with respect to a square ASI lattice.

The hysteresis loop measured at the 0° applied field H shows that the reduction of magnetisation starts from approximately 4 kOe field. Two significant steps are observed to occur during the magnetisation process, which are marked by the ranges from 'a' to'b' and from 'c' to 'd', respectively. With the field aligned diagonally with the ASI lattice, there are still two steps on one branch, highlighted by the 'e' ,'f','g' and 'h' letters. The first step is from 'e' to 'f' and second one ranges from 'g' to 'h'. Furthermore, when the field is at 0° orientation, the islands require a somewhat larger external field to switch their magnetic moment compared with the 45° case. Fig. 4.2 shows the coercive field is ± 373 Oe at 0° field, while ± 332 Oe at the 45° field with respect to ASI lattice.

4.3.2 Simulated hysteresis

In order to understand the features arising from element interactions, the results of micromagnetic simulations of hysteresis for single elements are also shown in Figs.4.3 (a) and (b) for comparison. The simulations were done for isolated elements representing separately the horizontal and vertical islands constituting the array. The saturation magnetisation M_s and exchange constant A of Permalloy material were taken as 800 kA/m and 10^{-11} J/m [3], respectively. A grid with 10 nm thickness and 2.4 nm $\times$ 2.4 nm lateral size of cell was used, which is less than the exchange length $l = \sqrt{2A/\mu_0 M_s^2} = 5nm$ [4]. The details of such simulations have been discussed in Section 3.8.

In the simulations, magnetic field was set to be slightly misaligned from the horizontal by 1° and the diagonal by 2° (misaligned 1° cannot introduce the significant difference between two groups of islands) due to the imperfection in experiment and avoiding the possible artefacts associated with unstable states. These states could appear with the field aligned in highly symmetric configurations, for instance, a closure magnetisation structure when the magnetic field is perfectly perpendicular to the hard axis of the island. Hysteresis loops of elements were calculated for the field aligned parallel to: the horizontal axis H_1; the vertical axis H_{89} (see Fig. 4.3 (a)); and the diagonal axes H_{43} and H_{-47} (see Fig. 4.3 (b)). Note that the subscript of symbol 'H' presents the simulated field angle with respect the long axis of an individual nanomagnet. These configurations are sketched in the insets of Fig. 4.3 for clarity. Therefore, in the simulation the ASI elements with respect to the orientation of field are denoted as H_1, H_{89}, H_{43} and H_{-47}. The hysteresis loops, in which the normalised magnetic moments are mean values over moments of all simulating grid cells, are shown in Fig. 4.3 (c) and (d) by the green lines. This average value can indicate the resulting magnetisation from the two groups of cases (H_1 and H_{89} /H_{43} and H_{-47}) without the inter-island interaction.

First consider the hysteresis with the field applied along a horizontal edge direction shown in Figs.4.3 (a) and (c). Going from positive field to negative, it shows that general features of the measured hysteresis are visible in the averaged simulation results (shown by the green lines). There is a change in slope beginning at 1 kOe, followed by sharp drops at 0 kOe (marked 'a' in Fig. 4.2 (a)) and 0.7 kOe (marked 'c' in Fig. 4.2 (a)) fields. To examine possible interaction effects, the simulated hysteresis for a five-by-five array of elements is also shown with a blue dotted curve at 0° field, as shown in Fig.

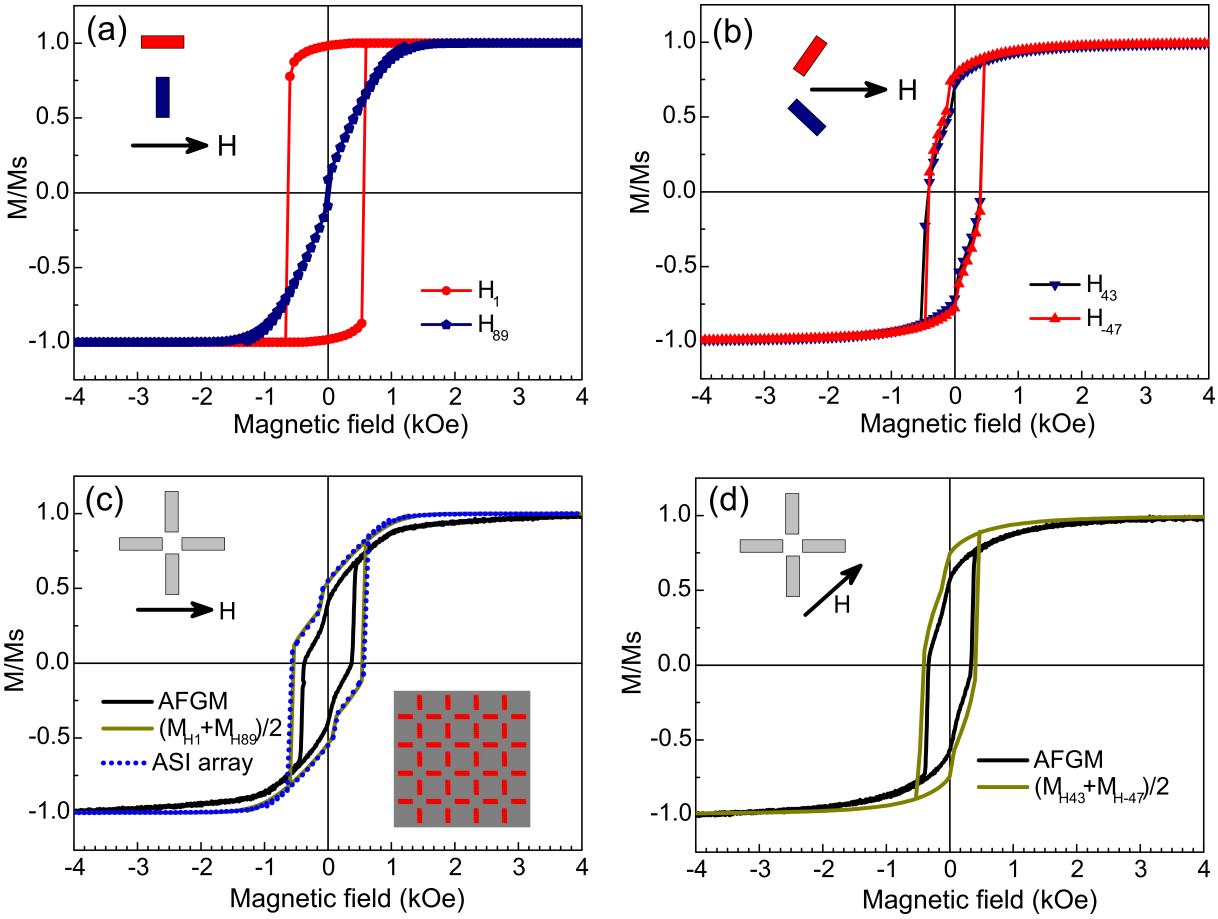

Figure 4.3: The simulated hysteresis loops of the independent magnetic elements at applied field of (a) 0° and (b) 45°. The comparison between the AFGM results and the average of simulated results at the (c) 0°and (d) 45° field with respect to the vertex of the square ASI. The left-top inserts show the direction of magnetic field with respect to a simulated individual island (in (a) and (b)) and a measured square ASI lattice (in (c) and (d)). The right-bottom insert of (c) represents the simulated ASI array.

4.3 (c). The simulated array follows the average curve exactly, suggesting that finite size effects that are associated with the reversal of elements at the edges in the array do not seem to play an important effect. It is also noted that the measured curve shows a decrease between 3 kOe and 1 kOe that is not visible in the simulations. This may be associated with imperfections of the elements. There is also disagreement between the coercive fields determined by measurement and simulation. In part, this may result from nucleation sites generated by irregularly shaped islands as opposed to the ideally identical shape of ASI island in the micromagnetic calculation [5]. Another possibility is that the temperature in simulation is absolute zero Kelvin, while measurements were performed at room temperature.

The analysis of the hysteresis for the field applied along a diagonal orientation is

shown in Figs. 4.3 (b) and (d). The agreement of the coercive field between measured and simulated curves is better in this case compared to that at 0° field. However, the magnetisation in the AGFM measurement is also smaller than that in the calculated loop at a given field probably due to the imperfect shapes of fabricated sample. The analysis of the hysteresis for the field applied along a diagonal orientation is shown in Figs. 4.3 (b) and (d). The agreement of the coercive field between measured and simulated curves is better in this case compared to that at 0° field. However, the magnetisation in the AGFM measurement is also smaller than that in the calculated loop at a given field probably due to the imperfect shapes of fabricated sample.

4.3.3 Static magnetisation configuration

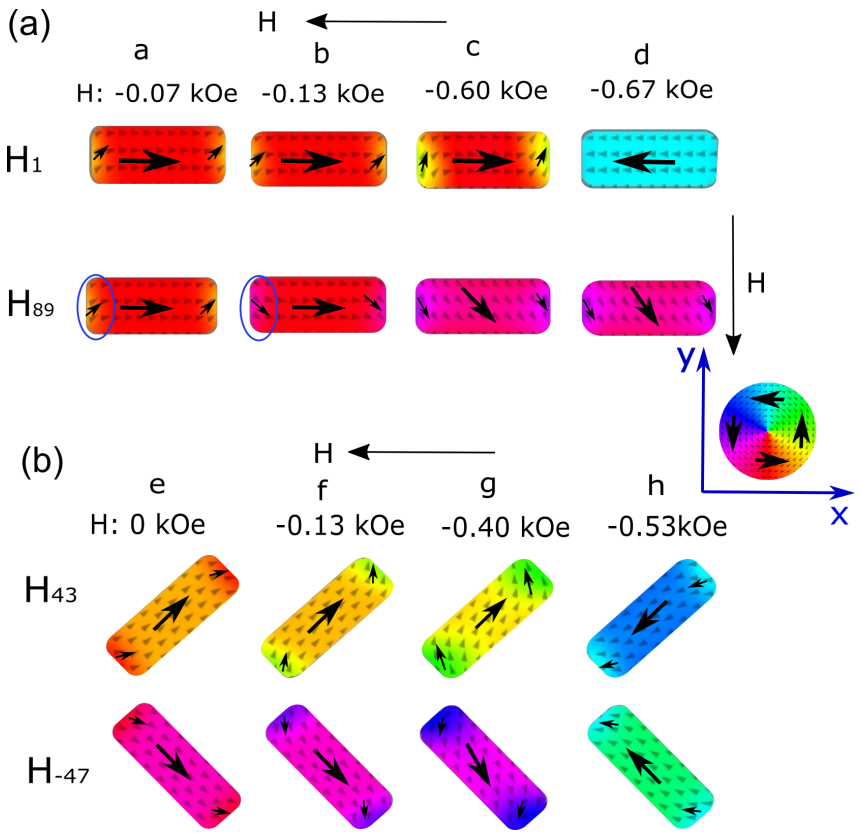

Figure 4.4: Ground-state magnetisation configurations of the isolated island at (a) 0° and (d) 45° applied field. The inset is colour code indicating the direction of magnetisation.

The static magnetisation configurations are also calculated in order to show the spatial magnetisation distribution of independent island at different magnitudes and angles of the magnetic field. The reversal of magnetisation within individual elements is predicted to occur differently for the horizontal (H_1) and vertical elements (H_{89}) in the ASI lattices

with respect to the field H. It was found that the end orientation and bulk moment switch respectively contribute to the two steps in the Fig. 4.2. Static magnetisation configurations are shown in Fig. 4.4 (a) where the magnetisation direction is mapped for H_1 and H_{89} elements using the inserted colour coding of Fig. 4.4. The magnetisation configurations are shown for positions on the hysteresis loops 'a', 'b', 'c' and 'd', which is indicated in Fig. 4.2 (a). In general, these two groups of the elements reverse through an 'S' magnetisation configuration with an unsaturated field. The drop at 'a' corresponds to rotation of the ends of hard axis elements H_{89} (shown by the blue circles), and the plummet at 'c' corresponds to the reversal of the magnetic moment in the easy axis island H_1.

For the 45° case, the two elements reverse in the same manner and there is good agreement at coercive fields. The ground state magnetisation states at the 'e', 'f', 'g' and 'h' positions of the loop are also presented, as displayed by Fig. 4.4 (b). Again, all islands reverse through 'S' magnetisation states.

For application of the field along a diagonal direction it appears possible to describe the magnetisation processes observed for the square ASI in terms of the reversal of individual non-interacting element. The situation is different for hysteresis with the field aligned along a horizontal edge. The general features observed in the hysteresis are qualitatively similar to what one would predict from an ensemble of non-interacting elements, but there are significant quantitative differences apparent in the unsaturated region. It is in this field region precisely that effects of inter-element interactions are most apparent as they modify locally the fields driving element reversals. Measurements of spin waves are presented in the next section, which are able to provide additional information about local effective fields.

4.4 Spin-wave excitations in square ASI

Spin wave excitations in the ASI array can be characterised by the BLS technique. BLS can detect spin wave modes at the low field range that are not visible using ferromagnetic resonance spectrum (FMR results will be detailed in Section 5.3). The BLS measurement was performed in order to investigate the spin-wave properties of such ASI array, two types of BLS measurement were performed to probe wavevector (presented in Section

4.4.1) and field dependence (in Section 4.4.2).

4.4.1 Spin wave dispersion

The spin wave dispersion is first measured, i.e. the evolution of frequency as a function of the wavevector ($q_{\parallel}$). In this case, the applied field was fixed at 3 kOe along directions at 0° and 45° with respect to the ASI lattices. The angle of incident light θ varied from 0° to 60° corresponding to in-plane wavenumber $q_{\parallel}$ from 0 to 2×10^7 m^{-1}, where $q_{\parallel} = 2k\sin(\theta)$ and k is the wavevector of light. Two scattering geometries were studied: the Damon-Eshbach (DE) mode for spin waves with wavevector k perpendicular to the external field H; and the Backward (BA) mode configuration for spin waves with wavevector parallel to the applied field.

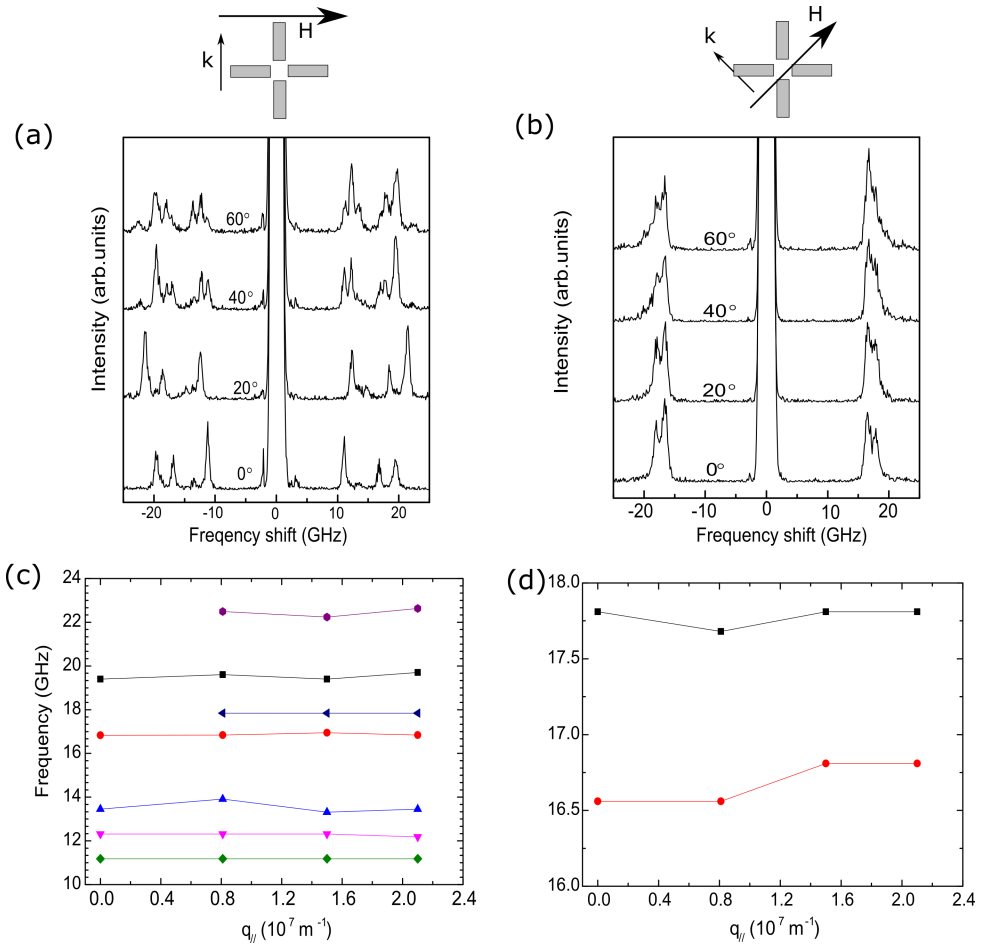

Figure 4.5: Sequence of BLS spectra measured at different incidence angles θ with the external field of 3 kOe at (a) 0° and (b) 45° upon the ASI lattices. The wavevector of the incident light is perpendicular to the field orientation in Damon-Eshbach configuration. Spin-wave frequency on the Stokes side as a function of the in-plane wavenumber at a 3 kOe (c) parallel field and (d) diagonal field. Dots are experimental data and lines are guides for the eyes [6]. [Published under CC BY 3.0 licence.]

The dispersion of spin waves was measured to indicate the possible inter-island dynamic coupling and propagation of collective spin waves through the array. Panels (a) and (b) of Fig. 4.5 are shown for the two different magnetic field orientations. Spectra are recorded in the DE configuration for a 3 kOe magnetic field aligned at 0° and 45° angle with respect to the horizontal-group elements of the ASI lattices. When the field is applied at 45°, there are two well-defined peaks in the spectra, while for 0° up to seven peaks are visible in two different frequency ranges with the larger in-plane wavevector. Frequencies measured for wavenumbers between 0 and 2×10^{-7} m^{-1} are shown in Fig. 4.5 (c) and (d) with the field applied along an array edge and diagonal orientation. In Fig. 4.5 (c), the dispersion curve is almost flat, displaying no significant variation in frequency as a function of wavenumber. This means the inter-island coupling is negligible in ASI system with this spacing. Another possibility as to why the square ASI would not produce bands with the DE geometry is because that edge modes would be excited for elements parallel to the applied field.

Figs. 4.6 (a) and (b) show the BLS spectra of the BA scattering geometry as a function of the incident angle of light θ for the different field orientations. In this case, only two modes are clearly visible with the diagonal magnetic field and four spin wave modes appear while applying a horizontal field with respect to one family of ASI islands. Compared with the DE modes, the modes are closer together in frequency for the 45° orientation and spread apart by several GHz for the 0° case. In terms of the dispersion, Fig. 4.6 (c) and (d) shows that all modes at both parallel field and diagonal field have no significant dispersion. This is because that the dispersion curve of magnons is approximated as the parabola based on the relation of $\hbar\omega = Dq_{\parallel}^2$, where D is the spin wave stiffness constant [7, 8]. Thus, the BLS results excludes the magnonic dynamic inter-island coupling effects in this square ASI system.

In recent work, E. Iacocca *et al.* [9] have calculated theoretically the magnonic band structure of square ASI array, and have shown that the frequency variations of band structure are of the order of 10^{-1} GHz for the ASI model which has the similar lattice constant (395 nm) with this measured sample. This reveals that the inter-element coupling dominated by dipolar interaction in ASI array is very weak, but it still reveals the dispersion behaviour. However, this is below the resolution ability of BLS technique, namely 0.2 - 0.4 GHz. Therefore, it can be asserted that the dynamic inter-element coupling is not

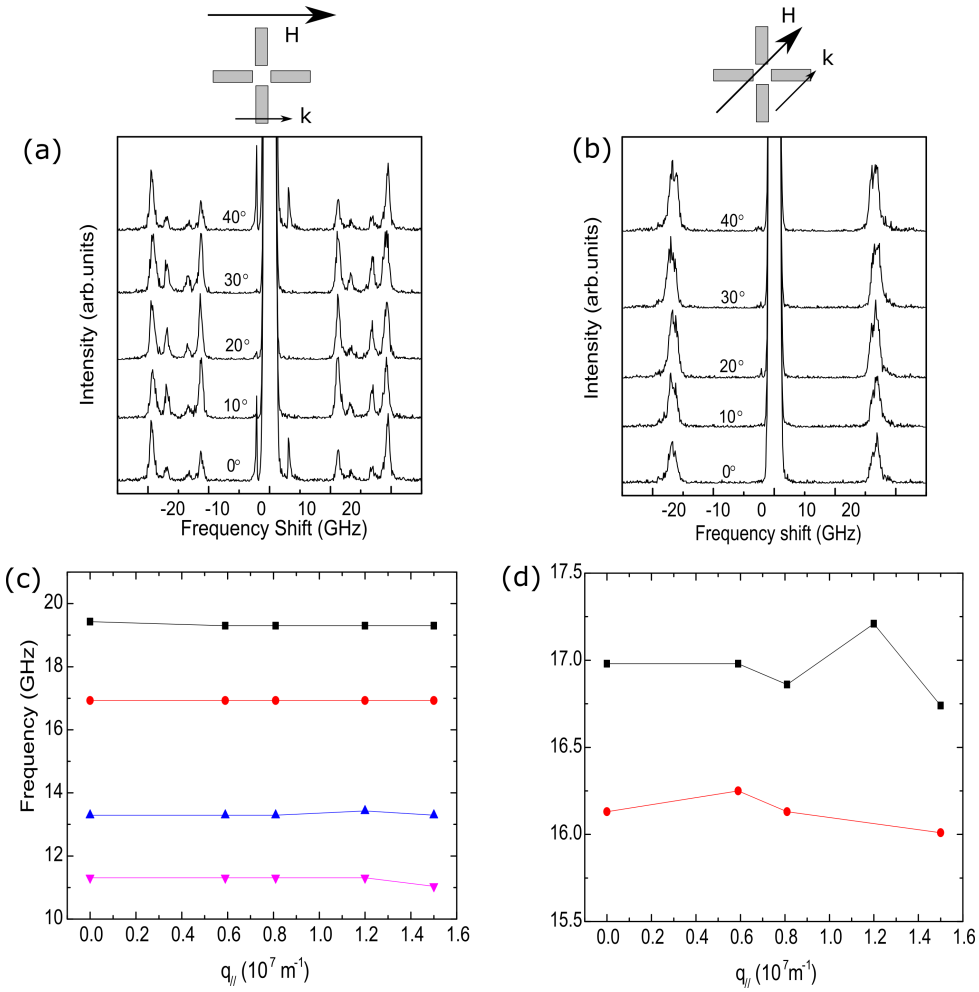

Figure 4.6: Sequence of BLS spectra measured at different incidence angles θ with the external field of 3 kOe applied at (a) 0° and (b) 45° with respect to the ASI lattices. The wavevector of the incident light parallels to the applied field in backward configuration. Spin-wave frequency on the Stokes side as a function of the in-plane wavenumber at a 3 kOe (c) horizontal field and (d) diagonal field with respect to the ASI lattice. Dot is experimental result and line is a guide for the eyes [6]. [Published under CC BY 3.0 licence.].

measurable by BLS.

4.4.2 Measured spin-wave eigenmodes

Now the angle of incidence of the illuminating laser is fixed at $\theta = 20°$. The external field H was varied from - 4 kOe to + 4 kOe and applied along the 0° and 45° orientations with respect to ASI lattices.

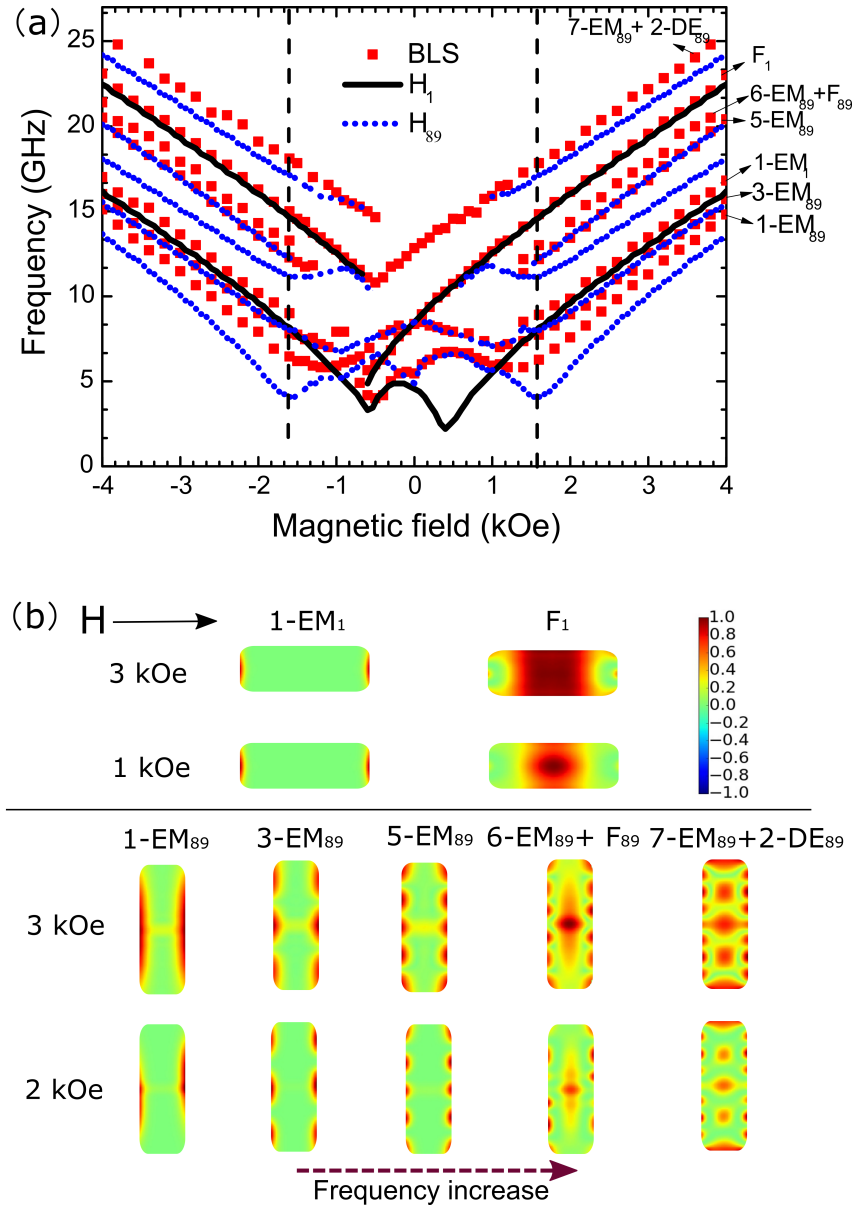

Figure 4.7: (a) Frequencies of the spin-wave eigenmodes as a function of applied field parallel aligned with one group of ASI islands. Dashed lines are the cut-off points between saturated and unsaturated regions of the hard-axis magnetization. (b) Spatial profiles of the eigenmodes at different field strengths for the H_1 (upper panel) and H_{89} (lower panel) orientations, with frequency increasing from left to right. The label of the spin-wave mode in (a) mainly indicate the experimental mode marked by the arrow [6]. [Published under CC BY 3.0 licence.]

The field-induced frequencies are obtained in the DE scattering configuration and presented in Fig. 4.7 (a) and Fig. 4.8 (a). In Fig. 4.7 (a), the measured frequencies are

shown by square symbols, and the magnetic field is oriented along the 0° direction. Several distinct modes are identified from the spectra, and each exhibits different behaviour for fields in the region of hysteresis between +4 and −4 kOe. The frequencies were recorded from spectra obtained by decreasing the field from positive to negative saturation, thereby following the upper branch of the magnetisation loop shown in Fig. 4.2 (a). Outside this region the behaviour of the frequencies is roughly linear with field, as one expects for saturated elements.

At magnetic field of approximately ±1.5 kOe, several modes appear to merge with others or disappear entirely. The two lowest frequency modes have minima near the coercive fields. At zero field, mode crossings appear in two higher frequency modes. These modes in the horizontal islands appear to be softening at negative applied fields. Except for the mode crossings, the behaviour of the mode frequencies for the vertical islands with applied field are symmetrical so that minima again appear for the lowest frequency modes at around ±1.3 kOe field marked by two black dashed lines, and there is a linear increase of frequencies for fields outside the hysteresis region. However, the more complex behaviour of magnetic excitation were observed under the unsaturated field.

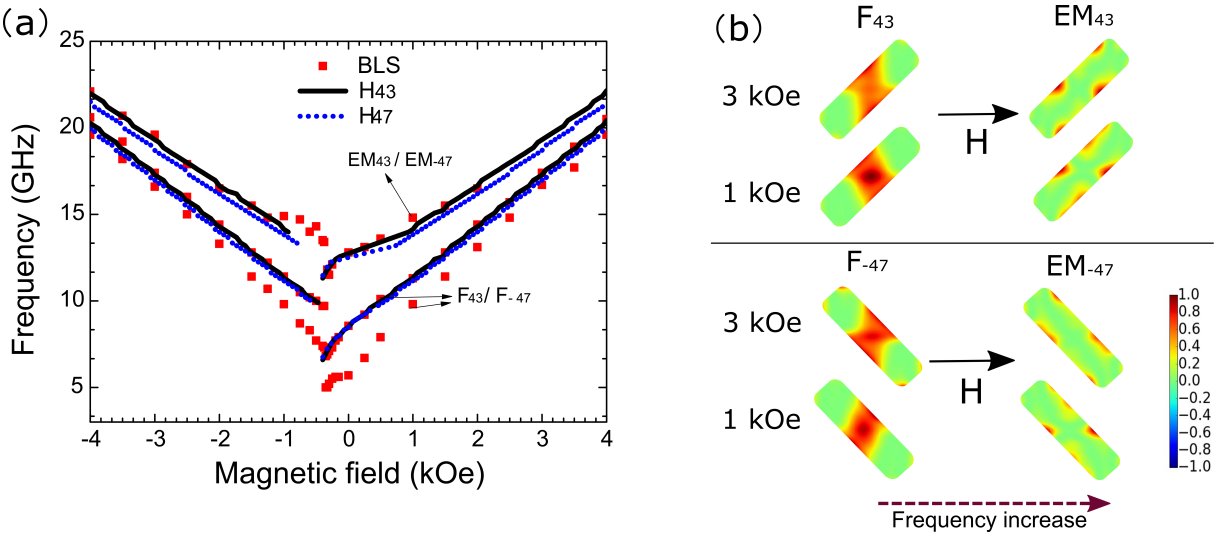

Figure 4.8: (a) Frequencies of the spin-wave modes vs applied field H with 45° angle with respect to the islands. (b) Spatial profiles of m_z component magnetisation dynamics at (upper panel) 43° and (lower panel) −47° field angles [6]. [Published under CC BY 3.0 licence.].

BLS spectra for the case when the external field is aligned diagonally along 45° with respect to both ASI lattices are shown in Fig. 4.8. Hysteresis appears in the modes as a gap at about -0.37 kOe, corresponding to reversal of the magnetisation. Unlike the foregoing case with the 0° field, in this symmetrical configuration, the modes appear the

same for all islands and the two observed spin wave mode. The frequency of spin-wave modes have almost linear relationship with the applied field.

4.4.3 Simulated spatial profiles

An analysis of the mode structure was performed using micromagnetic simulations. Using the same parameters as before, the dynamics was simulated using Mumax3 following the approach of Vansteenkiste *et al.* [10]. The field configuration is shown in Figs. 4.3 (b) and (d), and again only single elements are considered. The dimensionless damping parameter was set as 0.02 [11, 12], and gyromagnetic ratio $\gamma = 2.8$ GHz/kOe was used which was determined from a separate ferromagnetic resonance (FMR) measurement (which will be detailed in the next section of FMR measurement) and fitted by a Kittel function [13]. An external field is applied as before, and varied from +4 kOe to -4 kOe.

The frequencies were calculated in the following way. At each field step after relaxation to a steady state configuration a field pulse $H_e = I_0 \times \frac{\sin(t)}{t} \times \frac{\sin(\triangle ky)}{(\triangle ky)}$ is applied and orientated along the z axis. This gives rise to torques on each component m_x, m_y and m_z in each micromagnetic discretization cell, and their responses are recorded every picosecond. Frequencies and intensities of spin-wave modes are then calculated using a discrete Fourier transform (in the time and space) of the magnetisation component, m_z for each cell [14].

The frequencies calculated in this way are shown in Fig. 4.7 (a) by the solid lines for H_1 horizontal elements (for which the applied field is collinear) and the dotted blue lines for the H_{89} vertical elements (for which the applied field is perpendicular to the element axes). Taken together, these simulations describe well the measured frequencies. The small discrepancies may be due in part to the effects of edge roughness [15]. The saturation field can be quite large on the order of several hundred Oe.

To identify which of the confined modes are responsible for the spectra, the spatial profile of the magnetisation dynamics m_z was calculated, and examples are shown in Fig. 4.7 (b). For the analysis which follows, the same classification protocol is used as in [16]. The modes are classified into four categories: backward (m-BA), Damon-Eshbach (m-DE), edge (m-EM) and fundamental (F). In this classification, the integer m indicates the number of nodal lines. The BA mode is a mode with a nodal line perpendicular to the magnetisation. Nodal lines parallel to the magnetisation are called m-DE. The edge modes, m-EM, are localised at the ends of the islands and normally have a small intensity

in the BLS spectrum. The fundamental F is the Kittel uniform resonance ($m = 0$). This mode typically has the largest intensity.

The modes associated with the horizontal elements are labelled in Fig. 4.7 (a) as $1-EM_1$ and F_1, representing respectively the EM and fundamental modes. These mode profiles remain unchanged in intensity for magnetic fields between 3 kOe to 1 kOe. The F_1 appears to soften for fields more negative than -50 kOe, consistent with reversal of the magnetisation of the horizontal element. It is noted that the calculated $1-EM_1$ mode have two minima in the unsaturated region. This corresponds to curling of the edge magnetisation. Note also the difference in amplitude of the F mode for the 1 and 3 kOe fields.

Modes for the vertical elements are labelled $7-EM_{89}+2-DE_{89}$, $6-E_{89}M+F_{89}$, $5-EM_{89}$, $3-EM_{89}$ and $1-EM_{89}$ in Fig. 4.7(a). The corresponding spatial profiles shown in the bottom of Fig. 4.7(b). The $1-EM_{89}$ mode is type EM, and possesses the lowest frequency. In the $5-EM_{89}$ and $3-EM_{89}$ mode, the standing wave also emerges. Hybridisation is more apparent in the higher frequency modes, a mix of a F mode and a 6-EM mode and a mix with the 7-EM and 2-DE modes. As for the horizontal elements, there is significant dependence of the mode amplitudes on field as seen by comparing the profiles for 2 and 3 kOe. Furthermore, the frequency of the EM mode is smallest at 1.5 kOe as the magnetisation begins to saturate perpendicular to the element axis [17].

The spatial profiles of the independent island at a 45° field have two spin wave modes, which are F mode and EM mode, as displayed in Fig. 4.8 (b). There are subtle changes in the position of the amplitudes for the EM mode when the field is reversed from 3 to 1 kOe. Likewise, the shape of the F mode amplitude changes slightly as the field is reduced, and an edge mode contribution just visible at the corners disappears.

4.5 Discussion and conclusions

This chapter shows the static magnetic properties and spin-wave mode with two distinct orientations (0° and 45°) of field upon the square ASI lattice using the AGFM and BLS techniques. The micromagnetic simulations help us to understand the magnetisation reversal and dynamics of the isolated magnetic element. The square ASI geometry allows for comparisons of response of modes in elements with orthogonal alignment field direction.

The configuration in which the magnetic field is perpendicular to one set of elements (the 'vertical' elements in our geometry) reveals complex spectra due to the presence of many types of edge modes. The main features of the modes can be well described as arising from independent elements aligned parallel and perpendicular to the applied field. There is no significant evidence of interactions between elements associated with magnetisation dynamics. For magnetic elements in the saturated field, the shifts associated with the dynamic inter-element dipolar coupling could not be detected and would, in any case, be much smaller from possible contributions of edge defects or other imperfections of the magnetic elements in addition to the static shifts described above. Nevertheless, this ASI may act as a reconfigurable microwave resonator and that the exact spectrum observed depends on the microconfiguration of elements in the array.

Bibliography

[1] G Gubbiotti, M Conti, G Carlotti, P Candeloro, E D Fabrizio, K Y Guslienko, A Andre, C Bayer, and A N Slavin. Magnetic field dependence of quantized and localized spin wave modes in thin rectangular magnetic dots. *Journal of Physics: Condensed Matter*, 16(43):7709–7721, 2004.

[2] C Bayer, J Jorzick, B Hillebrands, S O Demokritov, R Kouba, R Bozinoski, A N. Slavin, K Y Guslienko, D V Berkov, N L Gorn, and M P Kostylev. Spin-wave excitations in finite rectangular elements of $Ni_{80}Fe_{20}$. *Physical Review B*, 72(6):064427, 2005.

[3] N Smith, D Markham, and D LaTourette. Magnetoresistive measurement of the exchange constant in varied-thickness permalloy films. *Journal of Applied Physics*, 65(11):4362, 1989.

[4] J Ben Youssef, N Vukadinovic, D Billet, and M Labrune. Thickness-dependent magnetic excitations in Permalloy films with nonuniform magnetization. *Physical Review B*, 69(17):174402, 2004.

[5] K Kohli, Andrew Balk, Li Jie, S Zhang, I Gilbert, P Lammert, V Crespi, P Schiffer, and N Samarth. Magneto-optical Kerr effect studies of square artificial spin ice. *Physical Review B*, 84:180412, 2011.

[6] Y Li, G Gubbiotti, F Casoli, F J T Gonçalves, S A Morley, M C Rosamond, E H Linfield, C H Marrows, S McVitie, and R L Stamps. Brillouin light scattering study of magnetic-element normal modes in a square artificial spin ice geometry. *Journal of Physics D: Applied Physics*, 50(1):015003, 2016.

[7] B Lenk, H Ulrichs, F Garbs, and M Münzenberg. The building blocks of magnonics. *Physics Reports*, 507(4-5):107–136, 2011.

[8] Y Zhang. *High wave vector spin waves in ultrathin Fe films on W(110) studied by spin-polarized electron energy loss spectroscopy.* PhD thesis, Martin Luther University of Halle-Wittenberg, 2008.

[9] E Iacocca, S Gliga, R L Stamps, and O Heinonen. Reconfigurable wave band structure of an artificial square ice. *Physical Review B*, 93:134420, 2015.

[10] A Vansteenkiste, J Leliaert, M Dvornik, M Helsen, F Garcia-Sanchez, and B Van Waeyenberge. The design and verification of MuMax3. *AIP Advances*, 4(10):107133, 2014.

[11] F J T Goncalves, G W Paterson, R L Stamps, S O'Reilly, R Bowman, G Gubbiotti, and D S Schmool. Competing anisotropies in exchange-biased nanostructured thin films. *Physical Review B*, 94(5):054417, 2016.

[12] J B Youssef, N Vukadinovic, D Billet, and M Labrune. Thickness-dependent magnetic excitations in permalloy films with nonuniform magnetization. *Physical Review B*, 69(17):174402, 2004.

[13] Charles Kittel. On the Theory of Ferromagnetic Resonance Absorption. *Physical Review*, 73(2):155–161, 1948.

[14] R D McMichael and M D Stiles. Magnetic normal modes of nanoelements. *Journal of Applied Physics*, 97(10):10J901, 2005.

[15] G Gubbiotti, S Tacchi, G Carlotti, P Vavassori, N Singh, S Goolaup, A O Adeyeye, A Stashkevich, and M Kostylev. Magnetostatic interaction in arrays of nanometric permalloy wires: A magneto-optic Kerr effect and a Brillouin light scattering study. *Physical Review B*, 72(22):224413, 2005.

[16] G Gubbiotti, Malagò P, S Fin, S Tacchi, L Giovannini, D Bisero, M Madami, G Carlotti, J Ding, A O Adeyeye, and R Zivieri. Magnetic normal modes of bicomponent permalloy/cobalt structures in the parallel and antiparallel ground state. *Physical Review B*, 90(2):024419, 2014.

[17] F Montoncello, L Giovannini, F Nizzoli, P Vavassori, M Grimsditch, T Ono, G Gubbiotti, S Tacchi, and G Carlotti. Soft spin waves and magnetization reversal in elliptical Permalloy nanodots: Experiments and dynamical matrix results. *Physical Review B*, 76(2):024426, 2008.

5

Role of nanomagnet thickness in magnetisation dynamics of artificial square ice

5.1 Introduction

The spin wave properties of rectangular magnetic islands have been investigated individually and in a variety of array geometries [1–4]. Many types of spin-wave eigenmodes have been identified in the GHz frequency range whose character is partially determined by the long-range dynamic dipolar interaction. Some works have appeared recently in which the ferromagnetic resonance and spin waves were measured in magnetic-element arrays with different ASI geometries, such as square, penrose and kagome [5–12]. The work of Y. Yahagi *et al.* [13] reveals two spin-wave eigenmodes responding to the two magnetisation orientations of two sub-lattices of an elliptic-disk array which align collinear or orthogonal

to the magnetic field. By way of contrast, the studies in chapter 4 show that a rich spectrum of standing spin-wave eigenmodes can be detected with BLS. These eigenmodes can be used to identify details of the magnetisation processes which occur during magnetic reversal and hysteresis that cannot be resolved using FMR or magnetometry.

In addition, the static and dynamic magnetisation of the 10 nm thick artificial square spin ice is discussed from Chapter 4. In this square array, the inter-island interaction is so weak as to be negligible in the measurements and simulations. Here another square ASI specimen is studied, which has the same intended in-plane dimension of 240 nm $\times$ 80 nm (the measured dimension being 252 nm $\times$ 86 nm) but with the thickness of 30 nm. The centre-to-centre separation between the second nearest islands is as before at 450 nm. Equivalently, the corner-to-corner distance, d, between the first nearest neighbouring islands is approximate 92 nm. In principle, the thicker magnetic array should produce the stronger stray field due to the large magnetic moment of each island.

In this chapter, a comparative investigation of the static and dynamic behaviour in the two patterned square array of 10 nm and 30 nm thicknesses is undertaken. The measurements of spin wave frequencies on square ASI structure in the GHz range were obtained using FMR and BLS. Spin waves in magnetic element geometries possess a stationary character [14] and dipolar stray fields associated with eigenmodes localised to the element edges extend outside elements [3], decaying with distance into the region between elements [15]. Emphasis has been given to the presence of soft magnetic eigenmodes which accompany the magnetisation reorientation and switching of islands [16, 17]. The case of the easy axis aligned parallel and orthogonal to the applied field direction is presented here. Substantial changes in the frequencies and number of detected spin wave modes are found as the thickness varies. The frequencies of those spin waves localised to element edges are observed to evolve non-monotonically with magnetic field and soften at certain critical fields. These critical fields enable us to extract information about the magnetisation reversal of individual islands within the array. Finally, the effect of separation between islands is discussed and possibilities for dynamic coupling through the overlap of collective edge modes as a function of island separation are examined.

In this chapter, two square ASI specimens were prepared by Dr. Sophie Morley at the University of Leeds. Hysteresis loops were measured by Francesca Casoli using AGFM in the Institute of Materials for Electronics and Magnetism (IMEM) of Italy. The BLS

measurement was performed by Gianluca Gubbiotti of CNISM Italy. Dr. Francisco J T Gonçalves and myself conducted the FMR meaurement. I operated all micromagnetic simulations and analysed all the data.

5.2 Thickness-dependent hysteresis

5.2.1 Experimental and simulated hysteresis loop

The measured results of AGFM for the 10 nm and 30 nm thick magnetic elements are shown in Fig. 5.1 by the black lines. As a bulk technique, AGFM probes the magnetic moment of the entire array. Therefore, the measured magnetisation is an average of the magnetisation components associated with different element orientations with respect to the applied field. There is a step visible at around zero field for the thiner magnetic elements, whereas it is not visible for the thicker magnetic islands. In addition, the experimental coercive field of the 10 nm thick array ($\approx 365\,\mathrm{Oe}\,(\pm 5)$) is smaller than that of the 30 nm thick one ($\approx 553\,\mathrm{Oe}\,(\pm 5)$), as listed in Table 5.1.

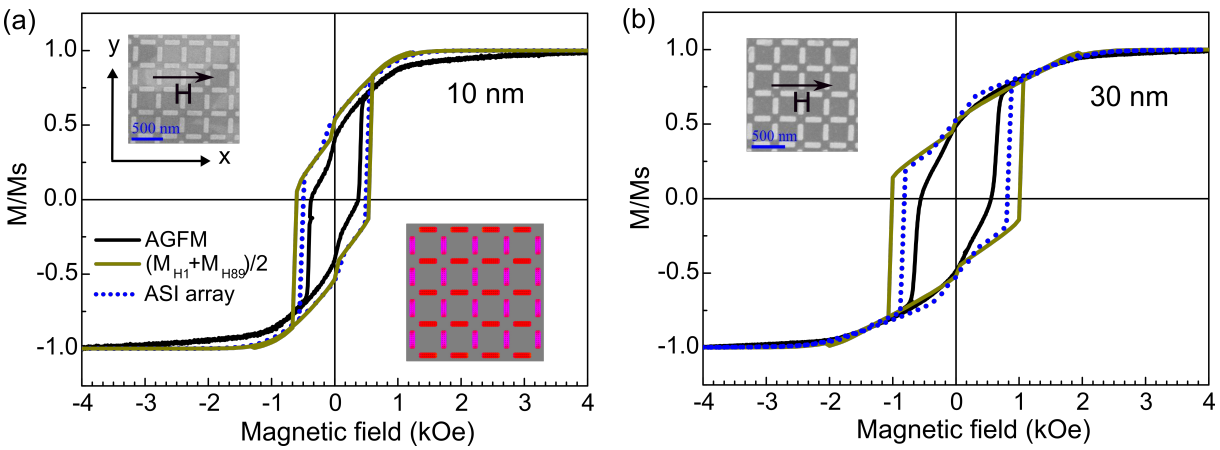

Figure 5.1: The measured AGFM (black line) and simulated (dark yellow and blue dotted lines) normalised hysteresis loops of the (a) 10 nm and (b) 30 nm thick ASI specimen. The dark yellow line represents the mean value of magnetic moment of independently horizontal (M_{H1}) and vertical (M_{H89}) island, and blue dotted line indicates the magnetisation of the 4×4 units ASI array in which each unit consists of four islands. Insets show the SEM images (top left) of the two studied ASI specimens and the schematic of simulated 4×4 unit array (bottom right).

To understand the thickness-dependent behaviour of static magnetisation of ASI, micromagnetic simulation were performed using MuMax. The magnetic parameters used and details in this simulation can be found in Section 3.8.2 and Section 4.3.2. Simulations

Table 5.1: Comparison of the coercive fields, H_c, of the 10 nm and 30 nm thick magnetic islands between AGFM experiment and micromagnetic simulations of isolated elements and an 4×4 array [18]. [Published under the CC BY 4.0 licence]

Thickness (nm)	AGFM H_c (Oe)	Isolated-island mean H_c (Oe)	4×4 units array H_c (Oe)
10	365(±5)	537 (±66)	497 (±81)
30	553(±5)	1023 (±67)	806 (±76)

were initially performed by assuming infinite spacing between elements so that hysteresis is an average of magnetisation from elements aligned parallel and perpendicular to the applied field, as presented in Fig. 5.1 by dark yellow line. This mean value is able to tell us the resulting magnetisation of interaction-free square ASI. Although this approximation cannot well describe the hysteresis loop measured for the 30 nm thick element (see Fig. 5.1 (b)), it matches well with that for the 10 nm thick array in Fig. 5.1 (a). Likewise, Table 5.1 illustrates that the coercivity difference of 10 nm thickness between experimental value and simulated average is four times less than that of 30 nm thick sample. This suggests a possible stronger inter-element coupling for the thicker array. To test this, simulations for a 4×4 units ASI array were calculated, in which one unit consists of four elements, and results are displayed by blue dotted lines in Fig. 5.1. Though the simulated coercivity of 10 nm thick ASI array almost agrees with that of the interaction-free case, a better agreement of the coercivity of 30 nm thick element between simulation and experiment is visible if the deviation (in Table 5.1) is taken into account. Note that the calculated hysteresis loop of 10 nm thick array is slightly different from that in Fig. 4.2 as the different shapes of the ASI array is used in the simulation. However, the experimental curve of the thicker array appears smoother than those of the simulated loops, which show two evident and sharp steps in the vicinity of zero and coercive field. The reason may be the contribution of the edge/volume disorders [19], which results in a distribution of switching fields which means an initial switch of an island's magnetisation can happen at a field lower than the average coercivity and then be propagated through the array due to interactions [20, 21]. This disorder is not accounted for in the simulations where the independently vertical (horizontal) island or all vertical (horizontal) islands of the array reverse simultaneously which is responsible for the sharp step near the zero field (coercive field).

5.2.2 Static field interaction

The static field interaction using micromagnetic simulations is also estimated. The energy difference $\triangle E = E_- - E_+$ of the central element shown in Fig. 5.2 (a) was calculated using two orientations: one aligned parallel to the static field produced by the neighbours (E_+), and one for the reversed orientation (E_-). The corresponding static field magnitude is $H_s = -\triangle E/(M_s V)$ where V is the volume of island. Note that there are sixteen possibilities of magnetisation configurations for the array in Fig. 5.2 (a), but here only present the case in which the central element experiences the largest static field. The static field, H_s, as a function of island thickness for the corner-to-corner separation between nearest neighbours from 1 nm to 141 nm is shown in Fig. 5.2 (b). The largest static field of the central element produced by the neighbours is about 80 Oe for the 10 nm thick array and 240 Oe for the 30 nm thick array. The strength of the static field roughly decreases by a factor of 10 as d changes between 1 nm and 141 nm. In addition, from Fig. 5.2 (b) one can see that the magnetostatic dipolar field from the neighbouring nanomagnet primarily affect the magnetisation localised at the corners of the central island.

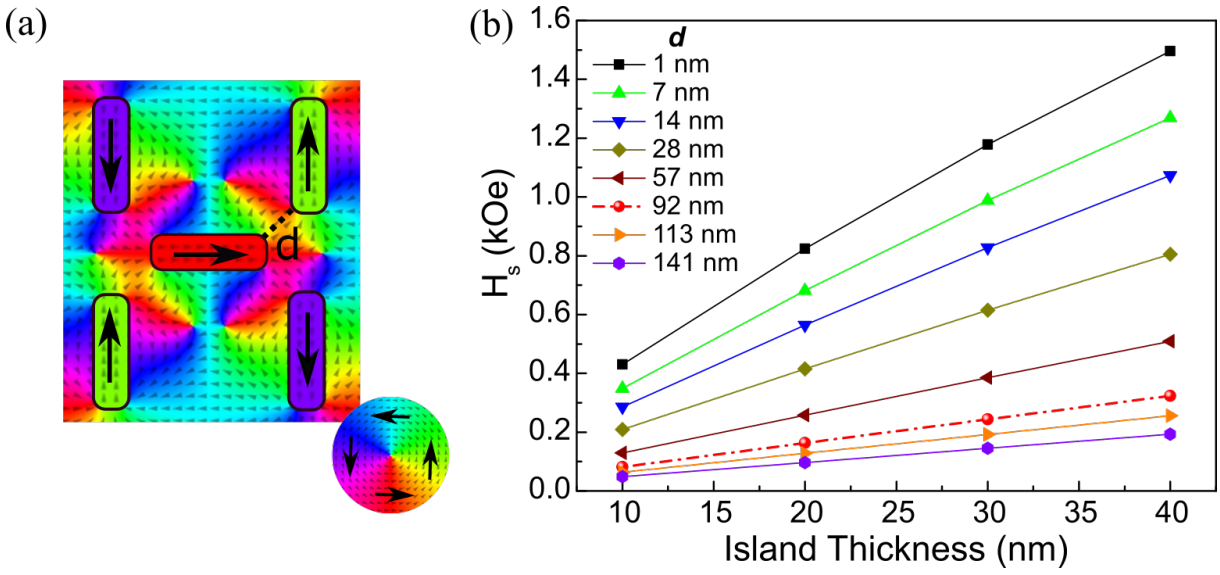

Figure 5.2: (a) Distribution of the largest average stray field of the 30 nm thick ASI array where d is the corner-to-corner separation between the nearest islands and the colour code disk represents the orientations of magnetisation in the element and the demagnetisation out of the elements. (b) The largest static field H_s acting on the central element in (a) from the neighbouring elements as a function of island thickness for the corner-to-corner separation d from 1 nm to 141 nm [18]. [Published under the CC BY 4.0 licence].

5.3 Ferromagnetic resonance (FMR)

The dynamic response of the 10 nm thick square ASI using BLS has been discussed in Chapter 4.4.2. A broadband ferromagnetic resonance spectroscopy was also performed to detect the dynamic magnetisation behaviour of two ASI arrays of different thicknesses. The dependence of the dynamic response on the thickness and field angle are explored using the VNA-FMR technique.

5.3.1 Thickness-introduced ferromagnetic resonance

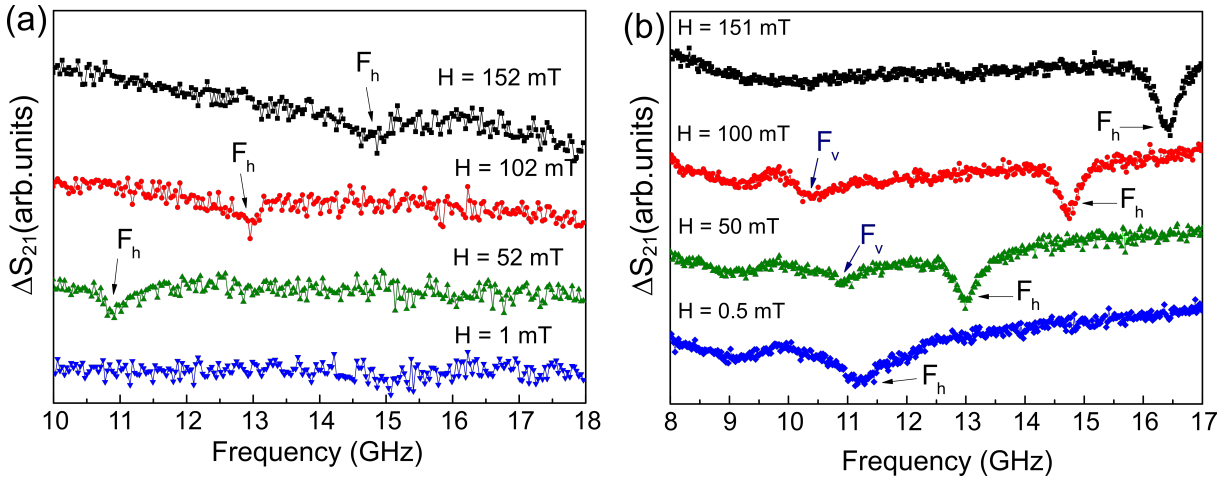

Figure 5.3: FMR absorption spectra of the (a) 10 nm and (b) 30 nm thick square ASIs at 1 mT (0.5 mT), 52 mT (50 mT), 100 mT and 150 mT 0° fields with respect to ASI lattices.

Figure 5.3 shows the FMR absorption spectra of 10 nm and 30 nm thick magnetic elements at 0° external fields of in the vicinity of 0 mT, 50 mT, 100 mT and 150 mT with respect the ASI array. The response of FMR signal to the square ASI of 10 nm thickness is obviously weak. This is a result of the small volume and hence the magnetic moment of the 10 nm thick island is weak so that the amplitude of absorption peaks are so small, as shown in Fig. 5.3 (a). One main peak can be clearly identified in most of spectra except that obtained under around zero external field. This resonance mode is the fundamental mode (or Kittel mode) from the ASI islands I_h whose easy axis is aligned with the applied field (see the inset of Fig. 5.4), which is referred to as F_h. Furthermore, the frequency of this mode increases as the strength of applied magnetic field increases. The fundamental mode is named as F_v when the hard axis of the nanomagnet is aligned with the magnetic field.

By contrast, the amplitude of the absorption peak for the 30 nm thick specimen is comparatively large, as presented in Fig. 5.3 (b). In the measured frequency range, two resonance peaks (F_h and F_v) are observed for the 50 mT and 100 mT fields, while only one peak (F_h) distinguished from the spectra under the field of 0 mT and 150 mT. For the case in which only a single peak is observed, the signal-to-noise ratio of F_v peak is probably too weak to be identified or the frequency of the resonance peak is perhaps outside the measured range. In Fig. 5.3 (b), the F_h mode occurs at a relatively higher frequency compared with F_v mode. The two resonance modes exhibit different field dependences. As the field strength increases, the frequency of mode F_h also increases. The frequency mode F_v decreases while the amplitude of field increases. It should be also noted that there is a very broad peak measured at the frequency of 9 GHz. However, this mode is not the resonances from the magnetic island as it is independent on the magnetic field, remaining unchanged with varying the field. This mode may arise from resonance generated in the experimental set-up [22].

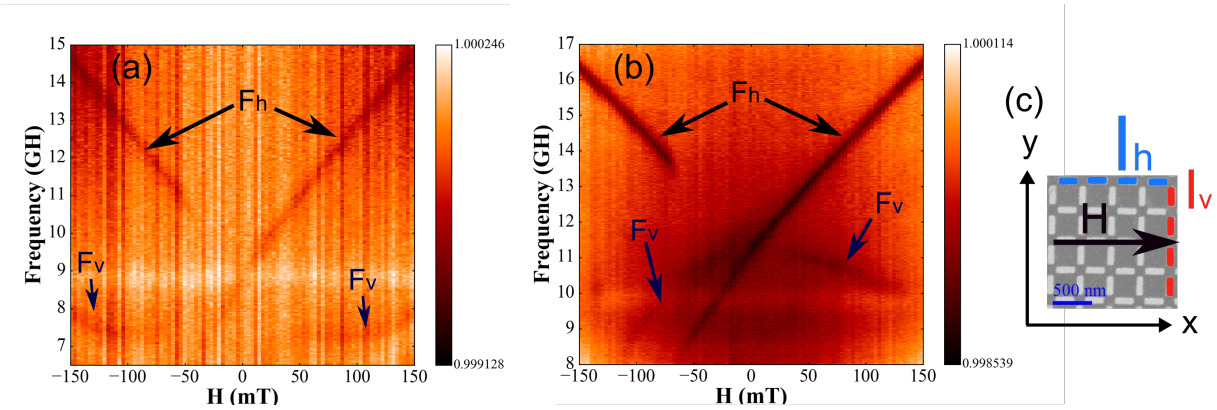

Figure 5.4: Contour plots of the normalised ΔS_{21}, indicating the measured ferromagnetic resonance of the square ASI of (a) 10 nm and (b) 30 nm thicknesses. (c) The schematic of the orientation of the external field with respect to the ASI array, in which two groups of magnetic islands, I_h and I_v, are marked in light blue and red.

To understand the relationship between the FMR resonance mode and the magnetic field, a field swept from + 150 mT to - 150 mT aligning the (1,0) direction was applied along the ASI sample. Shown in Fig. 5.4 are interesting plots of FMR response as a function of field and frequency for the 10 nm and 30 nm thick square ASI. In Fig. 5.4 (a), the FMR plots for 10 nm thick nanomagnet has poor contrast FMR signal and high background, while the contrast of 30 thick nanomagnet in Fig. 5.4 (b) is much better presentably due to the larger magnetic moment of each element. The F_h mode for both

thicknesses exhibits a linear dependence on the magnetic field. The larger magnetic moment of the thicker sample also leads to a higher frequency of the resonance mode F_h than that of the thinner one. The F_v mode nevertheless shows a different dependence on the magnetic field. As the field decreases, the F_h mode shifts to lower frequency, whereas F_v mode shifts to the higher frequency. The easy direction is along the long axis of each nanomagnet and hard direction is along the short axis in the plane. The F_h mode behaves like the easy-direction Kittel mode from the I_h islands in an array, the easy axis of which is aligned along the field. The F_v mode is the hard-axis Kittel mode localised to the magnetic islands I_v, whose hard axis is magnetised by the field.

Due to the limit for field strength in our FMR set up, the maximum available magnetic field is about $\pm 160mT$. Fig. 5.1 suggests that such a maximum is not sufficient to saturate the thicker array. Furthermore, a nonmonotonic resonance (F_v) is observed within a small field region which is too weak to be resolved clearly from the FMR measurements. Therefore, the BLS measurement on the same sample have been carried out, as discussed in Chapter 4. Fig. 5.5 shows a good agreement between the FMR and BLS results. However, BLS has the advantage that it can resolve spin-wave modes confined to the magnetic elements. A more detailed and comparative study of the thickness-dependent magnetisation dynamics using BLS will be presented and discussed in Section 5.4.2.

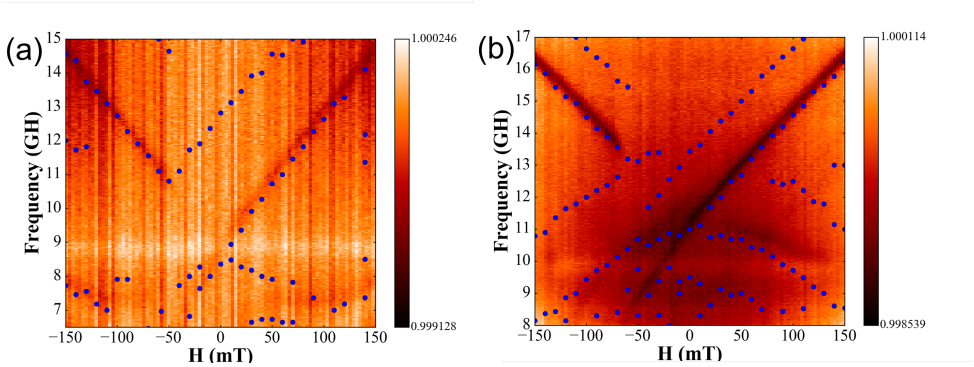

Figure 5.5: Comparison of the magnetisation dynamic modes dependent on magnetic field between the ferromagnetic resonance (colour contour shading) and the BLS (blue points) measurements.

5.3.2 Angular independence of FMR

FMR is frequently utilised to evaluate the anisotropy response of resonance mode in a magnetic material [10, 23–26]. In this investigation, FMR measurements were performed

to study of the influence shape anisotropy of the 30 nm thick ASI nanomagnets on magnetisation dynamics. The azimuthal angles (θ) of applied field was varied from 0° to 360° with respect to the y axis, as depicted in Fig. 5.6 (e).

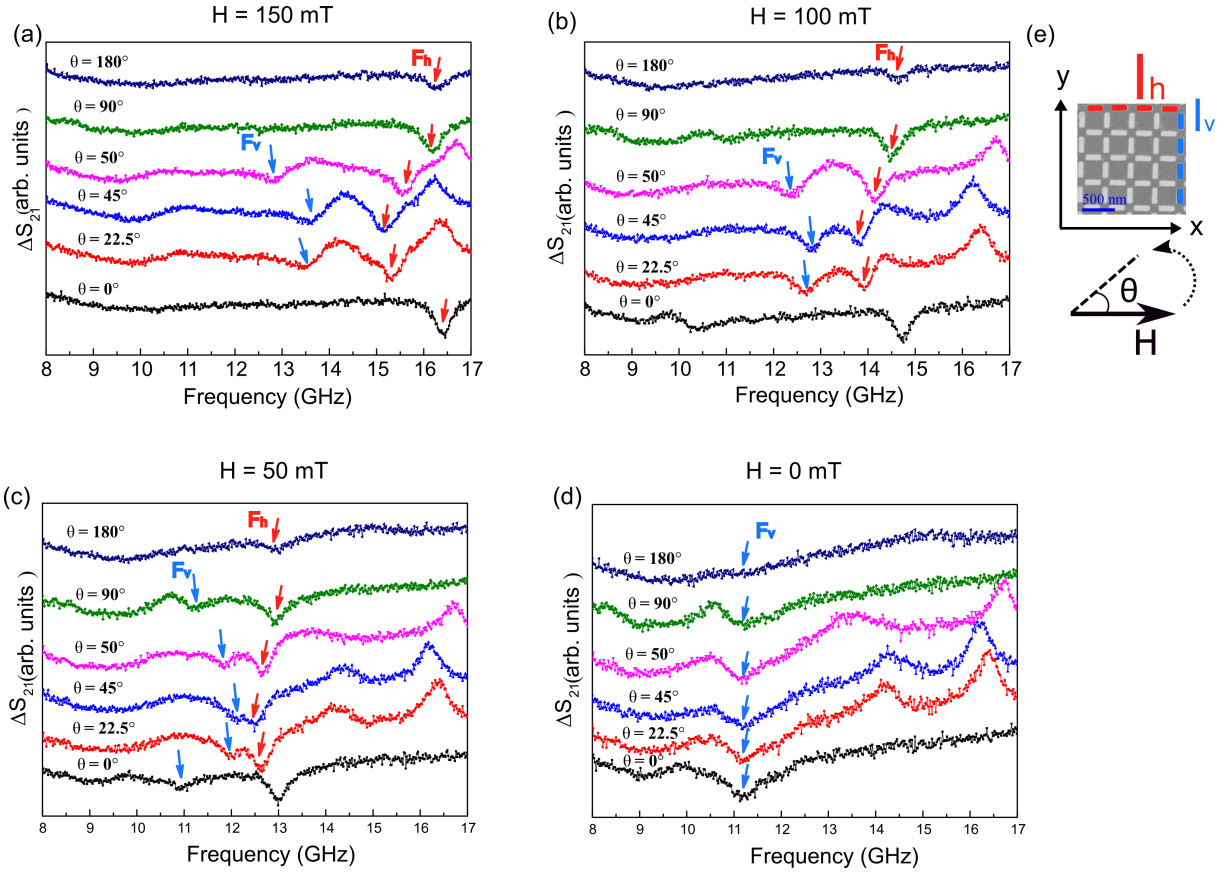

Figure 5.6: Angular-dependent FMR spectra at the (a) 150 mT, (b) 100 mT, (c) 50 mT and (d) 0 mT external fields. The red and blue arrows point out the F_h and F_v modes, respectively. (e) Schematic indicating the orientation of magnetic field with respect to the square ASI lattices.

Figure 5.6 demonstrates the angular field dependence of FMR at various strengths of external field. The red arrows indicate the resonance peaks of the F_h mode and the blue arrows label the F_v resonance. Our FMR data can be qualitatively interpreted to understand the angular-dependence behaviour of square ASI. In Fig. 5.6 (a), at the field of 150 mT, the F_h mode gradually shifts to lower frequency (from $\sim$ 16 GHz to $\sim$ 15 GHz) when the applied angle increases from 0° to 45°. However, the frequency of the F_h mode increases from $\sim$ 15 GHz back to $\sim$ 16 GHz as the field angle is varied from 45° to 90°. It is found that the low-frequency mode F_v behaves oppositely to that of the high-frequency mode F_h. Thus, the frequency of the low-frequency mode increases as the field angle increases betweem $\theta = 0°$ and $\theta = 45°$, while it decreases from 45° to 90°. This suggests that the behaviour of the resonance mode is related to the angle between

the applied field and the shape anisotropic axis of the islands. It is also noticed that the strength of the applied field contributes to the frequency difference between the F_h and F_v modes. Figs.5.6 (a-c) show a smaller frequency separation with a weak-amplitude field. In addition, only one resonance peak can be identified when the magnetic field decreases to 0 mT. Interestingly, in Fig. 5.6, a significant peak is seen between the region between 16 GHz and 17 GHz. This peak appears in all panels of Fig. 5.6. However, this is not the absorption peak so that it is not from the ferromagnetic resonance. The behaviour of this peak is independent on the field strength but slightly dependent on the field angle. Thereby, this mode might be generated from mechanical vibrations between the sample and coplanar waveguide in the experiment.

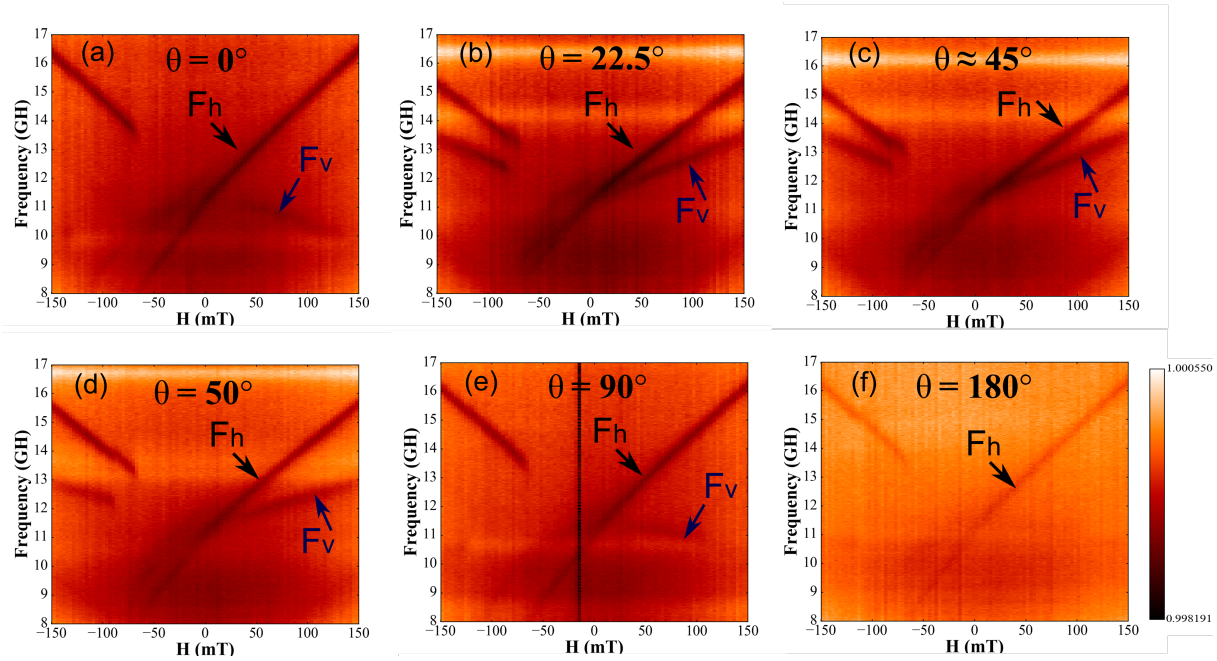

Figure 5.7: Contour plots of the ferromagnetic resonances of the 30 nm thick artificial square spin ice with the applied field H at the azimuthal angles (θ) of (a) 0°, (b) 22.5°, (c) 45°, (d) 50°, (e) 90° and (f) 180° to y axis.

Figure 5.7 presents the FMR resonances as the external field sweeps from + 150 mT to - 150 mT and at the various field angles between 0° and 180° to the ASI array (or y axis). There are two visible FMR resonances and each exhibits a different field dependence. One is linearly dependent, while the other is not, as shown in the panels of the Fig. 5.7 (a), (e) and (g). Two FMR resonances were obtained from the I_h and I_v nanomagnets. The resonance depends linearly on the field strength at the field angle an are shown for 22.5°, 45° and 50°.

5.3.3 Gyromagnetic ratio

In addition to the configuration anisotropy, FMR measurments also allow for the quantitative extraction of the magnetic parameters of saturation magnetisation and gyromagnetic ratio. The magnetisation dynamics measured in the FMR measurement obeys a Kittel equation which is given by [27]

$$\omega = \gamma\sqrt{[H + (N_z - N_H)4\pi M_s] \times [H + (N_{H,\perp} - N_H)4\pi M_s]}, \tag{5.1}$$

where ω is the frequency of the FMR mode; H represents the applied field; γ is the gyromagnetic ratio; N_z is the demagnetising factor along the z direction for nanomagnet thickness; N_H ($N_{H,\perp}$) is the demagnetising constant along (perpendicular to) the orientation of applied field H; M_s is the saturation magnetisation. The two groups of islands, I_h and I_v, have two different configurations with respect to the 0° field, as displayed in Fig. 5.8. Figure 5.8 (a) indicates that the easy direction (along the long axis) of nanomagnet is along by the field whereas the Fig. 5.8 (b) shows the configuration of hard direction (along the short axis) along the field. Correspondingly, the Kittel function of the I_h islands can be rearranged into

$$\omega = \gamma\sqrt{[H + (N_z - N_y)4\pi M_s][H + (N_x - N_y)4\pi M_s]}. \tag{5.2}$$

where the N_x, N_y and N_z are demagnetising factors along the x, y and z axis in Fig. 5.8. In the same way, the Kittel resonance of the I_v island against applied field H is explained by

$$\omega = \gamma\sqrt{[H + (N_z - N_x)4\pi M_s][H + (N_y - N_x)4\pi M_s]}, \tag{5.3}$$

The demagnetisation factors of a cuboid are able to be estimated using the method introduced by A. Aharoni [28]. In particular, the freely available calculator of the demagnetisation factor could be made use of, published on the "magpar" webpage [28, 29]. Our approximation of the demagnetisation factors of the cubic island with the 10 nm and 30 nm thicknesses are displayed in Table.5.2.

The BLS data to present the Kittel mode (F_h mode) was fitted using Eq. 5.3. This mode was identified from a number of BLS modes based on its overlap with FMR results,

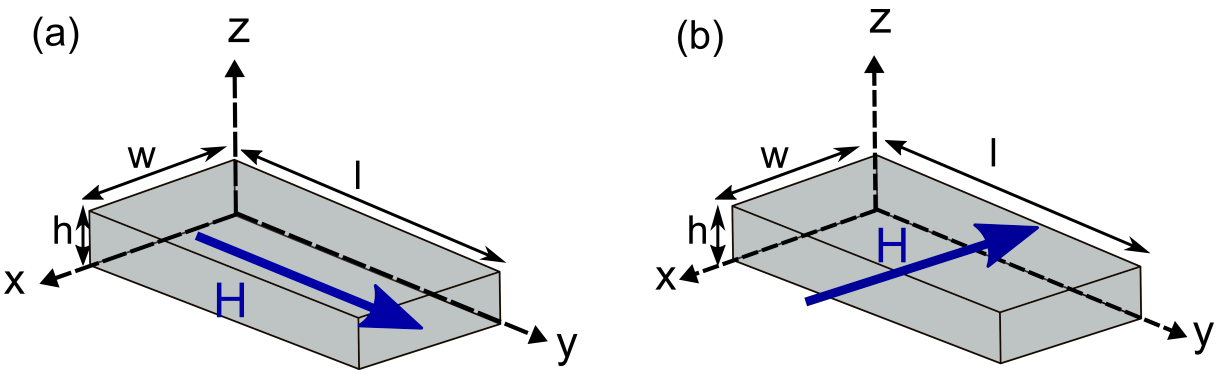

Figure 5.8: Configurations of the applied field H aligning to the (a) easy and (b) hard directions of a nanomagnet. Given dimension of each element (h = 10 (30) nm, w = 80 nm and l = 240 nm) allows us to calculate the demagnetising factors N_x, N_y and N_z.

Table 5.2: Comparison of the fitting magnetic parameters: demagnetising factors (N_x, N_y and N_z, saturation magnetisation (M_s) and gyromagnetic ratio (γ) between 10 nm and 30 nm thick nanomagnet deriving from Kittel equation.

Thickness (nm)	N_x	N_y	N_z	M_s (A/m)	γ (GHz/kOe)
10	0.04	0.13	0.83	7.79×10^4 ($\pm 0.09 \times 10^4$)	2.77 ($\pm$0.01)
30	0.08	0.27	0.65	7.93×10^4 ($\pm 0.01 \times 10^4$)	2.77 ($\pm$0.01)

as shown in Fig. 5.5. The BLS value is used to fit rather than the FMR figure as the maximum field in the FMR measurement is inefficient to saturate both I_h and I_v nanomagnets, while that in BLS is. The fitting results of M_s and γ extracted from the sample of 10 nm thickness are $7.79 \times 10^4 (\pm 0.09 \times 10^4)$ A/m and 2.77 ($\pm$0.01) GHz/kOe. The fitting value of 30 nm thick ASI are $7.93 \times 10^4 (\pm 0.01 \times 10^4)$ A/m and 2.77 ($\pm$0.01) GHz/kOe. The fits for both I_h and I_v cases are plotted in Fig. 5.9. Figure 5.9 shows that the Kittel mode from the easy-direction island I_h agrees well with the experimental BLS value. The numerical Kittel mode of the hard-axis nanomagnet I_v is in good agreement with the BLS experiment for the field larger than 2.2 kOe (saturation field).

Given gyromagnetic ratio ($\approx$ 2.8 GHz/kOe) of permalloy material is same as that has been obtained in another publication [30] using the Kittel equation. This value could be used as a parameter for Mumax simulation. However, the fitting saturation magnetisation M_s is less than one order of magnitude than the standard M_s, 8×10^5 A/m [31–33] and led to a lower-frequency simulated resonance in comparison to measured BLS modes. Therefore, the standard one was applied in all simulations and has produced a good agreement with the experiment (Fig. 5.11).

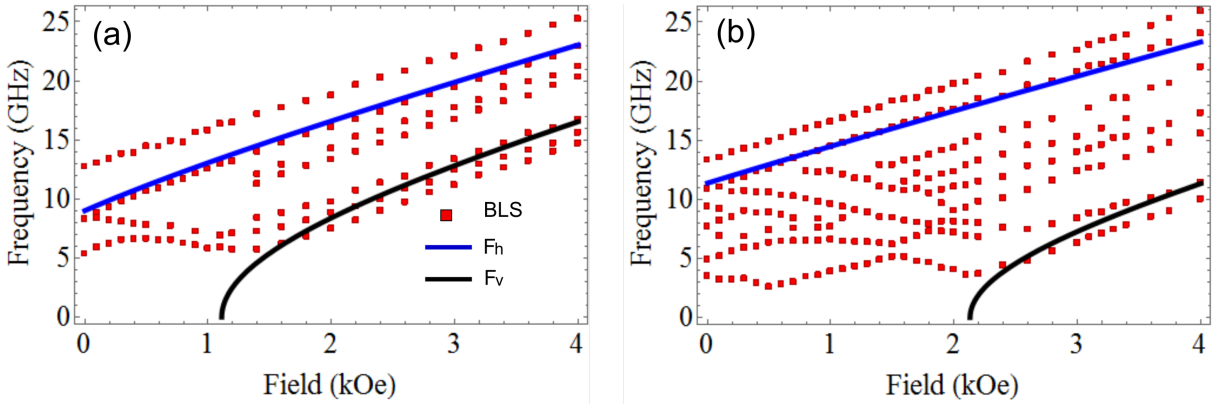

Figure 5.9: Comparison of resonance frequency for the (a) 10 nm and (b) 30 nm thick ASI between BLS value (red squares) and fitting lines using the Kittel function with 0° field in which the blue line arises from the I_h (Fig. 5.8 (a)) whose easy direction is aligned along the field, and black line from I_v (Fig. 5.8 (b)) the field laying to its hard axis.

5.4 Thickness dependence of spin-wave excitation

5.4.1 Spin wave spectra

Dynamical coupling between the islands can be measured by the spin wave frequency dispersion, which is spin wave frequency as function of the wavevector of the laser on the plane of sample, as shown in Section 4.4.1. This was studied in both the Damon-Eshbach and Backward Volume magnetostatic configurations when the applied field is horizontal (x-direction) with respect to the ASI principal axis.

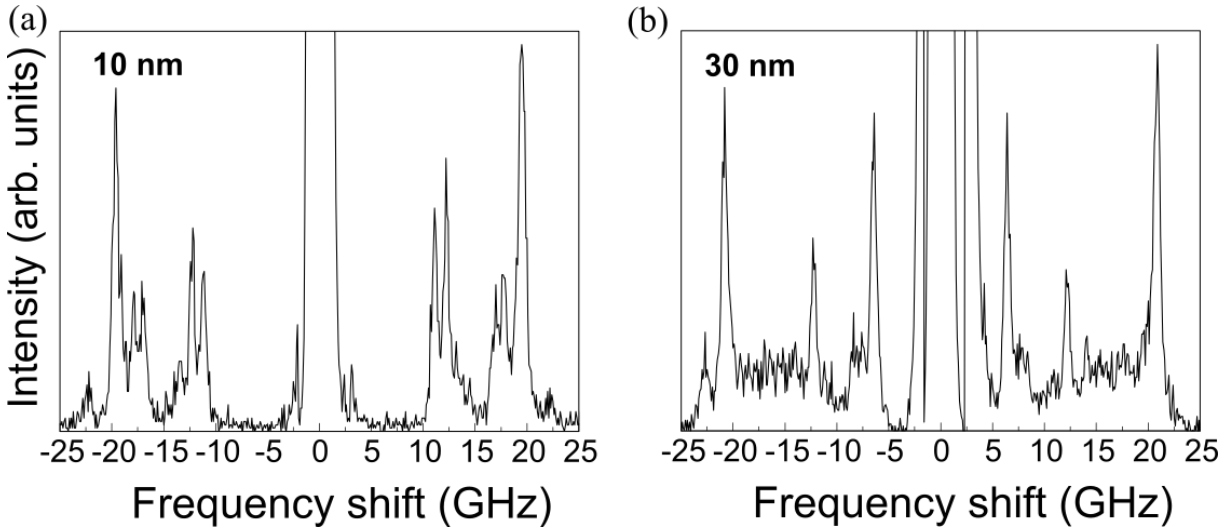

Figure 5.10: BLS spectra of the (a) 10 nm and (b) 30 nm thick ASI arrays at the external field of 4 kOe. The incidence angle of the laser light upon the sample is 20° [18]. [Published under the CC BY 4.0 licence].

Examples of measured BLS spectra under a 4 kOe field are shown in Fig. 5.10. Well-

defined, narrow BLS peaks were observed in the spectra obtained from the 10 nm thick ASI-like array (see Fig. 5.10 (a)) with a clear frequency separation of larger than 3 GHz between two families of eigenmodes. Contrarily, the peaks obtained in the spectra from 30 nm thick array (see Fig. 5.10 (b)) are broad and more closely spaced in frequency. This suggests that the nanomagnet thickness strongly affects on the number of observable spin-wave modes.

5.4.2 Spin-wave eigenmode and spatial profile

Figure 5.11 plots the frequencies of the BLS peaks (as displayed in Fig. 5.10) as a function magnetic field which sweeps from +4 kOe to −4 kOe. The experimental data are illustrated by red square symbols. Above the coercive field, indicated by the vertical blue dash-dotted lines, the dependence of the frequencies on field is linear. Below the coercive field, mode softening occurs as magnetisation of individual elements within the array reverse. It is found that the spin-wave modes exhibit a more complex behaviour below the saturated field.

An analysis of the mode structure using micromagnetic simulations was performed as described in Section 4.4.3. The elements are treated as independent elements in order to calculate a non-interacting reference for comparison. As discussed in the Section 5.2.1, the agreement of the static results with the interaction-free simulations and a magnetic array simulation that considers the possible dynamic inter-island interaction, suggest that the ASI array of 10 nm thickness possesses negligible dynamic inter-element interaction. The field dependence of spin-wave modes in a 2×2 units array with the 30 nm thick nanomagnet was also computed, showing the influence of the static field of neighbouring elements on the spin wave excitations, as presented in Fig. 5.12 (a). All spin-wave resonances excited from this array with a 3 kOe field are overlapped with the superposition of spin wave resonances excited from isolated islands (I_h and I_v) with less than 0.35 GHz frequency discrepancy, as shown in Fig. 5.12 (b). Therefore, using the independent-island model not only allows us to advantageously distinguish the contributions from the vertical and horizontal sublattices, but also is able to describe the spin wave behaviour of this square ASI array.

In Fig. 5.11, qualitative agreement is obtained between experiment and simulations for both element thicknesses using the same magnetic parameters, but differing only in

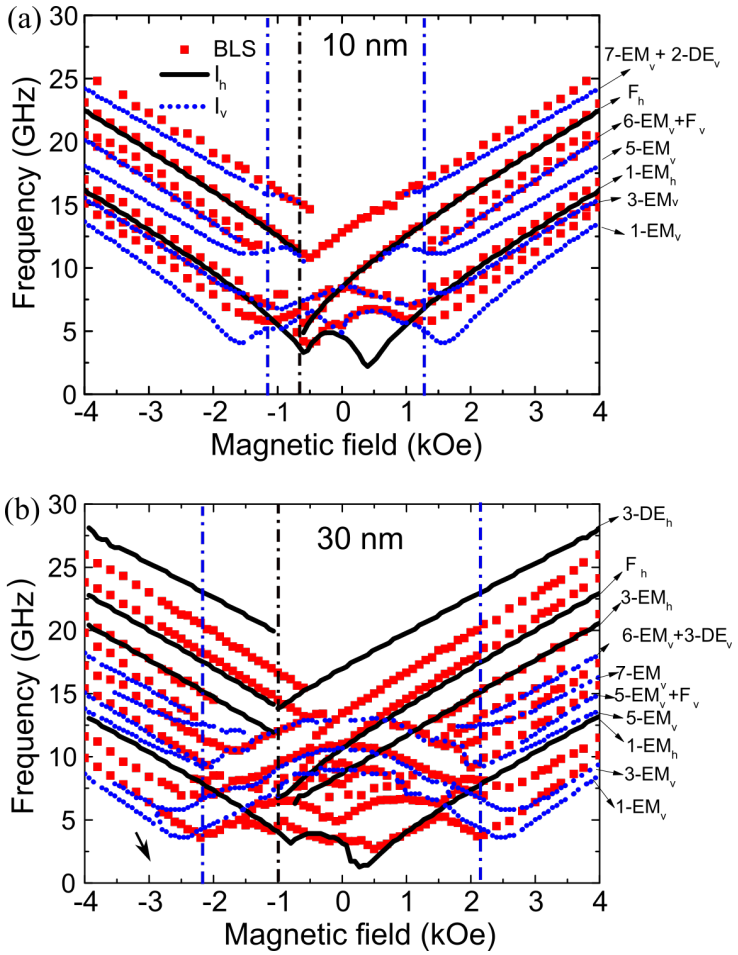

Figure 5.11: Frequencies of spin-wave eigenmodes as a function of magnetic field H, applied along the x-direction for the (a) 10 nm and (b) 30 nm thick islands in square ASI. The red squares are BLS experimental results; black solid and blue dotted lines indicate the simulation results for horizontally and vertically isolated islands with respect to the field, correspondingly. The blue and black dash dotted lines indicate the switching fields of the horizontal and vertical islands, respectively. Labels indicate the spatial characters of the eigenmodes. The spatial profile of eigenmodes will be imaged in the Fig. 5.13.

the element thickness. The 10 nm thick array shows a better agreement with experimental frequencies than those in 30 nm thick array. As noted in regards to the hysteresis simulations, the static field that is produced from its neighbouring elements is neglected. This leads to a coercivity that is too large because it does not take into account the different static field environment that elements at an array edge experience. In addition, edge imperfection on elements are not included in the model. Kohli *et al.* show that this can also cause differences in the coercivity compared to simulated 'ideal' islands [34]. In this regards, the evidence of stronger interaction coupling in the 30 nm thick sample may appear as a reduced coercivity compared to the simulated hysteresis loop. Also, the reduced coercivity field means that the lowest frequencies associated with softening at magnetic

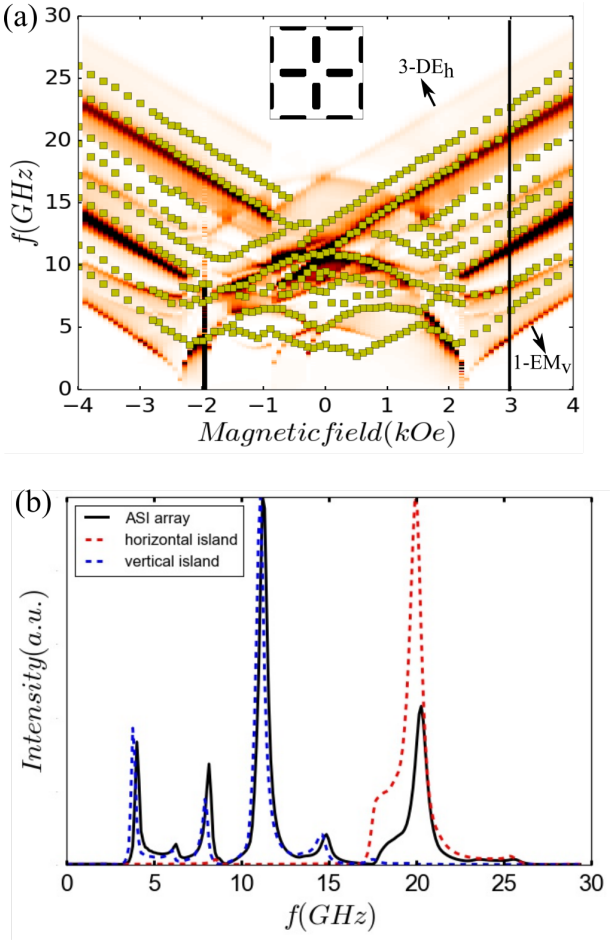

Figure 5.12: (a) Comparison of the frequencies of the spin wave modes of the 30 nm thick elements as a function of magnetic field between BLS results (yellow squares) and the simulation of a 2×2 units (12 elements) array. The intensity of the spin-wave modes is displayed by the colour contour shadings where dark shading indicates the maximum intensity and the light yellow to while colours signify the minimum intensity. (b) Line scan of the simulated spin wave mode intensity at the applied field of +3 kOe indicated by the vertically black line in (a). Intensities associated with modes on the horizontal and vertical islands are also indicated. The resonance intensity is calculated as the square of the time Fourier transformed calculation of the simulated m_z component [18]. [Published under the CC BY 4.0 licence].

transitions will shift to lower fields with an increase in frequency due to an stronger internal field. From the simulation data of isolated elements shown in Fig. 5.11 (b), it can be estimated that as a shift in field by an amount approximately equal to 0.5 kOe would increase the frequencies of the spin waves in the linear regime by approximately 2 GHz.

Regarding the frequency evolution of magnetic eigenmodes as a function of the external magnetic field, it is notable that, starting from +4 kOe and decreasing the field towards negative saturation, some of the eigenmodes are characterised by an almost linear behaviour (the black solid lines) with field while for some others there are frequency minima (the blue dotted lines). For fields between the minima the frequency of these

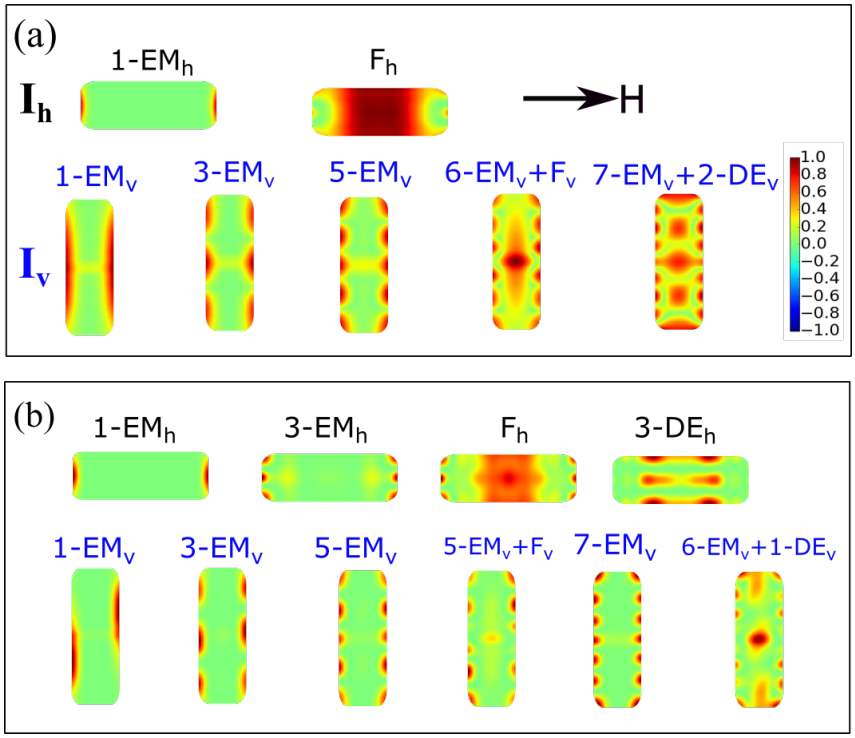

Figure 5.13: Spatial profiles of the out-of-plane m_z component of the dynamic magnetisation of the (a) 10 nm and (b) 30 nm thick isolated element magnetised by the magnetic field H of 3 kOe [18]. [Published under the CC BY 4.0 licence].

eigenmodes are characterised by a "bell" shape [35] and the lowest frequencies at small field are due to destabilising of the vertical element before reversal. The spin wave frequency, however, shows high field softening (the minima of the blue curves in Figs.5.11) and also a low field softening (the minima in the black curves in Figs. 5.11), which are respectively indicated by vertically blue and black dash dotted lines. This means that it is possible to access, through spin wave softening, to the separate reversal events of the field parallel (I_h) and field perpendicular (I_v) elements. In particular, by inspection of the simulated magnetisation curves, one can assert that the frequency minima of the I_v element measured for the lowest frequency eigenmodes are at $\pm$ 2.1 kOe (1.2 kOe) for the 30 nm (10 nm) thick array, are related to the saturation of the islands aligned perpendicular to the applied field while other minima correspond to reorientation of magnetisation in islands aligned collinear to field H. By way of contrast, hysteresis measurements reflect the sum of the two component orientations of sub-lattices with respect to the field. This alone however is unable to distinguish between these separate reversals.

Figs. 5.13 shows the calculated intensity profiles of the spin wave excitations of the independently horizontal and vertical islands, Ih and Iv. The eigenmodes are labelled

according to the scheme proposed by Zivieri *et al.* [31] where "F" indicates a fundamental resonance localised in the central portion of the islands oriented horizontally (F_h) or vertically (F_v) with respect to the applied field direction, H; "EM" indicates an edge mode; "DE" designates the Damon-Eshbach mode with nodal planes parallel to the direction of the applied magnetic field.

EM eigenmodes are highly susceptible to surface and edge specific local anisotropy and exchange fields that can strongly affect their frequency. Examples of these eigenmodes are shown in Figs.5.13. There are some discrepancies between the measured and calculated EM frequency in the Fig. 5.11. This can be ascribed to the non-ideal shape of the elements, edge roughness, and consequent reduced edge magnetisation and surface anisotropy on the edge surface which lead to a smaller effective demagnetisation field along the edges [36].

5.5 Internal field induced by the thickness

It is especially interesting to notice that the F_h and F_V eigenmodes in the 30 nm thick island have a smaller spatial extent than the same mode in the 10 nm thick island, as shown in Fig. 5.13. This is connected to the spatial profile of the internal magnetic field. The internal magnetic field defined as the sum of the Zeeman (H) and static demagnetising (H_d) fields, $H_{int} = H + H_d$, due to magnetic free charges arising at the edges of the magnetic elements, has been calculated using micromagnetic simulation, as discussed in Chapter 4. Figure 5.14 display that, for the thinner array, H_{int} is flatter in the central portion of the elements and more homogeneous. It is noticed that H_{int} for the 30 nm thick ASI array is always smaller than that of the 10 nm thick array and this difference is responsible for the frequency shift of eigenmodes with the same spatial profile as observed in Fig. 5.13. Finally, the spatial extent of the F mode (see Fig. 5.14) when H is applied along the x-direction is larger than when H is aligned parallel to the y-direction. This reflects the inhomogeneity region of H_{int} for the two magnetic field orientations with respect to the independent island.

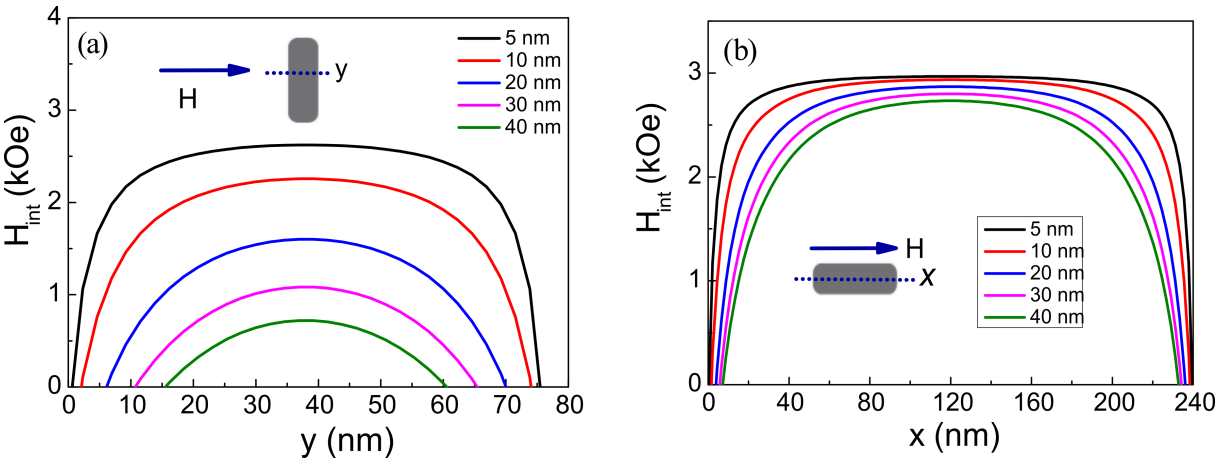

Figure 5.14: Thickness-dependence spatial profiles (a) x and (b) y of the internal field calculated along the central section of the element (the dotted line) for a external field H = 3.0 kOe applied along the arrow direction.

5.6 Discussion of dynamic interaction

Now, the possibility of dynamic field interaction between islands of the ASI array is discussed. Firstly, the spin wave dispersions for different field orientations have been measured, as described in the Section 4.4.1. No appreciable modification of the frequencies has been detected which suggests that these two arrays do not support a measurable magnon band width, and therefore spin waves are confined in each magnetic island other than propagation within the patterned array. Instead the array behaves as a collection of elements which are affected only by the weak static field from the neighbours. This is consistent with the mode profiles calculated in Fig.5.13. In a dense array of magnetic elements, the low frequency edge mode may couple elements via a stray dynamic dipole field. The strength of this coupling would determine the width of the magnonic band [37]. However, the fundamental mode is very much localised within an element, and the stray dynamic fields produced between elements is very small.

Here, a question of whether one can in principle design a square ice array that behaves as a magnonic crystal could be posed. The simplest case with two magnetic elements was studied by micromagnetic simulation. Figure 5.15 (a) displays the simulated spin-wave frequencies of two elements of 30 nm thickness as a function of the corner-to-corner distance between them. An applied field of 3 kOe is parallel to the horizontal island. The frequencies of the two lowest-frequency modes (1-EM and 3-EM) will rise within the range of 1 GHz as d decreases to 1 nm. This change in frequency is due to an increased static inter-element coupling field, as shown in the Fig. 5.2 (b). In Fig. (b) the spatial

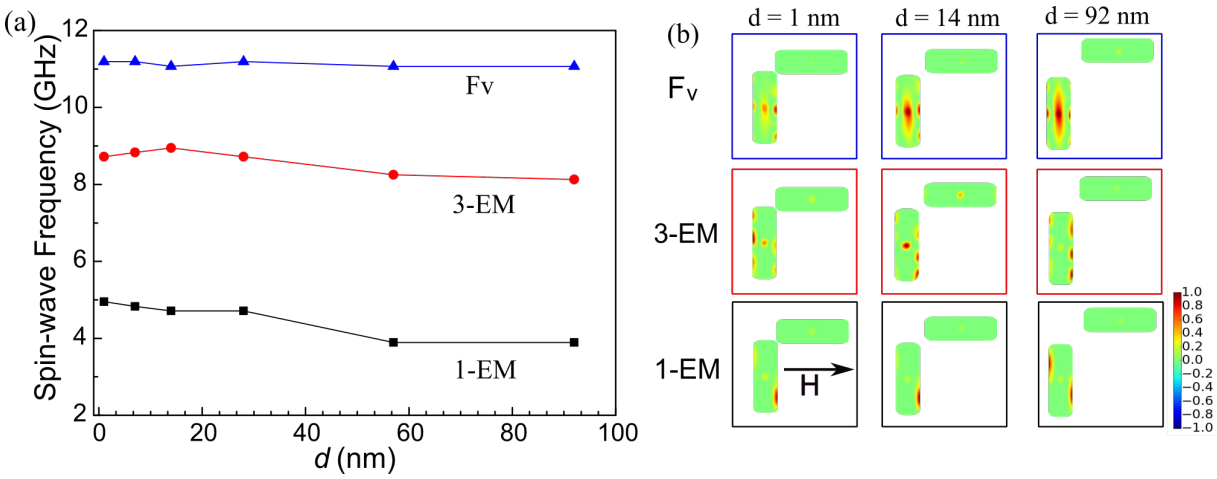

Figure 5.15: (a) Frequencies of spin-wave modes of 30 nm thick two-element array as a function of corner-to-corner separation d between the nearest neighbours. (b) Spatial profiles of the out-plane m_z component of the two elements with 1 nm, 14 nm and 92 nm separation. Note that the line is a guide to the eyes and the d is not scaled in the profile map [18]. [Published under the CC BY 4.0 licence].

profile of spin wave modes for 1 nm, 14 nm and 92 nm island separation of Fig. 5.15 (a) show that there is no overlap between the two EM modes even when the islands nearly touch each other. Note that the F_v mode, which has negligible overlap between islands, is independent of d.

5.7 Conclusions

In this chapter, the spin wave excitations of artificial square spin ice is discussed and the frequencies obtained from 10 nm and 30 nm thick nanomagnets with a corner-to-corner separation between nearest neighbouring island of 92 nm are compared. Softening observed in the edge mode spectra as a function of applied magnetic field can be identified with reversal of different orientations of magnetic islands. This allows us to use spin wave spectra to differentiate reversals of those elements with axes parallel to the applied magnetic field from elements with axes perpendicular to the applied field.

There is some evidence for observable static field interactions between 30 nm thick elements. This evidence is determined by the coercive fields of experiment and simulated array which are substantially less than those expected of isolated elements. The inter-element interactions may reduce the array coercivity by assisting reversal of elements at the array edges and corners through cooperative effects that can lead to reduced coercivity of the entire array. This interaction may also contribute weakly to the spin wave

frequencies.

Lastly, it is noted that most of the spin wave excitations observed in two ASI arrays of 10 nm and 30 nm thicknesses belong to the class of edge-localised eigenmodes. This means that their measurement provides at least in principle information about the effects of nanomagnet element that determine the frequency of spin wave eigenmodes confined to individual elements. This square ASI system primarily supports the standing spin wave.

Bibliography

[1] G Gubbiotti, M Conti, G Carlotti, P Candeloro, E D Fabrizio, K Y Guslienko, A Andre, C Bayer, and A N Slavin. Magnetic field dependence of quantized and localized spin wave modes in thin rectangular magnetic dots. *Journal of Physics: Condensed Matter*, 16(43):7709–7721, 2004.

[2] C Bayer, J Jorzick, B Hillebrands, S O Demokritov, R Kouba, R Bozinoski, A N Slavin, K Y Guslienko, D V Berkov, N L Gorn, and M P Kostylev. Spin-wave excitations in finite rectangular elements of $Ni_{80}Fe_{20}$. *Physical Review B*, 72(6):064427, 2005.

[3] M Dvornik, P V Bondarenko, B A Ivanov, and V V Kruglyak. Collective magnonic modes of pairs of closely spaced magnetic nano-elements. *Journal of Applied Physics*, 109(7):07B912, 2011.

[4] P S Keatley, P Gangmei, M Dvornik, R J Hicken, J Grollier, and C Ulysse. Isolating the dynamic dipolar interaction between a pair of nanoscale ferromagnetic disks. *Physical Review Letters*, 110(18):187202, 2013.

[5] V S Bhat, J Sklenar, B Farmer, J Woods, J T Hastings, S J Lee, J B Ketterson, and L E De Long. Controlled magnetic reversal in permalloy films patterned into artificial quasicrystals. *Physical Review Letters*, 111(7):077201, 2013.

[6] V S Bhat, J Sklenar, B Farmer, J Woods, J B Ketterson, J T Hastings, and L E De Long. Ferromagnetic resonance study of eightfold artificial ferromagnetic quasicrystals. *Journal of Applied Physics*, 115(17):17C502, 2014.

[7] J Sklenar, V S Bhat, L E DeLong, and J B Ketterson. Broadband ferromagnetic resonance studies on an artificial square spin-ice island array. *Journal of Applied Physics*, 113(17):17B530, 2013.

[8] M B Jungfleisch, W Zhang, E Iacocca, J Sklenar, J Ding, W Jiang, S Zhang, J E Pearson, V Novosad, J B Ketterson, et al. Dynamic response of an artificial square spin ice. *Physical Review B*, 93(10):100401, 2016.

[9] S Gliga, A Kákay, R Hertel, and O G Heinonen. Spectral analysis of topological defects in an artificial spin-ice lattice. *Physical Review Letters*, 110(11):117205, 2013.

[10] X Zhou, G-L Chua, N Singh, and A O Adeyeye. Large area artificial spin ice and anti-spin ice $Ni_{80}Fe_{20}$ structures: Static and dynamic behavior. *Advanced Functional Materials*, 26(9):1437, 2016.

[11] I R B Ribeiro, J F Felix, L C Figueiredo, P C Morais, S O Ferreira, W A Moura-Melo, A R Pereira, A Quindeau, and C I L de Araujo. Investigation of ferromagnetic resonance and magnetoresistance in anti-spin ice structures. *Journal of Physics: Condensed Matter*, 28(45):456002, 2016.

[12] Y Yahagi, C R Berk, B D Harteneck, S D Cabrini, and H Schmidt. Dynamic separation of nanomagnet sublattices by orientation of elliptical elements. *Applied Physics Letters*, 104(16):162406, 2014.

[13] Y Yahagi, C R Berk, B D Harteneck, S D Cabrini, and H Schmidt. Dynamic separation of nanomagnet sublattices by orientation of elliptical elements. *Applied Physics Letters*, 104(16):162406, 2014.

[14] G Gubbiotti, L Albini, G Carlotti, M De Crescenzi, E Di Fabrizio, A Gerardino, O Donzelli, F Nizzoli, H Koo, and R D Gomez. Finite size effects in patterned magnetic permalloy films. *Journal of Applied Physics*, 87(9):5633, 2000.

[15] E Iacocca, S Gliga, R L Stamps, and O Heinonen. Reconfigurable wave band structure of an artificial square ice. *Physical Review B*, 93:134420, 2015.

[16] F Montoncello, L Giovannini, F Nizzoli, P Vavassori, M Grimsditch, T Ono, G Gubbiotti, S Tacchi, and G Carlotti. Soft spin waves and magnetization reversal in elliptical Permalloy nanodots: Experiments and dynamical matrix results. *Physical Review B*, 76(2):024426, 2008.

[17] N Smith, D Markham, and D LaTourette. Magnetoresistive measurement of the exchange constant in varied-thickness permalloy films. *Journal of Applied Physics*, 65(11):4362, 1989.

[18] Y Li, G Gubbiotti, F Casoli, S A Morley, F J T Gonçalves, M C Rosamond, E H Linfield, C H Marrows, S McVitie, and R L Stamps. Thickness dependence of spin wave excitations in an artificial square spin ice-like geometry. *Journal of Applied Physics*, 121(10):103903, 2017.

[19] Z Budrikis, J P Morgan, J Akerman, A Stein, P Politi, S Langridge, C H Marrows, and R L Stamps. Disorder strength and field-driven ground state domain formation in artificial spin ice: Experiment, simulation, and theory. *Physical Review Letters*, 109:037203, 2012.

[20] E Mengotti, L J Heyderman, A Fraile Rodríguez, A Bisig, L Le Guyader, F Nolting, and H B Braun. Building blocks of an artificial kagome spin ice: Photoemission electron microscopy of arrays of ferromagnetic islands. *Physical Review B*, 78:144402, 2008.

[21] R V Hügli, G Duff, B O'Conchuir, E Mengotti, A F Rodríguez, F N, L J Heyderman, and H B Braun. Artificial kagome spin ice: dimensional reduction, avalanche control and emergent magnetic monopoles. *Philosophical Transactions. Series A, Mathematical, Physical, and Engineering Sciences*, 370(1981):5767–82, 2012.

[22] F J T Gonçalves. *Engineering of demagnetisation fields in exchange biased antidots studied using ferromagnetic resonance and Lorentz microscopy.* PhD thesis, University of Glasgow, 2015.

[23] F J T Goncalves, G W Paterson, R L Stamps, S O'Reilly, R Bowman, G Gubbiotti, and D S Schmool. Competing anisotropies in exchange-biased nanostructured thin films. *Physical Review B*, 94(5):054417, 2016.

[24] C Yu, M J Pechan, and G J Mankey. Dipolar induced, spatially localized resonance in magnetic antidot arrays. *Applied Physics Letters*, 83(19):3948–3950, 2003.

[25] X Liu, Y Sasaki, and J K Furdyna. Ferromagnetic resonance in $Ga_{1-x}Mn_xAs$: Effects of magnetic anisotropy. *Physical Review B*, 67(20):205204, 2003.

[26] B Heinrich, K B Urquhart, A S Arrott, J F Cochran, K Myrtle, and S T Purcell. Ferromagnetic-resonance study of ultrathin bcc Fe(100) films grown epitaxially on fcc Ag(100) substrates. *Physical Review Letters*, 59(15):1756–1759, 1987.

[27] Charles Kittel. On the Theory of Ferromagnetic Resonance Absorption. *Physical Review*, 73(2):155–161, 1948.

[28] A Aharoni. Demagnetizing factors for rectangular ferromagnetic prisms. *Journal of Applied Physics*, 83(6):3432, 1998.

[29] R Dittrich. “http://www.magpar.net/static/magpar/doc/html/demagcalc.html”.

[30] M Kostylev, G Gubbiotti, G Carlotti, G Socino, S Tacchi, C C Wang, N Singh, A O. Adeyeye, and R L Stamps. Propagating volume and localized spin wave modes on a lattice of circular magnetic antidots. *Journal of Applied Physics*, 103(7):07C507, 2008.

[31] R Zivieri, P Malago, L Giovannini, S Tacchi, G Gubbiotti, and A O Adeyeye. Soft magnonic modes in two-dimensional permalloy antidot lattices. *Journal of Physics: Condensed Matter*, 25:336002, 2013.

[32] A Y Rusanov, M Hesselberth, J Aarts, and A I Buzdin. Enhancement of the superconducting transition temperature in Nb/Permalloy bilayers by controlling the domain state of the ferromagnet. *Physical Review Letters*, 93(5):057002, 2004.

[33] R P Cowburn, D K Koltsov, A O Adeyeye, M E Welland, and D M Tricker. Single-domain circular nanomagnets. *Physical Review Letters*, 83(5):1042–1045, 1999.

[34] K Kohli, A Balk, J Li, S Zhang, I Gilbert, P Lammert, V Crespi, P Schiffer, and N Samarth. Magneto-optical Kerr effect studies of square artificial spin ice. *Physical Review B*, 84(18):180412, 2011.

[35] V Flovik, F Maciá, J M Hernández, R Bruˇ as, M Hanson, and E Wahlström. Tailoring the magnetodynamic properties of nanomagnets using magnetocrystalline and shape anisotropies. *Physical Review B*, 92(10):104406, 2015.

[36] R D McMichael and B B Maranville. Edge saturation fields and dynamic edge modes in ideal and non-ideal magnetic film edges. *Physical Review B*, 74(2):024424, 2006.

[37] S Tacchi, M Madami, G Gubbiotti, G Carlotti, H Tanigawa, T Ono, and M P Kostylev. Anisotropic dynamical coupling for propagating collective modes in a two-dimensional magnonic crystal consisting of interacting squared nanodots. *Physical Review B*, 82(2):024401, 2010.

6

Ferromagnetism and domain-wall topologies in an artificial pinwheel spin ice

6.1 Introduction

In Chapters 4 and 5, the effect of magnetisation configuration on spin wave response of square ASI using BLS and FMR is discussed, noting the roles of field strength, field direction and nanomagnet thickness. However, the nonlinearly complex magnetic behaviour in the presence of a nonsaturating field is not been fully understood yet since it is computationally infeasible to predict the magnetisation reversal of an array with a great many islands ($\approx 4000 \times 4000$ islands in this square ASI) using micromagnetic simulations. This problem can be solved by using a number of cutting-edge techniques to image *in-situ* changes of magnetisation state within individual nanomagnet in real time with varying temperature and field strength. Up to now, a number of imaging techniques have been utilised, such as Magnetic Force Microscopy (MFM) [1–10], Photo-Emission

Electron Microscopy (PEEM) [11–16] and Transmission X-ray Microscopy (TXM) [17]. In our study, Lorentz Transmission Electron Microscopy (LTEM) was employed to probe the magnetisation state of each permalloy island. This allows us to continuously image and track the magnetic state of a finite-size (1250 nanomagnets) ASI array over an whole sweeping field. Most importantly, the magnetisation changes under a switching field can be observed.

The study of magnetic configurations in ASI geometries has inspired exploration of exotic properties to be explored [4, 9, 10, 12, 18, 19]. For example, the square and Kagome ASIs exhibit some peculiar behaviours: residual entropy [20], monopole-like excitations [18,21,22] and reconfigurable magnetic resonance [23–25]. In addition, other geometries of ASI were also proposed as a way to study the new frustrations, for instance Shakti [9,26], Penrose [27–29] and a modified square [8], resulting in novel multifold degenerate ground states and magnetic charge ordering. Here, a "pinwheel" geometry is proposed, created by rotating each island in square ASI 45° around its central axis, as depicted in Fig. 6.1.

In this chapter, the nature of such a structure is explored, which possesses smaller energy spreads between vertices than those of square ASI so that it is highly degenerate. The angular dependence of the field-driven magnetisation process in pinwheel ASI is also studied using LTEM. The results show ferromagnetic domain growth and domain-wall propagation at certain applied field orientation with respect to the ASI array. Mesoscopic wall configurations in analogy with typical 180° and 90° ferromagnetic Néel wall observed in continuous films appear during magnetisation reversal. The unusual charged domain walls are also observed, where the charge ordering is dependent on the magnetisation alignments of the neighbouring domains. At the end, an AC field-induced demagnetisation protocol will be described as a method to anneal experimentally the pinwheel ASI system to its ground state.

The contributions from other collaborators and myself to this work are: Dr. Ciaran Ferguson fabricated the pinwheel ASI with the asymmetric boundary in the James Watt Nanofabrication Centre at the University of Glasgow and Dr. Sophie Morley prepared the pinwheel ASI with the symmetric boundary at the University of Leeds; Dr. Gary Paterson and myself operated the Lorentz TEM measurements and analysed the TEM data together; Dr. Ciaran Ferguson and myself carried out the demagnetisating ASI experiment. I analysed the all data of the demagnetisation measurements.

6.2 Pinwheel artificial spin ice

It is well established that square ASI has an antiferromagnetic ground state [10, 13] and, for a single vertex, it possesses four types of well-defined energy levels [2, 30]. The vertex is defined as a point at which four nearest islands meet on (Figs. 6.1 (a) and (c)). The energy of square vertex increases from the lowest energy state (T1), with the 'two-in-two-out' topology obeying 'ice rules', to the highest-energy 'four-in (four-out)' configuration (T4) [1], as shown in Fig. 6.2.

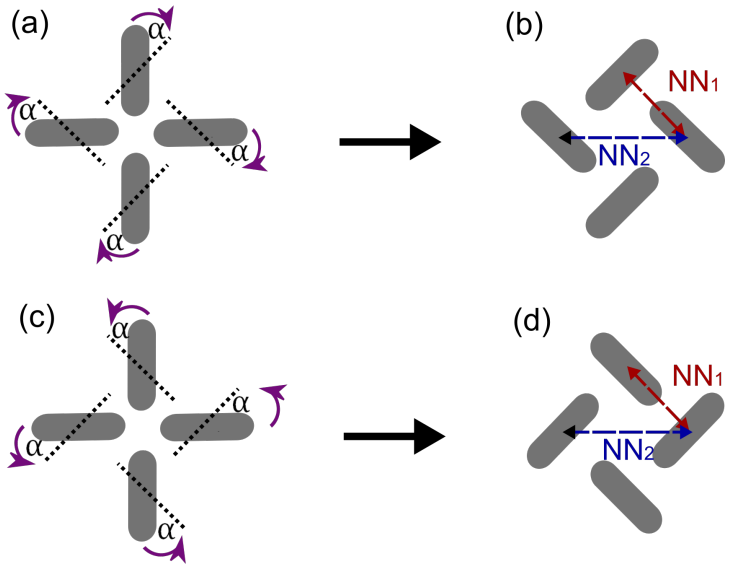

Figure 6.1: Schematic of the modification from (a, c) square ASI into (b, d) pinwheel ASI through rotating each element around its centre by 45°. The label 'NN_1' indicates the interactions between the first nearest neighbours (red dashed line), and 'NN_2' represents the interaction between the second nearest neighbours (blue dash line). Diagrams (b) and (d) compare two pinwheel structure with opposite chiralities.

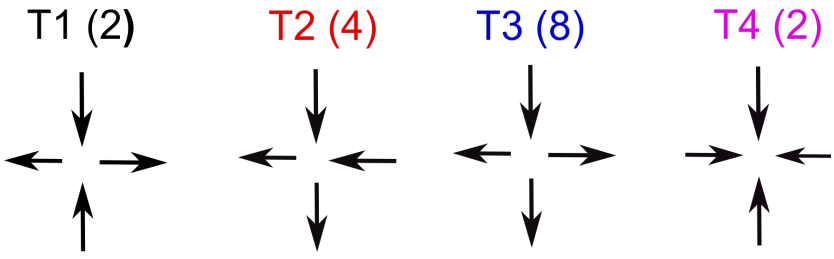

Figure 6.2: The four possible vertex magnetisation topologies, referred to as 'T1', 'T2', 'T3' and 'T4'. The vertex energy of square vertex increases from T1 to T4 [2]. The number in the bracket represents all possibilities of the degenerate of each vertex configuration.

A patterned square-lattice array has a ground state configuration of antiferromagnetic ordering created by tiling two degenerate T1 vertices. This gives rise to an antiferromagnetic moment arrangement. It is interesting to ask if a geometry of ASI, where the

interisland coupling leads to a ferromagnetic ground state, could be designed? By rotating each individual island of square ASI through 45°, as depicted by Fig. 6.1 (a), drives one end of island ends points toward the middle part of its nearest neighbour, which forms a 'pinwheel' geometry (see Fig. 6.1 (b) or (c)). In such a structure, the interaction arising from the neighbouring islands (NN_1 and NN_2) is modified. For the sake of simplification the interactions of a single pinwheel vertex is examined in the next section.

6.2.1 A nearly-degenerate system

How does the interaction vary as the arrangement of magnetic island changes? To address this problem, the vertex energies for square and pinwheel ASI were computed using Monte Carlo (MC) method on the basis of the dipole-dipole interaction model [13,18,31]. All MC results in this chapter have been acquired by our collaborator Fabio S. Nascimento at the Federal University of Viçosa, Brazil. The MC columns of Table 6.3 show the normalised vertex energy calculated by E_{dip}/D, where E_{dip} is total dipolar energy given by

$$E_{dip} = \frac{\mu_0}{4\pi} \sum_{i \neq j} [\frac{\vec{\mu_i} \cdot \vec{\mu_j}}{r_{ij}^3} - \frac{3(\vec{\mu_i} \cdot \vec{r}_{ij})(\vec{\mu_i} \cdot \vec{r}_{ij})}{r_{ij}^5}], \tag{6.1}$$

where $\vec{\mu_i}$ ($\vec{\mu_j}$) is the magnetic moment within each nanomagnet and r_{ij} is the distance between two macrospins, i and j; $D = \mu_0 \mu^2/(4\pi a^3)$ is the dipolar constant that is the energy between the nearest islands with the separation of a between magnetic islands. Energy increases from T1 to T4 for a square vertex. However, in a single *pinwheel* vertex the order of energy level is modified such that the T2 configuration is lowest state and the T1 (T4) becomes highest state. Meanwhile, the energy differences between vertices decline sharply. As we know, the dipolar-dipolar interaction is a long-range force. However, the separation between the magnetic islands in our pinwheel ASI specimen (which is 420 nm between nearest islands) are not in the "far-field".

To make a comparison, the vertex energy is also evaluated using micromagnetic simulation (MS) approach based on the Mumax package. This not only takes the magnetostatic energy into account but also the exchange energy. The dimension of the pinwheel vertex is $470 \times 170 \times 10$ nm^3 and the separation between nearest islands is 420 nm. The numerical vertex energy of MS similarly suggests that there are four distinct energy landscapes in both square and pinwheel ASI, as displayed in the MS columns of Table 6.1. The

Table 6.1: Comparison of the vertex energies and energy difference, ΔE (= $E_{highest}$ - E_{lowest}), between square and pinwheel ASI using MC and MS methods where E_{dip} is the total dipolar energy and $D = \mu_0\mu^2/(4\pi a^3)$; μ is the magnetic moment of each nanomagnet and a is the separation between islands.

Geometry	Square ASI		Pinwheel ASI	
Simulation Method	MC (E_{dip}/D)	MS (eV)	MC (E_{dip}/D)	MS (eV)
E_{T1}	-13	163	1	198
E_{T2}	-4	167	-1	199
E_{T3}	0	180	0	198
E_{T4}	21	220	1	197
ΔE	**33**	**57**	**2**	**2**

energy spread in the square vertices (from 163 eV to 220 eV) is much greater than that in pinwheel ASI (from 197 eV to 199 eV). However, the MS simulation predicts that T4 is the ground state for a single pinwheel vertex rather than T2. The energy levels are found to change when slightly varying the parameters of the MS simulation , i.e. island shape, cell size and lattice constant etc. Thus, it is difficult to confirm the ground state of a real pinwheel vertex as a result of the relatively small energy difference. Additionally, the energy difference (ΔE) between the highest ($E_{highest}$) and lowest (E_{lowest}) levels reduces by a factor of around 29 times compared to the square ASI. The pinwheel structure is therefore a nearly degenerated system. Note that the labelling of pinwheel vertex energy level here is consistent with that of the square vertex. However, the nomenclature of pinwheel vertex will be changed (see Fig. 6.3) according to its energy levels in the rest of this chapter which will be discussed in Section 6.2.2.

Note that if one calculates the vertex energy without relaxation in the micromagnetic simulation, the energy levels agree with the MC calculation, in particular, the levels are ordered as $E_{T2} < E_{T3} < E_{T1} = E_{T4}$. The lack of exchange energy in the free-relaxation calculation forces the moment of each nanomagnet to behave exactly as a macrospin. Hence, its vertex energies are similar to those of MC simulation. However, for the pinwheel-geometry case the simplest dipolar energy is no longer dominant since the dipolar interaction between the nearest neighbours NN_1 approaches zero. Moreover, the end states of island has been theoretically proven to play an essential role in inter-island coupling [32,33]. The stadium-shape magnetic islands have the onion magnetisation configuration after relaxing in the simulation. The relaxation process thus gives a more accurate picture of the energy landscape.

6.2.2 Pinwheel vertex classification

The study of pinwheel ASI in this chapter is focused on the field-induced behaviour of the mesoscopic 'domain' and 'domain wall' in terms of vertex net moment. The details of the pinwheel vertex will be detailed in this section. Figure 6.3 (a) illustrates the sixteen possible vertex magnetisation topologies. They can be categorised into four types based on their dipolar energy levels, named as 'Type I', 'Type II', 'Type III', 'Type IV'. Unlike square ASI, a pinwheel ASI array can exist as two sets of interleaved vertices with opposite chiralities. An equivalent group of pinwheel vertex topologies is displayed in Fig. 6.3 (b).

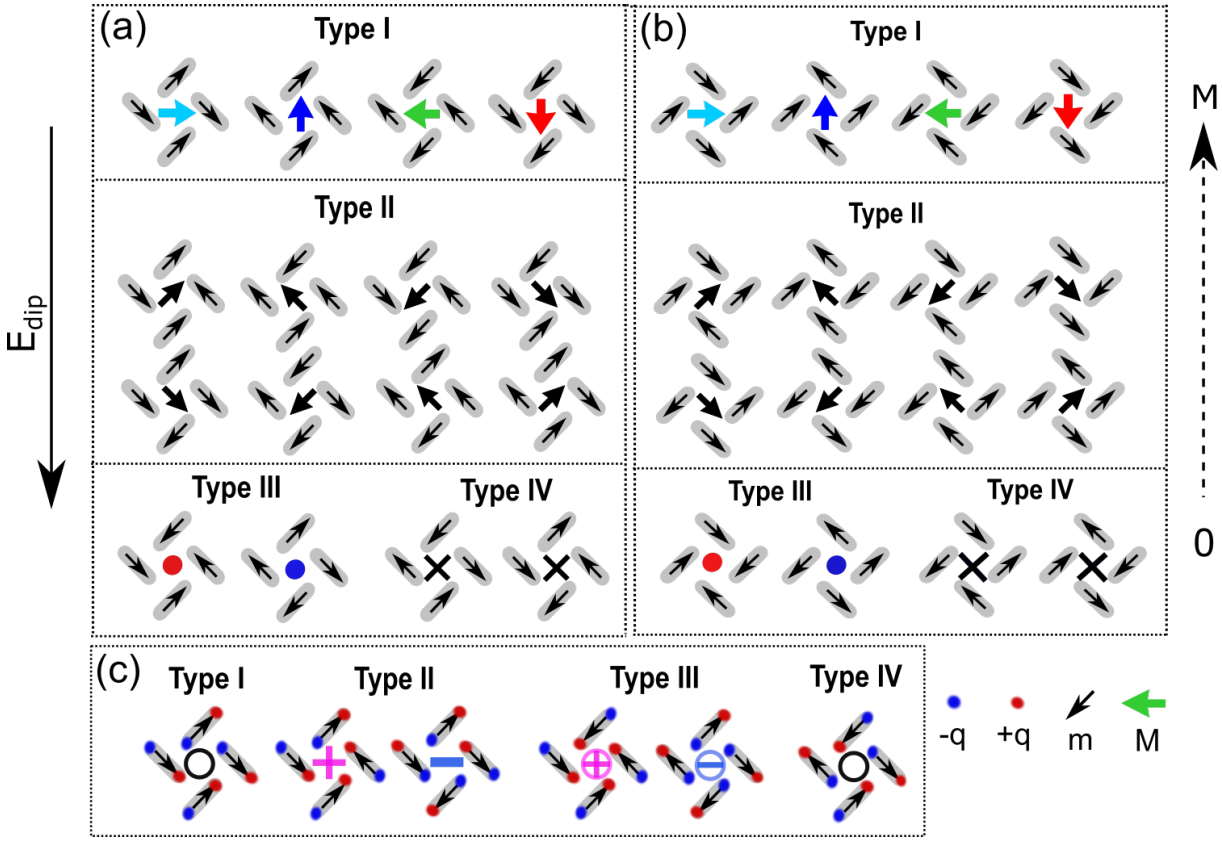

Figure 6.3: (a) The sixteen possible vertex configurations, consisting of four nearest nanomagnets, classified by means of vertex net moment, which decreases from Type I to Type III (Type IV), where the small black arrow in the grey nanomagnet indicates the magnetisation direction of nanomagnet; the larger arrows represent the direction of vertex net moment; the red, blue disks and cross represent the zero-moment vertex. (b) The matching set of configurations for vertices of opposite chirality. From Type I to Type IV the dipolar energy increase (see MC results of the pinwheel vertex in Table 6.1) whereas the net moment decreases from M to 0. (c) Net charge of each vertex is determined by the dipole charges (blue and red points at the both ends of island) of the magnetic element using dumbbell model, where '+/-' shows the two positive/negative net charges, '$\oplus$/$\ominus$' (corresponding to the vertices marked by red/blue disk) for four positive/negative net charges and circle (corresponding to the vertices marked by cross) for neutral vertex.

The vertex net moment is determined by the moment of nanomagnet (m) which is

plotted in Figs. 6.3 (a) and (b). The vertex net charge is calculated by summing the four dipolar magnetic charges which meet up at the central point of pinwheel vertex using the dumbbell model [34]. To be specific, in Type I vertex, the moment of one nanomagnet is aligned parallel with its second-nearest moment. This category of vertex has four degenerate states with the zero magnetic charge and the largest net moment, M. When one of the four magnetic moments flips it will be changed into Type II vertex, leading to one pair of the NN_2 neighbours aligned antiparallel, while the other moment pair still in the parallel alignment. Type II vertex possesses a smaller net moment($\sqrt{2}/2M$) and two net magnetic charge $\pm 2q$ (marked by '+/-' symbol). The full charged ($\pm 4q$, labelled by '$\oplus/\ominus$') vertex, Type III, has no moment as the antiparallel pair moments are cancelled with each other. In the same manner, the Type IV vertex has neither moment nor magnetic charge.

It should be emphasised again that the energy landscapes from the MC and MS simulation differ for the pinwheel vertex. This is presumably associated with two facts: the small spacing between islands at which the magnetic dipole-dipole interaction is not dominant and the inhomogeneous distribution of surface charge at both ends of each nanomagnet does matter. If one increases the separation between islands, the same energy landscape could be attainable which is governed by the dipolar coupling.

6.3 Sample realisation and magnetisation characterisation

The pinwheel ASI specimens were fabricated by Ciaran Ferguson at the University of Glasgow and Sophie A Morley at the University of Leeds. A 10 nm thick $Ni_{80}Fe_{20}$ film was fashioned into pinwheel geometry on an electron-transparent silicon nitride (Si_3N_4) membrane using electron-beam lithography and lift-off metalisation. An example of an in-focus bright-field TEM image is displayed in Fig. 6.4 (a). The lateral dimension of the 10nm thick magnetic nanomagnet under study is 470×170 nm, and the centre-to-centre separation between nearest neighbouring islands is 420 nm. A whole ASI array is formed by two interleaved 25×25 islands subarrays. A subarray (or sublattice) is a group of islands whose long axes are parallel aligned with one another in this pinwheel lattice. In this in-focus image, the darker contrast appearing on the island surface are the coated

carbon. This carbon layer is able to keep the metallic islands from charging during TEM imaging.

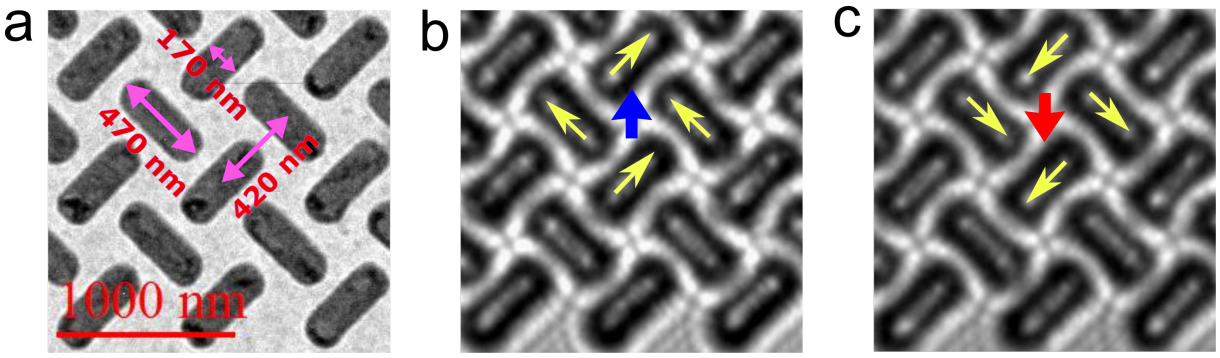

Figure 6.4: (a) In-focus TEM image showing part of pinwheel ASI array. The length and width of each nanomagnet are 470 nm × 170 nm, nearest islands separated by 420 nm. Fresnel images of the same region, magnetised by 0° magnetic fields of +271 Oe (b) and -271 Oe (c), in which the small yellow arrows indicate the magnetic moment identified from the magnetic contrast using Lorentz force, and the large blue (red) arrow displays the direction of vertex magnetisation.

All experimental results in this chapter are from Fresnel imaging. As has already been introduced in Section 3.7.2.2, in Fresnel imaging, the Lorentz force deflection of the electron-beam by the magnetic induction produced in each island creates a darker edge along one side of the long axis, from which the direction of magnetisation can be inferred [35, 36]. Fresnel imaging examples of the pinwheel lattices having opposite states are shown in Figs. 6.4 (b) and (c), where the small and large arrows indicate the magnetisation orientations of each nanomagnet and vertex, respectively. In this section, how to numerically extract the magnetic state of each nanomagnet by processing Fresnel image will be discussed. This process can be realised using cross correlations and convolutions, which can be implemented in any programming language, eg. 'MatLab' and 'Python' etc. This approach has been extensively applied to the pattern recognition in many-body systems, such as our any patterned arrays with repetitive feature.

Figures 6.5 (b) exhibits an averaged profile over 10 scanning lines across the short axis of one nanomagnet of Fig. 6.5 (a). This profile shows the intensity difference between the sides A and B of islands, here the side A reveals the lower intensity than side B. As discussed, this difference is a consequence of the deflection of the electron beam by a single-domain state in the nanomagnet. Ordinarily, electrostatic contrast should not be negligible when the specimen is tilted to a high angle (eg. ±25°). At the high tilted angle, the significant electrostatic contrast attributes to the different paths that electrons

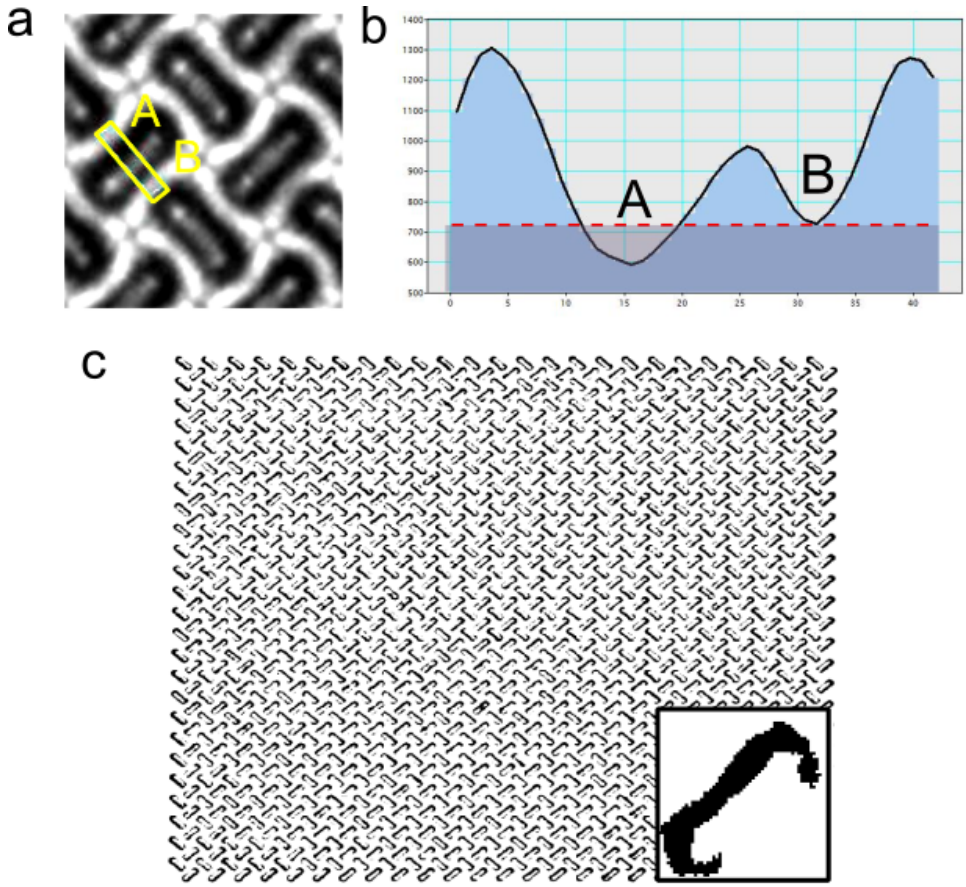

Figure 6.5: (a) A Fresnel image showing magnetic contrast. This contrast arises from the deflection of electron beam by the single-domain field of nanomagnet, in which the letters 'A' and 'B' represent the two long-axis sides. (b) The averaged profile of 10 scan lines across the short axis of one nanomagnet (marked by the yellow box in (a)) compares the intensity difference between the 'A' and 'B' edges and the red dash line is the selected threshold criterion. (c) A binary thresholding image of the pinwheel ASI lattices to segment magnetic feature of each nanomagnet from a gray-scale Fresnel image and the inset is a zoom-in fundamental element exhibiting magnetic contrast.

pass through at edges of the tiled sample. For instance, a darker fringe could be produced along the right (left)-side edge due to the longer cross section on the right (left) edge compared to that on the left (right) edge whilst tilting the thin film in Fig. 3.17 (a) ((c)). However, in our case this effect does not influence the long-axis magnetic contrast of islands if the field is at the low field angle θ (defined in Fig. 6.7 (i)) with respect to the ASI array. The reason is that in the measurement the pinwheel ASI array was tiled around x axis (see Fig. 6.7 (i)) thereby the electrostatic phase merely contributes to the direction aligned with x axis, that is, the short axis of island when $\theta = 0°$, as depicted in Fig. 6.7 (i). Beside, the magnetic field from the objective lens is fixed and only the specimen can be tilted in the sample holder in order to vary the field angle θ upon the

sample. Thus, only if the sample is rotated to 45°, at which the long axes of one subarray will be aligned to the x axis, the electrostatic phase would strongly affect the magnetic edge contrast. From the above, since the contrast difference between the two sides reveals its magnetic behaviour, the image process is able to take advantage of it to extract the magnetic information.

There are two key steps in the LTEM imaging process: extracting magnetic feature of nanomagnet and identify its magnetisation state.

In the first instance, the magnetic contrast can be segmented by applying a threshold criterion. All pixels below thresholding intensity are given the value of 0; all above threshold can then be grouped together and assigned the value of 1. This threshold is determined by the intensity difference between two long axes of one nanomagnet. For example, the red dash line of Fig. 6.5 (b) indicates the threshold intensity that is chosen. Figure 6.5 (c) shows a binary image of an entire array after thresholding.

The second step is to identify the magnetic state of each island and find its relative location in an array. The provided inset in Fig. 6.5 illustrates a perfect diagram of binary magnetic contrast for a single nanomagnet and its magnetic moment is able to be attained by application of the Lorentz force. As a result, this ideal referencing pattern is treated as a fundamental element and used to identify the magnetisation state of every island in an array. The top-left insets of Figs. 6.6 (a) and (b) display two possible reference patterns representing two distinct magnetisation orientations for one sublattice. These binary reference units are used to cross-correlate with every island in the thresholding array of Fig. 6.5 (c). In doing so, the magnetic-contrast state of each island in this subarray can be recognised. The colour-scale Figs. 6.6 (a) and (b) present the results of cross correlation with these two references. They are two location maps and shows the all coordinates of the corresponding reference pattern in its subarray. The lattice positions of these two maps are complementary. By finding all coordinates of the relative locations of these four types of reference patterns in the whole array, four matrices are obtained. Each matrix executes a convolution with its corresponding arrow so as to add this arrow to all locations. An example of nanomagnet magnetisation distribution is shown in Fig. 6.6 (c). Furthermore, Fig. 6.6 (d) is the net vertex moment map of Fig. 6.6 (c) in which the addition of each category of net moment label is implemented via the convolution method as well.

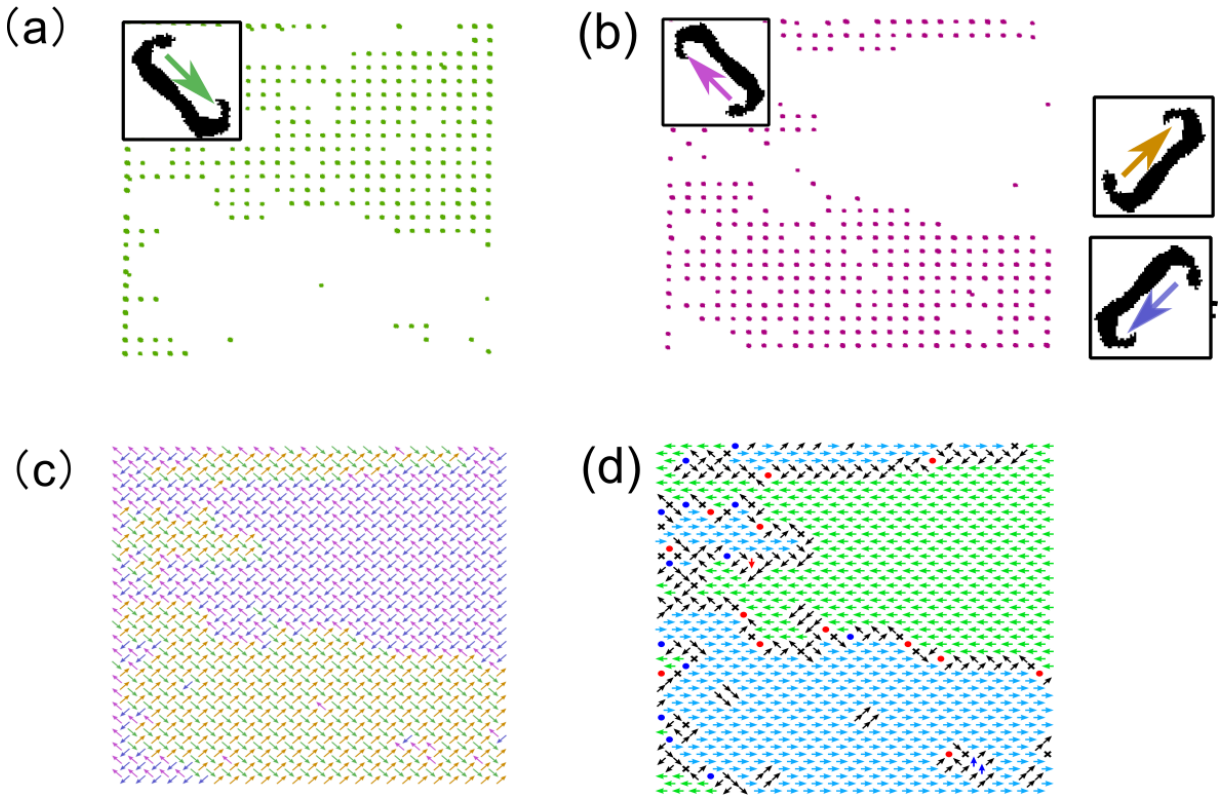

Figure 6.6: (a) (b)The cross-correlation results of the entire ASI array with two possible magnetic-contrast reference pattern (inset at the top-left corner) shows the positions of the corresponding the reference Fresnel patterns. Additionally, there are another two possible magnetic-contrast patterns for the other subarray presented on the right side. The arrow in the magnetic-contrast pattern indicate the direction of magnetic moment in the island. The examples of magnetisation maps about the (c) nanomagnet moments and (d) vertex moments are plotted by the convolution between their relative arrows and the coordinates of their corresponding maximum of the cross-correlation peaks.

This image analysis routine is developed by the collaboration with Gary Paterson and myself at University of Glasgow and it plays an essential role in this chapter. All results and interpretations in this thesis are based on this approach, namely, hysteresis loops, domain patterns, mesoscopic domain wall configurations and demagnetisation results.

6.4 Hysteretic property and domain growth

Once the magnetisation state of each nanomagnet is obtained, the hysteresis loops and domain configurations can be plotted. Note that these analyses, in some sense, resemble a pseudo-Ising like approach. In this section, the LTEM results of hysteresis and domain patterns induced by the field angle will be discussed.

6.4.1 Angular-dependent hysteresis

In the experiments, the in-plane component of the magnetic field was varied by tilting the sample between $\pm 25^\circ$ and $\mp 25^\circ$ in the 700 Oe magnetic field of the objective lens, H_{obj}, while a 10 fps video was recorded by CCD camera to track the evolution of the magnetisation. The videos were then processed to extract the magnetisation of each island. On account of the single-domain state of the island, acting as a macrospin, its magnetic moment, m, is assigned to be '± 1'. The net moment of the array aligned with the direction of field is given by

$$M_{\parallel H} = M_1 \times \cos(45 + \theta) + M_2 \times \cos(45 - \theta) \tag{6.2}$$

where θ is the angle between the applied field and the y axis (see Fig. 6.7 (i)), and total moment of each subarrays is computed by $M_1 = \sum_{i=1}^{625} m_{(1)}$ and $M_2 = \sum_{i=1}^{625} m_{(2)}$ in which $m_{(1)}(m_{(2)}) = \pm 1$ is the moments of each islands in two subarrays and i is the total number of nanomagnets. The normalised magnetisation parallel to field H is plotted, which is given by $M_{\parallel H}/M_S$ where M_S is the maximum of the magnetisation component along the field direction, against the magnetic field at the angle ranging from -6° to 90°, as shown in Fig. 6.7.

Our LTEM result suggests that such pinwheel ASI exhibits the ferromagnetic behaviour. The first of these is the existence of a square hysteresis (also referred to as 'M-H') loop at applied field angles of -6°, 0°, 45° and 90° to the vertical edge (y axis) of the array, as shown in Figs.6.7 (a), (b), (e) and (h). Note that a somewhat similar M-H loop is obtained in square ASI when the field is aligned at 45° to the square edge [37], because the component of the applied field along the easy-axis of islands of each orientation is the same, as it is in the pinwheel ASI at 0°. The square-shape magnetisation curves illustrates that the jump in the magnetisation takes place due to the simultaneous reversals of both subarrays.

With the applied field increasing from 0° to 15° (or from 45° to 75°), the down branch of M-H curve, the field sweeping from positive to negative saturation, is no longer smooth. Instead, a smaller step occurs when the field strength larger than the coercive field. However, the up branch has no second small step, as shown in Fig. 6.7 (c) (or Fig. 6.7 (g)).

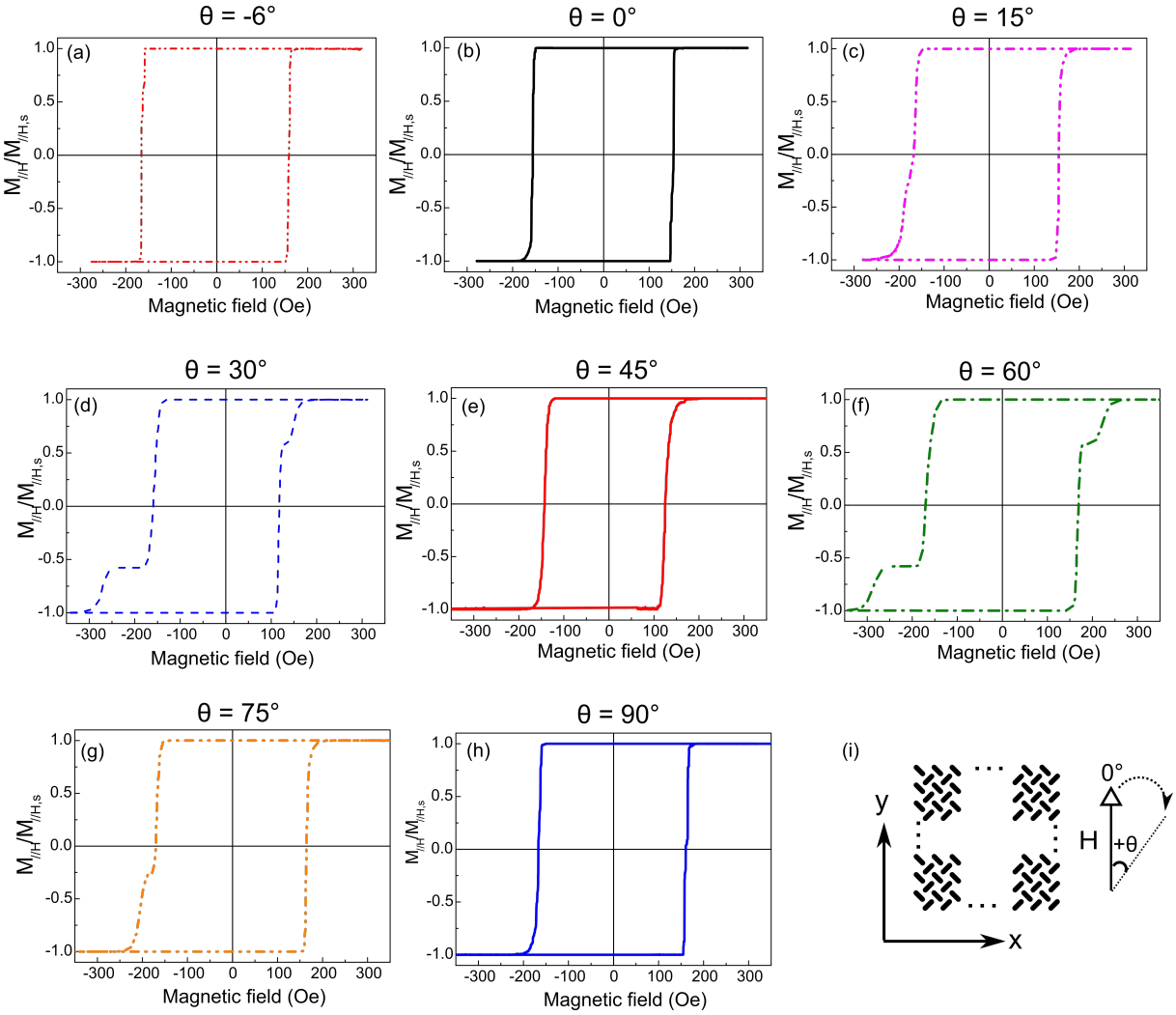

Figure 6.7: Normalised magnetisation curves of the pinwheel ASI magnetised at the external field of (a) −6°, (b) 0°, (c) 15°, (d) 30°, (e) 45°, (f) 60°, (g) 75° and (h) 90° with respect to the vertical edge of ASI array (y axis), M representing the magnetisation aligned to the magnetic field H. (i) The coordinate axes and the field direction with respect to the array are shown in the bottom right. For simplicity, the full array is not shown here; only those islands forming the four corners.

As the angle θ of the applied field increases from 15° to 45° (or from 75° to 90°), the easy axis of one subarray is closely aligned with the direction of the magnetic field, while the hard axis of the other becomes aligned along the field. In this situation, the different field components act on the two sublattices. Those islands whose easy axes are more aligned with the field will reverse first at a smaller field to produce the first step on each branch. Conversely, those islands with hard axes aligned with the field flip for a larger field. Therefore, one subarray switches before the other during a reversal. This gives rise to two-step hysteresis loop. Examples of this behaviour are displayed in Figs.6.7 (d) and (f) at the applied field angles of 30° and 60°. The hard-axis sublattice at a 30° field

requires a greater field ($\approx$ 250 Oe) to switch its moment than that at the 15° field ($\approx$ 190 Oe). As a result, a more distinct two-step magnetisation curve is generated. Interestingly, it was found that hysteresis loops are asymmetric, in other words, there are two steps on the down branch while only one switch occurs on the up branch (see Figs.6.7 (c), (d), (f) and (g)). This difference might be associated with the two possible causes: the first is the possible movement of sample in the TEM rod whilst tilting it to a certain angle; the second is due to the variation and precision in magnetisation configuration between field sweeps.

In short, the simultaneous reversal of both subarray produce a 'square' shape hysteresis loop, whereas the difference in the switching field of two sublattices generates the two-step hysteretic loop. It follows that there must exist some critical field angle at which the hysteresis loop switches from square shape to staircase type. This puzzle will be addressed in Section 6.6.2.

6.4.2 Domain nucleation and reversal regimes

By Fresnel imaging, the magnetisation of each nanomagnet at all points of the M-H curve can be mapped, allowing examination of the evolution of magnetisation of the net array state during a reversal. Fig. 6.8 shows some snapshots of the field-driven evolution of the mesoscopic domain configurations in the vicinity of the coercive field. Each row contains snapshots at the same field angles but at various field strengths. Two representative magnetisation processes are compared, which are exhibited and explored at the field angle of $-6°$, $0°$ and $30°$. Here a mesoscopic 'domain' is defined as a region in which the net moments of the pinwheel vertices point in the same direction. This region is formed by the polarised moments of the Type I vertices. The Type I vertex possesses the largest net moment and zero net charge, which is predicted to be lowest state from the MC calculation.

At low angles of applied field, the reversal starts through a small number of nucleation points, typically located at the edge of the array where the energy is lower, and the growth of new reversed domain occurs mediated by the domain wall propagating perpendicularly to the direction of the field, as shown in Figs.6.8 (a) and (b). Note that the reversal at low angles mimics that observed in the continuous ferromagnets [38], and is somewhat more coherent than that at -6° than at 0°.

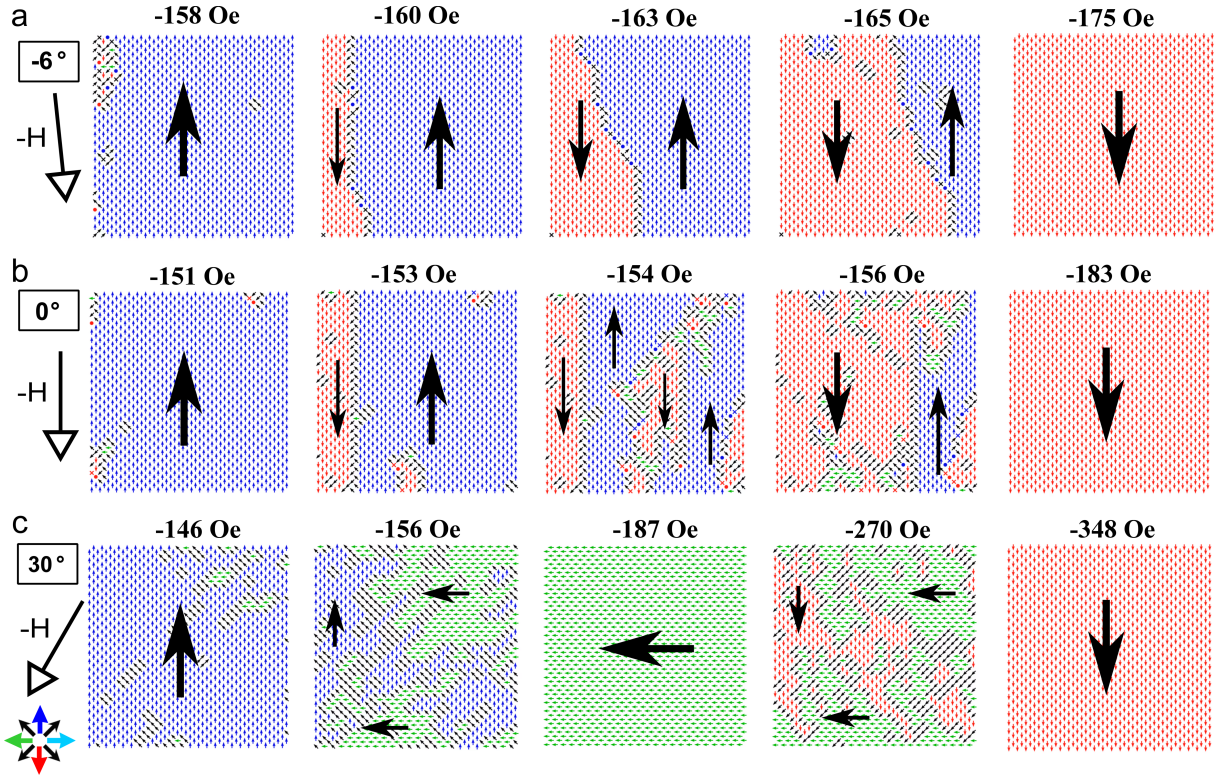

Figure 6.8: Field-induced domain growth and domain wall patterns in an entire ASI array with the applied field of $-6°$ (a), $0°$ (b) and $30°$ (c) on the up loop from positive to negative saturation (contrariwise, referred to as 'down' loop). The arrows in the colour code on the left side indicate the directions of the net moments of the vertices that are formed by four magnetic elements. The large arrows in the images represent the magnetisation orientation of the domains and its thickness of arrow indicate the strength of domain net moment. Further information on the net moment and magnetic charge for all possible domain and domain wall vertex configurations can be found in Figs.6.3 (a) and (b).

Magnetisation reversal at higher angles of applied field (see Fig. 6.8 (c)) is governed by an alternative mechanism. The easy-axis islands are more likely to reverse first since they couple most efficiently through their stray field to nearest-neighbour islands of the same subarray lying collinear with their easy axis. As these islands do not couple strongly to those in adjacent diagonal lines, reversal of the entire array occurs through many nucleation points, creating a more disordered reversal with scattered stripe domains. This reversal regime is termed as 'incoherent'. When one subarray completely switches at -187 Oe magnetic field in Fig. 6.8 (c), the net magnetisation lies perpendicularly to the previous domain state. The switch process then repeats for the other subarray, to complete the reversal. In this type of reversal regime the net moment direction of a reversed domain is always normal to the unreversed region and eventually aligned with the magnetic field.

6.5 Effect of the edge geometries on array anisotropy

Not shown in the M-H loop of Fig. 6.7 is the component of net magnetisation perpendicular to the applied field. Although this component is small at low angles of applied field, it is not negligible and does show an interesting dependence on the applied field angle. This can be more easily seen if both x- and y-components of the net magnetisation present in a polar coordinate. This plot can allow for tracing out the locus of points that go through the loops, as displayed in Figs.6.9 (a-d). In a polar coordinate, the radial-component magnetisation M_r is $M_r = \sqrt{M_x^2 + M_y^2}$, and angular coordinate β is $\beta = \tan^{-1}(M_y/M_x)$, where M_x and M_y are x and y component of the total magnetisation, respectively. Such a graph is able to reveal the orientation and magnitude of the total net moment of ASI array at each field point. It also indicates how M_r and β coordinate with field angle.

At angles of applied field which is far away from 0°, for instance 30°, the plot of Fig. 6.9 (d), a great difference of the applied field angle to two subarrays, which lead to field aligning one sublattice's easy axis and the other's hard axis, results in one subarray to completely reverse before the other one begins. Because of the nanomagnet shape anisotropy leading to a single domain, the island moment has two possible directions along its long axis. As a result, the net magnetisation is constrained to change along 45° lines from, say, pointing north to west and then, when the second subarray reverses, pointing west to south, and so on. Thus, the polar hysteresis loops at high angles of applied field appears as a rotated square.

As the field angle decreases, the spacing between two polar loops narrows (see Fig. 6.9 (a-c)). When the applied field is aligned with the easy anisotropy axes of the arrays, the two branches of the loop will completely overlap. The manifestation being the overlapping lines to and from 90° and 270°. Interestingly, this occurs at a non-zero applied field angle, for our sample approximately $-6°$ with respect to the array edge, as presented in Figs.6.9 (c). It is found that, following the field sweeping path of Fig. 6.7, from positive to negative saturation and then going back to the original position, the reversal of the net moment rotates in the clockwise sense at the field angle of -13 ° (see Fig. 6.9 (a)), which is misaligned toward the left side from the easy axis of -6 °. On the contrary, if the pinwheel lattices are magnetised by a field misaligned toward the right side from this easy anisotropy axis, such as 0 °, the magnetisation will rotate in an anticlockwise sense in Figs.6.9 (c) and (d).

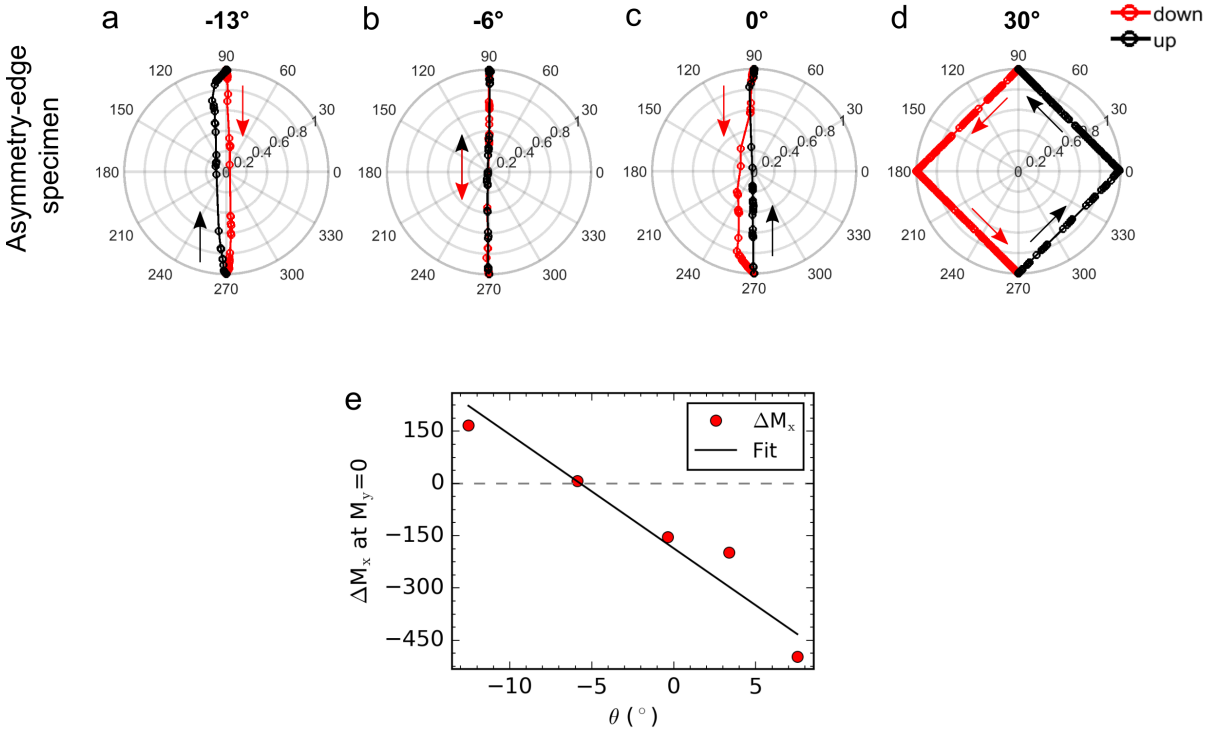

Figure 6.9: Net moment reversal of the entire array with an asymmetric boundary in Fig. 6.7 is transferred into a polar coordinates, with the field aligned at the angle of (a) $-13°$, (b) $-6°$, (c) $0°$ and (d) $30°$ with respect to ASI array. The 'down' (dH/dt<0) and 'up' branches are indicated by the colour (red and black) and the arrows represent magnetisation changing directions. The circle are experimental data and the lines are applied to guide the eyes. (e) The gap ΔM_x (separation between up and down loops) at $M_y = 0$ as a function of the field angle θ for the asymmetric-boundary arrays. The red point represents experimental ΔM_x. In addition, the black line is the fitting results with ΔM_x by orthogonal distance regression, grey dash line shows the small deviation between measurement and calculation. Most importantly, the field angle at which the ΔM_x is zero is predicted to approximately be $-5.7°$ ($\pm 1.4°$) with the asymmetric boundary.

As a measure of the angle between the applied field and array easy anisotropy axes, the width of the hysteresis loop when $M_y = 0$ as a function the field angle can be plotted, shown in Fig. 6.9 (e). Fitting a straight line to this data yields an easy axis of $-5.7°(\pm 1.4°)$) to the vertical line of array edge, the cross point of black solid and grey dash lines.

This peculiar finding is proposed to be a result of the asymmetric array boundary geometry of the ASI array. The 'asymmetric' boundary is shown in Figs.6.10 (a) and (c) and manifest different four array corners. Indeed, Fig. 6.10 (c) shows that there are four islands forming the two different top-left and bottom-right corners, whereas only two islands are at the top-right and bottom-left corners. Furthermore, the shadowed regions in Fig. 6.10 depict the relative arrangement of two subarrays in a whole array. For the

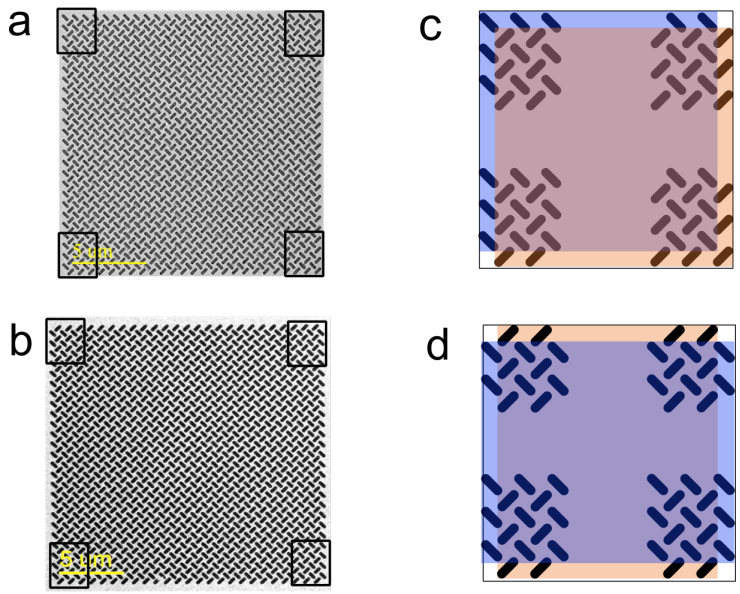

Figure 6.10: In-focus TEM images of the pinwheel ASI with (a) the "asymmetric" and (b) "symmetric" array boundaries. The zoom-in schematics of the four corners for the (c) asymmetric and (d) symmetric boundary are depicted, in which the light blue and orange shadows indicate the two subarray edges and also present how they are relatively arranged in an entire array (marked by black frame) to form the asymmetric or symmetric boundary.

entire array, this asymmetric boundary shift the easy axis by -6° from 0° axis what one might expect for.

So as to prove our conjecture, experimentally, an alternative pinwheel ASI specimen with a symmetric boundary was lithographically fabricated. The in-focus TEM image of such an array is displayed in Fig. 6.10 (b) and shows the array edge geometry. A zoomed image of Fig. 6.10 (d) displays four identical corners composed of two islands. In addition, these two subarrays are arranged symmetrically to form such symmetric edge. Note that the 'symmetric' array each subarray has 25 × 26 islands (or 26 × 25 islands), while there are 25 × 25 nanomagnets in the asymmetric case.

Performing a similar measurement on this symmetric-edge pinwheel array, i.e. varying the field angle from -9° to 8°, the net moment can be plotted in Fig. 6.11. The overlap of reversal lines is found to occur at on the order of magnitude -0.4°. The gap ΔM_x of the polar loop at the $M_y = 0$ versus the field angle θ is plotted in Fig. 6.11 (e). In the same manner, by fitting the measured data using orthogonal distance regression, the array anisotropy axis is estimated to be aligned with the axis of 0.7° (±0.4°). Like the pinwheel array with asymmetric boundary, the symmetric-edge array also exhibits the same behaviour of the rotation of the net moment. A negative misaligned field allows the total net moment of array to rotate clockwise. By contrast, the reversal of net moment

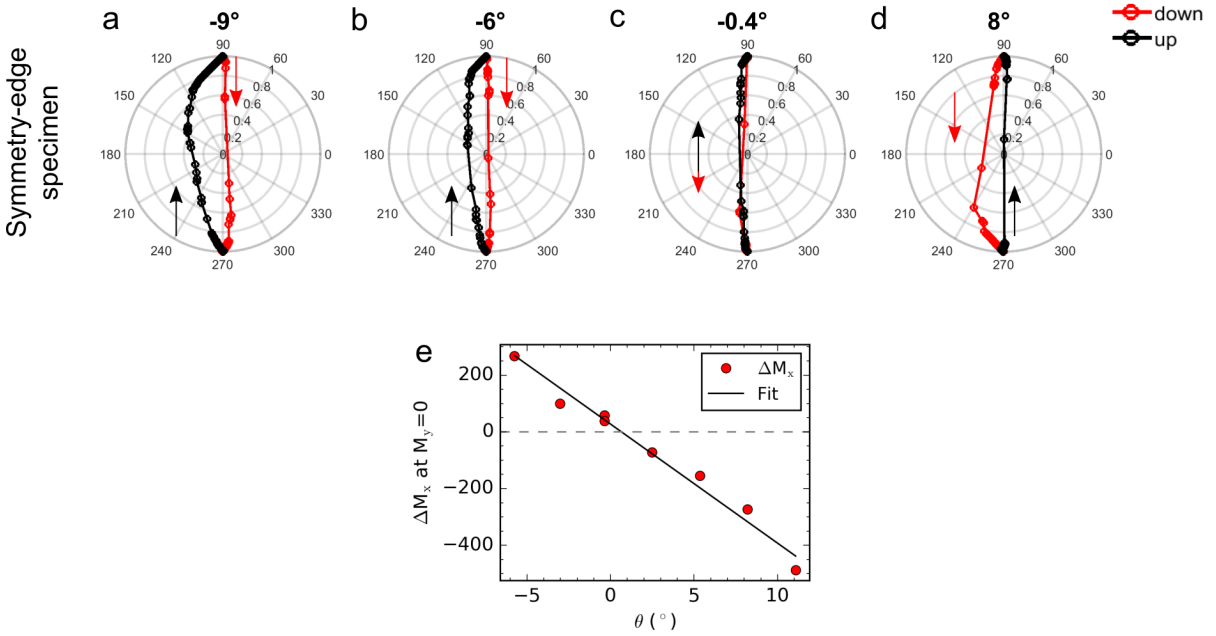

Figure 6.11: The plot of net moment orientation of the entire array with the symmetric boundary in polar coordinates at field angle of $-9°$ (a), $-6°$ (b), $-0.4°$ (c) and $-8°$ (d) with respect to the array. (e) The gap ΔM_x at $M_y = 0$ as a function of the field angle θ for the symmetric-boundary arrays. The field angle at which the ΔM_x is zero is predicted to approximately be $0.7°$ ($\pm 0.4°$) with the symmetric boundary.

is in the anticlockwise sense when the field angle is positive.

6.6 Mesoscopic domain wall topologies

In the domain configurations of Fig. 6.8, some transition regions within a boundary between two adjacent mesoscopic domains were observed. These transitions are defined as the 'domain walls'. In this section some interesting behaviours of different mesoscopic domain-wall topologies taking placing in the pinwheel ASI will be presented and discussed.

6.6.1 Domain wall category and characteristics

Figure 6.3 shows the examples of mesoscopic domain wall in our pinwheel ASI. Each wall consists of the arrangements of Type II, III and IV vertices. Considering all possible magnetisation arrangements, there are seven classes of domain walls. Their schematic are provided in columns of Figs. 6.12 (a-g), where the top row shows one possible magnetisation configuration for each nanomagnet; the middle row represents the magnetisation for each pinwheel vertex; the bottom row displays the vertex charge. Note that the charge of

the vertex is determined using the dumbbell model [34], as explained in Fig. 6.3 (c). The symbol of '+/-' represents the Type II vertex with two positive/negative magnetic net charges; '⊕' indicates the Type III vertices possessing four positive charges, and a black circle represents the uncharged Type IV vertices. The wall which contains four negative charges is labelled by '⊖' in Fig. 6.13.

Each class of domain wall has other possibilities of arrangement of magnetisation configurations. The number of all possible wall topologies is indicated in the third row of Table 6.2 and other possible configurations are given in Fig. 6.13. These seven domain walls can be categorised into 180° or 90° domain walls by the angle between magnetisation orientations of the adjacent domains. All walls can be further categorised by the alignment of the adjacent domains (either antiparallel, head to head (HH), tail to tail (TT), head-to-tail (HT) and vice versa) and by the net charge and moment of their constituent vertices, as summarised in the remaining rows of Table 6.2.

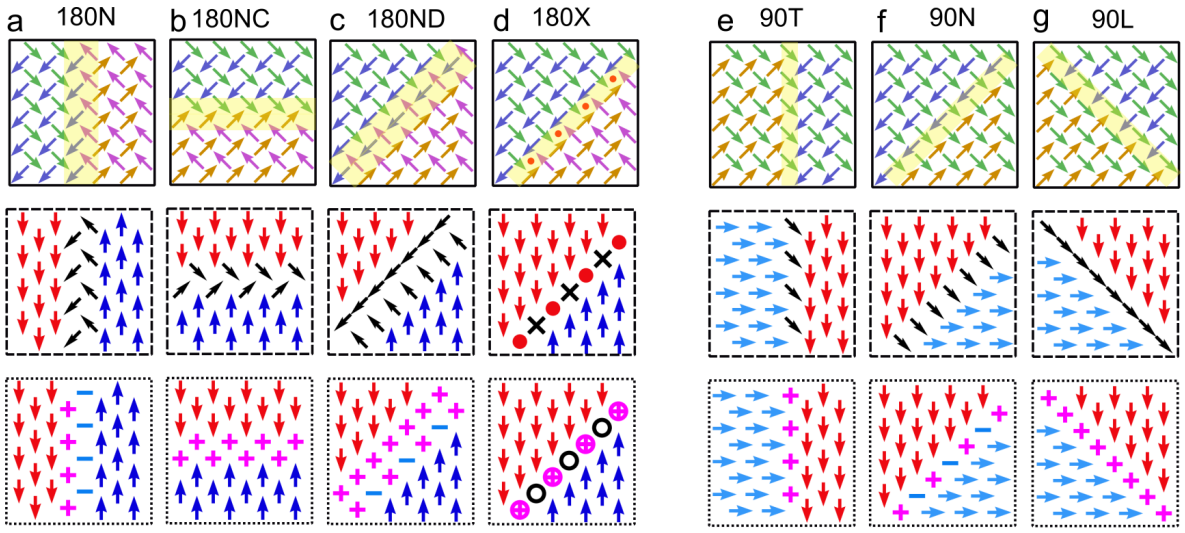

Figure 6.12: Schematic examples of the possible 180° DW configurations in the pinwheel ASI containing four categories of domain wall (DW): '180N' (a), '180NC' (b), '180ND' (c) and '180X' (d). **e-g** Schematics of possible 90° DW configurations consisting of three types: '90T' (e), '90N' (f) and '90L' (g). The smaller arrows of the configuration at the top, framed by the black solid box, represent the magnetic moments of the ASI elements and wall boundaries are highlighted by the yellow. The larger arrows in the middle and bottom row images indicate the vertex moments of the domains and walls. Type II and Type III vertices carry net charges but no moment, in contrast, the uncharged Type I has a net moment. The bottom images (the dotted frames) shows the net-charge distributions of the DWs, where the '+/-' signs reveal the net magnetic charges of Type II vertices with ±2q, the '⊕/⊖'symbols indicate the charged Type III vertices with ±4q and the open black circles represents the zero-charge Type IV vertices. The net charge of each vertex is determined by the dipole magnetic charges of the island using dumbbell model (see Fig. 6.2.1 c).

All walls are denoted in the pinwheel ASI by the angle between adjacent domains followed by the minimum number (one or two) of letters denoting the wall type. For the 180° walls (Figs.6.12 (a-d)), the walls call Néel ('N'), charged Néel ('NC'), diagonal Néel ('ND') and cross-tie wall ('X'). In the "Néel" wall, the net vertex moments exhibit a Néel-like rotation as one passes through the wall. In this sense, the 180N walls are analogues of a classical Néel wall [39, 40]. Like a classic Néel wall, the 180N wall is uncharged. The 180X wall resemble a cross-tie wall [41] formed by alternating Type III and Type IV vertices, which always appears in pairs. To the best of our knowledge, the remaining 180NC and 180ND walls are analogues of the charged wall in ferroelectric materials [42] and ferromagnetic nanowires [43]. By inspection of the configurations of the 180ND and 180X walls, it can be seen that the latter can be converted to the former by reversal of one line of a subarray thereby retaining the net charge, albeit redistributed over twice the width, and creating a net moment.

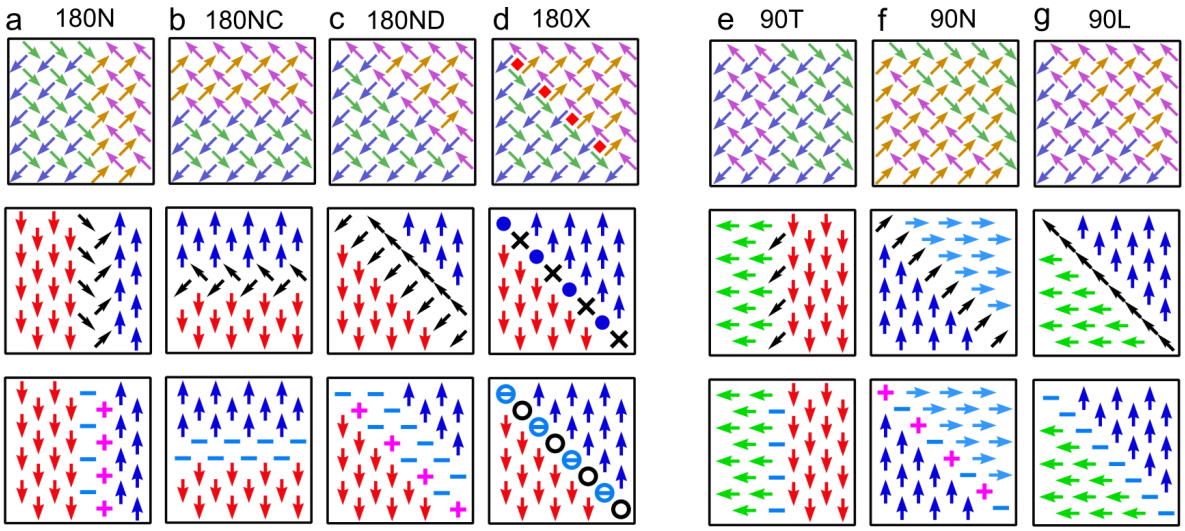

Figure 6.13: Schematic examples of possible 180° DW configurations, with negative charged domain wall, in the pinwheel ASI containing four categories: '180N' DW (a), '180NC' DW (b), '180ND' DW (c) and '180X' DW (d). (e-g) Schematics of possible 90° DW configurations consisting of three types: '90T' DW (e), '90N' DW (f) and '90L' DW (g).

90° walls (Figs. 6.12 e-g) separate magnetic domains in which the magnetisation directions are at right angles. These walls also exhibit Néel-rotation behaviour. These are denoted as '90T', '90N' and '90L', where the letters 'T' and 'L' represents the magnetisation alignment of the adjacent domains. As before, the 90N wall is analogous to a classical Néel wall and possesses no net charge. As for 180° wall, the charged 90° Néel walls is produced due to the energetically unfavourable head-to-head (see Fig. 6.12g) or

Table 6.2: A summary of domain wall features regarding to magnetic moment and charge, in which 'HH', 'TT', 'HT' and 'TH' are short for 'head-to-head', 'tail-to-tail', 'head-to-tail' and 'tail-to-tail', and wall 'Unit' defined in Section6.6.2

Nomination	180N	180NC	180ND	180X	90T	90N	90L
Type	180°DW				90°DW		
Configurations	4	4	4	8	8	4	4
Domains align	Antiparallel	HH (TT)	HH (TT)	HH (TT)	'T'shape	HT(TH)	HH (TT)
Unit net charge	0	+2q(-2q)	+2q(-2q)	+2q(-2q)	2q/-2q	0	+2q(-2q)
Unit net moment	2M	2M	2M	0	M	M	M

tail-to-tail (see Fig. 6.13g) alignment.

At the level of individual islands, the main difference between the formations of 180° and 90° walls arises from the distinct moment reversals of the two subarrays, as illustrated by the top row images of Figs.6.12 (a-g). When one goes through the domain wall of a 180°, the spins in both lattices reverse simultaneously, whereas for a 90° wall, only one subarray flips. This fact can be used to map the transition between the ferromagnetic magnetisation of pinwheel ASI at low angles of applied field to the other regime of incoherent reversal with higher angles of applied field. As one subarray becomes more aligned with the field, the other nevertheless is perpendicular to the field, one expects a transition from 180° to 90° walls.

The charge ordering of walls (see the "Unit net moment" row in Table 6.2) is found that it is dependent on the magnetisation orientation of the adjacent domains. The bottom panels of Fig. 6.12 a-g present the charge distribution of vertices within the wall boundary. Neutral walls occur in both 180N and 90N walls. The magnetisation states of their neighbouring domains are energetically favourable states with the antiparallel and head-to-tail alignment. Both walls resemble the behaviour of the magnetic charge in the 180° or 90° Néel walls of continuous film. Moreover, 180NC, 180ND, 180X, 90T are charged walls which carry the net magnetic charges. The occurrence of charged walls is always in the case in which the adjacent domains meet head on (tail on). As is well known, the head-to-head (tail-to-tail) alignment is energetically unfavourable. It is found that the positive (negative)-charge wall is created within the boundary with the neighbouring domains aligned head-to-head (tail-to-tail), as shown in the bottom row of Fig. 6.12 (Fig. 6.13). This peculiar property of specific charge ordering in pinwheel ASI is a direct result of the high anisotropy within a system of discrete magnetisation.

6.6.2 Role of domain wall

Seven types of domain-wall topologies were observed experimentally. The population of the domain wall with the field angle is able to be quantitatively analysed by counting the corresponding domain wall unit statistics. Only the number of vertices to create these domain walls that are Type II, Type III and Type IV is counted. In this way all the reversed regions would also be included, some of which however do not belong to the mesoscopic domain wall defined here. Additionally, by counting the pinwheel vertex it is unlikely to distinguish the population of seven categories of walls. For example, the both 180N and 90N walls are composed of Type III vertices. Therefore, instead of using vertex, the 'domain-wall unit', the smallest cluster of spins, is proposed and utilised as unit from which to count. Figure 6.14 displays one example of possible wall units, this cluster of macrospins forming the neighbouring domains and domain wall. Such a method allows us to obtain unique statistic population related to the specific wall type. Note that the 180ND, 90N, 90T and 90L units are weighted twice the amount of other units as not only treat these cluster as the domain wall in which there are at least two units but also the two adjacent units could reduce the likelihood of misidentification of the wall.

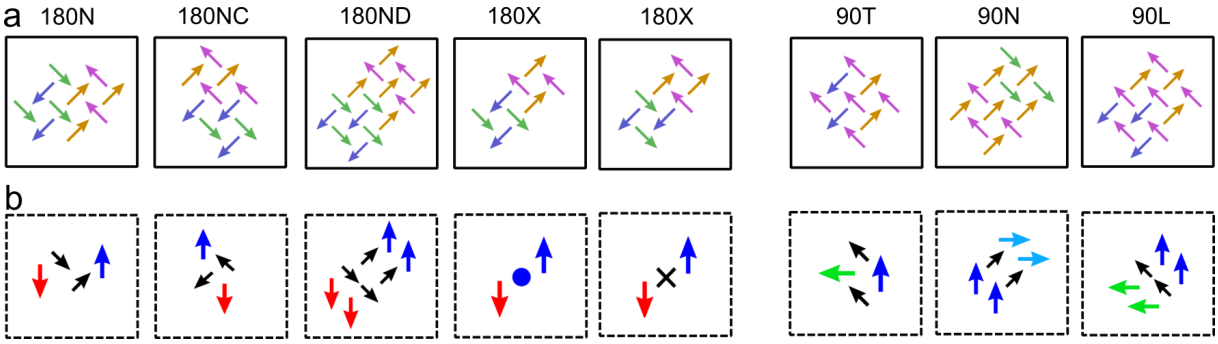

Figure 6.14: Examples of domain wall units in terms of (a) nanomagnet and (b) vertex magnetisation topologies for the different magnetisation configurations. Other possible DW units exist but, for brevity, are not shown here. The 180ND, 90N, 90T and 90L units are weighted twice the amount of other units.

The domain wall populations were first calculated by counting the number times a domain wall 'unit' at each applied field strength, and then summing across all applied field strengths to obtain the total for each full M-H loop in Fig. 6.7. Figure 6.15 shows the normalised populations of all 180° and 90° domain walls as a function of applied field angle between -8° and 90°. Normalised domain-wall populations are given by means of the summing the populations of 180° (90°) wall at each angle point divided by the maximum

population of 180° (90°) among all field angle points. The max population in both 180° and 90° walls is not used as the population of 90N wall always have a relatively large domain-wall population which stems from its formation only requires two macrospins to reverse. Thus, a low fraction of 180° wall population would be obtained, but this would not significantly reflect and compare the changes of two types of wall topologies. Figure 6.15 reveals that the domain wall populations switch from being exclusively dominated by 180° walls to 90° walls for incoherent magnetisation processes, as indicated by the shaded background. In other words, the 180° wall is dominant at the low-angle field, but is suppressed at high field angle.

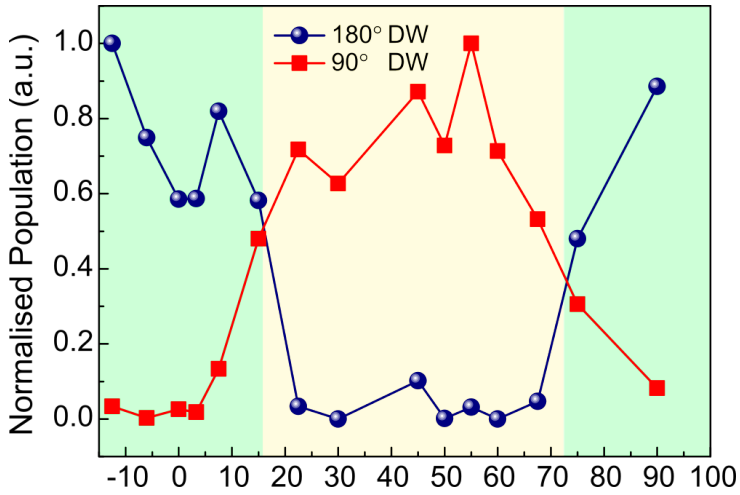

Figure 6.15: Normalised population of 180° and 90° DWs as a function of field angle θ from $\approx$ 12° to 90°, showing the critical angles of $\approx$ 16° and $\approx$ 73° marking the transition between the two magnetisation processes; ferromagnetic (green background) and incoherent (yellow background).

Crossover points between the two regimes take place at approximately 16° and 73°, and is a measure of the easy axis of the pinwheel-lattice array. Interestingly, both curves are almost centred at 45° but have a cycle of larger than 90° (see Fig. 6.15), consistent with the easy anisotropy axes being misaligned to the array axes. As presented in Section 6.4, two types of hysteresis loops were observed, square and two-step curves, which depend on the field angle. There exists a critical angle separating two regimes. This graph suggests that such transition is likely to occur in the vicinity of these crossover points.

The histogram of the summed population of the seven categories of walls is plotted at the same applied field angles used in the polar hysteresis plots of -13°, -6°, 0° and 30° in Fig. 6.16 (a-d) in order to illustrate how the wall populations evolves as the field angle changes. At -6° field, the apparent anisotropy axis of the array, the antiparallel Néel wall (180N) and the cross-tie (180X) walls dominate all others, as one would expect

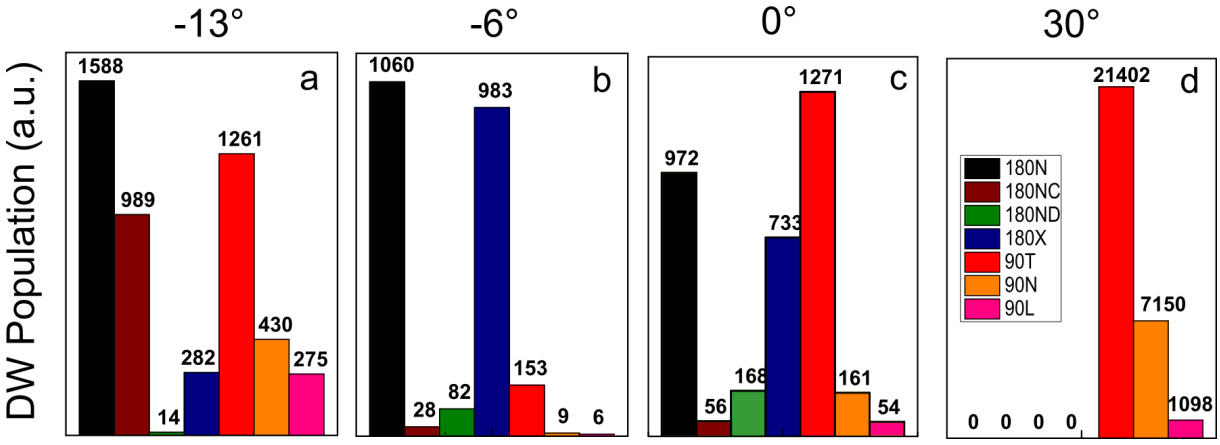

Figure 6.16: (a-d) Domain wall population histograms for the seven domain wall classes discussed in the main text, at the indicated applied field angles of -13°, -6°, 0° and 30° matching those used in the polar magnetisation loops. The number above each column indicates the amount of domain wall units.

of domain propagation perpendicular to the applied field as occurs in a ferromagnet. By 30°, while all 180° walls are excluded and there is a mix of 90T, 90N, and 90L walls, in decreasing numbers. These relative populations may be indicative of the domain wall energies. At -13° and 0° field angle the population distribution has a similarly matched number between 180° and 90°.

Furthermore, if one compares the two wall topologies in panels (a) of Figs. 6.12 and Figs.6.13, they show that two possible wall states, pointing in opposite directions, which results from the opposite magnetisation states of macrospins in the same column. The 180N wall should in principle have four possible topologies, as indicated in Fig. 6.17. It is likely to see all of them in a experiment during a magnetisation reversal. All of them were observed in the experiment. For example, the image of mesoscopic domain patterns in Fig. 6.8 (b) at the field angle of 0° shows different 180N wall configurations.

What determines which type of 180N wall froms during a reversal? The wall population of these four types of 180N walls is computed via counting their corresponding wall units, and then the population fraction is estimated compared to the total population of 180N. The field angle was set at 0° and to ensure the accuracy of the experimental results, the measurements were repeated four times, most importantly, at different times. The resulting population fractions are listed in Table 6.3 and they are in agreement in four experiments. The 180N I is always the dominant wall configuration. The 180N IV is the second largest population, except for the second measurement, in which the amount of 180N III become a little bit more (>1%). The structure of 180N II is absent for the 0°

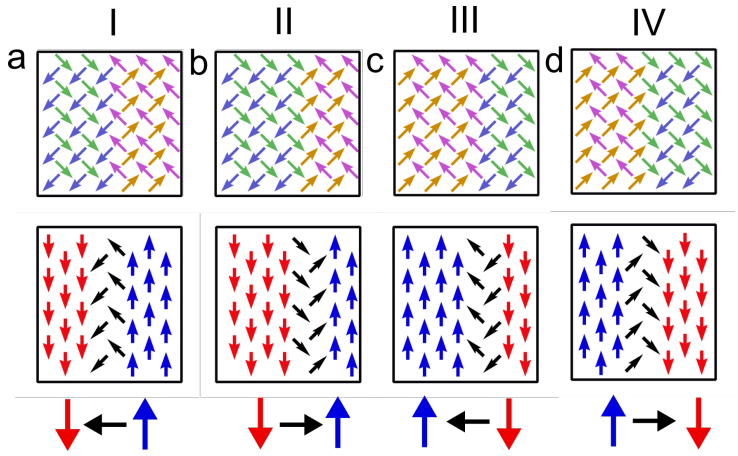

Figure 6.17: Four possible examples of the 180N wall topologies, referred to as 'I', 'II', 'III' and 'IV'. The images from the top to bottom are magnetisation configurations of the nanomagnet, the net moment and the schematic description.

Table 6.3: The comparison of the population fraction among four types of 180N wall configurations at the 0° magnetic field in the four times repeated measurements.

Measurements	180N I	180N II	180N III	180N IV
1^{st}	66%	1%	1%	31%
2^{nd}	89%	0	6%	5%
3^{rd}	58%	0	13%	29%
4^{th}	61%	0	9%	29%

field during the measurements. By inspection of the walls of 180N I and IV, they have a same feature, the net moment always discretely rotate from the north to south, in other words, the magnetisation direction of wall points to the adjacent domain whose moment direction is downward. This unique direction of the rotation of the Néel wall could suggest that this 180N wall formation mimics somehow the chiral-wall behaviour [44].

Three factors could be considered to cause this results: the misaligned field, artefacts of sample fabrication and the chirality of array. Firstly, the effect from the misaligned field can be excluded as the same energetic preference of 180N wall occurred with the -6° field. Secondly, this could suggest that in this case the formation of 180N wall configuration appears a preference. Thirdly, the areas of nanomagnets have been calculated in a part of array (about 170 islands for each subarray) and results are almost the same thereby this preference is not relative to the factor of imperfection of fabrication. Finally, as mentioned in Figs. 6.1 and 6.3, there are two categories of pinwheel vertex presenting two opposite chiralities structure. Meanwhile, Figures 6.10 (a) and (c) show the rotating direction of nanomagnets of our present pinwheel ASI specimen in the anticlockwise sense, as depicted

in Figs. 6.1 (c) and (d). This problem could be tested by a measure of the sample having the opposite chirality and this will be the further work.

6.7 Demagnetisation protocol for the pinwheel ASI

It has proven impossible to realise a global ground state consisting of twofold 'two-in-two-out' vertices in square ASI using field-driven demagnetisation. Up to now a number of demagnetisation protocols have been conducted and aimed to attain the ground state of artificial spin ice. They can be basically classified into two methods: athermal (AC-field rotation) demagnetisation [2, 5, 45–48] and thermal demagnetisation [13, 16, 49] protocols. The rotational field-induced demagnetisation create the local ground state, i.e. a preponderance of two lowest-energy vertices but mixed in other higher energy vertices [2]. On the contrary, the long-range ground state of artificial spin ice is achievable through thermal demagnetisation, where driven-temperature increases above the blocking temperatures, and then decreases to room temperature at a constant cooling rate [49]. It is also possible to create a long-range ground state at room temperature for *thin* spin-ice arrays over relatively long relaxation time (a few hours) [13].

In the demagnetisation protocol carried out here, a rotational-field demagnetisation approach was employed. This protocol was performed instead of the thermal relaxation as the pinwheel ASI specimen is too thick to anneal at room temperature or attainable temperature range in our TEM holder (from $-170\,^{\circ}\mathrm{C}$ to $250\,^{\circ}\mathrm{C}$). The demagnetising result reveals a short-range ground state obtained using the AC demagnetising protocol.

6.7.1 Experimental set-up

The pinwheel ASI specimen, the same one used in Section 6.3, is subjected to a demagnetisation process by an assembly of the sample-rotation platform and an AC magnetic field that varies its magnitude and direction as a function of time. This experiment set-up is shown in Fig. 6.18. In addition, another demagnetisation protocol has been examined in which the sample is held still and an AC magnetic field was applied. Nevertheless, the demagnetising effect is not good as the observed magnetisation of array is similar to that before demagnetising.

The pinwheel ASI specimen was initially saturated by an applied field. It was then

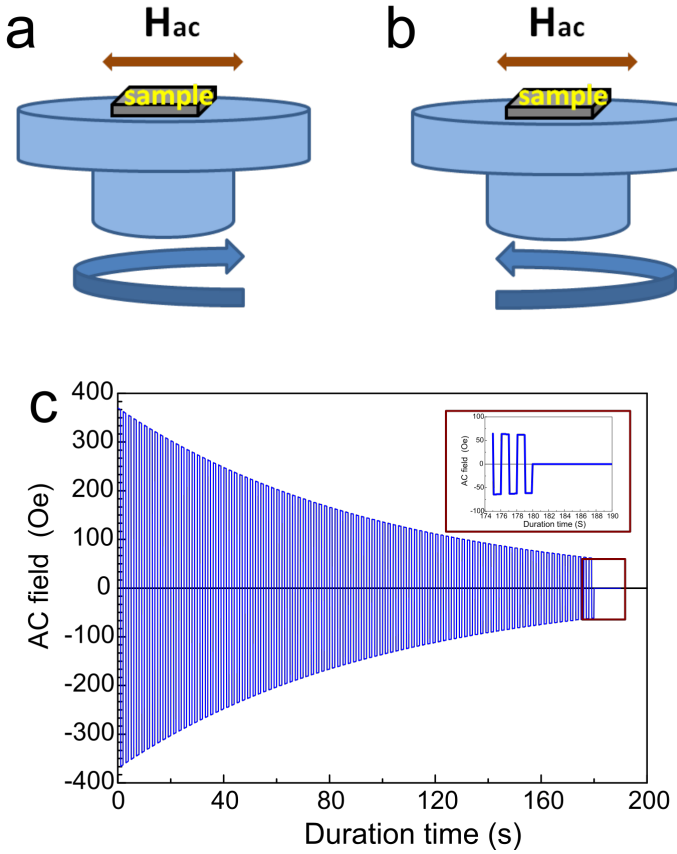

Figure 6.18: The diagram of experimental set-up for the AC field demagnetisation protocol with the (a) clockwise (R1) and (b) anticlockwise sample rotation. (c) The variation of AC field as function of the time. The inset is a zoom-in graph to explicitly show the ac field patterns.

placed on a rotational platform of micro step motor (see Figs.6.18 (a) and (b)) at a 12 rpm rotational speed, actuated by a microcontroller, 'Arduino'. Meanwhile, they were rotated within an AC magnetic field which was induced by a time-varying current in copper coils and could also be controlled by a LabView script. This applied field started from larger saturation field (≈370 Oe) and its strength decreased exponentially over time and, ultimately, to 0 Oe field, as emphasised in the inset of Fig. 6.18 (c). The key step is that the pinwheel ASI were magnetised in the neighbourhood of coercive field for a relatively long time. The final state after demagnetisation was imaged in TEM in which the stray field from the objective was set to approximately 0 Oe. Note that two rotational directions, in the clockwise (D1) and anticlockwise (D2) senses, were performed in the measurement so as to test how the rotational orientation influences on the geometry pinwheel ASI vertex which has two potentially chiral shapes.

6.7.2 Demagnetisation results

Figure 6.19 displays the magnetisation configurations of each nanomagnet (a-c) and vertex (d-f) of an entire array before and after the D1/D2 demagnetising processes. Prior to demagnetisation, the pinwheel ASI array was fully saturated with the polarised states, as shown in panels of Fig. 6.19 (a) and (d). After undergoing the protocol, the multidomains, separated by mesoscopic domain walls, are formed with various magnetisation directions. There are also the increasing number of Type III and Type IV vertices (red and blue disks) in Figs. 6.19 (e) and (f). The D1 and D2 demagnetisation protocols, differing only in the rotational orientations of the sample, gives rise to different domain patterns.

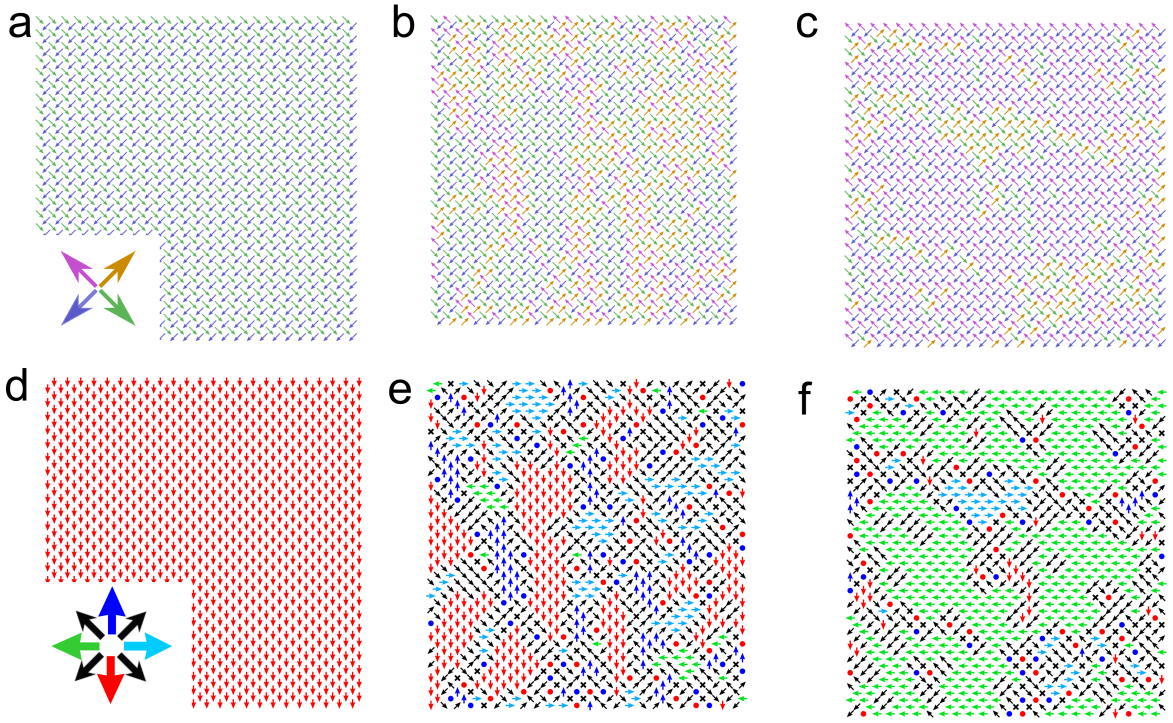

Figure 6.19: The magnetisation configurations of the (a-c) nanomagnets and (d-f) vertices (a, d) before and after (b, e) D1 and (c, f) D2 demagnetisation protocols. The colour codes represents the magnetisation directions of the colour arrows.

Moreover, the fractional population of vertices are also computed and plotted by a bar chart in Fig. 6.20. Before the demagnetising the polarised ASI array is formed by just Type I vertex. The D1 demagnetisation protocol attains to anneal the sample and lead to an increase in other types of pinwheel vertices: 51% vertices Type I, 35% Type II, 7% Type III and 7% Type IV. Undergoing the D2 protocol the demagnetised consequence is constituted by 43% Type I, 42% Type II, 8% Type III and 7% Type IV. Somewhat interestingly, the populations of Type I and Type II are nearly equivalent, and a similar

pattern for Type III and Type IV vertices as well. In fact, this trend is also observed in Section 6.4.2 and shown in Fig. 6.12 d, that is the Type III and Type IV vertices always appear in pair to tilt 180X wall so that implies the similar fractional populations. Additionally, the chirality of the vertex has not been observed in these demagnetisation experiments. The fractional populations of four categories of Type III vertice are almost consistent, approximately 2% over all vertex population.

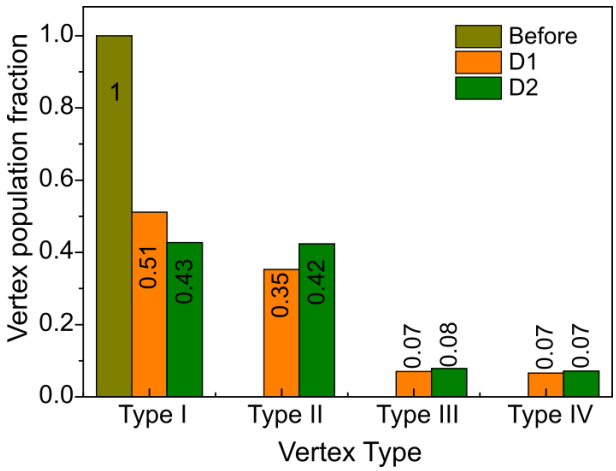

Figure 6.20: Comparison of histogram of vertex population fraction through the before, after D1 and D2 demagnetisation protocols.

As predicted by Monte Carlo simulation (in Section 6.2.1), the long-range ground state of pinwheel array should be tilted by the lowest-energy Type I vertices. The further Monte Carlo simulation indeed suggests a global flux "closure" structure occurring in a **square**-shape array, where four categories of Type II topologies forming the four head-to-tail aligned domains so that the total energy is minimised via the reduction of surface charges [50]. This behaviour is analogous to the emergence of the ground state in continuous ferromagnetic materials, for instance, a rectangular Permalloy film [51]. Though this demagnetising protocol does not lead to a 'global' flux closure structure, the number of the vortex (Type III) and antivortex (Type IV) indeed equally grow. These 'local' defects are responsible for the formation of domain-wall boundaries to separate the random fourfold domains. Responding to the rotational field demagnetisation, the pinwheel ASI lattice generate a short-range ground state, a mix existence of four distinct vertex typologies, which may account for the somewhat near-degenerate vertex energy landscape and nonequilibrium dynamics in a frustrated system.

6.8 Conclusions

To sum up, in this chapter, a simple modification of a square ASI by rotating each island 45° around its centre is able create a system with the nearly-degenerated energy levels. This geometry behaves as a synthetic ferromagnet through the domain nucleation and growth mediated by domain wall propagation. Domain wall topologies, such as Néel and cross-tie walls, were observed resembling those seen in natural ferromagnetic film. In addition, new domain walls also exist in this artificial patterned system. These walls emerge with well-defined charge ordering. Interestingly, the easy axes of the array appear to be misaligned with the array geometry. This is speculated as a result of array boundary effect. So far there are no results published which show the observation of a detailed magnetisation structure within the Néel wall. This synthetic patterned array nevertheless is able to indicate a distinct magnetisation arrangement within the wall. Furthermore, a method has been developed to quantitatively analyse the magnetic contrast from Fresnel images. Finally, a demagnetisation protocol was conducted using a rotational external magnetic field and the short-range ground state was achieved.

Bibliography

[1] J P Morgan, A Stein, S Langridge, and C H Marrows. Thermal ground-state ordering and elementary excitations in artificial magnetic square ice. *Nature Physics*, 7(1):75, 2011.

[2] R F Wang, C Nisoli, R S Freitas, J Li, W McConville, B J Cooley, M S Lund, N Samarth, C Leighton, V H Crespi, et al. Artificial 'spin ice' in a geometrically frustrated lattice of nanoscale ferromagnetic islands. *Nature*, 439(7074):303, 2006.

[3] A Schumann, B Sothmann, P Szary, and H Zabel. Charge ordering of magnetic dipoles in artificial honeycomb patterns. *Applied Physics Letters*, 97:022509, 2010.

[4] K Zeissler, M Chadha, E Lovell, L F Cohen, and W R Branford. Low temperature and high field regimes of connected kagome artificial spin ice: the role of domain wall topology. *Scientific Reports*, 6:30218, 2016.

[5] J Li, X Ke, S Zhang, D Garand, C Nisoli, P Lammert, V H Crespi, and P Schiffer. Comparing artificial frustrated magnets by tuning the symmetry of nanoscale permalloy arrays. *Physical Review B*, 81(9):092406, 2010.

[6] C Nisoli, J Li, X L Ke, D Garand, P Schiffer, and V H Crespi. Effective temperature in an interacting vertex system: Theory and experiment on artificial spin ice. *Physical Review Letters*, 105:047205, 2010.

[7] S Zhang, J Li, I Gilbert, J Bartell, M J Erickson, Y Pan, P E Lammert, C Nisoli, K K Kohli, R Misra, V H Crespi, N Samarth, C Leighton, and P Schiffer. Perpendicular magnetization and generic realization of the Ising model in artificial spin ice. *Physical Review Letters*, 109:087201, 2012.

[8] Y-L Wang, Z-L Xiao, A Snezhko, J Xu, L E Ocola, R Divan, J E Pearson, G W Crabtree, and W-K Kwok. Rewritable artificial magnetic charge ice. *Science*, 352(6288):962, 2016.

[9] I Gilbert, G-W Chern, S Zhang, L O'Brien, B Fore, C Nisoli, and P Schiffer. Emergent ice rule and magnetic charge screening from vertex frustration in artificial spin ice. *Nature Physics*, 10(9):670, 2014.

[10] S Zhang, I Gilbert, C Nisoli, G-W Chern, M J Erickson, L O'Brien, C Leighton, P E Lammert, V H Crespi, and P Schiffer. Crystallites of magnetic charges in artificial spin ice. *Nature*, 500:553–557, 2013.

[11] E Mengotti, L J Heyderman, A Fraile Rodríguez, A Bisig, L Le Guyader, F Nolting, and H B Braun. Building blocks of an artificial kagome spin ice: Photoemission electron microscopy of arrays of ferromagnetic islands. *Physical Review B*, 78:144402, 2008.

[12] I Gilbert, Y Y Lao, I Carrasquillo, L O'Brien, J D Watts, M Manno, C Leighton, A Scholl, C Nisoli, and P Schiffer. Emergent reduced dimensionality by vertex frustration in artificial spin ice. *Nature Physics*, 12:162–165, 2016.

[13] A Farhan, P M Derlet, A Kleibert, A Balan, R V Chopdekar, M Wyss, J Perron, A Scholl, F Nolting, and L . Heyderman. Direct observation of thermal relaxation in artificial spin ice. *Physical Review Letters*, 111:057204, 2013.

[14] R V Hügli, G Duff, B O'Conchuir, E Mengotti, A F Rodríguez, F N, L J Heyderman, and H B Braun. Artificial kagome spin ice: dimensional reduction, avalanche control and emergent magnetic monopoles. *Philosophical Transactions. Series A, Mathematical, Physical, and Engineering Sciences*, 370(1981):5767–82, 2012.

[15] B Canals, I-A Chioar, V-D Nguyen, M Hehn, D Lacour, F Montaigne, A Locatelli, T O Menteş, B S Burgos, and N Rougemaille. Fragmentation of magnetism in artificial kagome dipolar spin ice. *Nature Communications*, 7:11446, 2016.

[16] A Farhan, A Kleibert, P M Derlet, L Anghinolfi, A Balan, R V Chopdekar, M Wyss, S Gliga, F Nolting, and L J Heyderman. Thermally induced magnetic relaxation in building blocks of artificial kagome spin ice. *Physical Review B*, 89(21):214405, 2014.

[17] S A Morley, A Stein, M C Rosamond, D Alba Venero, A Hrabec, Philippa M Shepley, M-Y Im, P Fischer, M T Bryan, D A Allwood, P Steadman, S Langridge, and C H. Marrows. Temperature and magnetic-field driven dynamics in artificial magnetic square ice. In *Spintronics VIII*, volume 9551, page 95511Q. International Society for Optics and Photonics, 2015.

[18] E Mengotti, L J Heyderman, A F Rodríguez, F Nolting, Remo V Hügli, and H-B Braun. Real-space observation of emergent magnetic monopoles and associated dirac strings in artificial kagome spin ice. *Nature Physics*, 7(1):68, 2011.

[19] J Drisko, T Marsh, and J Cumings. Topological frustration of artificial spin ice. *Nature Communications*, 8:14009, 2017.

[20] P E Lammert, X L Ke, J Li, C Nisoli, D M. Garand, V H Crespi, and P Schiffer. Direct entropy determination and application to artificial spin ice. *Nature Physics*, 6:786–789, 2010.

[21] R C Silva, R J C Lopes, L A S Mól, W A Moura-Melo, G M Wysin, and A R Pereira. Nambu monopoles interacting with lattice defects in a two-dimensional artificial square spin ice. *Physical Review B*, 87:014414, 2013.

[22] S Ladak, D E Read, W R Branford, and L F Cohen. Direct observation and control of magnetic monopole defects in an artificial spin-ice material. *New Journal of Physics*, 13:359–363, 2011.

[23] X Zhou, G-L Chua, N Singh, and A O Adeyeye. Large area artificial spin ice and anti-spin ice $Ni_{80}Fe_{20}$ structures: Static and dynamic behavior. *Advanced Functional Materials*, 26(9):1437, 2016.

[24] M B Jungfleisch, W Zhang, E Iacocca, J Sklenar, J Ding, W Jiang, S Zhang, J E Pearson, V Novosad, J B Ketterson, et al. Dynamic response of an artificial square spin ice. *Physical Review B*, 93(10):100401, 2016.

[25] S Gliga, A Kákay, R Hertel, and O G Heinonen. Spectral analysis of topological defects in an artificial spin-ice lattice. *Physical review letters*, 110(11):117205, 2013.

[26] G-W Chern, M J Morrison, and C Nisoli. Degeneracy and criticality from emergent frustration in artificial spin ice. *Physical Review Letters*, 111(17):177201, 2013.

[27] D Shi, Z Budrikis, A Stein, S A Morley, P D Olmsted, G Burnell, and C H Marrows. Frustration and thermalisation in an artificial magnetic quasicrystal. *Nature Physics*, 14:309, 2018.

[28] V S Bhat, J Sklenar, B Farmer, J Woods, J T Hastings, S J Lee, J B Ketterson, and L E De Long. Controlled magnetic reversal in permalloy films patterned into artificial quasicrystals. *Physical Review Letters*, 111(7):077201, 2013.

[29] V S Bhat, J Sklenar, B Farmer, J Woods, J B Ketterson, J T Hastings, and L E De Long. Ferromagnetic resonance study of eightfold artificial ferromagnetic quasicrystals. *Journal of Applied Physics*, 115(17):17C502, 2014.

[30] Z Budrikis, J P Morgan, J Akerman, A Stein, P Politi, S Langridge, C H Marrows, and R L Stamps. Disorder strength and field-driven ground state domain formation in artificial spin ice: Experiment, simulation, and theory. *Physical Review Letters*, 109(3):037203, 2012.

[31] G W Chern, P Mellado, and O Tchernyshyov. Two-stage ordering of spins in dipolar spin ice on the kagome lattice. *Physical Review Letters*, 106:207202, 2011.

[32] E Iacocca, S Gliga, R L Stamps, and O Heinonen. Reconfigurable wave band structure of an artificial square ice. *Physical Review B*, 93:134420, 2015.

[33] S Gliga, A Kákay, L J Heyderman, R Hertel, and O G Heinonen. Broken vertex symmetry and finite zero-point entropy in the artificial square ice ground state. *Physical Review B*, 92:060413, 2015.

[34] C Castelnovo, R Moessner, and S L Sondhi. Magnetic monopoles in spin ice. *Nature*, 451(7174):42, 2008.

[35] D B Williams and C B Carter. The transmission electron microscopy. In *Transmission electron microscopy*, page 14. Springer, New York, 1996.

[36] Y Qi, T Brintlinger, and J Cumings. Direct observation of the ice rule in an artificial kagome spin ice. *Physical Review B*, 77(9):094418, 2008.

[37] Y Li, G Gubbiotti, F Casoli, F J T Goncalves, S A Morley, M C Rosamond, E Linfield, H Marrows, S Mcvitie, and R L Stamps. Brillouin light scattering study of magnetic normal mode in square artificial spin ice. *Journal of Physics D*, 50:015003, 2017.

[38] Y L Li, K Xu, S Y Hu, J Suter, D K Schreiber, P Ramuhalli, B R Johnson, and J McCloy. Computational and experimental investigations of magnetic domain

structures in patterned magnetic thin films. *Journal of Physics D: Applied Physics*, 48(30):305001, 2015.

[39] S Middelhoek. Domain walls in thin Ni-Fe films. *Journal of Applied Physics*, 34(4):1054–1059, 1963.

[40] D Lee, R K. Behera, P P Wu, H X Xu, Y L Li, S B. Sinnott, S R. Phillpot, L Q Chen, and V Gopalan. Mixed Bloch-Néel-Ising character of 180° ferroelectric domain walls. *Physical Review B*, 80(6):060102, 2009.

[41] M Löhndorf, A Wadas, H A M Van Den Berg, and R Wiesendanger. Structure of cross-tie wall in thin Co films resolved by magnetic force microscopy. *Applied Physics Letters*, 68(25):3635–3637, 1996.

[42] D Meier. Functional domain walls in multiferroics. *Journal of Physics: Condensed Matter*, 27(46):463003, 2015.

[43] K J O'Shea, S McVitie, J N Chapman, and J M R Weaver. Direct observation of changes to domain wall structures in magnetic nanowires of varying width. *Applied Physics Letters*, 93(20):202505, 2008.

[44] G Chen, T P Ma, H Kwon, C Won, Y Z Wu, A K Schmid, et al. Tailoring the chirality of magnetic domain walls by interface engineering. *Nature Communications*, 4:2671, 2013.

[45] C Nisoli, R F Wang, J Li, W F McConville, P E Lammert, P Schiffer, and V H Crespi. Ground state lost but degeneracy found: The effective thermodynamics of artificial spin ice. *Physical Review Letters*, 98:217203, 2007.

[46] J H Rodrigues, L A S Mól, W A Moura-Melo, and A R Pereira. Efficient demagnetization protocol for the artificial triangular spin ice. *Applied Physics Letters*, 103(2013):092403, 2013.

[47] X Ke, J Li, C Nisoli, Paul E Lammert, W McConville, R F Wang, V H Crespi, and P Schiffer. Energy minimization and ac demagnetization in a nanomagnet array. *Physical Review Letters*, 101(3):037205, 2008.

[48] R F Wang, J Li, W McConville, C Nisoli, X Ke, J W Freeland, V Rose, M Grimsditch, P Lammert, V H Crespi, and P Schiffer. Demagnetization protocols for frustrated interacting nanomagnet arrays. *Journal of Applied Physics*, 101:09J104, 2007.

[49] J M Porro, A Bedoya-Pinto, A Berger, and P Vavassori. Exploring thermally induced states in square artificial spin-ice arrays. *New Journal of Physics*, 15(5):055012, 2013.

[50] R Macẽdo, F S Nascimento, G M Macauley, and R L Stamps. Apparent ferromagnetism in pinwheel-tiled spin ice. *Physics Review B*, 98:014437, 2018.

[51] W Rave and A Hubert. Magnetic ground state of a thin-film element. *IEEE Transactions on Magnetics*, 36(6):3886–3899, 2000.

7

Summary and outlook

7.1 Summary

ASI systems not only act as potential reconfigurable microwave resonator (in which the magnetisation dynamics can be governed by the underlying magnetisation configuration [1]) due to their complex magnetisation configurations being controlled by magnetic fields or temperature, but they also provide macropsins analogous of certain microscopic structures in atomic systems allowing insight into fundamental physics (i.e., mimics the geometrical frustration of the spin ice materials). This thesis investigates the static and dynamic magnetisation responses of the square and pinwheel ASIs to magnetic fields through experiments and simulations. The static magnetisation properties of square ASI was probed via alternating gradient force magnetometry. The magnetic behaviour of resonant dynamics in square ASI was characterised using Brillouin light scattering and ferromagnetic resonance methods. Micromagnetic simulations using Mumax package were carried out to aid interpretation of the magnetic properties. Finally, Lorentz transmission

electron microscopy was used to visualise magnetic structure of pinwheel ASI induced by an external field.

The field-dependent property of spin-wave excitations was initially explored in a square ASI array consisting of the 10 nm thick 240 × 80 nm^2 nanomagnets with a 450 nm centre-to-centre separation between the second nearest neighbours. The square ASI provides a way to compare the response of standing spin wave modes in two groups of elements, which are orthogonally aligned to one another, under the same magnetic field. It has been found that the frequency of spin-wave modes of an element is dependent upon whether the magnetisation lies along the easy or hard directions of the elements. When a saturating magnetic field is applied at 0° with respect to the square ASI lattices, the nanomagnet whose hard axis is aligned with the field appears more complex spin-wave modes than those whose easy axes lie with the field. This is due to the formation of more edge modes in the former. The main features of resonant dynamic modes can be well described as arising from an individual nanomagnet in a simulation, where interaction from neighbouring nanomagnets is not considered. This is the evidence to demonstrate that, at a saturation state of the ASI array, the inter-island interaction between those nanomagnets is not sufficiently strong to shift the spin-wave frequency. Furthermore, the field angle with respect to the ASI lattice was found to create significant variance in standing spin-wave frequency spectrum. This suggests that square ASI could be possible to act as a reconfigurable microwave resonator.

In principle the inter-island interaction is a key requirement to create a tunable magnonic crystal [1]). To strengthen the interaction, a 30 nm thick square ASI array of the same in-plane dimension was examined to compare to the 10 nm thick sample. These thicker nanomagnet possess larger local magnetic moment and generate stronger stray field, increasing the coupling between nanomagnets. BLS experiment and simulations demonstrate that the coercivity and dynamic response of the ASI array can be tailored through changes in nanomagnet thickness. In particular, the 30 nm thick elements show the evidence for stronger static field interactions. The inter-element interaction was found to reduce the coercivity of entire array by the cooperative effects assisting the reversal of elements at the array edges. A comparison between BLS experiments and simulations suggests this interaction may also contribute weakly to the spin-wave spectra as the agreement is not as good as the 10 nm thick specimen. Most of the standing spin wave modes

arise from the pinning excitations at the island edge. Softening observed in edge mode spectra as a function of applied magnetic field can be identified with reversal of different orientations of magnetic islands. This allows us to distinguish reversals of elements with axes parallel and perpendicular to the applied magnetic field.

Lastly, it has been experimentally demonstrated that a square ASI can be tuned to a 'pinwheel' ASI behaving as a 'synthetic ferromagnet', where one can observe a ferromagnetic magnetisation process mediated by the domain-wall-like configurations. This modified square ASI is named 'pinwheel ASI'. The transformation of the geometry leads to a dramatic change in the energy landscape, showing that the maximum energy spread between vertex configurations of pinwheel lattice sharply reduced by a factor of 29 times in comparison with that of square lattice. This system is said to be nearly degenerate. An interesting finding in such a system is the presence of domain-wall-like magnetisation topologies. Some of these mesoscopic domain walls topologies, such as 180N, 90N and 180X walls, resemble the magnetic structure Néel and cross-tie walls seen in natural ferromagnetic film, whereas others mimic the configuration of charged walls found in ferroelectric materials. These charged walls have the well-defined charge ordering and the Néel rotation over the discrete moments. Intriguingly, the easy axes of this ASI array appears to be misaligned with the array geometry.

Monte Carlo simulations suggest that the ground state of an pinwheel array possesses "closure" structures [2]. However, by employing AC-field demagnetisation experiment, results show that the final state of the pinwheel array approaches a short-range ordering, a mixture of four types of vertex topologies, due to the intrinsic nature of a nearly-degenerated energy landscape and nonequilibrium dynamics in a frustrated system.

7.2 Future work

Building upon the results in this thesis, a number of research projects are currently or will be carried out. Five preliminary and prospective directions are described below.

Although the magnetisation dynamics of square ASI systems can be controlled by the orientation of magnetic field with respect to the lattices, such square ASI systems have weak effect of inter-island interaction on the magnetisation dynamics. For the purpose of creation of magnonic crystal, ways to enhance the dipole stray field arising from each

nanomagnet should be considered. Currently, the vast majority of ASI samples were patterned on an oxidised silicon substrate so that the stray fields of the nanomagnets primarily permeate their surrounding air and silicon. As is well known, the factors that determine the strength of the stray field in an ASI system are the magnetic moment of nanomagnet, the lattice constant and the magnetic permeability of surrounding materials. The influences of the magnetic moment and the lattice constant have been explored experimentally and numerically. However, the magnetic dynamics in our square ASI lattices is not significant in the measurement. Here the question of what if the magnetic permeability is increased in an ASI array can be posed? To attain this attempt, one approach is to pattern ASI array on a magnetic layer with high magnetic permeability, such as Yttrium iron garnet (YIG) [3]. Another approach is to form the islands in FeAl film by low dose FIB irradiation which transforms the paramagnetic film to ferromagnetic in the irradiated regions without milling it. By varying the dose in and between the islands, the coupling could be varied between different arrays and even across a single array. Another advantage of this approach is that the magnetisation can be more easily imaged, since the mean inner-potential is approximately unchanged by irradiation and, because of this, the edge states of each island can be more easily observed in TEM.

An interesting prediction in pinwheel ASI is a ferromagnetic ground state with the structures of the closure (in a square-shape array) or Landau (in a rectangular-shape array) domains [2]. The AC field demagnetisation protocol developed here did not produce a long-range closure ground state in the pinwheel ASI, a *square*-shape array , but obtained a short-range magnetisation structure instead. Another possible method to attain the ground state is to thermally anneal the system [4–6]. One feasible way is to investigate the temperature-induced magnetisation dynamics using in-situ imaging in our state-of-the-art Lorentz TEM at the University of Glasgow.

The dynamic behaviour of the mesoscopic domain wall also is of interest. For example, open questions include what the velocities of these domain walls are and how stable they are. To solve the problem of measuring time-dependent dynamics, Medipix3 [8], a direct electron detector developed at the University of Glasgow, can be performed to image the propagation of domain wall. This Medipix3 detector can offer a sustainability of acquisition on the order of millisecond. Thus, it allows us to image time-dependent magnetisation dynamics of ASI system with much greater time resolution in comparison

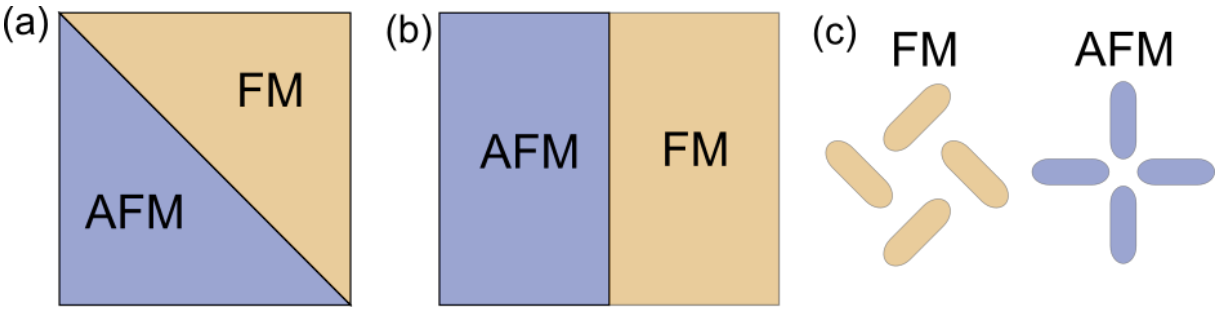

Figure 7.1: Possible schematics to realise hybrid ASI sample that consists of the square and pinwheel ASI arrays. The interface separating two structures is localised along (a) diagonal and (b) vertical directions. (c) The units of square and pinwheel lattices [7].

to the conventional CCD detector.

Intriguingly, it was found that the pinwheel ASI specimen studied in Chapter 6 emerged the time-dependent behaviour when the magnetic field is in the vicinity of the coercive field. Specifically, the macrospin in some nanomagnets were observed to flip during a time period at a fixed field. The Medipix3 provides a possibility to study this thermally relaxing phenomenon of the pinwheel ASI.

Finally, a hybrid ASI, constructed by an antiferromagnetic square ASI array and a ferromagnetic pinwheel ASI array (see Fig. 7.1), is proposed [7]. This system presents a possible way to investigate exchange anisotropy. This is a result of the interaction between antiferromagnetic and ferromagnetic orders. The exchange interaction leads to a displacement of the hysteresis loop along the field axis. This phenomenon has been observed in magnetic materials, consisting of the ferromagnetic fine cobalt particle and the antiferromagnetic cobaltous oxide, below its Néel temperature [9].

With this programme of future work, artificial spin ice is certainly no frozen field of science!

Bibliography

[1] L J Heyderman and R L Stamps. Artificial ferroic systems: novel functionality from structure, interactions and dynamics. *Journal of Physics: Condensed Matter*, 25(36):363201, 2013.

[2] R Macẽdo, F S Nascimento, G M Macauley, and R L Stamps. Apparent ferromagnetism in pinwheel-tiled spin ice. *Physics Review B*, 98:014437, 2018.

[3] V Korenivski, R B Van Dover, P M Mankiewich, Z-X Ma, A J Becker, P A Polakos, and V J Fratello. A method to measure the complex permeability of thin films at ultra-high frequencies. *IEEE Transactions on Magnetics*, 32(5):4905–4907, 1996.

[4] J M Porro, A Bedoya-Pinto, A Berger, and P Vavassori. Exploring thermally induced states in square artificial spin-ice arrays. *New Journal of Physics*, 15(5):055012, 2013.

[5] A Farhan, P M Derlet, A Kleibert, A Balan, R V Chopdekar, M Wyss, L Anghinolfi, F Nolting, and L J Heyderman. Exploring hyper-cubic energy landscapes in thermally active finite artificial spin-ice systems. *Nature Physics*, 9(6):375, 2013.

[6] A Farhan, A Kleibert, P M Derlet, L Anghinolfi, A Balan, R V Chopdekar, M Wyss, S Gliga, F Nolting, and L J Heyderman. Thermally induced magnetic relaxation in building blocks of artificial kagome spin ice. *Physical Review B*, 89(21):214405, 2014.

[7] Gavin Macauley at the University of Glasogw designed the hybrid ASI sample and Sebastian Gliga plan to conduct the thermal measurement using peem combined with xmcd.

[8] M Krajnak, D McGrouther, D Maneuski, V O'Shea, and S McVitie. Pixelated detectors and improved efficiency for magnetic imaging in STEM differential phase contrast. *Ultramicroscopy*, 165:42–50, 2016.

[9] W H Meiklejohn and C P Bean. New magnetic anisotropy. *Physical Review*, 105(3):904, 1957.